Study of Inclined Dense Jet Behavior on Sloped Bottom in Stagnant Water through Numerical and Experimental Approaches

Wang, Xinyun

Thesis submitted to the University of Ottawa
in partial Fulfillment of the requirements for the
Doctorate in Philosophy Civil Engineering

Department of Civil Engineering
Faculty of Engineering
University of Ottawa

Abstract

Desalination plants have contributed significantly to relieving global freshwater scarcity. However, the highly concentrated byproduct brine from the desalination process is usually discharged back into the ocean, making the design of the outfall system a critical concern to prevent further pollution and damage to the oceanic ecosystem. Inclined dense jet is a common method for discharging highly concentrated brine. Numerous studies of inclined dense jet have been done, and the discharge performance is influenced by several factors. However, research on the receiving bottom remains limited, especially considering the long-term effects of continuous discharge. Investigating the behavior of inclined dense jet on sloped bottoms is therefore essential. This study focuses on the characteristics of single-port inclined jets on sloped bottoms and their impact on the jet development process. We investigate the behavior of inclined dense jet over sloped bottoms using experimental measurements and computational fluid dynamics (CFD) simulations. Laboratory experiments were conducted with laser-induced fluorescence (LIF) to analyze concentration distributions of inclined dense jet with three common discharge angles (30°,45°,60°) on four different sloped bottoms (0°,1°,3°,5°) discharged into a stationary environment. Large Eddy Simulation (LES) was employed to simulate jet dynamics and assess its reliability by comparing experimental results with one practical discharge angle (60°) on two different bottom conditions (0° and 5°). In addition, four different common Reynolds-Averaged Navier-Stokes (RANS) models were compared as a supplementary study to evaluate their performance for predicting the single-port inclined dense jet with three discharge angles (30°,45°,60°) on a horizontal bottom. Moreover, gene expression programming (GEP) was explored as an extended tool to develop predictive models based on part of experimental and numerical data to simply and easily access the geometrical and mixing properties of the inclined dense jet on different sloped bottoms.

The experimental results show that geometrical characteristics prior to the impact point are not affected by the bottom slope. However, both the impact point nondimensional location and the dilution value on different bottom surfaces can be described by linear equations. Increased turbulence intensity, higher dilution along the bottom, an extended mixing zone, and a thicker bottom layer jointly suggested that a sloped bottom could enhance mixing efficiency. In addition,

the Froude number (Fr) was found to significantly influence brine mixing along the sloped bottom, which suggested a potential direction for future studies.

In the numerical simulation, a multilayer mesh is used for LES, and the results are in good agreement with LIF experimental data. The concentration distribution at the impact point area can be described by a Gaussian surface-fitting formula. The comparison with the RANS models also verifies that LES has better performance than the RANS model in simulating larger discharge angles and dilution characteristics.

Although RANS models have been adopted in many studies of inclined dense jet or other engineering practices due to their low computational cost and reasonable results, the selection of different turbulence models will also affect the accuracy of the simulation results. As an extension of this research, a comparative study of different RANS models confirmed that they generally underestimate brine mixing. The results showed that when the jet angle exceeds 45°, RANS models tend to underpredict the jet trajectory and dilution, whereas their results remain reasonable when the discharge angle is below 45º.

In addition to traditional experimental and CFD approaches—which can be time-consuming for analyzing key characteristics of inclined dense jets over sloped bottoms—Gene Expression Programming (GEP), an evolutionary algorithm-based modeling approach, offers a user-friendly and efficient alternative. GEP could generate regression equations and provide a mathematical relationship between input and output variables. Based on experimental and LES data, it enables direct estimation of key geometric and concentration characteristics of the inclined dense jet with different discharge angles, including information along different bottom angles after the impact point.

These findings enhance the understanding of inclined dense jet behavior under different receiving bottom conditions and provide a practical approach for predicting important geometric and concentration characteristics. Future studies could explore a wider range of receiving bottom conditions and investigate the influence of Froude number on dilution results. Advanced experimental techniques such as PIV, 3D LIF, or other high-resolution methods are recommended to capture the velocity field and detailed turbulence characteristics along different bottom conditions. For numerical simulations, further investigations into alternative meshing strategies (such as dynamic mesh) or different CFD methods, such as SPH (Smoothed Particle Hydrodynamics), could help improve computational efficiency while reducing costs. The expansion of datasets from experiments, numerical simulations, and field studies of inclined dense jets under various conditions could enhance the training of GEP models as a potential predictive tool for estimating key jet parameters efficiently for rapid and early-stage design.

Acknowledgements

First and foremost, I would like to express my deepest gratitude to my supervisor, Dr.Abdolmajid Mohammadian. Over the past seven years, he has provided me with immense support and encouragement, not only in my academic journey but also in my life. Without his guidance and support, I would not have been able to successfully complete my master's and doctoral studies at the University of Ottawa.

Additionally, I am especially grateful to one Italian professor, Dr.Simone Ferrari, who provided me with a valuable experimental opportunity at the University of Cagliari in 2023 and offered laboratory facilities that enabled me to complete the most critical experimental part of my research. I also sincerely thank Dr. Phillip Roberts for his invaluable suggestions during the experiments and revision of the paper.

I would also like to extend my appreciation to the members of my PhD thesis committee, Dr. Hossein Bonakdari, Dr.Ahmad Shakibaeinia, Dr.Ousmane Seidou and Dr.Hamidreza Shirkhani, who kindly agreed to review my thesis and offered valuable comments and feedback during the defence.

Special thanks to Mark and Leo for their various forms of assistance during my experiments at the University of Ottawa. Other thanks go to my fellow members at the University of Ottawa, Danial, Sina, Mostafa, Ahmad and Ruijie for their support and assistance throughout my research. I am also grateful to Xueming and Chuyao, even after they returned to China, they kept in touch and encouraged me during my PhD journey. Additionally, I would like to thank my friend Vicky and many others in Ottawa for their warmth and support in my daily life.

Finally, I would like to express my heartfelt gratitude to my parents, Jiangwen Wang and Xiuqin He, and my husband, Mohan Ni and my mother-in-law, Hua Lyu. Without their unconditional support and encouragement, it would have been incredibly difficult for me to persevere through this journey. Lastly, my deep thanks to my adorable cat, JoJo, whose companionship has also brought laughter and joy.

To mom and dad, who gave me life and a body strong enough to carry my dreams.

To Mohan, for a love that doesn't shine, but stays.

To Max, a living miracle and the brightest part of my world.

To myself- may I keep eating well, lifting heavy, staying sharp, and standing strong.

Table of Contents

List of Figures

List of Tables

List of Abbreviations

IDJ	Inclined Dense Jet
LES	Large eddy simulation
RANS	Reynolds Averaged Navier Stokes
SWRO	Seawater Reverse Osmosis
RO	Reverse osmosis
MSF	Multi-Stage Flash
MED	Multi-Effect Distillation
PIV	Particle Image Velocimetry
LIF	Laser-Induced Fluorescence
AI	Artificial Intelligence
PTV	Particle Tracking Velocimetry
DPTV	Digital Particle Tracking Velocimetry
PLIF	Planar Laser-Induced Fluorescence
LA	Light Attenuation
PIV	Particle Image Velocimetry
USEPA	U.S. Environmental Protection Agency
CORMIX	Cornell Mixing Zone Expert System
DNS	Direct Numerical Simulation
LES	Large Eddy Simulation
RANS	Reynolds-Averaged Navier–Stokes
SST	Shear Stress Transport
RNG	Renormalization Group
LRR	Launder–Reece–Rodi
SGDH	Standard Boussinesq Gradient Diffusion Hypothesis
GGDH	Generally Gradient Diffusion Hypothesis
RTSN	Regional Turbulence Schmidt Number
SGS	Sub-Grid Scale
GEP	Gene Expression Programming
GA	Genetic Algorithms

GP	Genetic Programming
CFD	Computational Fluid Dynamics
FVM	Finite Volume Method
MAPE	Mean Absolute Percentage Error
MSE	Mean Squared Error
RMSE	Root Mean Squared Error
MAE	Mean Absolute Error
MAD	Mean Absolute Deviation
MARE	Mean Absolute Relative Error
RAE	Relative Absolute Error
RSE	Relative Squared Error
RRSE	Root Relative Squared Error
MCA	Monte Carlo Analysis

List of Symbols

Symbol	Description
C	local brine concentration
C_0	initial concentration
C_{max}	maximum concentration
D/d	diameter of the discharge port (m)
Fr/F	densimetric Froude number
g	gravitational acceleration (m/s^2)
U_0	discharge velocity (m/s)
ρ_a	ambient water density (kg/m^3)
ρ_0	brine density (kg/m^3)
α	discharge angle (º)
β	sloped angle (º)
u, v	velocity in x-, y- direction, respectively
Δ	LES filter width
k	turbulent kinetic energy (m^2/s^2)
ε	turbulent dissipation rate (m^2/s^3)
L, W, H	length, width and height of the computational domain (m)
C_1,C_2	empirical coefficients for geometrical and dilution information
t	Time (s)
x, y, z	Cartesian coordinates in the horizontal, vertical and lateral direction
Xi	impact point location (m)
Xc	horizontal location of the centerline peak (m)
Yc	vertical location of the centerline peak (m)
Yt	terminal rise height (m)
S	dilution
Sm	dilution at the centerline peak
Si	dilution at the impact point
R	correlation coefficient

$E(\kappa)$	energy spectrum (m^3/s^2)
κ	Wavenumber (m^{-1})
$\bar{u}(x)$	time-averaged component in RANS
$u'(x)$	fluctuating component in RANS
σ^2	variance of concentration (–)
s	streamwise distance along centerline (m)
b_c	spreading width based on concentration (m)
b_u	spreading width based on velocity (m)
τ_{ij}	SGS Reynold stress (m^2/s^2)
μ	viscosity ($N.s/m^2$)
M_0	kinematic momentum flux (m^4/s^2)
p	pressure (N/m^2)
Q	flow rate (m^3/s)
S_{ij}	the strain tensor
τ_{ij}	Reynolds stress

Chapter 1 Introduction

1.1 Background

"Thousands have lived without love, not one without water." - W. H. Auden.

We cannot overemphasize the importance of water to our planet.

Oceans cover over 70% of Earth's surface, yet directly accessible surface freshwater accounts for only about 0.3% of Earth's total water. Most freshwater is inaccessible, stored underground or locked in glaciers. According to a United Nations report, global freshwater use has been increasing by 1% annually, with agriculture accounting for over 72% of total water withdrawals, rising by 5% per year (UNESCO World Water Assessment Programme 2024). As the global population is predicted to reach 9.8 billion by 2050, freshwater demand will grow significantly. Meanwhile, climate change, driven by droughts and shifting precipitation patterns, exacerbates water shortages. Currently, over half of the world's population faces severe water scarcity (Figure 1.1), with more than a quarter experiencing 'extremely high' water stress, using over 80% of their renewable freshwater supply. This crisis is particularly severe in arid and semi-arid regions such as the Middle East, North Africa, and South Asia.

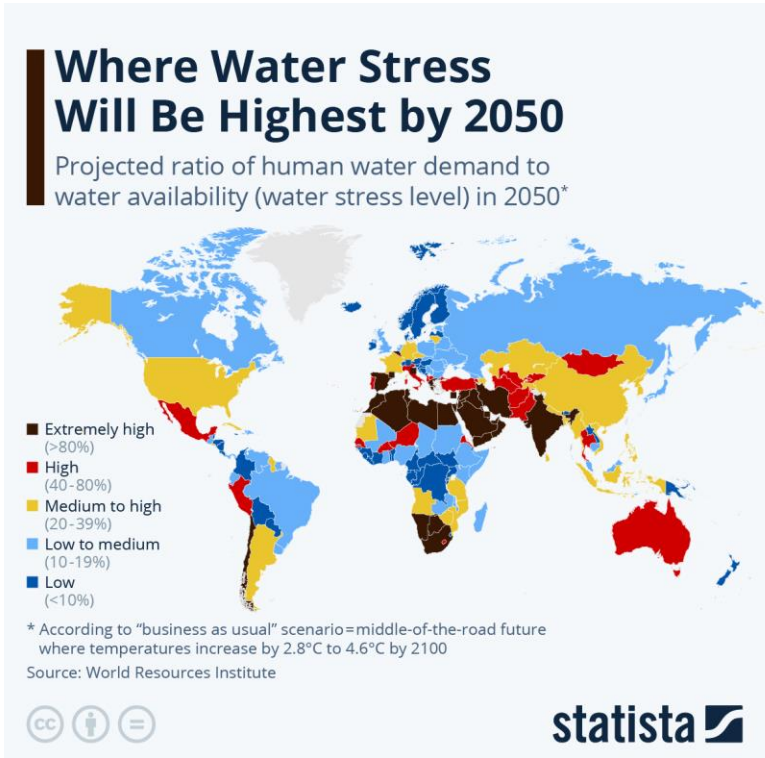

Figure 1.1 Water scarcity map(https://www.statista.com/chart/26140/water-stress-projections-global/)

Desalination technology is now considered a critical method for addressing water shortages by converting seawater into usable freshwater. Currently, 15,906 plants are operating worldwide. As shown in Figure 1.2, many desalination plants are primarily concentrated along the Mediterranean coastlines, the Persian Gulf, and around the Red Sea(Jones et al. 2019). These desalination plants can produce 95.37 million cubic meters of freshwater daily (34.81 billion cubic meters annually), which significantly relieves the local water scarcity.

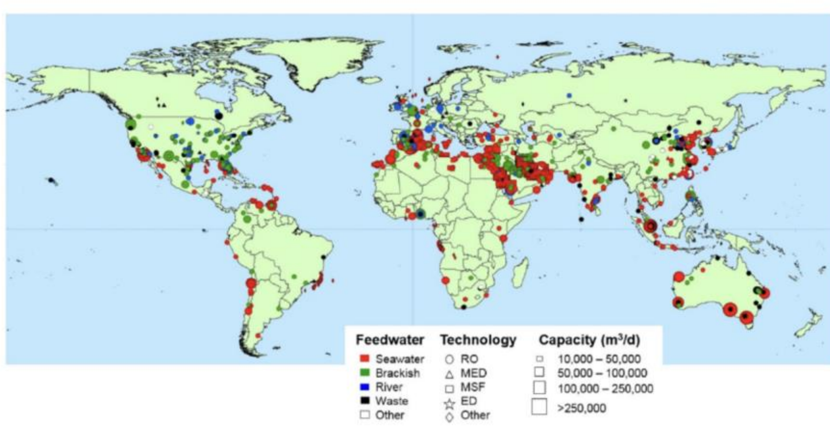

Figure 1.2 A global overview of desalination plants(Jones et al. 2019).

1.2 Current challenges faced by desalination plants

Despite over 60 years of desalination advancements, the constantly increasing demand for water and facilities still faces many challenges, including high energy consumption, environmental impacts, and concentrated brine disposal. For example, as shown in Figure 1.3, a typical SWRO (Seawater Reverse Osmosis) desalination process involves multiple steps, and each step has its challenges.

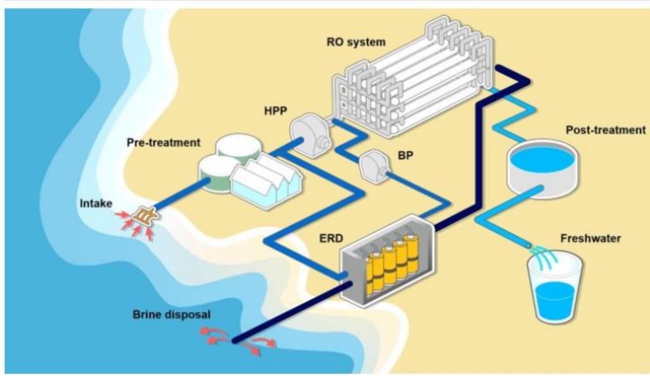

Figure 1.3 Schematic view of a typical SWRO desalination process. A pre-treated feed is supplied to the RO system with pressurization by HPP and BP, and the hydraulic pressure in the concentrate is recovered by ERD. RO: reverse osmosis. HPP: high-pressure pump. BP: booster pump. ERD: energy recovery device. (Kim et al. 2019)

(1) Intake System and Environmental Impact

The intake system requires a stable supply of clean water with minimal ecological impact. However, the ocean's dynamic nature, such as fluctuating shorelines, seabed conditions, and severe weather like hurricanes and typhoons, will pose challenges to the intake system. Seawater corrosion and marine organisms also contribute to clogging the intake system and increased maintenance demands (Missimer and Maliva 2018; Navarro and Lizaso 2021).

(2) High Energy Consumption

Most of the desalination technologies adopt membrane and thermal processes. Reverse osmosis (RO) is dominating due to its lower energy consumption and cost, which accounts for 64% of the global market. Multi-stage flash (MSF) distillation holds 23%, multi-effect distillation (MED) 8%, and other methods take 5%. Table 1.1 presents energy consumption types for different types of desalination technologies, including thermal and electrical needs, with examples of global desalination plants.

Table 1.1 Overview of main desalination technologies and energy requirements

Technology Type	Power Supply Method	Energy Consumption (Heat: MJ/m³)	Energy Consumption (Electricity: kWh/m³)	Principle	Typical Desalination Plants Worldwide
Multi-Stage Flash (MSF) Distillation	Mainly Thermal (Electricity as Secondary	200-380	3.6-4.4	Evaporation and condensation	The Jebel Ali Power and Desalination Plant (UAE), (Brebbia et al. 2013) Shuaiba (Saudi Arabia)
Multi-Effect Distillation (MED)	Mainly Thermal (Electricity as Secondary)	200-380	2.3	Evaporation and condensation	Yanbu (Saudi Arabia) (Al-Mutaz 2015)
Reverse Osmosis (RO)	Electricity	-	3.0-60	Pressure-driven filtration that separates salts from water through a semi-permeable membrane	Carlsbad (USA) (Graham 2005), Ashkelon (Israel) (Sauvet-Goichon 2007), Al Khafji (Saudi Arabia) Fujairah (UAE) (Sanza, Bonnélyea, and Cremerb 2007),
Electrodialysis	Electricity	-	5-8.0	Electric-driven separation of ions through selective ion-exchange membranes	Smaller-scale, limited use
Membrane Distillation	Mainly Thermal (Electricity as Secondary)	100-300	0.75	Evaporation through membranes with gas as a separating medium	Used in research and small-scale projects
Forward Osmosis	Extremely low energy consumption	-	-	Water extraction through osmotic pressure differences with the use of specific solution systems	-

The energy consumption of the desalination plants is still the main barrier to the expansion of desalination plants. For example, the Carlsbad desalination plant in California could process 190 million litres of seawater daily. However, with the high demand for electricity, its annual energy consumption could power 24,000 households, which is equivalent to a town of 70,000–80,000 people (Water 2019).

(3) Chemical Use and Disposal

During the desalination process, numerous chemical materials are used in each step. Especially for the intake system, some pretreatment chemicals are added to the intake water. For example, 21 desalination plants in the Red Sea region, including the Gulf of Aqaba and the Gulf of Suez, reported that the daily chemical discharges include 2,708 kg of chlorine, 36 kg of copper, and 9,478 kg of antiscalants (Hoepner and Lattemann 2003). Lattemann and Höpner (2008) analyzed the typical effluent properties from the RO and thermal MSF, including chlorine to control the biofouling, coagulants for the suspended solid removal(e.g. iron-III-chloride), heavy metal contaminants because of the corrosion, and cleaning chemicals, including alkaline or acidic solutions with plenty of additives (detergents (e.g. dodecyl sulphate), complexing agents (e.g. Ethylenediaminetetraacetic acid), oxidants (e.g. sodium perborate), biocides (e.g. formaldehyde). The use of these chemicals has raised another major concern regarding the desalination outfall system.

(4) Brine Management and Discharge Systems

This part is a critical component for the desalination plants. Since the desalination process removes most of the salt and mineral components of the seawater, the remaining concentrated solution (i.e. high-salinity brine) contains a very high concentration of salts, as well as the chemical material listed in the last subsection. Therefore, the proper brine discharge system aims to minimize environmental impact by diluting or carefully dispersing it back into the water resource environmental system. Improper discharge from desalination plants has led to significant environmental consequences in recent years. One notable example is the Mar Menor lagoon in southeastern Spain, where desalination plants have been discharging brine for years. Combined with untreated agricultural runoff, this has caused severe ecological degradation. In 2016, rising salinity and nutrient pollution triggered harmful algal blooms, resulting in the death of millions of fish and aquatic plants. A massive fish die-off was reported in 2019 (Figure 1.4). Heartbreakingly, this is not an isolated incident. Without effective management measures, this environmental hazard may continue to occur in more regions.

Figure 1.4 The casualties of an algal bloom in Mar Menor in 2018 (https://geographical.co.uk/science-environment/saving-mar-menor-europes-largest-salt-lagoon).

Figure 1.5 shows that, regardless of the desalination treatment method used, brine production results in varying total concentrations.

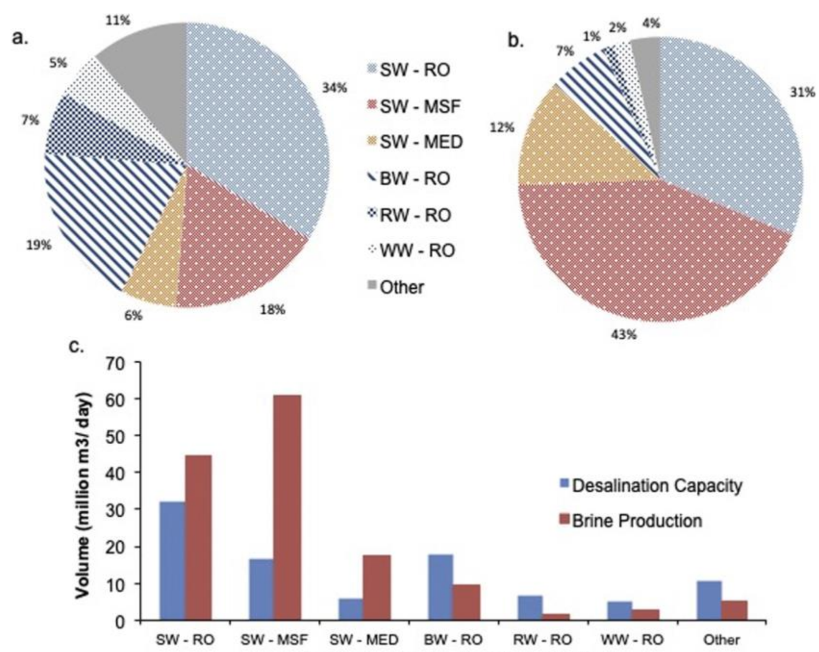

Figure 1.5 Major desalination feedwater-technology combinations by (a) global share in the desalinated water production (%), (b) global share in brine production (%) and (c) total desalination capacity and volume of brine produced (million m3/day(Ahmed et al. 2000).

Currently, the global brine production is around 141.5 million m^3/day, equal to 51.7 billion m^3/year, which is equivalent to one-third of Lake Ontario. The brine production is mainly concentrated in the Middle East and North Africa region, which accounts for 70.3% of global brine production. With this huge amount of brine water, various discharge methods have been proposed and studied to reduce the environmental impact of concentrated brine discharge. The treatment of the brine can be categorized as dilution and dispersion method, evaporation and concentration method, resource recovery and alternative disposal methods (Ahmed et al. 2000). No matter which method is used, brine has a high concentration of salts and other compounds, and its large volume will inevitably return to the natural environment. Therefore, it is crucial to minimize its harmful impact as much as possible.

(5) Long-term Monitoring and Environmental Assessment

Due to the long duration of desalination plant construction and operation, continuous monitoring and environmental assessment are important. As discussed above, the discharge of brine and the use of various chemicals can affect the salinity, temperature, and biodiversity of surrounding waters, particularly in sensitive areas such as coral reefs and mangroves. These facilities are typically associated with high energy consumption and emissions, which can impact air quality and contribute to the carbon footprint. With systematic monitoring and assessment, desalination plants can achieve a balance between environmental sustainability and water resource demands, ensuring that their long-term environmental impacts are effectively managed and predictable.

(6) Regulatory and Other

The desalination process involves the use of chemicals, high-salinity wastewater discharge, and high energy consumption. Therefore, governments need to establish strict standards to regulate discharge, energy use, and operations to mitigate ecological damage and reduce carbon emissions.

Desalination produces highly concentrated brine, and wastewater management remains a major challenge. The discharge of brine can lead to increased salinity in localized marine areas, affecting ecosystems and potentially causing pollution. Therefore, selecting an appropriate discharge method to minimize environmental impact has become a key issue in research and practice.

1.3 The method of discharge

Various discharge methods have been proposed and studied to reduce the environmental impact of concentrated brine discharge. Depending on the location of desalination plants, about 80% of brine is produced within 10 kilometres of the coastline and is typically discharged untreated into the sea. Therefore, ocean discharge is the primary choice globally. However, this method is unsuitable for inland desalination plants, which commonly discharge brine into sewers, deep well injection or use brine evaporation ponds.

(1) Surface discharge

Very few desalination plants have adopted direct surface discharge, the Hamma Water Desalination Plant (HWD) in Algeria being one of the few exceptions (Amokrane and Salmi 2021). This plant releases high-concentration brine directly into the shallow marine area through a single port without diffuser (Figure 1.6). The absence of diffusers or multiport designs causes the brine from the single outfall to quickly interact with the water surface, which creates a visually noticeable area of brine spreading. Surface spreading is difficult to define precisely due to environmental factors and brine characteristics, making its behavior complex and unpredictable. It implies that the outfall system of the HWD plant would face the risk of causing an ecological disaster similar to that of the Mar Menor lagoon.

Figure 1.6 Location of the HWD plant: image taken at 1.18 km altitude. From (Amokrane and Salmi 2021)

(2) Deep Well Injection

Deep well injection is not a common method for large-scale desalination plants, but some facilities adopt it, and it can also serve as a treatment for groundwater. For example, in the province of Friesland (in the Northern part of the Netherlands), the upwelling of brackish water has caused the salinization of well water, leading to challenges in fresh groundwater extraction(Wolthek et al. 2013). To address this, they extract the upwelling brackish water, desalinate it, and use the treated water as an additional source of drinking water. The concentrated brine is then discharged into a deeper aquifer through deep well injection. This helps maintain the stability of the fresh-brackish water interface in the aquifer.

(3) Brine Evaporation Pond

There are smaller desalination plants that adopted evaporation ponds to deal with the brine (Ahmed et al. 2000). For those desalination plants that are not located near the ocean, evaporation ponds are suitable for the disposal of brine in arid and semi-arid areas. The evaporation ponds are easy to build and have fewer maintenance and operation requirements compared with other discharge methods. It provides significant benefits both economically and environmentally. However, it is related to weather conditions, and it also has other environmental problems, such as soil salinity and the risk of potential leakage into the groundwater.

(4) Zero Liquid Discharge ZLD- Integrated Processes for Desalination and Salt Production

Zero Liquid Discharge is one of the most promising alternatives for brine management (Wenten et al. 2017)). This method is reusing brine, it not only helps reduce environmental pollution and achieve zero liquid discharge, but also enables the recovery of valuable salts. Figure 1.7 shows the total desalination cost and the value of recovered salts from many types of integrated processes. This approach increases water recovery, produces economically profitable salt, and helps reduce overall desalination costs by selling the valuable salt.

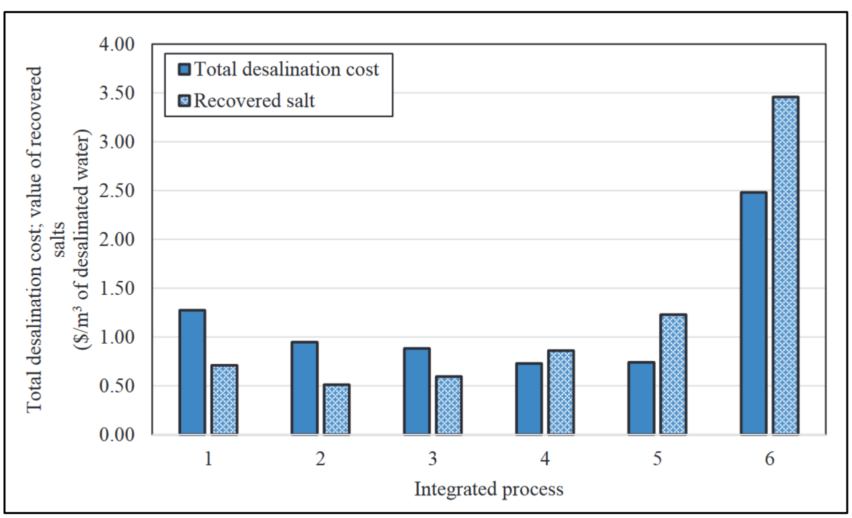

Figure 1.7 Total desalination cost and the value of recovered salts from integrated processes. Integrated process scheme: (1) ED-MSF-Crystallization; (2) UF-NF-MSF-Crystallization; (3) UF-NF-RO-MSF-Crystallization; (4) MF-NF/MCr-

RO/MCr; (5) MF-NF/MCr-RO/MD; (6) Precipitator/MF/drying bed/NF/RO/ED/MED/Precipitator/Evaporator-crystallizer (Sorour et al. 2015; Turek 2003; Turek and Dydo 2003; Wenten et al. 2017)).

(5) Marine Discharge

The application of the above discharge methods is often limited by factors such as production requirements, the ecological environment or hydrological dynamic conditions, climate, construction complexity and costs. Therefore, large desalination plants still primarily discharge brine directly into the ocean. This discharge method combines pipelines, diffusers, and discharge ports to enhance the mixing of brine. Brine is discharged through pressurized pipelines as a turbulent jet flow through a round nozzle and is commonly set submerged. This setup enhances the rapid mixing of the brine and the environmental impact on nearby marine areas.

Generally, the design of outfalls is classified based on different areas of emphasis. Based on the density difference between the brine and the surrounding receiving water, brine can be categorized as positive or negative buoyancy. Positive buoyancy generally occurs when the brine is treated before discharge and has a higher temperature than the surrounding water, causing the jet to rise toward the surface. In this case, temperature and density become key factors that control the jet's behavior. However, in most cases, brine exhibits negative buoyancy, meaning that its density is typically higher than that of the receiving water. Studying the characteristics of negatively buoyant jets is important for designing outfalls and other engineering applications.

Outfalls can be classified based on the number and distribution of ports as single-port or multiple-ports. If multiple ports are sufficiently far apart, they can be considered as single-port for research purposes. Thus, the distribution distance between multiple ports is a key area of study; depending on the receiving environment, it can be categorized into stagnant water and dynamic water environments. Stagnant water is rare in natural settings but can be considered the worst scenario for receiving environments. However, it is a good condition to study the detailed characteristics of brine jets and flows. Dynamic water environments typically include crossing flows and waves, the wave conditions being more realistic and more challenging to study. Density distribution also affects jet characteristics, leading the receiving water to be classified as stratified density and uniform density receiving water. The depth of the receiving water also affects the jet characteristics. Typically, discharge is fully submerged to minimize surface and visual pollution. These different areas of emphasis and conditions have been extensively studied experimentally and numerically. Table 1.2 lists several common jet studies under different classification conditions.

Table 1.2 Jet studies under different classification conditions.

	Single	Multiple
Numbers of port	12 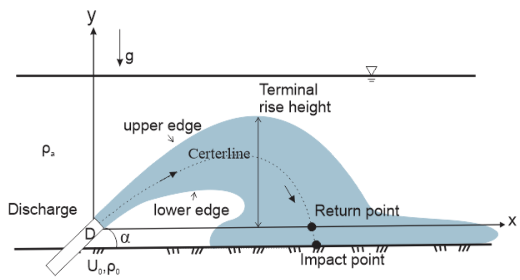	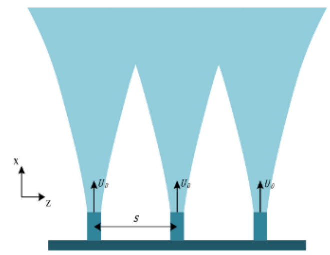 (Saeidi Hosseini et al. 2022)
	Stagnant water	Cross flow
Dynamical environment	 (Lai and Lee 2012)	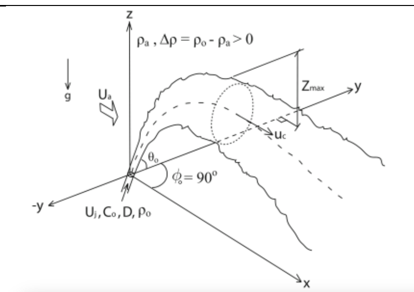 (Lai and Lee 2014)
	Uniform stagnant water	Un-uniform
Receiving water	 (Lai and Lee 2012)	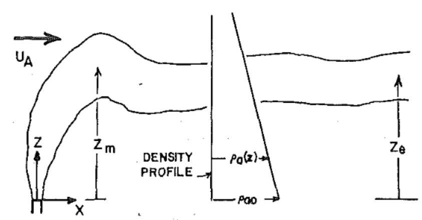 (J.Wright 1984)
	Fully submerged	Shallow water

Receiving water depth	 (Lai and Lee 2012)	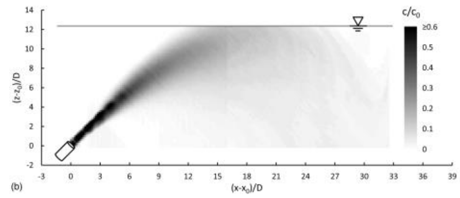 (Jiang, Law, and Lee 2014)

1.4 Statement of problem

Among the classifications mentioned, few studies have focused on the influence of sloped bottom surfaces on jet behavior. Considering the naturally sloped seabed, along with the high density and continuous discharge of brine at desalination outfalls, it is important to examine how brine spreads and mixes over inclined bottom surfaces. Even under complex ambient conditions, attention should be paid to the spreading and mixing characteristics of IDJ over sloped bottoms, as well as the potential impact of bottom slope on the overall mixing process. To the best of the author's knowledge, most existing studies on brine jets assume a horizontal bottom surface. While many investigations have explored the general behavior of dense jets, the specific dynamics of inclined dense jets interacting with sloped beds in stagnant water have not been thoroughly examined.

1.5 Research objectives

The primary objectives of this research are:

1. To use Laser-Induced Fluorescence (LIF) techniques to measure the concentration of IDJ at various discharge angles on different sloped bottom conditions in the stationary receiving environment. Analyze the behavior of inclined jets under varying bottom slope conditions.

2. To employ RANS and LES models to simulate the flow characteristics of IDJ over sloped bottoms, analyze the flow field structure and concentration distribution patterns, and evaluate the accuracy of these numerical approaches.

3. To evaluate the performance of different k-epsilon (k-ε) models for predicting IDJ in stagnant water. Assess the accuracy and applicability of these models and highlight their strengths and weaknesses to support model selection and application.

4. To train the Gene Expression Programming (GEP) model using selected experimental data and LES simulation results, and to develop equations for efficiently predicting key characteristics of IDJ under various discharge angles and bottom slopes. Additionally, to compare and analyze the effects of different model setups on prediction accuracy.

5. To investigate concentration variations of jets under various bottom conditions, and to support the design of discharge systems and long-term pollution management.

1.6 Novelty and contributions

1.6.1 Novelty

1. Comprehensive experimental coverage: Unlike previous studies that focused on limited bottom angles, this study systematically investigates inclined dense jets using LIF under a wide range of conditions, including three discharge angles, four bottom slopes, and three Froude numbers. Both longitudinal and transverse concentration profiles were captured and they provided important experimental data for near-bed mixing analysis.

2. Numerical modeling approach: The study combines LES and RANS models to simulate IDJ behavior over sloped bottoms and performs a comparison with experimental results. This assessment under varied slope conditions offers new insights into model reliability.

3. Integration of AI modeling (GEP): This study is among the first to integrate Gene Expression Programming with both experimental and LES data to generate predictive equations for IDJ with different discharge angles and sloped bottom. It not only demonstrates the potential of AI-based models in hydraulic applications but also evaluates how different GEP model settings affect prediction accuracy.

4. Evaluation of multiple RANS turbulence models: The study compares different RANS model formulations for predicting inclined jets, identifies the most appropriate model for various conditions, and highlights their limitations as guidance for future engineering use.

1.6.2 Contribution

This research fills a gap in existing studies by addressing the influence of sloped bottom on the characteristics of IDJ-a factor often overlooked in previous studies. By combining experimental observations with numerical simulations, the results demonstrate that bottom boundaries have an impact on the geometrical and dilution properties of IDJs. These findings emphasize the importance of considering receiving bottom configurations in the study of IDJs. The experimental and numerical studies also provide a comprehensive dataset for future comparison and validation. Furthermore, this study introduces Gene Expression Programming (GEP) to simplify the prediction of jet behavior under various discharge conditions. It also conducts a comparison of different turbulence models in the numerical simulation. The results may contribute to better understanding and decision-making in desalination outfall design and environmental protection efforts.

1.6.3 Structure of this thesis

This thesis is organized in a paper-based format and is divided into eight chapters.

Following this introduction chapter, Chapter 2 presents a detailed literature review on inclined jets and their environmental impacts.

Chapter 3 presents an experimental investigation of IDJs over sloped bottoms, and this work is submitted to *Desalination* and is currently under review.

Chapter 4 involves numerical simulations of IDJs on sloped bottoms and is submitted to *Environmental Fluid Mechanics* and is currently under review.

Chapters 5 and 6 extend the study through a data-driven approach using Gene Expression Programming (GEP). These chapters have been officially accepted as Chapter 14 and Chapter 15, respectively, in the edited volume Intelligence Systems for Earth, Environmental and Planetary Sciences: Methods, Models and Applications (Elsevier, 2024).

Wang, X. and Mohammadian, A. (2024). Application of gene expression programming for prediction of dilution of inclined dense jet after the impact point based on experimental data. In H. Bonakdari and S. J. Gumiere (Eds.), Intelligence systems for Earth, environmental and planetary sciences: Methods, models and applications (Chapter 14). Elsevier. ISBN: 9780443132926

Wang, X. and Mohammadian, A. (2024). Evolutionary prediction of geometrical and dilution characteristics of inclined dense jet over a sloped bottom using large eddy simulation. In H. Bonakdari and S. J. Gumiere (Eds.), Intelligence systems for Earth, environmental and planetary sciences: Methods, models and applications (Chapter 15). Elsevier. ISBN: 9780443132926

Chapter 7 further compares the performance of k-ε turbulence models in simulating inclined dense jets and has been published as a book chapter in Computational Fluid Dynamics: Novel Numerical and Computational Approaches – Methodology and Numerics (Springer Singapore, 2025).

Wang, X. and Mohammadian, A. (2025). A comparison of k-ε–type turbulence models for prediction of inclined dense jets. In D. Zeidan, A. Hidalgo, L. T. Zhang, and E. G. Da Silva (Eds.), Computational fluid dynamics: Novel numerical and computational approaches – Methodology and numerics (pp. 185–217). Springer Singapore. https://doi.org/10.1007/978-981-97-8152-2

Finally, Chapter 8 concludes the thesis by summarizing key findings, research contributions, and offering directions for future research.

The numerical simulations in this study were conducted using OpenFOAM. Key input files for Chapter 4 and Chapter 7 are included in Appendix D.

Chapter 2 Literature review

This chapter provides a comprehensive review of existing research on inclined dense jet discharge (single port) into stagnant water. The literature review is organized into the following sections, beginning with an introduction to the basic concepts of jet behavior and dense jet. Then, the author covers findings related to inclined dense jet under various conditions, as well as different research methods and approaches (mainly experimental and numerical). The existing literatures the on sloped bottoms are also included.

2.1 Negative buoyancy jet

Turbulent jets and plumes are very common in both natural environments and engineering applications, such as wastewater discharge, thermal releases, and desalination outfalls. The turbulent jets are momentum-driven flows, plumes are buoyancy-driven flows influenced by temperature or concentration differences(Turner 1966). Research on jets primarily focuses on their diffusion, momentum and mass transfer.

Schmidt (1957) used experiments with heated air jets to investigate the jet diffusion path, velocity, and temperature distribution in a uniform environment, He applied Prandtl's mixing - length hypothesis (Prandtl 1925) to assume that the turbulent transfer of the momentum and mass were locally similar under certain conditions, and based on this, he derived the variation of velocity and concentration profiles at jet's different heights. Albertson et al. (1950) conducted a foundational study on the diffusion characteristics of submerged jets; they combined theoretical analysis with experimental data to develop a model to describe the mean flow patterns from slots and orifices. They found out that the similarities of velocity profile and linear expansion of normal jet boundary and the velocity profile follows a Gaussian distribution. Velocity along the centerline u was inversely proportional to its travelling distance ($u \sim x^{-1}$)(Figure 2.1a). They also found that the volume flux over a cross-section increased linearly with the x-axis.

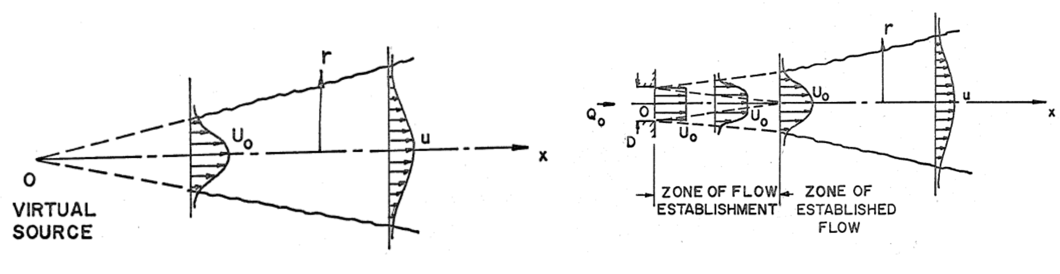

(a) (b)

Figure 2.1 The velocity profile of a simple jet (axisymmetric case) a: concept of a virtual source b: zone of flow establishment and zone of established flow (modified from Albertson et al. (1950))

For a practical problem, the jet will have two flow regions. First is a short region, so-called 'zone of flow establishment,' followed by the Gaussian distribution velocity region, which is called the 'zone of established flow' (Figure 2.1b). The length of establishment is around 6.2D (D is diameter) from experimental measurements. Forstall and Gaylord (1955) investigated the momentum and mass transfer characteristics of a submerged water jet diffusing into stagnant water. They used sodium chloride to map the diffusion profiles. They confirmed that the behavior of water jets resembles that of air jets, indicating that experimental constants derived from air jet studies, such as the turbulent Schmidt and Prandtl numbers, are also applicable to water jets.

Morton et al. (1956) have done some experiments on jets and plumes, and they extended the studies from the classical jet theory to buoyant jets and plumes. Unlike the jet, the plume has no initial momentum and is entirely driven by buoyancy, the plume's direction follows the direction of the buoyant force, and its momentum flux increases with height as the plume rises. In 1956, (Morton, Taylor, and Turner 1956) experimented with the convective expansion of the continuous and instantaneous buoyant sources in uniform and stratified environments, they injected a lighter fluid into the salty surrounding water to observe the development of buoyancy-driven flow. After three years, the same author (Morton 1959) conducted another experimental study to explore the diffusion behavior of forced plumes under the combined influence of buoyancy and momentum. He proposed an integral analysis to treat forced plumes as virtual point sources, simplifying the analysis of complex fluid diffusion driven by both forces. The behavior of plumes differs significantly between uniform and stratified environments: in uniform environments, plumes can rise indefinitely, while in stratified environments, increased buoyancy and momentum initially reduce plume height, only very high momentum flux could lead to greater diffusion height.

In studies of buoyancy-driven jets, buoyancy momentum is typically from density or temperature differences. The density differences would cause jets to deviate from initial paths, forming curved trajectories. This phenomenon is particularly relevant in combustion and environmental engineering, where buoyancy-driven jets occur frequently due to temperature or density gradients. C.H. Bosanquet, Horn, and Thring (1961) experimentally investigated how density variations influence turbulent jet trajectories. They used magnetite slurry into a transparent tank to simulate jet diffusion and observed how buoyancy affects jet paths. Figure 2.2 shows a photo of the jet during the experiments, where the jet path can be easily defined. They also developed a model predicting jet axis trajectories with initial velocity, density ratio, nozzle diameter, and inclination.

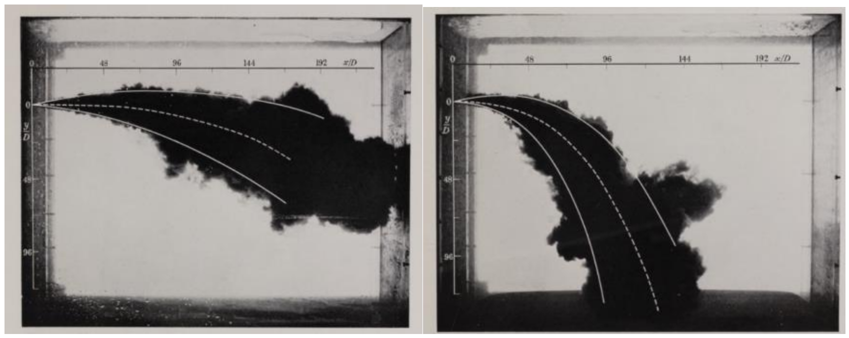

Figure 2.2 Photograph of jet path. Dash curve, predicted path full line curves, smoothed boundary (a)U_0 = 27.28 f t./s (b))U_0 = 8.87 f t./s (Bosanquet, Horn, and Thring, 1961)

Frankel and Cumming (1965) made concentration measurements in the buoyant jets to determine the center-line dilution ratios along the jet path. They concluded that density differences affect the jet behaviour. Turner (1966) examined the effects of negative or reversing buoyancy on jet and plume dynamics, particularly under conditions where buoyancy initially drives upward motion but eventually causes the flow to reverse or oscillate. He discharged a salt jet vertically into a tank full of fresh water to observe the height of jet. The results show that buoyant jet would rise to a certain height before the effect of gravity caused it to reverse direction and fall back down (Figure 2.3). Besides the experiments with buoyant jet, Turner also utilized a mixture of alcohol and glycol to create a "reversing buoyancy" effect that simulated nonlinear density changes of the plume flow (Figure 2.4).

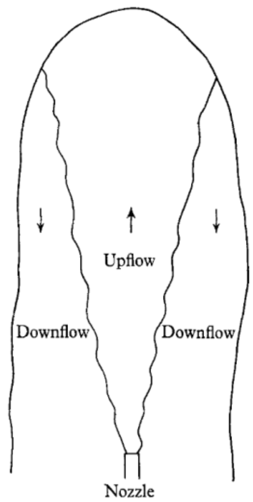

Figure 2.3 Sketch of the up-downflow regions in a heavy salt jet projected upwards. The outer boundary is approximately to scale but the inner boundary is schematic only (Turner 1966)

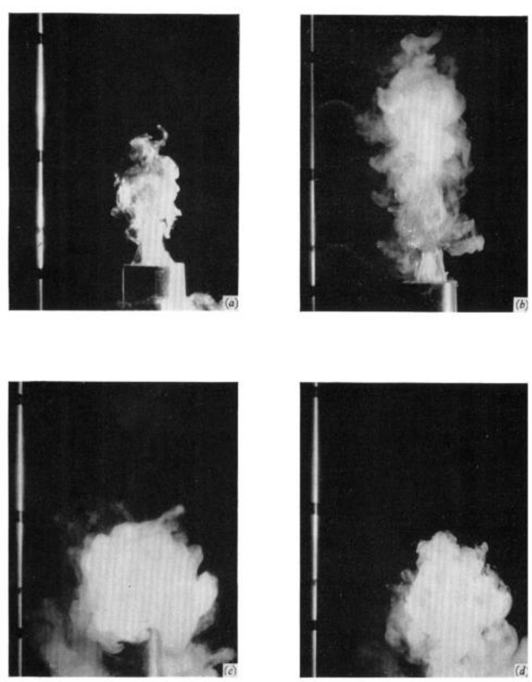

Figure 2.4 Photographs showing the various stages of growth and decay of an 'evaporating' plume described in the test: (a)the motion begins like n 'starting plume'; (b)negative buoyancy accumulat.rs in the cap; (c) the plume collapses; (d) a new 'tower' begins to break through (Turner 1966).

Abraham (1967) carried out research similar to Turner's. However, he focused more on the negative buoyancy jet in the uniform environment, especially the diffusion path of the salty dense jet, which was projected by the initial momentum. They proposed a mathematical solution to predict the process of the jet rising to a "ceiling" height and falling back to the bottom due to the density difference and gravity. Similar to Figure 2.3, Abraham found that the flux changes and the ceiling height is not constant when the flow first reaches the ceiling. However, once the flow stabilizes, the ceiling height can become constant.

2.2 Inclined dense jet- IDJ

When the jet has a higher density and is discharged with an upwards inclination angle of less than 90 degrees, it will show different properties and development as a vertical negative buoyancy jet. It is usually called inclined dense jet (IDJ). IDJs are widely used in desalination plant outfalls because they can effectively mix with the surrounding water. Figure 2.5 shows the typical schematic figure of the IDJ discharged into a stagnant and homogeneous water environment.

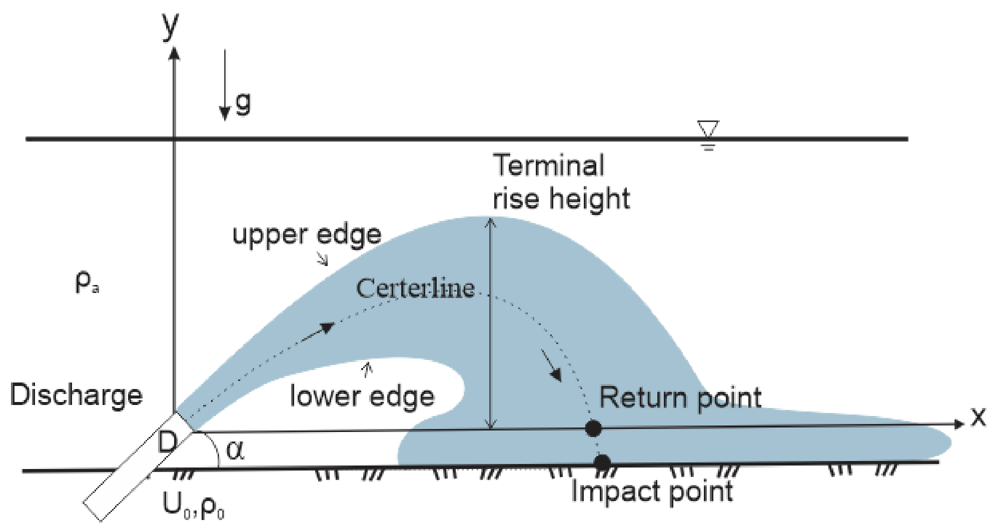

Figure 2.5 Diagram of IDJ discharged into stationary ambient water submerged.

Unlike vertical jets in stagnant water, which tend to fold back onto themselves, IDJ moves initially in the direction of its initial momentum due to the inclination angle to the horizontal bottom(α). When the IDJ reaches its maximum height, it then falls back to the bottom due to density differences and gravity. IDJ has a longer trajectory, and it will continue moving along the bottom after it falls on the ground if it is not diluted completely. This process helps dilute the brine and reduce its impact on the marine environment. The terminal rise height refers to the maximum height the jet can reach, the return point is where the jet returns to the height of the discharge nozzle, and the impact point is where the jet touches the bottom. The properties of these points are critical in outfall design. The main goal of studying IDJ is to support the design and analysis of outfall systems, which need to be adjusted based on site-specific conditions. To ensure the results are generalizable, it is important to apply dimensionless coefficients for scaling.

Dimensional analysis of IDJ

Back to the research of (Turner 1966), he pointed out that all the characteristic parameters of the negatively-buoyant jet are mainly controlled by two terms, which are the source momentum flux M_0 and the (negative) source buoyancy flux B, the equation is written as

$$M_0 = \pi D^2 U_0^2 \quad (2.1)$$

$$B = \pi D^2 U_0 g \quad (2.2)$$

where the D is the nozzle radius, U_0 is the discharge velocity (m/s), g' is the effective gravitational acceleration, written as:

$$g'_0 = g\frac{(\rho_0 - \rho_a)}{\rho_a} \quad (2.3)$$

All the properties of the IDJ can be scaled in terms of the combination of these two fluxes.

For example, the geometric properties such as the maximum height of the jet Z_m or Y_t, can be expressed with these two fluxes as :

$$Z_m = \boldsymbol{C} M_0^{\frac{3}{4}} B_0^{-\frac{1}{2}} \quad (2.4)$$

C is the constant that can be derived from experiments or practical applications.

Based on the above analysis, Pincince and List (1973), Roberts, Ferrier, and Daviero (1997) and Roberts and Toms (1987) presented more detailed dimension analysis for IDJ. According to Roberts et al. (1997), the IDJ can be described by momentum M and buoyancy B, which are the same as Turner's research, but one extra flux of volume Q is also considered into the jet analysis, the fluxes of volume Q can be expressed as

$$Q = \frac{\pi}{4} D^2 U_0 \quad (2.5)$$

Two new length scales L_Q and L_m can be derived from the above three $Q, M \; and \; B$. L_Q is the length at which the volume flux of the entrained ambient is equivalent to the initial volume flux,Q; Similarly, L_m represents the length at which the buoyancy flux B is equivalent to the initial momentum flux, M.

These two length scales can also be expressed as:

$$L_m = \frac{M^{3/4}}{B^{1/2}} \tag{2.6}$$

$$L_Q = \frac{Q}{M^{1/2}} \tag{2.7}$$

Another important dimensionless parameter of IDJ - densimetric Froude number is also introduced from Abraham (1967), which is expressed as:

$$Fr = \frac{U_0^2}{\frac{(\rho_j - \rho_0)gD}{\rho_0}} \tag{2.8}$$

With Froude number, two length scales in 2.6 and 2.7 can be written as:

$$L_m = \left(\frac{\pi}{4}\right)^{\frac{1}{4}} FrD \tag{2.9}$$

$$L_Q = \left(\frac{\pi}{4}\right)^{\frac{1}{2}} D \tag{2.10}$$

From the experiment of Roberts and Toms (1987), the effect of the volume flux Q can be negligible, so only L_m is adopted in the dimensional analysis. Hence, in an IDJ, any characteristic length $\boldsymbol{X}$ can be expressed as:

$$\frac{\boldsymbol{X}}{L_m} = C_1 \ or \ \frac{\boldsymbol{X}}{DFr} = C_1 \tag{2.11}$$

For example, in (2.4), the maximum height of the jet can be written as:

$$Z_m/DFr = \mathbf{C} \tag{2.12}$$

Similarly, the dilution information can also be scaled based on the Froude number given by:

$$\frac{s}{Fr} = C_2 \tag{2.13}$$

Where dilution is defined as $s = \frac{C_0 - C_a}{C - C_a}$, where C is the local time-averaged concentration. $C_0$and C_a are the concentration of brine and receiving water, respectively.

As mentioned earlier, certain characteristic points of the jet are critical in jet studies, including the maximum height (terminal rise height), the point where the jet descends and contacts the bottom (return/impact point), and the concentration characteristics at these points, as well as the jet trajectory(Figure 2.5). These dimensionless parameters can be represented using Equations

(2.11)and (2.13). Generally, the constants C_1, C_2 can be obtained through experiments and numerical simulations.

In addition to these conventional methods, Artificial Intelligence (AI) can be used to supplement and extend the study of inclined jets by using existing experimental and numerical simulation results.

Therefore, the following sections will review the literature in three key areas of IDJ research: experiments, numerical simulations, and artificial intelligence.

2.3 The Experimental Research of IDJ

Experiments generally provide a direct and effective way to analyze jet behavior. They capture key characteristics and details, offering essential data for theoretical modeling and numerical validation. With their high accuracy, experiments remain a fundamental and straightforward method for understanding IDJ behavior.

2.3.1 The development of image capturing in the study of IDJ

In early research on IDJs, researchers typically took photographs and point measurements to capture the geometrical and concentration information of the IDJ. By adding colored dye to visualize the jet's movement and using high-speed cameras to record its motion, they were able to observe the diffusion and mixing processes more intuitively.

In addition to determining jet concentration based on variations in pixel values from photographs, point measurements allowed for more accurate analysis at specific locations. Common instruments include conductivity probes, hot-wire anemometers, and Acoustic Doppler Velocimeters (ADV), which are used to measure concentration or velocity at a fixed point. Compared to photographs, these instruments offer the advantage of high-frequency and direct measurements that capture fine-scale temporal variations. However, to minimize disturbances to the flow field, the devices must be compact in design. Generally, in experiments of IDJ study, to ensure the jet remains turbulent (high Reynolds number) and to minimize the usage amount of concentrated brine and receiving water, the nozzle for IDJ in laboratories is typically small (around 3mm~6mm). Therefore, intrusive measurement instruments have the risk of disturbing the flow field. Also, point measurement techniques cannot simultaneously capture the entire flow field's characteristics. To overcome these limitations, non-intrusive measurement techniques have become more widely used and have gradually played a leading role in jet experiments. These techniques typically utilize laser and optical methods, such as Laser-Induced Fluorescence (LIF), Particle Image Velocimetry (PIV) and Particle Tracking Velocimetry (PTV).

LIF has been applied in many types of applications, including environmental monitoring (Forbes 2010; Ren et al. 2004; Rogers et al. 2012), biomedical sciences (Schomacker et al. 1992; Taylor and Lai 2021), industrial applications (Michelsen et al. 2015), and the agricultural and food industry (Baumann, Haaszio, and Niessner 2000; Saito 2012). This technology uses the laser to excite fluorescent dyes and capture their emission intensity. The emitted fluorescence is then captured by a camera or detector, which could provide a high-resolution image of the concentration field or temperature distribution. Since the concentration of the fluorescent dye is directly proportional to its fluorescence intensity, it becomes possible to conduct quantitative measurements. PIV technology measures velocity field information by adding neutrally buoyant particles to the fluid. A laser sheet illuminates these particles, and a high-speed camera is used to capture their motion with the flow. The velocity field of the fluid can be determined by analyzing the location of the particles in a continuous image. It provides detailed visualization of complex flow structures, such as vortices, shear layers, and recirculation zones, and helps researchers study fluid mechanics and turbulence. PIV also has a wide range of applications, including aerodynamics, hydrodynamics, environmental science. (Bilsky, Gobyzov, and Markovich 2020; Lai 1996; Westerweel, Elsinga, and Adrian 2013). Through the cooperation of multiple lasers, LIF or PIV can even generate 3D flow field data. These methods provide more comprehensive and accurate data without physically interacting with the fluid.

2.3.2 Review of experimental studies related to IDJ

As discussed in the previous section, many experimental studies of vertical jets or the plumes adopted coloured dye or deep flurry and photos to capture the geometrical information. Zeitoun (1970) conducted an experiment for IDJ using a camera operating at two frames per second (fps) to capture the entire jet field with three different discharge angles: 30°, 45°, and 60°. Rhodamine B dye was added to visualize the jet. The results were obtained by averaging data from five consecutive photographs. The concentration data was collected by simultaneously extracting samples from different points using capillary tubes, then the values were measured using a fluorometer. The normalized profiles of the upper boundary of the dense jet for the three discharge angles are shown in Figure 2.6. They observed that jet properties were correlated with the discharge angle. The study found that a 60° discharge angle results in the longest trajectory, which could lead to maximum dilution. However, due to the instability of the flow patterns, obtaining accurate concentration values was difficult. They also pointed out that during the ascending phase of the jet, entrainment follows a linear function of the Froude number.

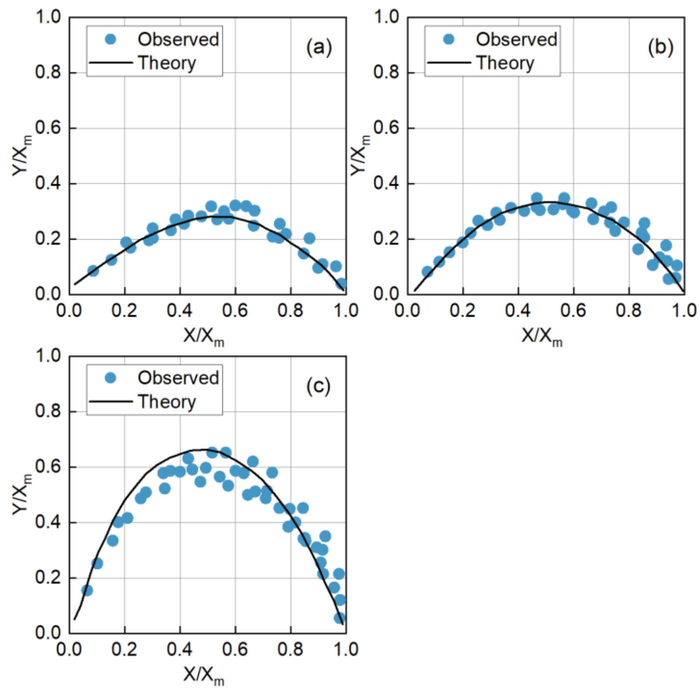

Figure 2.6 Normalized profile of upper boundary of dense jet with three discharge angles (a) discharge angle= **30°***;(b) discharge angle=* **45°** *;(c) discharge angle=* **60°** *(modified from (Zeitoun et al. 1970))*

According to Zeitoun's research conclusions, the key parameters of IDJs are mainly influenced by the discharge angle and the properties of the discharged brine. Therefore, many studies have focused on the optimal discharge angle and discharge characteristics, such as initial velocity, density, and nozzle diameter, to optimize outfall design and jet mixing performance.

Jame et al. (1983) used a conductivity probe to measure the concentration of a negatively buoyant jet discharged at a 60° discharge angle with a Froude number of 50. Rhodamine WWT was added to the brine as a tracer, and geometric information was obtained through photography. They discovered that, in addition to the parameters related to the densimetric Froude number, the nozzle height is also a significant design parameter. They also concluded that a 60° discharge angle provides maximum dilution in stationary water. A predictive equation for dilution at the bottom was developed through regression analysis. The equation's reliability was further validated through a field study conducted in the Gulf of Mexico.

Roberts and Toms (1987) have done experimental research on the effect of the crossing flow condition on the IDJ with a 60° discharge angle. The dilution information was collected from a rack of sampling tubes at locations of the maximum edge height and the impact point. The geometrical information was derived from the time-averaging three photos. Tong and Stolzenbach (1979) conducted the experimental study in a laboratory flume with different discharge and cross-flow conditions, although they just focused on the vertical discharge into the crossing flow, they provided a valuable conclusion that in the near field, the flow can be separated into four regions: the jet region, impact region, upstream region and downstream region. They also provided some empirical equations for the jet geometrical and dilution information based on the dimensional analysis.

List (1982) did a comprehensive review of the fluid mechanics of the turbulent jets and plumes, and he summarized the characteristics of the diffusion and entrainment process. He analyzed the paths and mixing efficiency of the vertical and the IDJ in uniform and stratified environments. He pointed out the impact of the turbulent structures on mixing efficiency: the initial jet dilution is caused by vortices; each vortex can wrap ambient fluid and then develop a vortex pair. This process will continuously mix the ambient and jet.

Lane-Serff, Linden, and Hillel (1993) carried out experimental studies on the characteristics of the IDJ with shadowing graphs and intrusive equipment-conductivity probes. The maximum height of the jet is estimated from the photographs. They observed that the jet was transferred from a symmetrical shape to an asymmetrical shape, and the buoyancy force can create a stabilizing stratification, which may cause entrainment. The detrainment occurs at the lower side of the jet. They also concluded that the shape of the jet is determined by the angle of the source and the source mass flux.

Bloomfield and Kerr (2002) studied the geometrical information of IDJ (the discharge angle ranges from 30º to 90º to horizontal) in the uniform and stratified environment using the Shadowgraph method(Figure 2.7).

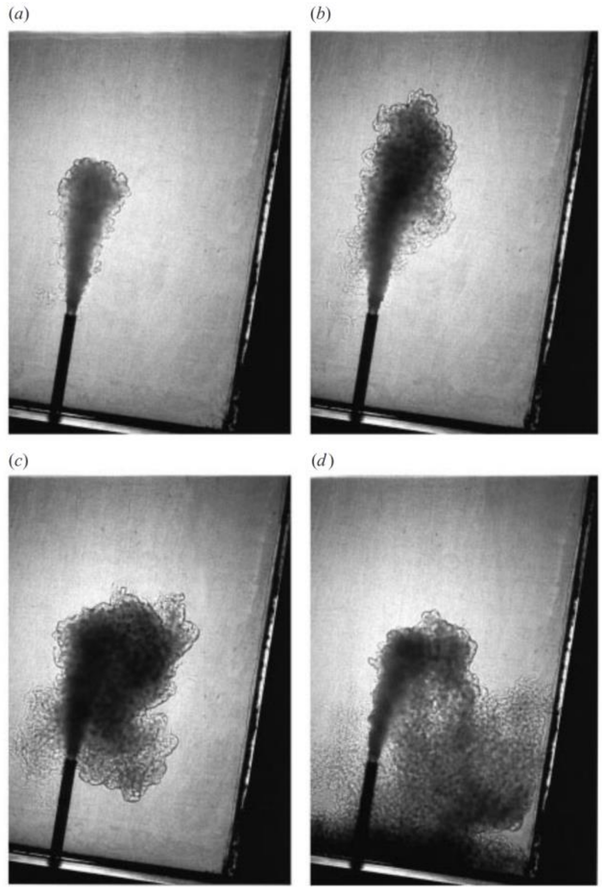

Figure 2.7. Photographs of a turbulent axisymmetric fountain formed from a source inclined at 10◦ to the vertical. (a) The initial flow is jet-like. (b) The downward buoyancy force brings the fluid to rest at an initial maximum height. (c, d) The fluid then falls as a plume and partially interacts with the upflow, resulting in a smaller final height of the fountain(Bloomfield and Kerr, 2002).

They investigated how the angle of the inclination influences the initial height, final height and spreading height. Results show that in the uniform receiving water, jet height is a function of the inclination angles, which is the same as many previous studies' observations. At the discharge angle of 80º, the final height firstly reaches an initial peak height, and then decreases and then ultimately reaches the maximum height. In a stratified environment, however, the inclination angle has minimal impact on both the spreading and final heights.

The time-averaging of photos captured from the jet flow field is still a simple and trusted method to collect the information of the IDJ. With the development of image-capturing technology, researchers have found that the behavior of IDJ is influenced by multiple factors beyond just the discharge angle. Cipollina et al. (2005) carried out laboratory research to investigate more geometrical information of the IDJ discharged into the stationary environment. They have tested four jet parameters, including jet velocity (U_0), jet density (ρ_j), nozzle diameter (D) and a wide range of Froude number (13 to 120) to meet most practical needs. Their results showed that while many properties are indeed sensitive to the discharge angle, other parameters also play important roles in determining jet characteristics. Papakonstantis et al. (2011a; 2011b) investigated the geometrical and concentration characteristics of IDJ discharging into a calm homogeneous fluid. Experimental results for six different discharge angles ranging from 45° to 90° were presented. The key geometrical characteristics include the initial and final terminal rise heights, the horizontal distance to the terminal height, and the return point. The study found that the terminal rise height and the trajectory length depend significantly on the discharge angle and the densimetric Froude number (Fr). Higher discharge angles and Fr values could result in longer trajectories and higher rise heights. The concentration measurements were conducted using a micro-scale conductivity probe. The probe captured the mean and RMS (turbulent intensity) concentration distributions at various points along the jet's trajectory. Concentration measurements were taken at three discharge angles (45°, 60°, and 75°) to assess the vertical and transverse distributions of concentration. The results revealed that the vertical distribution of mean concentration is asymmetric, while the transverse distribution approximately follows a Gaussian profile. Bashitialshaaer, Larson, and Persson (2012) also carried out one laboratory study of the IDJ in stagnant water. In this study, the trajectory and behavior of IDJ were observed using dyed saline water (coloured with potassium permanganate) discharged into a glass tank filled with fresh water. The jet's evolution was visually recorded to capture key geometrical parameters. The jet trajectory and mixing behavior under different discharge angles (30°, 45°, 60°) were also analyzed.

In the recent 10 years, many studies have still used dye-coloured flow and video recordings to visualize the jet flow field and analyze geometrical characteristics efficiently. Papakonstantis and Tsatsara (2018) investigated the trajectories of IDJ with discharge angles ranging from 15° to 70°, using high-resolution cameras to capture dye-coloured jet movements. They collected key trajectory parameters, such as the initial and final rise heights and the horizontal location of the impact point. Similarly, Azizi, Goharikamel, and Vafaei (2020a) investigated the effects of nozzle angles ranging from 15° to 90° on inclined dense jets in stagnant water. Using Rhodamine dye and high-definition cameras, they captured jet trajectories and lateral spreading. The study revealed that maximum dilution occurs at a nozzle angle of approximately 60°, while the longest trajectory is observed between 60° and 75°. Expanding further, Papakonstantis and Mylonakou (2021) studied the geometrical characteristics of IDJ using blue dye for flow visualization and high-definition cameras to capture the motions; they examined jets discharged at angles from 15° to 90°. Again, their study measured critical parameters of IDJ, and they found out that the initial and final terminal heights peaked at 85º and 80º, respectively, while the horizontal distances were maximized at 45º.

From the above review, it can be seen that many experimental studies on IDJ still primarily chose photography and point measurements using probes to capture geometrical and concentration information. These methods provided direct insights into jet behavior; however, intrusive equipment still has limitations. They could slightly disturb concentration measurements, and photographic techniques were still challenging in capturing detailed jet flow dynamics even with the high-speed camera. So, in some experimental studies, the non-intrusive method also contributes to the study of IDJ.

Roberts et al. (1997) are the first authors to adopt laser-induced fluorescence (LIF) in a study that researched the 60-degree inclined dene jet discharged into the stationary receiving water. Figure 2.8 shows one example of a time-averaged and instantaneous image from their experiments. In Figure 2.8, it can be observed that instantaneous images have many random features and turbulence structures compared to time-averaged images.

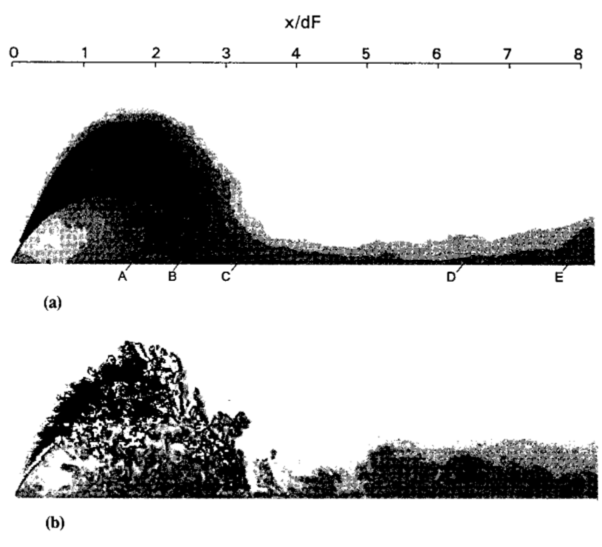

Figure 2.8 Laser-Induced Fluorescence Images of Dense Jet: (a) Time-Averaged Images; (b) Instantaneous Images (Roberts et al. 1997)

With the LIF technology, the measurements were not confined to a single point, but a planner field could be observed and analysed. Therefore, they reported more precise data on the

IDJ, such as the terminal rise height and the dilution at an impact point. They also reported the dilution information along the bottom, and the end of the mixing zone was defined. Webster et al. (2001) used Digital Particle Tracking Velocimetry (DPTV) and Planar Laser-Induced Fluorescence (PLIF) techniques to measure the velocity and concentration field of the turbulent jets. Figure 2.9 presents a sample image of the simultaneously measured velocity and concentration fields. It can be observed that the jet width expands with downstream distance, and noticeable entrainment occurs around the jet. Although Webster's research was not directly related to IDJ, it is clear that, compared to using only cameras and point measurements, the non-intrusive technology showed greater potential and capability, as it can provide more detailed velocity data and simultaneous concentration information of the studies in the relevant field.

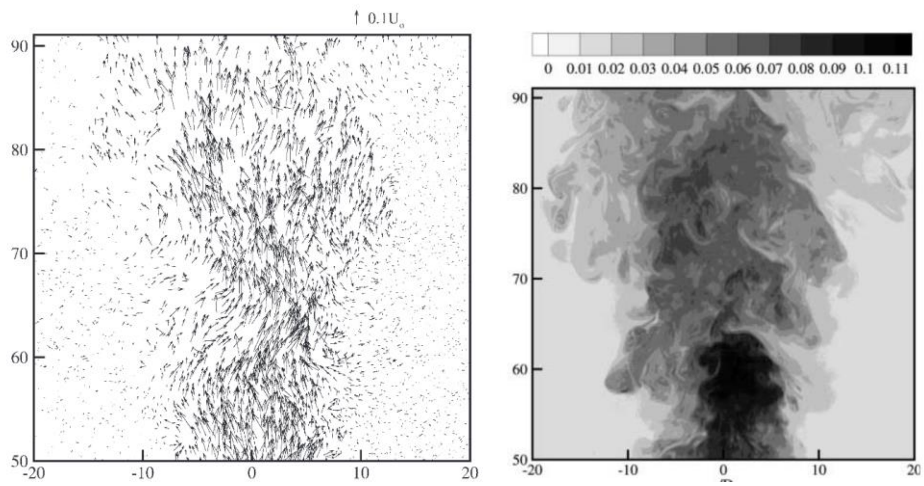

Figure 2.9 Sample simultaneous velocity ®eld. b Sample simultaneous concentration (Webster et al., 2001)

Kikkert et al. (2007) investigated the behavior of IDJ using light attenuation (LA) and LIF techniques. Their experiments involved discharge angles ranging from 0° to 75° and Froude numbers from 14 to 99. The primary aim of their experimental studies was to validate and compare their analytical solutions, and also to compare the results with CorJet and VisJet, two numerical models that are reviewed in section 2.10.

From the previous study, the 60º discharge angle is recommended because it has the longest travel path and provides more dilution, but the higher discharge angle would have a higher terminal rise height thus, it is not suitable for the shallow receiving water, and it is necessary to have more precise information about a wide range of discharge angle. Shao and Law (2010) combined the Particle Image Velocimetry (PIV) and Planar Laser Induced Fluorescence (PLIF) technology to obtain the velocity and concentration field information simultaneously of IDJ with discharge angle of 30º and 45º. The trajectory of the jet was obtained, the velocity and concentration spreading width, and concentration decay along the jet axis were also reported in their studies. Besides these, they also observed the Coanda attachment between the jet flow and the receiving boundary, which should be considered in outfall design, as it can influence the jet mixing behavior. Ferrari and Querzoli (2010) conducted an experimental study on IDJ to understand the phenomenon of re-entrainment, where the jet fluid mixes with itself rather than the surrounding fluid. They used LIF to visualize the jets and measured the concentration fields to analyze turbulent mixing and entrainment (Figure 2.10).

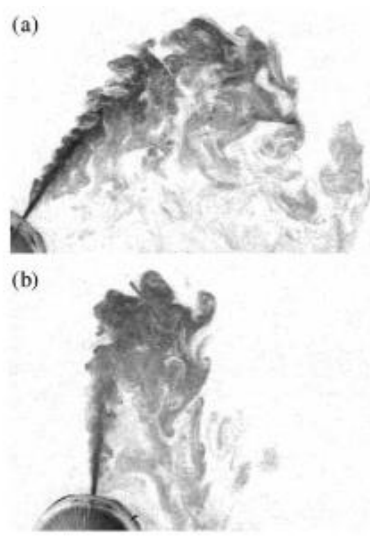

Figure 2.10 Two instantaneous visualizations of concentration fields for two NBJs with 14.8 (a) discharge angle=55°; (b) discharge angle = 85° (Ferrari and Querzoli, 2010).

They found that re-entrainment occurs when the jet angle exceeds 75° and it is influenced by the Froude number. When the jet angle is higher than 80º, as Figure 2.10b shows, the re-entrainment appears, making the jet reduce in maximum height and horizontal distance. Also, the Kelvin-Helmholtz instability can be noticed, and it plays a crucial role in the initial mixing.

It can be noticed that some common discharge angles were adopted in most of the experimental studies, such as 30º, 45º and 60º. Lai and Lee (2012) conducted a comprehensive experimental study of six jet discharge angles: 15°, 30°, 38°, 45°, 52°, and 60°. The jet velocity was measured by Particle Image Velocimetry (PIV). They also adopted the VisJet model to interpret the experimental results. Key findings include empirical correlations for the maximum jet rise height, jet dilution at maximum rise, and impact dilution. Unlike geometrical parameters that mainly depend on the discharge angle, the dilution showed little variation between 38° and 60°, with a constant centerline dilution at the maximum rise point of St/Fr = 0.45.

A series of studies conducted by Besalduch, Ferrari, and Querzoli (Besalduch et al. 2013, 2014; Ferrari et al. 2013, 2014) investigated the behavior of IDJ discharged in stagnant water, which provided a comprehensive understanding of IDJ's near-field dynamics and turbulent characteristics. They adopted a non-intrusive technique called Feature Tracking Velocimetry (FTV) to measure instantaneous velocity fields (Figure 2.11).

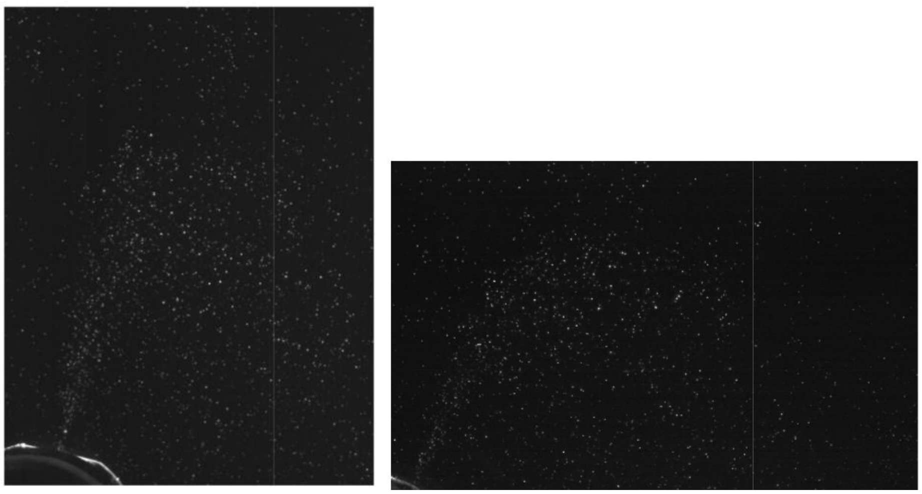

Figure 2.11A snapshot of a negatively buoyant jet (a)densimetric Froude number of 15 and a release angle on the horizontal of 80°.(b) Froude number of 15 and a release angle on the horizontal of 65° (Besalduch et al. 2013)

The discharge angle was 80º and 65º. It can be seen that the 80º discharge angle has a higher terminal height. Their initial study (Besalduch et al. 2013) focused on the general behavior of IDJ, they pointed out the transition from momentum-dominated to buoyancy-dominated stages and the jet widening was influenced by the Froude number. They also observed the re-entrainment, which could limit the spreading and dilution. This phenomenon was observed at discharge angles exceeding 75º, as already discussed in research from Ferrari and Querzoli (2010). Based on this, Ferrari et al. (2013) further investigated the jet's asymmetry near the nozzle, they found that the lower portion of the jet spreads wider than the upper portion due to unstable stratification. After analyzing the turbulent kinetic energy (TKE), they found the enhanced Kelvin-Helmholtz wave development at the upper boundary. One year later, Besalduch et al. (2014) focused on the near-field behavior of the jet. The results showed an asymmetric velocity profile near the nozzle. They also presented quantitative comparisons between IDJ and simple jets in terms of jet spreading, velocity decay, and turbulent kinetic energy (TKE). Ferrari et al. (2014) have extended the investigation to analyze the effects of the densimetric Froude number on the velocity field and turbulence characteristics of IDJ. They found that the IDJ with the lower Froude number (more buoyancy momentum) will have more significant asymmetric characteristics and faster velocity decay compared to the high Froude number. This series of studies provides a detailed understanding of how momentum, buoyancy, and turbulence interact to shape the behavior of IDJ.

Abessi and Roberts (2015) have conducted an experimental study to investigate the effect of a wider range of nozzle orientation angles on the behavior of IDJ in stagnant water, focusing on angles ranging from 15° to 85° using the laser-induced fluorescence (LIF). They measured the time-averaged concentration fields and investigated how nozzle angle influences the jet mixing characteristics, such as the impact point dilution. The results showed that impact point dilution was relatively insensitive to nozzle angles between 45° and 65°, the maximum dilution occurred at 60º. Christodoulou and his colleagues (Christodoulou, Papakonstantis, and Nikiforakis 2015) suggested that in deep water, a discharge angle of 60º–75º is optimal for achieving higher dilution along a longer travel path. In contrast, in shallow water, a discharge angle between 30 and 45 degrees is recommended to minimize the impact of limited water depth. They also emphasized the importance of positioning the nozzle at an appropriate height to prevent the jet from reaching the water surface. Similarly, Crowe and his research team (Crowe, Davidson, and Nokes 2016) investigated the jet characteristics of the IDJ with 15°, 30°, 45°, 60°, 65°, 70°, and 75° discharged into stationary water, they used PTV to confirm that when the jet discharge angle is higher than 70º, the re-entrainment would occur. The inner side of the jet shows some detrainment, which is affected by the unstable density gradient, and the outer side of the jet has a more symmetric flow profile because of the stable stratification.

Jiang's team (Jiang, Law, and Lai 2019) applied the Particle Image Velocimetry (PIV) to study the turbulence characteristics of a 45º IDJ. Many jet's key parameters were selected to test, including nozzle diameter, discharge velocity and density difference (Froude number 11 to 35). The turbulence energy spectra showed that near the nozzle, the spectrum was flat due to underdeveloped turbulence; along the jet trajectory, the inertial subrange emerged with a classic -5/3 slope, indicating fully developed turbulence. Although the focus of this study is not on concentration but on turbulence characteristics, their findings on turbulence can still guide practical engineering applications, such as designing more efficient jet discharge systems. Azizi (Azizi, Goharikamel, and Vafaei 2020b) also conducted similar experimental research on IDJs with various discharge angles (15º – 90º), using light attenuation (LA) to obtain key geometrical and dilution data. These results can support the design, estimation, and optimization of large-scale outfall systems.

Based on the above review, it is clear that the main objective of experimental studies on IDJ is to identify the factors that affect IDJ's behavior, such as discharge angle, density difference, and ambient conditions. These studies provide clear visual observations and quantitative data, which help explain jet characteristics and support the design and optimization of outfall systems.

2.4 Modeling

Although experimental research can directly provide useful data such as geometrical and concentration information, as well as direct observations of how jet characteristics change under different initial conditions, many studies have also explored integral models, analytical models, and CFD (Computational Fluid Dynamics), which play an equally important and irreplaceable role in the research of IDJ. Compared to experiments, these methods offer greater convenience, faster results, and broader applicability, but they still rely on experimental data for validation and evaluation. Modeling requires fewer setups than experiments and offers greater flexibility. It allows researchers to conduct multiple trials under different conditions and quickly obtain results for various scenarios, which would be time- and labour-intensive in experimental studies. As a result, these methods significantly improve research efficiency. They also allow long-term simulations, which serve as a powerful tool to evaluate the long-term impact of infrastructure in practical applications.

The following section reviews the common modeling methods recently applied in the study of IDJs.

2.4.1 Integral models with their tools

Integral models are used to describe the conservation of mass, momentum, buoyancy and scalar of the IDJ. They consider the jet to have a self-similar behavior. It usually relies on several assumptions, such as a Gaussian distribution and a constant entrainment rate, to simplify the problem. The development of the integral model of the buoyant jet has evolved gradually. As early as the 1920s, Prandtl (1925) applied the boundary layer theory to free turbulent flows (jets), which laid the theoretical foundation for the following studies. In the 1940s, Reichardt (1942) proposed that the concentration and velocity of the jet cross-section is a Gaussian distribution, which provides a framework for the parameterized integral model. Afterwards, Schmidt (1941) developed this method for the research of buoyancy-dominated plumes. In 1956, Morton and his colleagues (Morton et al. 1956) proposed the entrainment hypothesis; they believed that a turbulence jet is entraining the surrounding water as the velocity is proportional to the centerline velocity of the jet, and this theory became a core of the subsequent integral model development. In 1952, Rouse (Rouse, Yih, and Humphreys 1952) applied experimental studies to validate this entrainment hypothesis theory, and they also provided key parameters for the integral model. Abraham and Nien Fan (Abraham 1967; Nien Fan 1967) each proposed their own integral models for turbulent jets. Fan's model introduced the entrainment for closing the function, this method expanded the application of the integral model for the discharge prediction.

Fox (Fox 1970) analyzed the turbulent buoyant jet in the stratified ambient water, they developed a more comprehensive model based on Morton's entrainment hypothesis, they pointed out that the entrainment process not only related to the centerline velocity of the jet, but also affected by the densimetric Froude number, Reynold stresses and distribution of the density difference. They pointed out that the entrainment parameter in the integral model varies with flow conditions and should not be treated as a constant. This research can be regarded as one of the fundamental contributions to the integral model of the turbulent buoyant jet. Reaching the 1990s, with the development of the high technology PIV and LIF for measuring the details of the mixing process of the turbulence jet, Wang and Law (2002) adopted experimental research to verify the entrainment hypothesis from the previous study, they improved the integral model to the second-order model that can more accurately describe the transition process of the turbulent buoyant jets from jet-like to plume-like.

2.4.1.1 Corjet

The integral modeling tool for predicting the IDJ was developed by Gerhard H. Jirka in 2004(Jirka 2004). Built upon the foundational work of earlier studies, Jirka implemented his model in a computational program called CorJet, a Fortran-based software. CorJet applies an integral approach to solve the conservation equations of mass, momentum, buoyancy, and scalar quantities in turbulent jet flows. It uses an entrainment-based closure to represent jet diffusion. The model is robust and capable of capturing complex interactions between the jet and the surrounding fluid.

It is worth noting that CorJet can handle a wide range of ambient conditions, including uniform density, stable stratification, stagnant environments, and sheared currents. This flexibility allows it to simulate various flow scenarios, making it a powerful and practical tool in the field of environmental fluid mechanics. Jirka (2004) and his team validated the model's accuracy by measuring instantaneous and averaged concentration values in cross-sections of the jet with previous LIF experiments(Wang and Law 2002). These experiments helped to refine the entrainment coefficients used in the model and ensure that it could reliably predict jet behaviour under various conditions.

The development of the Corjet is aimed at solving the discharge problem of a single port or simple diffuser. However, the primary limitation of CorJet is its assumption of an unbounded receiving environment. In real-world applications, horizontal or lateral boundaries often exist, such as the free surface or the physical bottom, which would exist in complex flow interactions. These interactions may include jet impingement, attachment, internal hydraulic jumps, instabilities, and recirculation, all of which might go beyond the predictive capabilities of the integral model. Still, CorJet represents a significant advancement in the modeling of turbulent buoyant jets, as it could provide accurate and reliable predictions for a wide range of environmental conditions. Its development and validation made a significant contribution to the field of fluid dynamics, especially in areas such as pollution control, wastewater disposal, and environmental impact assessment.

2.4.1.2 Visjet

VISJET is a PC-based flow visualization tool developed by Lee et al.(2000) to simulate and analyze multiple buoyant jets, particularly focusing on rosette-shaped outfall plumes in marine environments. This tool integrates the Lagrangian jet model (JETLAG) (Lee and Cheung 1990) with computer graphics technology, which can provide an interactive and virtual environment that allows users to visualize the complex behaviour of buoyant jets. The key feature of the Lagrangian model is its ability to discretize the flow into individual elements. It extends traditional integral models by moving from a continuous domain to a discretized one. Although Lagrangian model differs from conventional integral models, it still follows the principles of mass, momentum, and buoyancy conservation and adopts the entrainment hypothesis. Due to its ability to simulate complex three-dimensional turbulent jet flows, such as predicting jet trajectories in stratified environments, the Lagrangian model is regarded as an essential tool within the framework of integral model methodologies.

Building upon the JETLAG model, VISJET computes buoyant jet mixing without relying on traditional Eulerian differential equations. Instead, it applies shear-induced and vortex entrainment mechanisms to track plume evolution and accurately predict jet trajectories, dilution rates, and plume interactions. Its primary function is to provide an intuitive representation of buoyant jet interactions at different discharge angles. This capability is especially useful for visualizing plume merging and dispersion under ambient currents. The predictive accuracy of VISJET has been validated through experimental data and applied to diverse flow conditions, such as straight jets, plumes, advected line puffs, thermals, near-to-far-field buoyant plume transitions, and counterflowing buoyant jets. As an interactive simulation tool, VISJET has evolved into a valuable resource for modeling and education. It plays a key role in advancing research on buoyant jets and their engineering applications. Figure 2.12 below is a screenshot of one simulation of rosette jet discharge using VISJET (Lee et al. 2003). It can be seen that VISJET is a very user-friendly tool for environmental assessment and education.

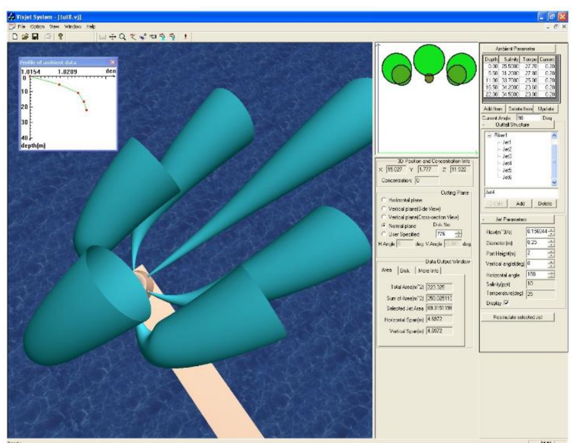

Figure 2.12 VISJET main screen showing a rosette-type jet group from an ocean outfall riser (Lee et al. 2003)

2.4.1.3 CORMIX [1]

CORMIX (Cornell Mixing Zone Expert System) is a comprehensive tool designed to analyze both near-field and far-field behaviours of buoyant discharges, mainly focusing on mixing zones. It is developed by Doneker and Jirka (2007). It offers powerful tools for outfall design,

[1] http://www.cormix.info/

mixing zone analysis, and regulatory compliance. It includes multiple submodules, as shown in Figure 2.13.

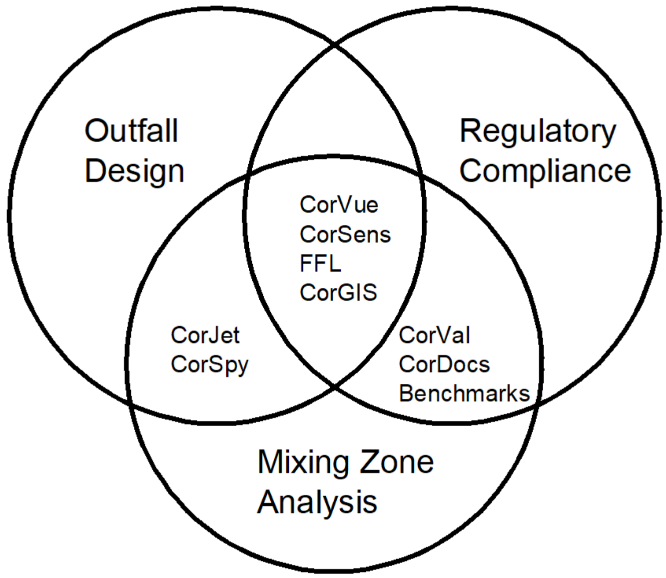

Figure 2.13 The CORMIX-GI system tools integrate to give a comprehensive analysis (modified from http://www.cormix.info/index.php).

It consists of three types of models: CORMIX1(Doneker and Jirka 1990; Jirka and Domeker 1991), CORMIX2(Akar and Jirka 1991)(Jirka and Akar 1991)(Mendez-Diaz and Jirka 1996), and CORMIX3(Jirka et al. 1981)(Jones and Jirka 1993)(Jones et al. 2007), which address single-port submerged discharges, multi-port submerged discharges, and surface discharge sources, respectively. It covers a wide range of effluent types, including conservative substances, non-conservative substances, heated discharges, and suspended sediments. The system employs a rule-based expert system with over 2,000 rules to classify and simulate discharge scenarios, ensuring data consistency and compliance with regulations. The intelligent Windows-based graphical user interface (CORMIX-GI) facilitates users to learn about the rule bases, hydrodynamic models, and advanced design tools, such as CorSpy for 3D outfall visualization, CorVue for interactive plume visualization, and CorSens for automated sensitivity analysis.

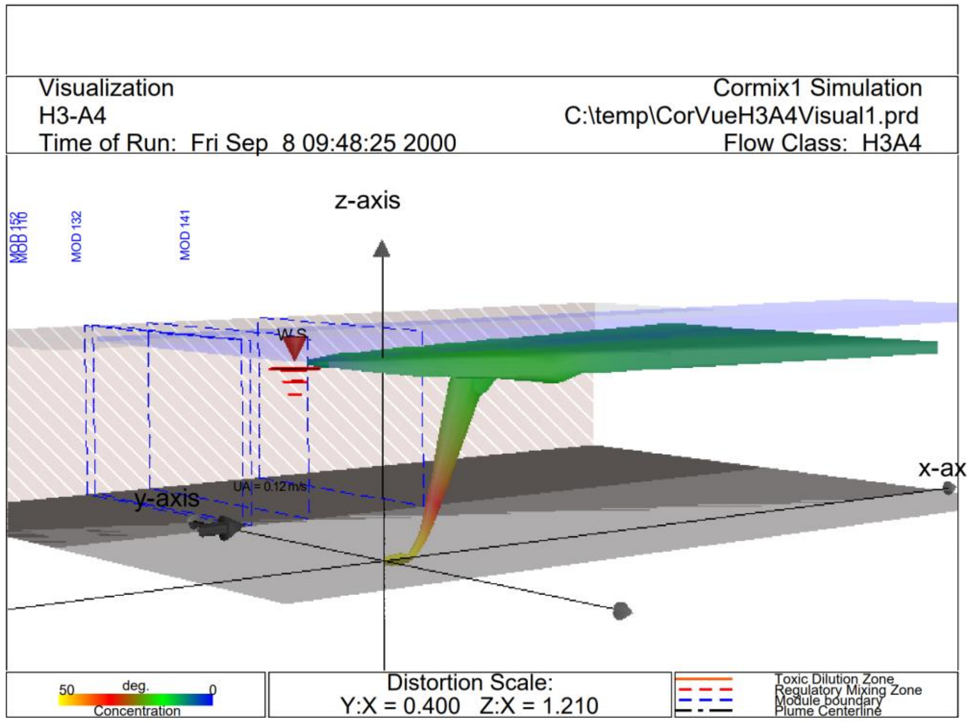

Figure 2.14 CorVue - Interactive plume visualization tool (http://www.cormix.info/corvue.php)

Figure 2.14 presents a visualization window example from CORMIX, showing the interaction of a positively buoyant jet with the water surface. The visualization interface allows users to view the simulated discharge results easily and straightforwardly.

CORMIX is a comprehensive modeling system that includes various hydrodynamic models, analysis tools, and visualization modules to support a wide range of environmental mixing problems — from small industrial discharges in deep lakes to large power plant outfalls. It systematically accounts for boundary interactions and provides detailed analyses of hydrodynamic mixing processes. This system is approved by the U.S. Environmental Protection Agency (USEPA) and integrates robust hydrodynamic modeling with regulatory compliance evaluation.

2.4.1.4 VISUAL PLUMES [2]

VISUAL PLUMES is a Windows-based public domain software again developed by the US Environmental Protection Agency (USEPA) to predict the mixing behavior of surface water effluents, such as plumes and jets. Released in 2001(CEAM 2001), it builds upon the earlier DOS-based PLUMES - a modeling system developed by the USEPA in the early 1990s to simulate

[2] https://www.epa.gov/hydrowq/visual-plumes

buoyant plume behavior- incorporating a new user interface, enhanced models, and expanded capabilities, which make it more user-friendly and suitable for environmental assessments. The software has advanced modeling capabilities, including multi-stressor bacterial decay models that account for solar insolation, salinity, and temperature effects on decay rates. Its graphical user interface provides input windows for discharge parameters, ambient conditions, and special settings, which allow users to conduct sensitivity analyses and visualize results in both text and graphical formats. As a significant advancement in environmental modeling software, Visual Plumes offers a robust platform for simulating, analyzing, and visualizing mixing zone dynamics, it is a valuable tool for environmental scientists, regulators, and engineers (Frick 2004). Laputz and his team (2010) further evaluated the capabilities of Visual Plumes by assessing its performance in predicting effluent dispersion under various environmental conditions. Their study pointed out the model's strengths in near-field plume dynamics and identified its limitations in simulating far-field mixing and stratified flows. They also proposed improvements to the entrainment model and the treatment of transitions between near-field and far-field regions to improve accuracy.

The above integral models and related commercial tools are very useful and have also been applied in many cases. Palomar, Lara, and Losada (2012) have done a detailed investigation of these three commercial tools to analyze and compare them. They have compared three commercial software (CORMIX, VISUAL PLUMES and VISJET) and provided very important recommendations for these applicable ranges. The commercial models might have the ability and advantage to provide reasonable predictions; however, they still have some limitations, such as the underestimation of the geometrical information for the larger discharge angle. Also, these three commercial tools are very conservative when predicting the dilution value. They also show some limitations when applied to the dynamic receiving environment.

2.4.2 Analytical solutions

Analytical solutions are a distinct category from integral models. They rely on mathematical methods to derive simplified equations that can be solved directly. This approach provides fast results and solutions that can be applied to a wide range of cases. Kikkert and his colleagues (Kikkert et al. 2007) developed an analytical solution to predict the important parameters of the IDJ from the initial momentum flux (Eq.(2.1)) and buoyancy-generated momentum flux (Eq.(2.2)). They have separated the jet flow into the jet-like region and the plume-like region. In each region, some relationships can be derived, including the geometrical, concentration information, and the trajectory. Their predictions have reasonable accuracy compared with the experimental study, but the dilution predictions from the analytical solution are relatively conservative. Christodoulou and Papakonstantis (2010) collected all the results from the previous studies and provided simplified methods for predicting the key information, such as the location and dilution at the terminal rise height and impact point of the jet in the stationary environment. The results from simplified equations are all compared with previous experimental studies, and the results have reasonable agreement. They also provided a 2nd-degree polynomial approximation to predict the trajectory of IDJ.

Given the limited performance of integral modeling and analytical solutions in predicting important geometrical and dilution information, other approaches, such as Computational Fluid Dynamics (CFD), are also gaining attention for addressing these challenges and improving prediction accuracy in recent decades.

2.4.3 CFD - Computational Fluid Dynamics (CFD)

Computational Fluid Dynamics (CFD) is an advanced technology that applies high-performance computers to simulate fluid flow with high precision based on the governing Navier–Stokes equations of mass, momentum, and energy conservation (Anderson and Wendt 1995). Over the past half-century, CFD has developed rapidly and has become a key method in both engineering and scientific research. It addressed the limitations of experimental studies and earlier models and provided a deeper understanding of complex flow behavior. CFD simulations follow three main methods: Direct Numerical Simulation (DNS), Large Eddy Simulation (LES), and Reynolds-Averaged Navier–Stokes (RANS). Among them, LES and RANS are the most widely used approaches. Many researchers used these methods to study the behavior of IDJ under different flow conditions.

Vafeiadou and his team (2005) were the first authors to carry out a CFD simulation of IDJ with discharge angles between 45 and 90° using Shear Stress Transport (SST) with ANSYS CFX software. Oliver et al. (2008) compared predictions from a k-ε model with experimental data from Kikkert (2007). Their study used a standard k-ε model and a calibrated form where the turbulent Schmidt number in the tracer transport equation was adjusted. The results achieved reasonable predictions for positively buoyant vertical discharges and IDJ discharges. The calibrated k-e model performed slightly better than the standard one when compared with experimental data.

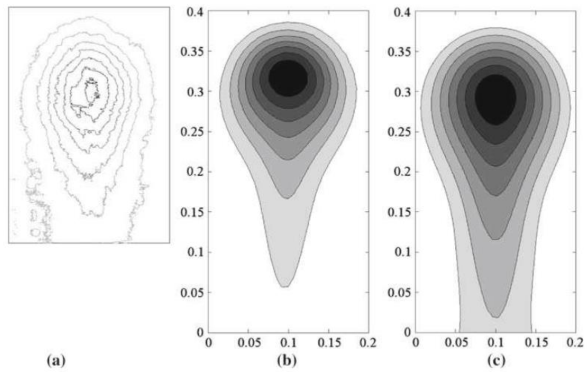

Figure 2.15 Cross-section planes at maximum trajectory height, for 45◦ discharge at Fr0 = 48.66. a Uncalibrated LIF image from Kikkert(2007). b Standard k-ε image, with coordinates in meters. c Calibrated k-ε image, with coordinates in meters (Kikkert 2007)

Compared with the concentration contour at cross-section at maximum height from the experimental study in Figure 2.15, both the standard k-ε and calibrated k-ε models fail to accurately predict the cross-sectional spread of the jet, particularly they overestimated the stabilizing effects of density gradients on the outer side of the flow. There is also some evidence of increased mixing on the inner side of the flow, but it is not as significant as observed in the LIF contours. It can be noted that the k-ε model provides more detailed output than integral and analytical models, but it does not show significant improvement in accuracy for key parameters such as centerline dilution.

Seil and Zhang (2010) used SST and Renormalization Group (RNG) models using ANSYS FLUENT software to do the simulation of the single or multiple ports of discharge. The results were compared with previous experimental studies (Nemlioglu and Roberts 2006) (Roberts et al. 1997b), and the results show good agreement.

One interesting perspective is that the simulation results can vary significantly depending on the choice of turbulence model. Kheirkhah (Kheirkhah et al. 2015) studied the performance of five different RANS turbulence models on IDJ with three different discharge angles using the open-source software OpenFOAM. The geometrical and mixing characteristics were studied and compared with one experimental study (Shao and Law, 2010). They concluded that Launder–Reece–Rodi (LRR) and realizable $k - \varepsilon$ models had better performance among these two-equation turbulence models. In 2016, same authors (Kheirkhah et al. 2016) presented another numerical study on the geometry and characteristics of IDJs with two discharge angles (30° and 45°)with these two turbulence models. They also investigated the effect of buoyancy on the production and dissipation of turbulent kinetic energy with a modified standard k-ε model using SGDH (standard Boussinesq gradient diffusion hypothesis) and GGDH(general gradient diffusion hypothesis) approaches. The results were compared to the previous experimental data and it showed that applying the buoyancy term in the turbulence model showed improvement on the prediction performance.

Many researchers have demonstrated the reliability of the Realizable k-ε model. Ardalan and Vafaei (2019b) carried out similar numerical modeling research on IDJ using the realizable k-ε turbulence model. The model's results were compared with a previous experimental study (Ardalan and Vafaei, 2018). Tahmooresi and Ahmadyar (Tahmooresi and Ahmadyar 2021) carried out one CFD simulation on the 45° IDJ using realizable k-ε model, they applied a Regional Turbulence Schmidt Number (RTSN) configuration on different flow region to figure out the influence of the different turbulent Schmidt number (Sct). Seven different Sct values ranging from 0.4 to 1.0 were applied. The results show that the effect of Sct depends on the different turbulence modeling approaches and the Sct rangring from 0.4 to 0.8 presents 35% higher than the results from integral models from Palmar(2012). Tahmooresi and Ahmadyar recommended adopting $0.5 \leq Sct \leq 0.6$ in the realizable $k-\varepsilon$ models, which can improve the result of dilution characteristics, however, it will show poor prediction of the geometrical parameters. They concluded that the Sct number plays an important role in distribution of the scalar field in the simulation domain. Galeshi's team (Galeshi et al. 2023) conducted numerical simulations of a 45° inclined dense jet in both stagnant water and wave environments using a modified k-ε SST turbulence model. The results showed that, compared to the experimental data under identical conditions, the numerical simulations underestimated both the geometrical and dilution characteristics by approximately 10% to 30%.

The advantage of the RANS model is its reasonable accuracy and computational cost, which makes the RANS model suitable for the long-term simulations in industrial applications, but it still lacks higher accuracy and the ability to capture complex transient flows. As a result, the Large Eddy Simulation (LES) has been recently applied to the prediction of IDJ to obtain turbulent structures and provide more precise physical observations and results. It is more suitable for research simulations or applications requiring high accuracy.

Zhang (Zhang et al. 2016b) presented a detailed investigation of IDJ with 45° inclined angle using LES models with Smagorinsky and Dynamic Smagorinsky sub-grid scale (SGS) models. The results showed that LES could predict satisfactory geometrical information, while the dilution is slightly underestimated; the reason might be the inaccuracy of the SGS models for such applications. After one year, these authors carried out another LES simulation on IDJ with two different discharge angles of 45° and 60°(Zhang et al. 2017b). The same conclusion was drawn that the LES model reasonably predicted the jets' trajectories and other geometrical information, and it showed better performance than the RANS (k-epsilon) model, but the dilution was still underestimated by ~20%, and this might correspond to the mesh quality and grid resolution. In this research, the authors also found that the LES model can clearly present that localized concentration build-up at the impact point, while RANS models cannot.

The numerical simulations of IDJ conducted over the past decades were thoroughly reviewed by Mohammadian et al. (2020), who provided a comprehensive overview of recent CFD studies on jet mixing. Their work pointed out key developments in modeling techniques and emphasized the growing role of CFD in capturing the complex behavior of such discharges, especially within near-field mixing zones.

Among various CFD modeling tools, OpenFOAM—an open-source platform that is widely adopted—was also reviewed by Mohammadian et al. (2023). Their work not only summarized recent advances but also provided practical OpenFOAM-based examples and guidance for future research on the prediction and analysis of mixing characteristics associated with desalination plant discharges. The book offers detailed discussions on numerical simulations under different ambient conditions and discharge configurations, bridging the gap between academic research and engineering applications.

2.5 Study related to the bottom condition

The above section has reviewed the development of the research on the IDJ from simple direct experiment methods such as color-dye and photos or video recording to the advanced non-intrusive technology such as the PIV, LIF, and PLIF to capture the instantaneous field information of the IDJ in different flowing situations. Besides that, some analytical solutions and integral models with commercial tools and applications with CFD are also introduced. It is easy to notice that most of these studies focus on jet parameters, jet development, and the mixing characteristics of the surrounding water.

However, as mentioned before, when IDJ is discharged into the environment, it eventually falls to the receiving bottom due to its higher density unless it is fully diluted. Characteristics at impact point are important for outfall design. Since the properties near the impact point are clearly influenced by the condition of the receiving bottom, this section reviews studies that focus on bottom surface effects.

2.5.1 Built-up on the physical bottom – horizontal bottom

Most existing studies on IDJs assume a horizontal receiving bottom. Under this assumption, the primary objective is often to determine the maximum horizontal distance the jet can reach, denoted as (X_i). It is worth noting that two characteristic points are commonly referenced in the analysis, depending on how the IDJ is defined: the return point—where the jet returns to the nozzle elevation—and the impact point—where the jet makes contact with the physical bottom. Because the bottom is typically assumed to be horizontal and the nozzle height negligible, these two points often coincide in physical space. As a result, many studies do not distinguish between them and choose one based on experimental convenience. However, only a limited number of studies have investigated the jet behavior after bottom impingement, leaving a gap in understanding the post-impact development and the influence of the physical bottom on the behavior of IDJ.

Roberts (Roberts et al. 1997) observed that during experiments, the brine built up near the impact point area due to the heavier elements and concentration. This decreases the dilution along the centerline of the IDJ and then increases due to brine impingement and build-up. This build-up will change the mixing process, which makes the ultimate mixing hard to predict. Papakonstantis and Christodoulou (2010) conducted a comprehensive experimental study to investigate the radial spreading of density currents resulting from the impingement of IDJ on a horizontal bottom. Their research aimed to understand the spreading behavior of IDJ with different discharge angles on the horizontal bottom after the impact point (Figure 2.16). They used coloured saltwater solutions to discharge in a calm freshwater environment, and the spreading fluid was recorded using a video camera installed above the tank. The experiments were conducted for jets discharged at angles of 45°, 60°, 75°, and 85°.

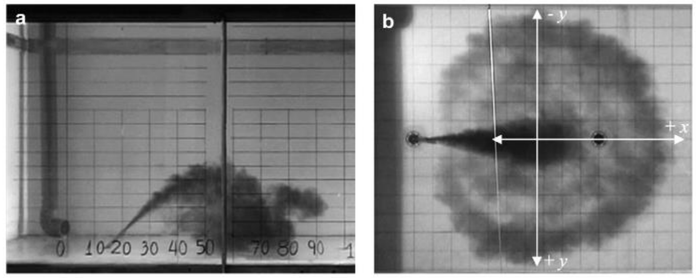

Figure 2.16 (a) Bottom impingement of a 45 inclined negatively buoyant jet (Fr=16.9) (b) density current spreading on the bottom 19.12 s after the jet impingement

The study found that the outer boundary of the density currents was almost circular (Figure 2.16 (b)). The radial distance R from the impingement point to the outer boundary was correlated with time(t) as $R \sim t^{1/2}$. The spreading behavior was found to be independent of the discharge angle and densimetric Froude number.

The study by Shao and Law (2011) also noticed that there would be a brine accumulation for the dense jet. They investigate the boundary impingement and attachment behaviours of horizontal offset dense jets with horizontal physical bottom (Figure 2.17). Their research used particle image velocimetry (PIV) and planar laser-induced fluorescence (PLIF) to analyze the mixing processes and jet behavior in different discharge conditions. In their experiments, they explored the effects of varying the discharge densimetric Froude number (Fr) and the bed proximity parameter (z_0/l_m).

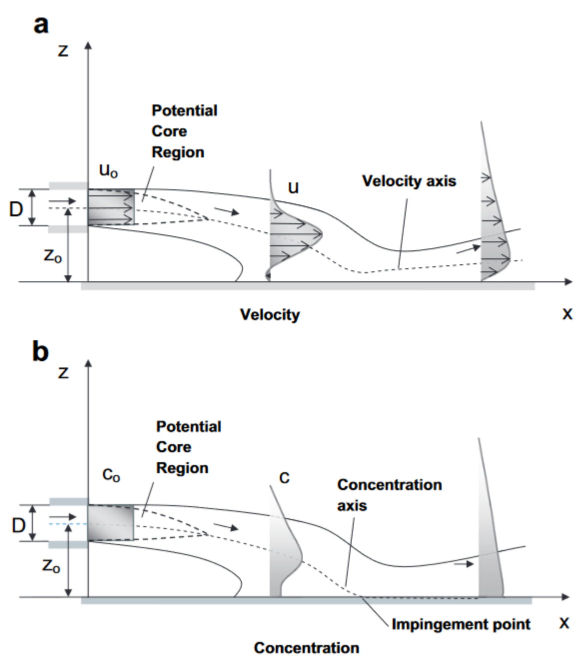

Figure 2.17 Flow pattern evolution of horizontal dense jets.

They found that the horizontal dense jet curves towards and eventually impinges on the seabed due to negative buoyancy. The proximity to the seabed significantly affects the entrainment of ambient water and the jet's trajectory. When the seabed is close to the discharge nozzle, the jet shows a Coanda attachment, which leads to reduced mixing and dilution.

2.5.2 Sloped bottom

More recently, a few studies have explored the behavior of IDJ over sloped bottom surfaces. These works aim to better reflect realistic seabed conditions and provide new insights into jet development, impact point characteristics, and behavior of the jet along the bottom after the impingement. Jirka (2008) is the first researcher to apply the integral model-CorJet to investigate the effect of a sloped bottom on submerged negatively buoyant jet mixing. (Figure 2.18).

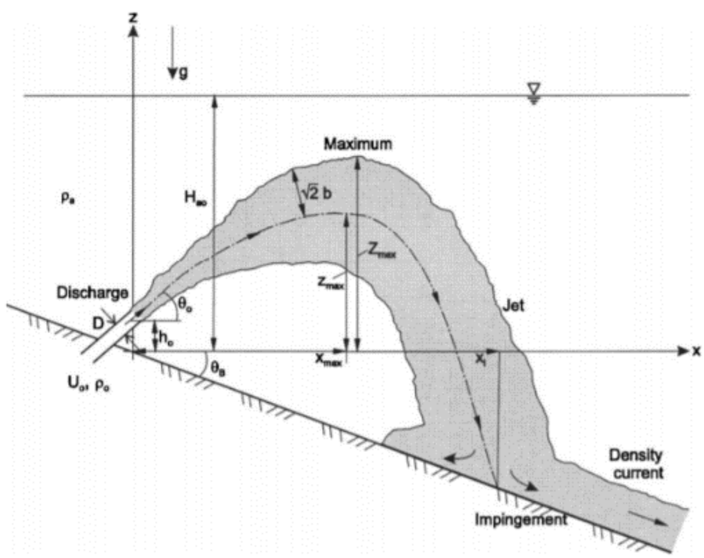

Figure 2.18 Schematic side view of inclined dense jet in stagnant ambient water on a sloping bottom(From Jirka, 2008).

The integral model is validated with existing research data on trajectory and dilutions of jet. The complete range of discharge from 0° to 90° and for the wide slope angles (0°~30°) with zero discharge height were used in this model, and the predictions of jet trajectory with six discharge angles ($\alpha = 0°, 15°, 30°, 45°, 60°, 75°, 90°$) and four bottom angles ($\beta = 0°, 10°, 20°, 30°$) were shown Figure 2.19.

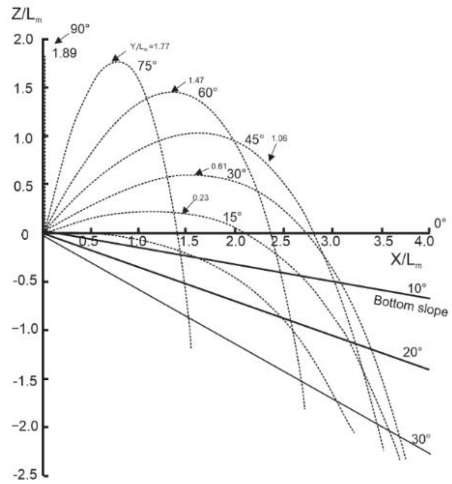

Figure 2.19Trajectory of inclined dense jets with different angles of discharge and sloping bottom (Modified from Jirka, 2008)

From the results, the terminal rise height of the jet increases with increasing discharge angle. The bottom slope also influences the location of the impact point. On a horizontal bottom, the longest horizontal distance to the impact point occurs at a discharge angle of 45°. However, as the slope increases, the discharge angle associated with the longest impact point shifts. On steeper slopes—greater than 10°—the longest impact point is observed for smaller discharge angles (α=30°).

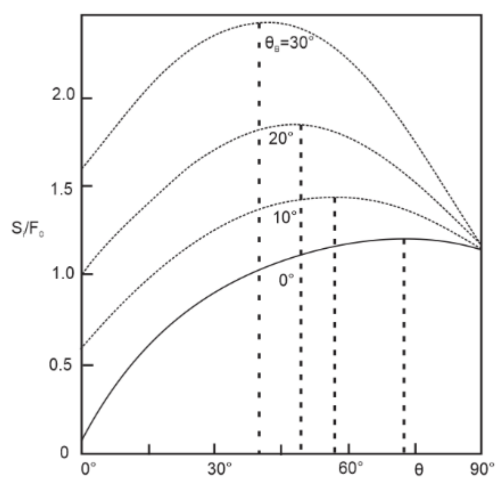

Figure 2.20 Dilution at impact point with different inclinations and different sloped angles using Corjet (Modified after Jirka 2008)

Besides the location of the impact point, Figure 2.20 presents the normalized dilution at impact point. Interestingly, according to the results from CorJet, when using a **horizontal** bottom

($\beta_B = 0°$), the highest dilution at the impact point can be reached with a discharge angle of 60° - 75°. With a moderate slope (sloped bottom:$10° \leq \theta_B \leq 20°$), maximum dilution at the impact point may be achieved with a discharge angle of 45-60°. But with a steep slope ($\theta_B = 30°$), maximum dilution can be achieved with a flatter discharge angle of 30°-45°. One notable trend is that as the bottom slope increases, the dilution at the impact point initially increases but then decreases beyond a certain slope.

A semi-analytical solution for jet characteristics with varying discharge angles (30°–60°) and nominal bottom slopes (5°–15°) was presented by Oliver et al. (2013). The study focused on the behavior of dense discharges beyond the return point. To validate the semi-analytical solution, the authors conducted experiments using a LIF system to measure the jet trajectory and centerline mean dilution for discharge angles of 30°, 45°, and 60° above nominal bottoms. Figure 2.21 shows the schematic diagram of IDJ on a nominal sloped bottom. The semi-analytical solution to predict the location and the dilution of return and impact points is listed in Table 2.1. The results showed that higher discharge angles (45° and 60°) led to greater dilution, and dilution generally increased with boundary slopes. Compared to experiments that used a nominal boundary, extended semi-analytical solutions provided more accurate predictions. The study highlighted that source height and boundary slope play a significant role in determining the impact point location and overall jet behavior.

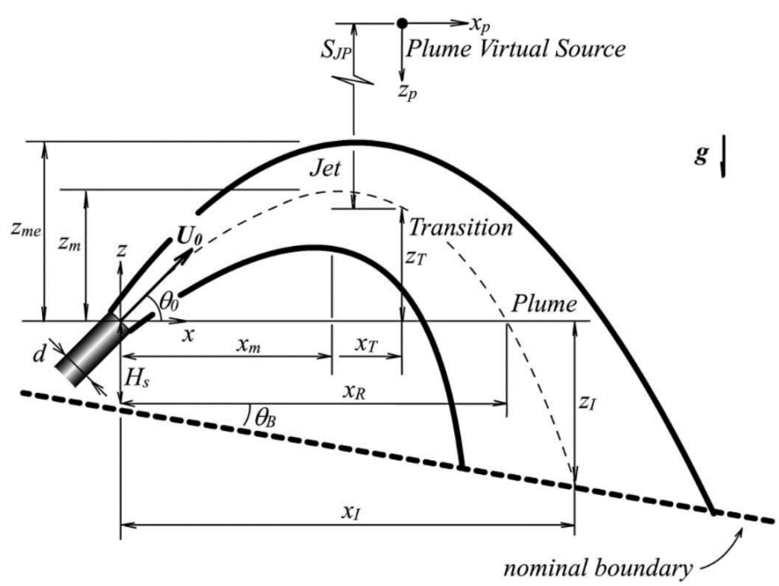

Figure 2.21 Schematic diagram of a negatively buoyant discharge on the nominal slope boundary (Figure from Oliver 2013a)

Table 2.1 The dilution and location of the return point and impact point

	Return point	Impact point
Dilution	$\frac{1}{F_0}\frac{C_0}{Cm} = K_{R_I}\frac{12^{1/3}}{1.61}\sqrt{k_t}K_{R\theta}^{5/3} = k_{RI}0.55K_{R\theta}^{5/3}$ $K_{R\theta} = 1 + \sin\theta_0\left\{1 - \frac{1}{tan^2\theta_0}\left[-1 + \frac{1}{2\sqrt{\sin\theta_0}}ln\left(\frac{1+\sqrt{\sin\theta_0}}{1-\sqrt{\sin\theta_0}}\right)\right]\right\}$	$\frac{C_0}{c_t} = \left(12\frac{k_t^4}{F_0^2}\right)^{1/3}\left(\frac{z_p}{d}\right)^{5/3}$ $\frac{S_{JP}}{d} = \frac{F_0}{\sqrt{k_t}}$
Location	$\frac{x_{R*}}{F_0} = \frac{1}{\sqrt{k_t}}\cos\theta_0\left\{\frac{1}{2\sqrt{\sin\theta_0}}ln\left(\frac{1+\sqrt{\sin\theta_0}}{1-\sqrt{\sin\theta_0}}\right) + 12^{1/3}\left[1 - \left(\frac{1}{K_{R\theta}}\right)^{1/3}\right]\right\}$	$x_{p*} = 12^{1/3}S_{JP*}\cos\theta_0\left[1 - \frac{1}{\left(z_{p*}/S_{JP*}\right)^{1/3}}\right]$ $z_{I*} - H_{S*} = x_{I*}\tan\theta_B$ $x_{I*} = x_{p*} + x_{T*}$ $z_{p*} = S_{JP*} + z_{T*} + z_{I*}$

The first experimental study of IDJ on a sloping bottom was conducted by Nikiforakis et al. (2014). They used a conductivity probe to take point measurements to determine the concentration of the brine flow after the impact point with different Froude numbers (11~23). They found out that after the impact point, the vertical concentration profiles are essentially linear and that the dilution value for discharge inclination 60° is greater than 45°. However, they did not offer information about the geometrical and mixing features at the impact point on the sloped bottom, and they did not compare their findings to other studies related to the sloped bottom.

Wang (Wang and Mohammadian 2022) conducted a numerical simulation of the 15-degree IDJ on the sloped bottom, the results show that the sloped bottom would affect the location of the impact point. The dilution at the impact point also increases due to the sloped bottom.

Habibi (Habibi, Azadi, and Firoozabadi 2022) adopted LES to investigate the influence of the sloped bottom on the IDJ, the results were compared with Oliver's (2013) experiment results. It was in agreement with the experimental results. They pointed out that the sloped bottom enhances the dilution, and the most significant improvement was observed for the steeper slopes. For a 20° bed slope, dilution at the impact point increased by 167.75%, 81.13%, and 107.43% for nozzle angles of 30°, 45°, and 60°, respectively. Among all configurations, the 60° nozzle angle consistently achieved the highest dilution across all bed slopes, the higher slopes also reduced brine build-up on the bottom. These results indicated that a 60° nozzle angle is environmentally favourable. However, the dilution information along the different bottoms is still limited.

2.6 The Applications of Gene Expression Programming (GEP) in Fluid Dynamics

Gene Expression Programming (GEP) is a computational method based on evolutionary algorithms that combines the advantages of Genetic Algorithms (GA) and Genetic Programming (GP). This method was first proposed by Ferreira (2001). Its core principle mimics biological evolution, following the "survival of the fittest" rule to select and optimize chromosomes within a population and identify the most suitable individuals. These individuals are then used to generate mathematical expressions that describe the relationships between data points. GEP is particularly effective in symbolic regression, where it can automatically discover hidden mathematical formulas to accurately predict target variables based on input data. Compared to traditional evolutionary algorithms, GEP can more easily generate complex mathematical expressions while improving problem-solving performance. Compared with the common research methods for IDJ introduced in the previous section, the use of GEP remains new. However, the extensive data collected over the past decades—such as the geometrical and concentration characteristics of IDJs under various conditions—provides a solid foundation for GEP model development. GEP offers a simpler and faster way to predict the physical and concentration features of jets under different environmental conditions and could serve as a promising and efficient alternative for IDJ prediction across various scenarios.

Bonakdari and Mohammadian(2019) carried out the first research on applying GEP in the study of IDJ. They predicted geometrical and dilution information for IDJ in shallow water: discharge angle, ambient water depth, and Froude number are input variables for the GEP model. The resulting equations can estimate the trajectory and provide important information on the IDJ under different receiving water depths. Yan and Mohammadian (2020) also used the MGGP algorithm to generate explicit equations for inclined dense jets at multiple ports, predicting in-plane parameters and evaluating their best equation using confidence analysis. They concluded that MGGP is a valuable tool for constructing models to predict mixing features of inclined dense discharges from multiport diffusers.

2.7 Research needs

The presence of a sloped bottom significantly influences the mixing and behavior of inclined dense jets in stationary ambient water. It is essential to investigate the brine distribution and mixing dynamics on different sloped bottoms, as the brine eventually settles on the ground and continues to move along the bottom. Once the jet impacts the ground, the brine spreads in all directions, and understanding how the sloped bottom affects this spreading behavior is a critical area for further research. Additionally, the far-field mixing of the jet requires attention as the brine discharge is a long-term application.

Although some studies have explored the influence of sloped bottoms using integral models or numerical simulations, the lack of comprehensive experimental studies has hindered the validation of numerical models. This limitation affects the reliability of these models in providing accurate results for future studies. In other words, the physical effects of sloped bottoms on inclined dense jets in stationary water have not yet been fully considered. Therefore, the present study aims to examine the effects of physical sloped bottoms with different angles on inclined dense jets. This includes investigating their impact on various discharge angles, jet trajectory, dilution characteristics, mixing along the bottom, and concentration near the impact point through both experimental and numerical approaches. The numerical methods, specifically RANS and LES, will be compared against experimental results to evaluate the performance and accuracy of these models.

This study will also test the GEP to develop a predictive model for IDJ on different sloped bottoms under varying discharge angles. The outcomes of this study are expected to fill the research gap and support the design and analysis of brine discharge systems. All the key geometrical and dilution parameters of the IDJ reviewed in this chapter are collected and listed in Appendix A.

Chapter 3 Experimental Investigation of the Influence of a Sloped Bottom on the Behavior of Inclined Dense Jets

Xinyun Wang(corresponding author)[1,*], Abdolmajid Mohammadian[1], Simone Ferrari[2], Philip J. W. Roberts[3]

[1] Department of Civil Engineering, University of Ottawa, 75 Laurier Ave E, Ottawa, ON K1N 6N5, Canada

[2] Department of Civil-Environmental Engineering and Architecture (DICAAR), University of Cagliari, Via Marengo 2, 09123, Cagliari, Italy

[3] School of Civil and Environmental Engineering, Georgia Institute of Technology, Atlanta, GA 30332, USA

Abstract

This study presents an experimental investigation on the effect of a sloped bottom on inclined dense jets in a stationary environment. A total of 36 experiments were conducted using Laser-Induced Fluorescence (LIF), covering three discharge angles ($\alpha = 30°, 45°, 60°$), four bottom slopes ($\beta = 0°, 1°, 3°, 5°$), and three densimetric Froude numbers ($F = 17.3, 22.1, 28.1$).

The results indicates that the location of the impact point and the dilution level increase linearly with the slope angle. On a 5° slope, the dilution at the impact point increases by 31%, 22%, and 22% for the three discharge angles. After impact point, the jet attaches to the bottom surface and behaves like a wall jet combined with a free-density current. On sloped bottoms, Kelvin–Helmholtz (KH) vortices become more distinct due to stronger shear, which increases concentration variance and enhances mixing. Energy spectrum analysis shows that concentration fluctuations follow Kolmogorov's –5/3 power law. The turbulence energy levels on sloped bottoms are consistently higher than those on horizontal beds. In addition, the mixing zone length (X_e/dF), bottom layer thickness, and concentration variance increase with both slope and discharge angle. These results suggest that sloped bottoms lead to stronger and more sustained mixing.

The Froude number of the brine also influences the mixing behavior. When $Fr < 20$, buoyancy dominates, and the difference in dilution between horizontal and sloped bottoms remains small, even though the slope enhances mixing to some extent. When $Fr > 20$, jet momentum becomes more significant, and the sloped bottom further enhances entrainment and dilution. These

findings offer valuable guidance for optimizing bottom configurations under various discharge conditions to enhance dilution and support environmentally outfall design.

Keywords: inclined dense jet; sloped bottom; mixing; outfalls

3.1 Introduction

Approximately 97% of the Earth's water resource is ocean water, which holds incredible potential to relieve freshwater scarcity. With the increase of pressure on freshwater resources, desalination plants have become a significant and effective method to address this issue (Voutchkov and Kaiser 2020). Currently, many arid urban coastal regions in the Middle East, Europe, Africa, Australia and the USA rely on over 16,000 desalination plants to ensure an adequate water supply during increasing periods of drought worsened by climate change in recent decades (Jones et al. 2019). However, the desalination process raises issues with its main byproduct, the brine (concentrated salty water), which requires particular consideration, especially when discharged into a marine body through a submerged outfall. Improper discharge may pose risks and harm marine habitats, particularly affecting the near-bottom marine communities (Lattemann and Amy 2013).

The inclined dense jet is a common method applied in outfall systems of desalination plants due to its simplicity and ability to minimize the negative impact on the marine environment (Roberts, Ferrier, and Daviero 1997; Zeitoun et al. 1970; Pincince and List 1973). Figure 1 illustrates a single-port inclined dense jet discharged into a stationary receiving environment. This setup has a submerged pipeline to discharge the brine through a round nozzle: if the brine has sufficient velocity, it acts as a turbulent jet. With an inclination angle to the horizontal, the path of the brine is extended, so this setup can increase the mixing of the jet and reduce the environmental impacts. The jet ascends, reaching a maximum height, then falls back to the sea floor due to the higher density, and continues moving along the seabed. During this process, the geometrical and mixing features at specific points, such as maximum rise height and return point, are very important because they are related to the design of the outfall system.

Many experimental and numerical studies have been conducted to investigate the properties of the discharge mixing and brine transport based on specific conditions at the discharge port and receiving water conditions. For example, large desalination plants often apply multiple-port diffusers for their large discharge capacity. The spacing and discharge angles of the ports are key points of research of multiple ports and practical projects (Yan and Mohammadian 2019; S. A. R. Saeidi Hosseini et al. 2022; S. Saeidi Hosseini et al. 2023). The single-port diffuser has also raised attention in recent decades because it is a simple and economical way to discharge brine (Al-Mutaz 1991; Kikkert, Davidson, and Nokes 2007; Roberts, Ferrier, and Daviero 1997). Zeitoun et al. (Zeitoun et al. 1970) was the first study that conducted experiments to investigate the geometrical and dilution properties of inclined dense jets in stagnant water with different discharge angles of 30°, 45° and 60°. They found that the jet's properties depend on the discharge angle. Cipollina et al. (2005) conducted a lab-scale study to investigate the jet trajectory and geometrical information of inclined dense jets discharged into stationary ambient water with a wide range of discharge angles, nozzle diameters, jet densities and discharge flow rates. Kikkert, Davidson, and Nokes (2007) developed an analytical solution to predict the behavior of the inclined dense jet with the discharge angle ranging from 0 to 75° and Froude number from 14 to 99. Compared with previous studies, the analytical solutions were accurate and provided the detailed characteristics of the single-port inclined dense jet discharged into stationary receiving water. Papakonstantis et al. (2011a,b) studied the detailed geometrical and concentration characteristics of inclined dense jets with different initial discharge angles. The 60°-discharge angle is recommended as the industry standard for brine discharges because it can provide the highest dilution and a longer trajectory.

In addition to geometrical information and concentration at specific points, which are more relevant to practical predictions, various researchers have also explored more complex aspects such as the evolution, interaction, and mixing development of inclined dense jets. Shao and Law (Shao and Law 2010) adopted Particle Image Velocimetry (PIV) and Planar Laser Induced Fluorescence (PLIF) to study the velocity and concentration fields of inclined dense jets with 30° and 45° discharge angles in stationary receiving water. In addition to analyzing the geometrical and dilution characteristics at specific points, they also examined the concentration and velocity profiles at various downstream locations and the spread width along the jet trajectory. Lai and Lee (2012) also used the LIF technique to visualize the concentration field and explore the properties of inclined dense jets at a wider range of discharge angles, from 15° to 60°. In addition, they applied an entrainment formulation to predict the jet's behavior under different discharge angles. Ferrari and Querzoli (2010) used the LIF technique to analyze the behavior of inclined dense jets during the mixing process, focusing on the re-entrainment phenomenon. Their study provided insights into hydrodynamic features along the jet axis and how they affect the jet's trajectory and mixing efficiency. In addition to these experimental studies, many numerical investigations of inclined dense jets in stationary receiving water conditions have also been conducted (e.g. Kheirkhah Gildeh et al. 2015; Zhang et al. 2016). The simulation results provide more comprehensive predictions, enhancing the understanding of the characteristics and behavior of inclined dense jets at different angles.

Fewer studies address the influence of the receiving bottom conditions. In stagnant water, the brine would eventually fall back to the sea bed and may affect the bottom environment. Roberts et al. (1997) studied the phenomena occurring after the jet moved along the bottom. They summarized that the "end of the mixing zone" for 60° discharge angle in stagnant water on the horizontal bottom is around X/dF=9 (where X is the x-axis direction, D is nozzle diameter, F is densimetric Froude number). Jirka (Jirka 2008) was the first author to use an integral model to predict some important properties of the inclined dense jet with a 30°~60° discharge angle and a wide range of receiving bottom angle (0°~30°). He suggested that the 30° and 45° discharge angles are more suitable when the water depth and sloped bottom are considered. There are few numerical studies about the effect of the sloped bottom on the inclined dense jet (e.g. Habibi et al. 2022; Wang and Mohammadian, 2022). Habibi et al. (2022) used large eddy simulation to predict the characteristics of inclined dense jet with discharge angle (30°, 45° and 60°) on sloped bottom (0°,5°,10°,15° and 20°). They found that a larger slope could increase the mixing rate, and the dilution at the impact point also increases with an increase in the inclination of the bottom. They compared their results with the integral model-Corjet (Jirka, 2008) and obtained a good agreement. However, the lack of experimental results for validating the numerical studies highlights a necessity for conducting related experimental studies, including the impact of a sloped receiving bottom.

For this reason, a comprehensive experimental study was carried out using a laser-induced fluorescence (LIF) technique, covering a wide range of discharge conditions and receiving bottom inclinations, to investigate the effect of the inclined bottom on jet mixing after the jet impinges on the bottom. This study aims to extend research on inclined jet discharges to different receiving bottom environments and provide more valuable and predictive information for practical engineering applications and the protection of nearshore environments around outfall systems.

3.2 Dimensional analysis

Figure 3.1(a) and (b) show a representative inclined dense jet in a stationary water condition on both horizontal and sloped bottoms. The brine has a higher density (ρ_0) than the stagnant surrounding water (ρ_a). It discharges through a circular nozzle (d) with an initial velocity U_0. The angle of the inclined jet discharge is α. The bottom inclination angle is β. It is clear that the slope does not affect the return point, i.e. the point where the jet returns and reaches the elevation of the nozzle. However, the slope significantly affects the location of the impact point where the jet hits the bottom.

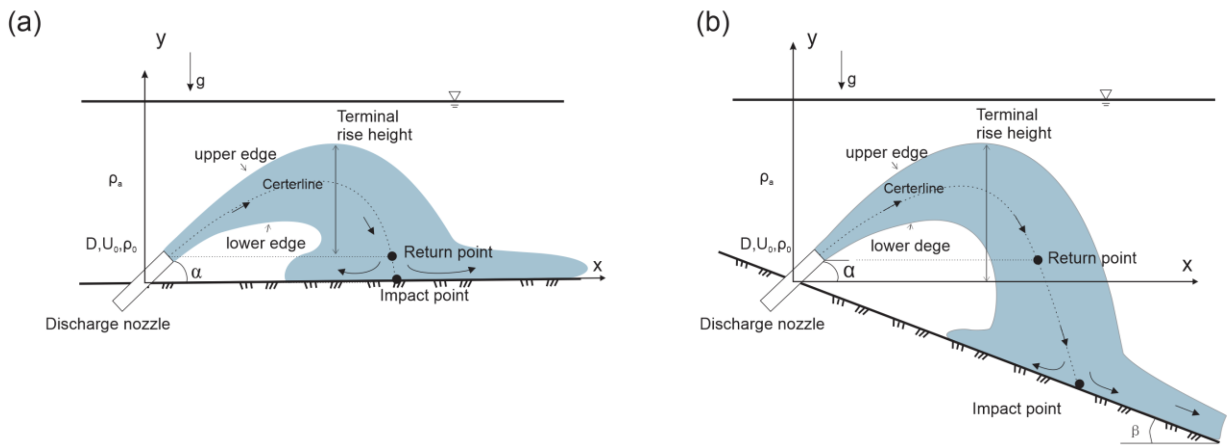

Figure 3.1. Schematic of an inclined dense jet discharged into stagnant water on (a) horizontal bottom, (b) sloped bottom

The inclined dense jet can be described by the fluxes of volume Q, momentum M, and buoyancy B, defined as:

$$Q = \frac{\pi}{4} d^2 U_0 \quad (3.1)$$

$$M = UQ = \frac{\pi}{4} d^2 U_0^2 \quad (3.2)$$

$$B = \frac{\pi}{4} d^2 U_0 g_0' \quad (3.3)$$

Where $g_0' = g\frac{(\rho_0 - \rho_a)}{\rho_a}$ and g is the gravitational acceleration.

Two length scales L_m and L_Q can be derived from the above three quantities: Q, M and B. L_m is a measure of the distance required for the buoyancy to create momentum roughly equal to the initial momentum flux, M; L_q is a measure of the length over which the volume flux of the entrained ambient fluid becomes roughly the same as the initial volume flux, Q. These two length scales can also be expressed with another important dimensionless parameter of dense jet, the densimetric Froude number, which is expressed as

$$F = U_0/\sqrt{dg'_0} \tag{3.4}$$

Therefore, the two length scales can be described as

$$L_m = \frac{M^{3/4}}{B^{1/2}} = \left(\frac{\pi}{4}\right)^{\frac{1}{4}} dF \tag{3.5}$$

$$L_Q = \frac{Q}{M^{1/2}} = \left(\frac{\pi}{4}\right)^{\frac{1}{2}} d \tag{3.6}$$

For typical brine diffuser conditions, the effect of the volume flux Q is negligible (Roberts et al. 1997), so only L_m is adopted in the dimensional analysis. Hence, in an inclined dense jet, the characteristic length X can be expressed as:

$$\frac{X}{dF} = C_1 \tag{3.7}$$

Where dF is a fundamental length-scale of the flow. The scaled dilution is given by(Roberts, Ferrier, and Daviero 1997).

$$\frac{s}{F} = C_2 \tag{3.8}$$

Where dilution is defined as $s = \frac{C_0 - C_a}{C - C_a}$, where C is the local time-averaged concentration and C_0 and C_a are the concentrations of brine and receiving water, respectively.

3.3 Methodology

The experiments are carried out at the Hydraulics Laboratory of the University of Cagliari, Sardinia, Italy. Figure 3.2 shows the experimental setup, including the experimental tank and laser system.

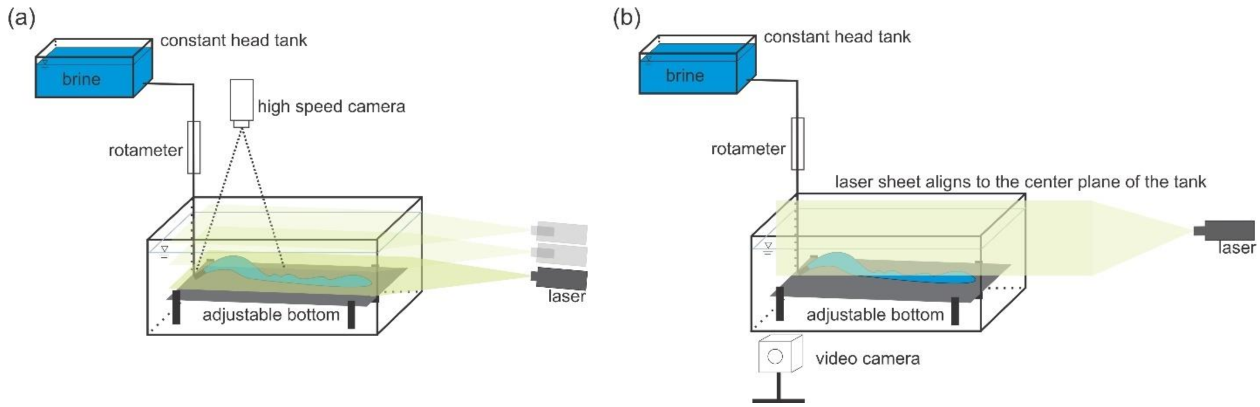

Figure 3.2. Schematic images of the LIF experimental setup for (a) transverse and (b) vertical sections

The experimental tank is constructed from transparent Perspex with dimensions of 200 cm in length, 100 cm in height, and 100 cm in width. A 2.5 cm thick black acrylic board, measuring 150 cm in length and 80 cm in width and framed by metal bars in the lower part, is equipped with four supporting legs and placed inside the tank as the physical bottom. One side of this bottom board is manually adjustable to desired sloping angles; for this study, it is fixed at four distinct angles: $\beta = 0°, 1°, 3°,$ and $5°$. These sloped angles are chosen according to real bottom inclinations, as the sloped bottom of the ocean gradually slopes from the shore to the deeper ocean.

The nozzle is located in the middle of the left side of the tank, with a diameter of 3.5mm. Its discharge angle can be manually adjusted using a protractor. To minimize boundary effects between the nozzle tip and the bottom surface, Shao and Law (2010) recommended that the ratio of nozzle height to the jet characteristic length ($\frac{Z_0}{dF}$) should be greater than 0.2. In this study, the nozzle height is within the range of 7 cm to 10 cm, depending on different discharge angles, the ratio $\frac{Z_0}{dF}$ ranges from 0.714 to 1.02, which is sufficient to avoid boundary effects. Additionally, to prevent interference from tank walls, such as fluid reflection and jet flow deflection, the horizontal distance between the nozzle tip and the tank walls is ensured to be sufficiently large to avoid wall effects, minimize laser reflections, and improve measurement accuracy. The bottom plate, support legs, and nozzle system are painted black, and all tank walls—except for the observation and laser measurement sides—are covered with matte black paperboard to reduce unwanted laser reflections.

The brine is prepared using tap water and sea salt. A small amount of Titanium dioxide is added as a tracer, and the brine's density is measured using a handheld bubble density meter. The density of the brine is between 1023 and 1061 kg/m^3 based on the brine densimetric Froude number. The brine solution for the experiment is discharged from a constant head tank positioned 250cm above the main experimental tank, ensuring a stable and continuous source of brine. An additional tank is utilized to continually refill the head tank, maintaining a constant brine level and stable flow rate. The constant head tank and nozzle are connected by a polyethylene tube, and an OMEGA rotameter is installed to measure flow rates from 0.1 to 1 litre per minute (1.67×10^{-6} to 1.67×10^{-5} m^3/s). The Reynolds number (Re) of the jet is approximately 2193 to ensure fully turbulent flow. The ambient water used in the experiment is also tap water. The tank is cleaned and refilled before each experiment. During the experiments, the laboratory was kept dark. A green laser sheet generated by a 5 W diode-pumped solid-state (DPSS) continuous laser was used to illuminate the jet slice for imaging. To capture transversal images, a digital charge-coupled device (CCD) camera (Mikrotron EoSens 4CXP CoaXPress) was installed above the tank, with its lens oriented vertically downward at a frequency of 50 Hz. This camera was positioned about 180 cm above the water surface to capture the nozzle and the impact point area. To capture vertical section images of the jet flow, another video camera was positioned at a distance of about 100 cm from the lateral vertical wall of the tank. It records videos at a resolution of 2336 x 1728 pixels and a frame rate of 30 frames per second (fps) for approximately 200 seconds for each experiment.

Thirty-six (36) experiments were conducted, including three discharge angles (α = 30°,45°, 60°), four sloped bottoms (β = 0°, 1°, 3°, 5°), and three densimetric Froude numbers (F = 17.3, 22.1,28.1). The detailed setup is listed in Table 1. All experiments included vertical and transverse section measurements.

Table 3.1 Experimental initial conditions

Num. of Experiment	Discharge angle(°)	Bottom angle (°)	Density of brine (kg/m^3)	Discharge(L/min)
1	30	0	1061	0.31
2	45	0	1061	0.31
3	60	0	1061	0.31
4	30	0	1037	0.31
5	45	0	1037	0.31
6	60	0	1037	0.31
7	30	0	1023	0.31
8	45	0	1023	0.31
9	60	0	1023	0.31
10	30	1	1061	0.31
11	45	1	1061	0.31

12	60	1	1061	0.31
13	30	1	1037	0.31
14	45	1	1037	0.31
15	60	1	1037	0.31
16	30	1	1023	0.31
17	45	1	1023	0.31
18	60	1	1023	0.31
19	30	3	1061	0.31
20	45	3	1061	0.31
21	60	3	1061	0.31
22	30	3	1037	0.31
23	45	3	1037	0.31
24	60	3	1037	0.31
25	30	3	1023	0.31
26	45	3	1023	0.31
27	60	3	1023	0.31
28	30	5	1061	0.31
29	45	5	1061	0.31
30	60	5	1061	0.31
31	30	5	1037	0.31
32	45	5	1037	0.31
33	60	5	1037	0.31
34	30	5	1023	0.31
35	45	5	1023	0.31
36	60	5	1023	0.31

Figure 3.3 shows a flow chart of the main experiment procedure for both transversal and vertical sections. According to the jet flow dimensions, during the experiments (related to Fr), the transversal slices would be at 8 to 16 different heights, with intervals of 1to 2 cm based on different discharge angles. Background images were recorded for around 20 seconds, and jet flow images were recorded for around 60–100 seconds with a total of 5000 frames. For the vertical sections, because only the center plane is of interest, the laser sheet was adjusted vertically and aligned to the center plane of the jet. For each experiment, the video was recorded for 3 to 4 minutes, starting from the moment the jet was discharged until backflow was caused by the blockage of the tank wall. To further analyze the raw image data and video clips, MATLAB, Paraview, and Origin software were used. During the post-processing, each slice was first processed with a time-averaging of 150 to 200 background images using MATLAB code. Then, each main image was

subtracted from the background image, and these 4000 main images were time-averaged. In this process, some abnormal regions, such as reflections caused by the nozzle or extremely high light intensity points caused by tiny debris and bubbles in the water, were filtered and removed from both backgrounds and the main images. After calculating the time-averaged light intensity and variance, the data were stored in Tecplot format. These Tecplot data could be read through Paraview to obtain the average light intensity and variance of the flow field, while all the figure plotting was completed using Origin software.

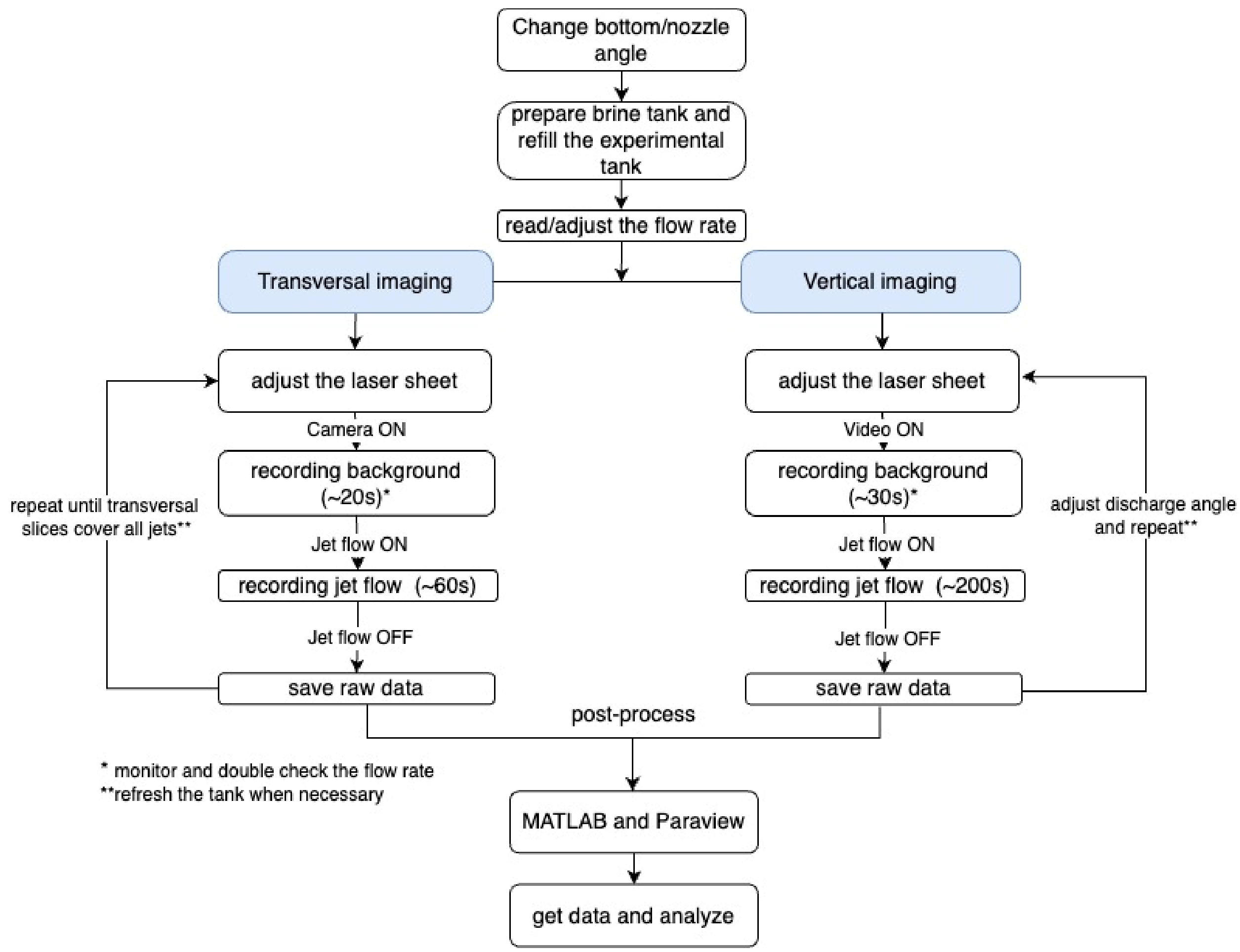

Figure 3.3. Flow chart of experimental procedures.

3.4 Results and discussion

The results will be presented and discussed in the following order: First, general observations of the jet will be introduced to provide a clear understanding of the effects of the sloped bottom on the inclined dense jet. Next, important geometrical information, such as trajectory, terminal rise height, centerline peak, and return point, will be collected and compared with previous research for validation. A detailed analysis of the sloped bottom's effects on the impingement area will follow, focusing on the lateral spreading, the location of the impact point and concentration characteristics. The concentration distribution beyond the impact point on different sloped bottoms will also be examined. These results will provide valuable references for comprehensive outfall performance predictions, pollutant management, and protection of the surrounding marine environment.

3.4.1 General jet behavior – Instantaneous images

Figure 3.4 shows the central vertical section of discharges, with a Fr=17.3, at angles α of 30°, 45°, and 60 ° above four sloped bottoms(0 °,1°,3°,5°), captured in snapshots at different times of 5s, 10s, 20s, and 50s. These figures present an overview of the initiation, development, and evolution of inclined dense jets on different sloped bottoms.

1. $\beta = 0°$

Time	$\alpha = 30°$	$\alpha = 45°$	$\alpha = 60°$
t=5s	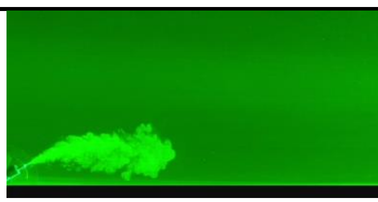	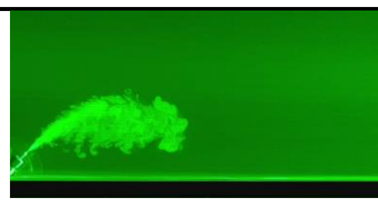	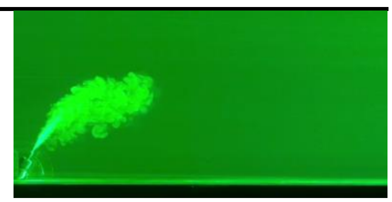
t=10s	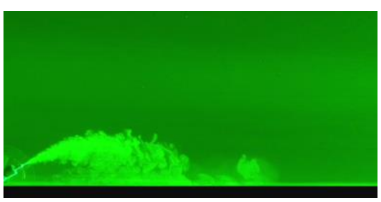	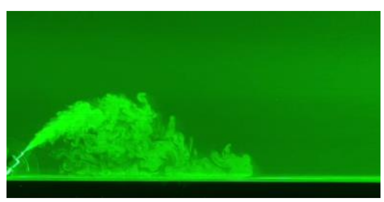	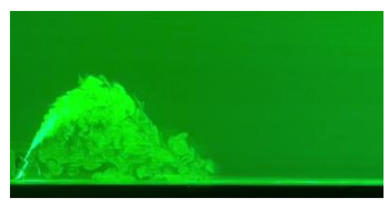
t=20s	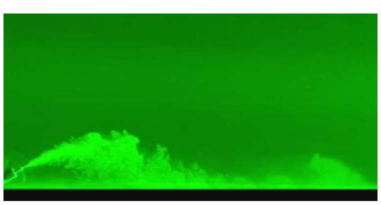	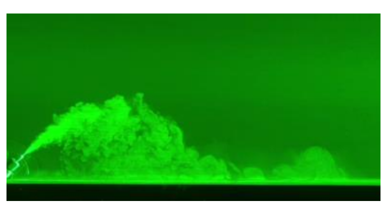	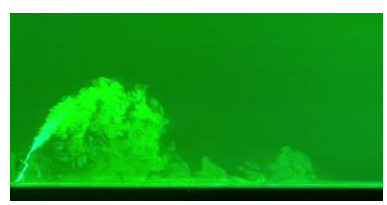
t=50s	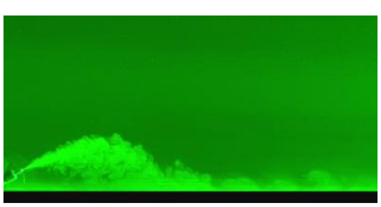	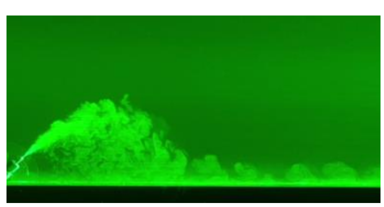	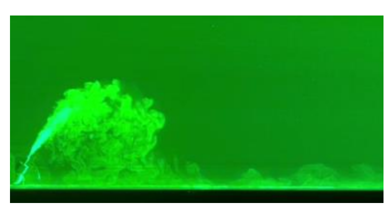

2. $\beta = 1°$

Time	$\alpha = 30°$	$\alpha = 45°$	$\alpha = 60°$
t=5s	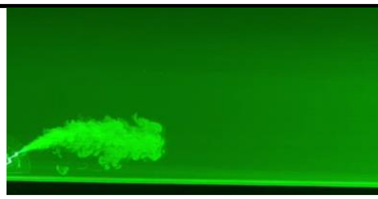	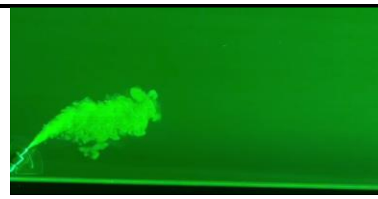	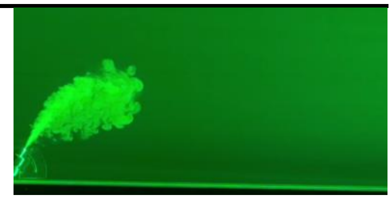
t=10s	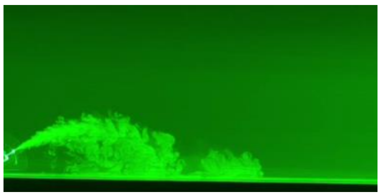	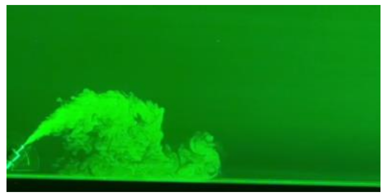	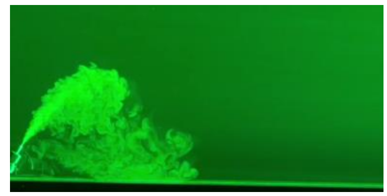
t=20s	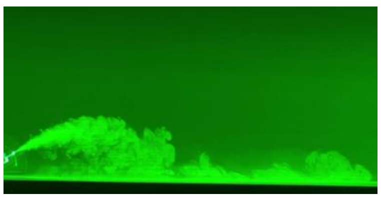	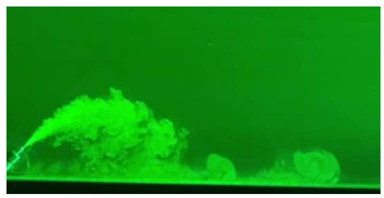	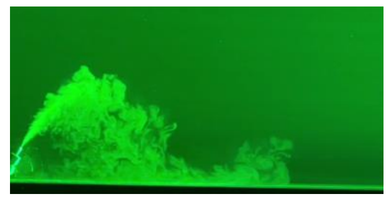
t=50s	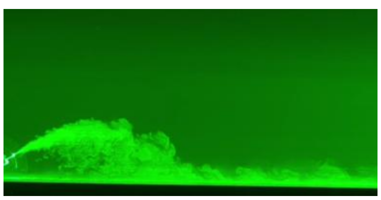	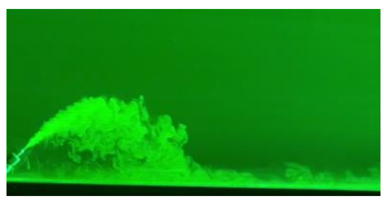	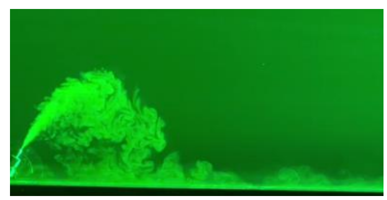

3. $\beta = 3°$

Time	$\alpha = 30°$	$\alpha = 45°$	$\alpha = 60°$
t=5s	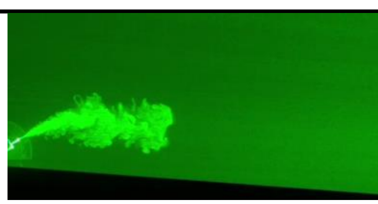	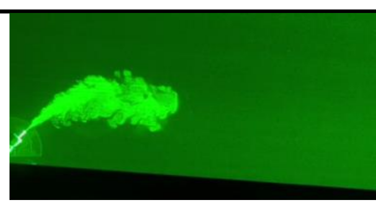	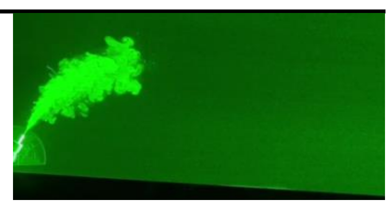
t=10s	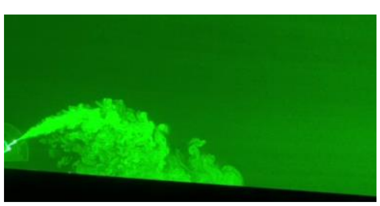	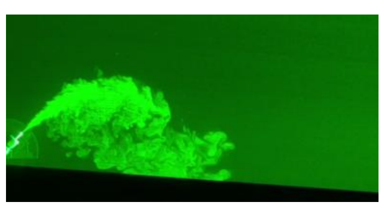	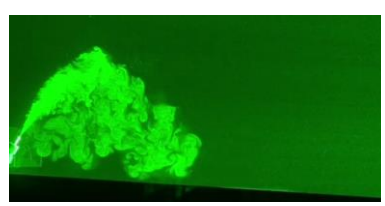

t=20 s

t=50 s

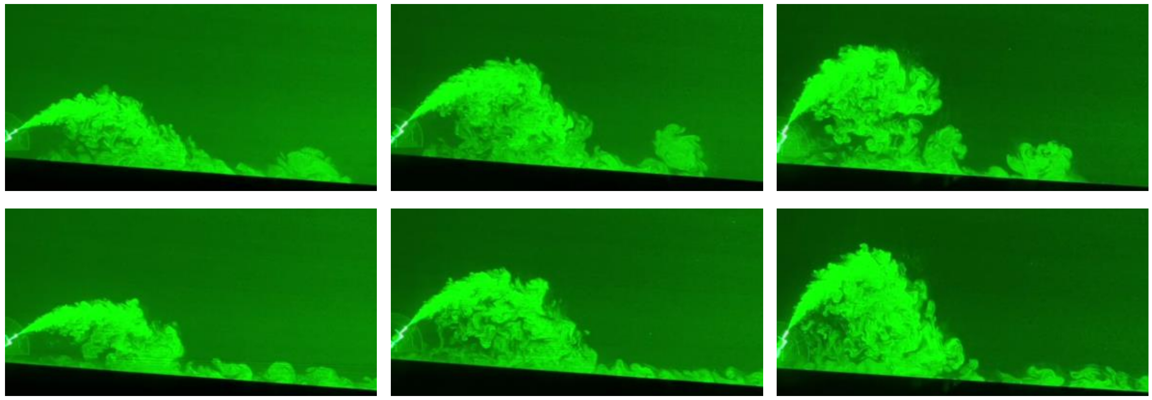

4. $\beta = 5°$

Time	$\alpha = 30°$	$\alpha = 45°$	$\alpha = 60°$
t=5s			
t=10 s			
t=20 s			
t=50 s			

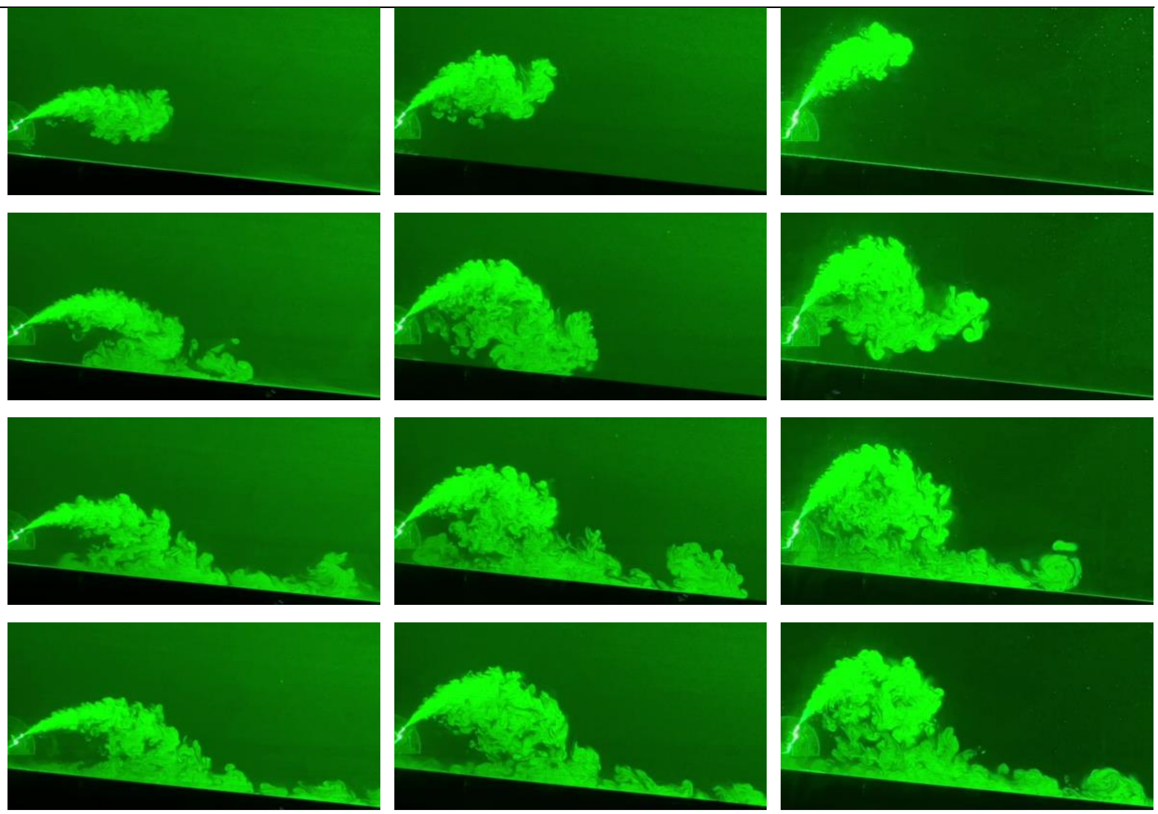

Figure 3.4 Evolution of dense jets, with the same F=17.3, at three different discharge angles ($\alpha = 30°, 45°, 60°$) on four different bottom angles ($\beta = 0°, 1°, 3°$ and $5°$) over time (at 5s, 10, 20s and 50s)

Some consistent observations are evident from the evolution of jets at different discharge angles over time steps. An inclined dense jet has high velocity and narrow width near the discharge nozzle, where the momentum is dominated, then it spreads and reaches the maximum height as velocity decreases after it falls to the bottom due to the negative buoyancy, then it impinges the bottom and eventually forms a density current on the bottom. The shape of the inclined dense jet during the ascending and descending phases is only affected by the discharge angle but has no relation with the bottom angles. For all three discharge angles, the upper boundary of the jet was sharp and clear, but the flow at the inner part was peeling off from the main flow due to the negative buoyancy, which made the inner boundary more blurred. When α=60º, the inner part was wider than the smaller discharge angles (α=30º and α=45º). This observation was consistent with LIF experiments from Lai and Lee (2012).

After the brine flow fell to the bottom (t =20s), the jet formed a series of Kelvin-Helmholtz (KH) vortices along the bottom. These vortices were induced by shear-induced turbulence. These vortices continuously appeared after the impingement (at 50s) and also on the sloped bottom (Figure 3.5). Notably, the positions of these Kelvin-Helmholtz (KH) vortices were irregular. The flow continued slowly along the bottom, resembling a ring vortex chain, but not all vortices collapsed at a fixed position. A few vortices were still formed due to the shear flow. Additionally, due to the limitations of the experimental tank size, some fluids reached the side of the tank and flowed out of the physical bottom boundary and returned, affecting the shear-induced turbulence in the jet flow. Most of the mixing occurred through these vortices, which were directly related to the shear-induced turbulence. The experimental results of Roberts et al. (1997) and Lai (2012) indicate that the shear-induced turbulence at the lower boundary gradually increases the dilution of the brine.

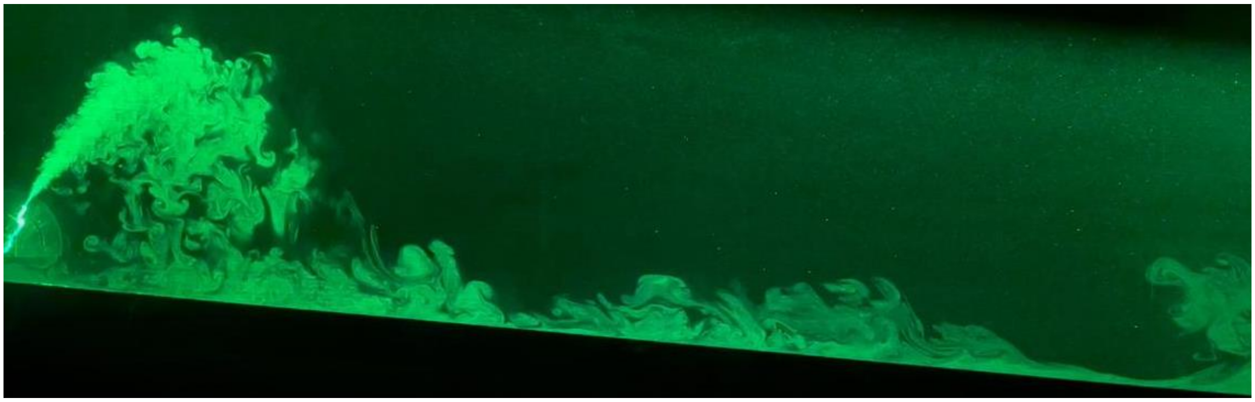

Figure 3.5.The series of vortices on the bottom ($\alpha = 60°, F = 22.1$) on (a) Horizontal bottom and (b) $5°$ sloped bottom.

From Figure 3.4, in the panels showing the instantaneous images of the jet at the 20s, it can be observed that, after the jet reached the bottom, a large vortex-shape formation was formed regardless of the discharge angle or bottom slope. Figure 3.6 presents raw images captured from cross-sections near the bottom (3 cm above the physical bottom) of the impingement areas, with a discharge angle of 60° and a Froude number of 17.3 on a 0° and 5° sloped bottom. It can be seen in Figure 3.6a and Figure 3.6b, respectively corresponding to horizontal and sloped bottoms, that when the jet flow fell and touched the bottom, it spread in all directions and formed a round-shaped structure near the impingement area. As the discharge continued, a large "ring" shape cloud could be seen (Figure 3.6c,Figure 3.6d). On the right side (downstream), this ring separated from the main structure, creating a gap with no brine, and the size of the ring increased. Before it moved out of the image frame, another ring structure appeared, but with more chaos and random eddies near it. Regardless of the bottom slope value, near the impact point area, smaller rings with vortices continued to appear in irregular sizes. They maintained a nearly round shape but most of them broke into small pieces surrounded by more chaotic flows.

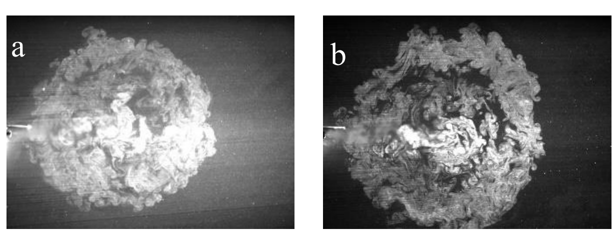

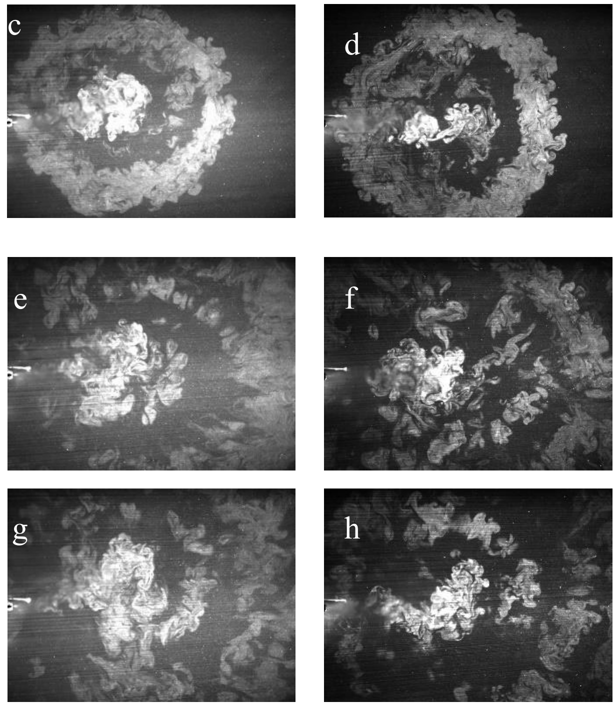

Figure 3.6 Instantaneous camera images of development and evolution at traverse planes near the impact point (left column shows temporal evolution of the 60° discharge angle on horizontal bed, right column shows temporal evolution of the 60° discharge angle on 5° sloped bed).

As the flow moves outward, this largest ring remains at the forefront of the flow. The formation of the large ring aligns with the findings of Roberts et al. (1997), who observed similar large-scale ring vortices at the front of the jet, which tended to propagate outward and collapse at the end of the mixing zone.

The slope caused gravity to increase the flow velocity, which enhanced the shear between the moving flow and the surrounding water. As a result, the ring formations became larger and separated faster on the sloped bed compared to the horizontal bed. Fig. 6e, 6f, 6g and 6h illustrate that, after the formation of the largest ring structure, additional rings of varying sizes continue to appear around the impact point area, but they lack regularity and a complete ring structure. This indicates the complexity of brine flow dynamics at the impact point area due to the influence of the physical bed. As the brine moves along the bed, these vortex structures gradually weaken and eventually dissipate due to mixing and dilution with the surrounding water. Moreover, after the brine flow fell to the bed, it moved in all directions, including upstream. On the horizontal bottom, the flow moves with an almost circular shape. In contrast, on the sloped bottom, the flow is constrained by the sloped bed, resulting in a slower movement toward the seashore and a deformation of the flow shape. Additionally, it should be noted that the transverse motion of the brine along the bed is affected by the slope.

3.4.2 Geometric information - Trajectory and jet development

The mean concentration field was obtained by time-averaging 4000 frames of instantaneous images, with a specific area of interest selected for analysis using MATLAB and visualized with ParaView. Figure 3.7 presents the time-averaged image of the vertical section of the jet over both horizontal and sloped bottoms. Some important information about the jet will be derived from the mean concentration field.

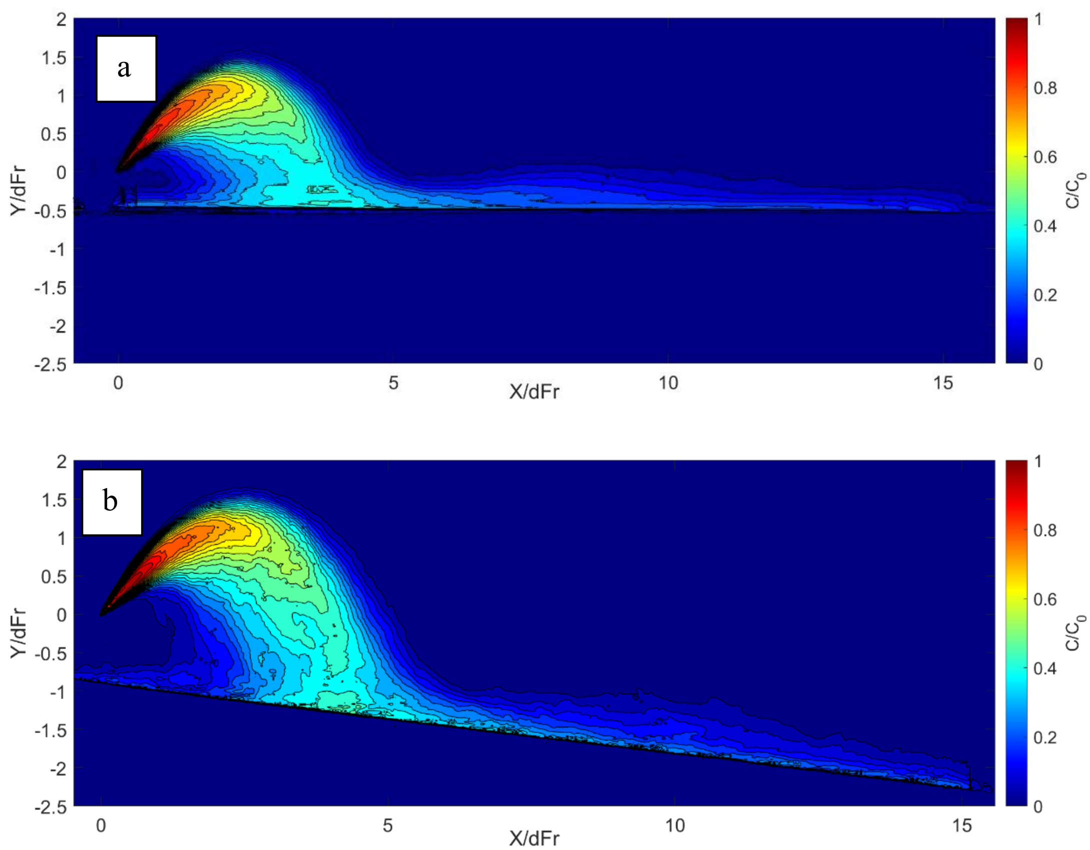

Figure 3.7 Mean concentration field of an inclined dense jet with a Froude number of 22.1, a discharge angle of 45°, on (a) 0° and (b) 5° bottom

Identifying the trajectory of the inclined dense jet can help predict and describe its shape, impacted area, and movement path. Jet trajectories are typically calculated based on the maximum concentration or velocity at each location in the perpendicular slices of the jet. It has been reported that the difference between the maximum concentration and the velocity is small (Wang and

Mohammadian 2022); therefore, the trajectory was determined from the concentration in this study and compared to previous studies (Shao and Law, 2010; Lai and Lee, 2012; Palomar, Lara, and Losada, 2016, Kikkert 2006). In Figure 3.8, the trajectory is normalized using the Froude number and nozzle diameter (dF): the results of the present study are consistent with those of previous experiments, further confirming the accuracy of the experiments of this study.

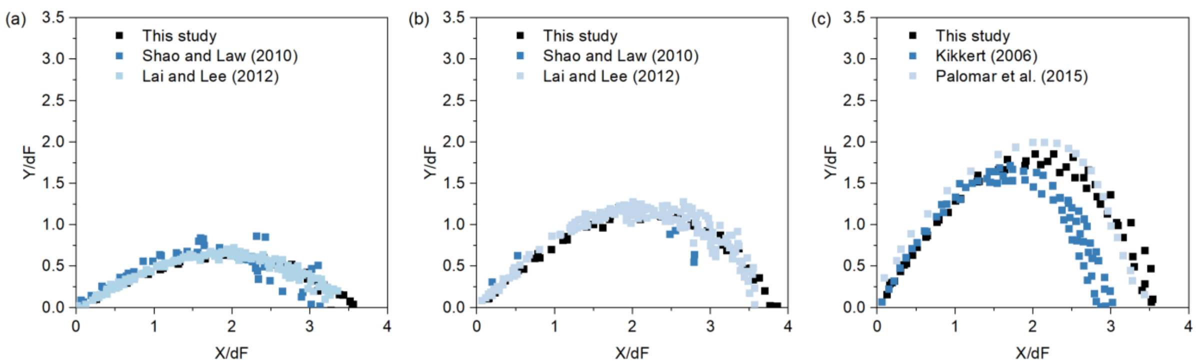

Figure 3.8 Trajectory of inclined dense jet of different discharge angles (a. 30°, b. 45°, c. 60°) on the horizontal bottom.

Figure 3.9 displays five representative concentration distributions from the inclined dense jet, examining three discharge angles (30°, 45° and 60°) with one Froude number (22.1). The concentration, C, was derived from five different cross-sections and normalized by the maximum concentration C_m, at each specific cross-section. C/C_m is then plotted against the dimensionless normal coordinate r/b_{gc} , where b_{gc} represents the radius defined by the equation $C/C_m = 1/e \approx 0.37$. Observations from Figure 3.9 indicate that the brine flow exhibited a widening along its axis, with the characteristics of an axisymmetric turbulent jet close to the nozzle, and then transitioned to a non-axisymmetric structure.

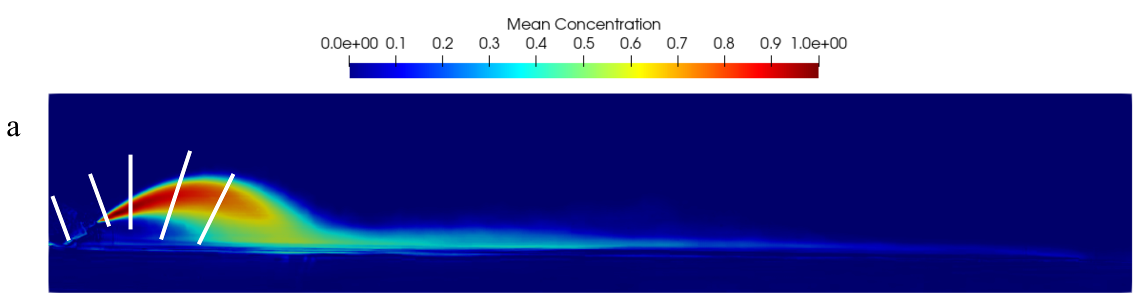

b

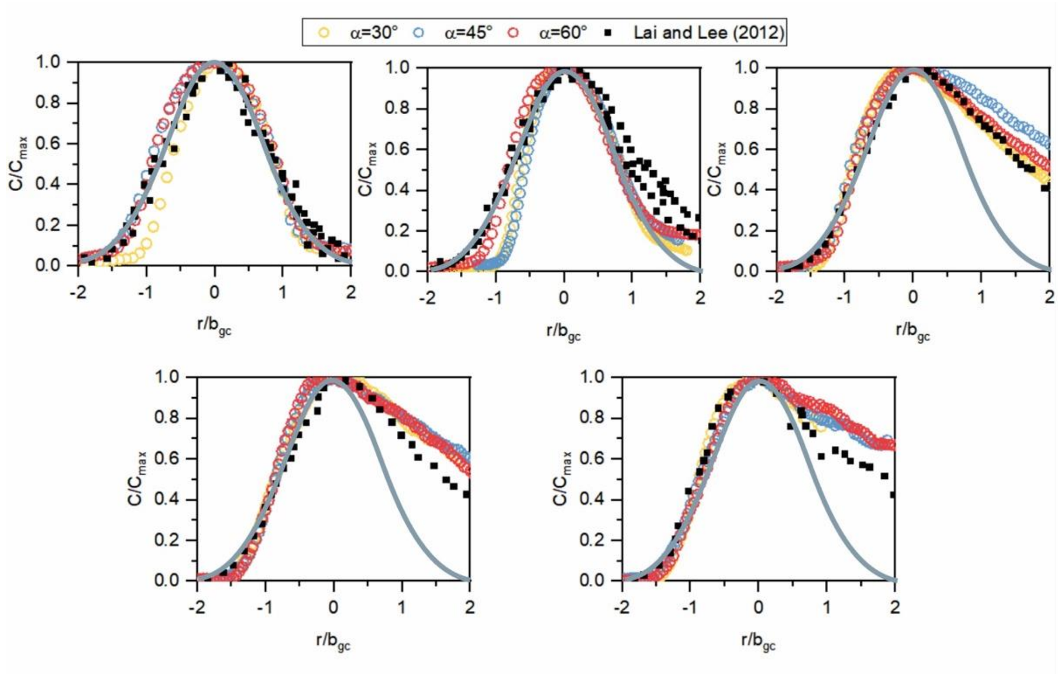

Figure 3.9. Concentration (C/C_m) field of inclined dense jet with three discharge angles: (a) time-averaged LIF image, with an example of the sections perpendicular to the jet axis (white lines); (b) representative cross-sectional profiles. r is the distance along the section perpendicular to the jet.

A comparison between this study and a previous study by Lai and Lee (2012) showed good agreement: Lai and Lee only presented results for a 60° discharge angle, and our study observed similar mixing patterns in inclined dense jets with discharge angles ranging from 30 °to 60°. From Figure 9b, it can be observed that the concentration field shows non-symmetrical behavior. Near the nozzle, the concentration field follows the Gaussian distribution, near the terminal rise height and after the jet, the inner half of the jet departs from the main flow, but the upper half remains Gaussian. This asymmetry of the jet is caused by the difference in stability between the upper and lower layers of the flow (Ferrari, Badas, and Querzoli 2018). In the upper layer, a stable stratification forms that allows the Kelvin-Helmholtz (KH) unstable vortex to fully develop and eventually break up. In contrast, in the lower layer, an unstable stratification forms, and the KH wave evolves into a downward plume, causing distinctive flow dynamics.

Except for the jet concentration development along the jet trajectory, the variance values at different heights of the jet also require attention, because they can show the mixing changes in the ascending and descending parts of the inclined dense jet. Compared to studies focused on the center plane of the jet, this analysis can provide more detailed information about the spatial variations and complexities of the mixing process. Figure 3.10 presents four heights indicating the locations marked by black lines and the numbered 1, 2, 3, and 4, and plots the nondimensional variance of concentration ($\delta^2\ /C^2_{\mathrm{max}}$),$\delta$ is the concentration variance) against X/d.

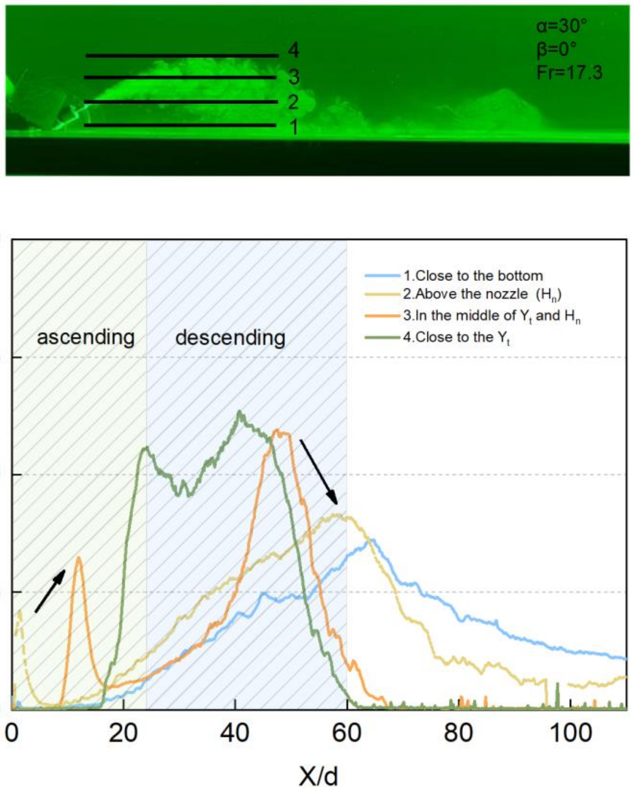

Figure 3.10 Variance at different heights of the jet (x: streamwise direction)

Above the nozzle (positions 2, 3, and 4), peaks are observed during both the ascending and descending phases, situated at the outer boundaries of the jet. In the ascending phase, the peak values increase, whereas in the descending phase, the peak values decrease. The highest values are found near the terminal rise height, suggesting more intense mixing in the region where the jet transitions from ascending to descending. Lower variance values are observed inside the jet (Line 2), suggesting that the core region of the jet is minimally involved in the mixing process. Combined with the real-time image analysis in Figure 4, it is evident that the outer side of the jet primarily detaches due to shear effects, which induce instabilities and cause the peeling-off process. This observation is consistent with the findings of Taherian et al. (2024). Furthermore, after the impact point, the variance gradually decreases along the bottom, indicating that fluctuations decrease on the bottom surface as the brine moves along the bottom.

3.4.3 Geometrical features relevant to the outfall system design

Since the sloped bed does not affect the jet's characteristics before it falls to the bottom, some geometrical information for designing purposes has been presented in Table 3.2, Table 3.3, Table 3.4 and compared with previous studies. This section also aims to verify the accuracy of this study. All the geometrical parameters include the terminal rise height (Y_t), the location of the centerline peak (X_c, Y_c), and the return point (X_r). To keep the results consistent and comparable, only the results from the horizontal bottom have been selected for comparison. Results show a good agreement between the data of the present study and the previous ones.

Table 3.2 Experimental results of 30° discharge angle

Parameters		This study	Lai and Lee (2012)	Shao and Law (2010)	Kikkert (2007)	Zeitoun and McIlhenny (1971)	Cipollina et al. (2005)
Terminal rise height (Y_t)	Y_t /dF	1.05	0.95	1.05	1.19	1.15	1.08
Horizontal location of centerline peak	X_c /dF	1.92	-	1.54	1.85	-	1.95
Vertical location of centerline peak	Y_c /dF	0.61	-	0.66	0.66	-	0.79
Return point (X_r)	X_r /dF	3.10	3.18	3.00	3.44	3.48	3.03

Table 3.3 Experimental results of 45° discharge angle

Parameters		This study	Lai and Lee (2012)	Shao and Law (2010)	Ferrari and Querzoli (2010)	Kikkert (2007)	Cipollina (2005)	Crowe (2013)	Papakonstantis (2011)	Zeitouns (1971)
Terminal rise height (Y_t)	Y_t /dF	1.66	1.58	1.47	-	1.61	1.61	1.73	1.59	1.43
Horizontal location of centerline peak	X_c /dF	1.91	2.09	1.69	-	1.81	1.80	1.96	2.16	-
Vertical location of centerline peak	Y_c /dF	1.13	1.19	1.14	1.19	1.07	1.17	-	1.17	-

Return point (X_r)	X_r /dF	3.42	3.34	3.33	3.03	3.20	2.82	-	3.16	3.33

Table 3.4. Experimental results of 60° discharge angle

Parameters		This study	Lai and Lee (2012)	Shao and Law (2010)	Ferrari and Querzoli (2010)	Kikkert (2007)	Cipollina (2005)	Papakonstantis (2011)	Zeitouns (1971)	(Roberts and Toms 1987)	(Roberts et al. 1997)
Terminal rise height (Y_t)	Y_t /dF	1.82	2.08	-	-	2.43	2.32	2.15	2.04	2.08	2.2
Horizontal location of center line peak	X_c /dF	1.80	1.78	-	-	1.75	1.42	-	-	-	-
Vertical location of center line peak	Y_c /dF	1.80	1.64		1.67	1.71	1.77	1.68	-	-	-
Return point (X_r)	X_r /dF	3.08	2.84	-	2.67	-	-	-	-	-	2.4

3.4.4 Impingement on the bottom and impact point

When the source height is low, the return and impact points on the horizontal bottom tend to be close to each other. Although geometric differences at these points are often negligible, the physical bottom has a noticeable influence on the mixing and development of inclined dense jets. This highlights the importance of analyzing the region of the impact point (Zhang, Law, and Jiang, 2017; Roberts, Ferrier, and Daviero, 1997).

Figure 3.11 presents the time-averaged concentration (C/C_0) scalar map near the impact region between the brine flow and the physical bottom, with a Froude number of 22.1. The results are shown for three different discharge angles ($\alpha = 30°, 45°, 60°$) on a 0° and 5° bottom.

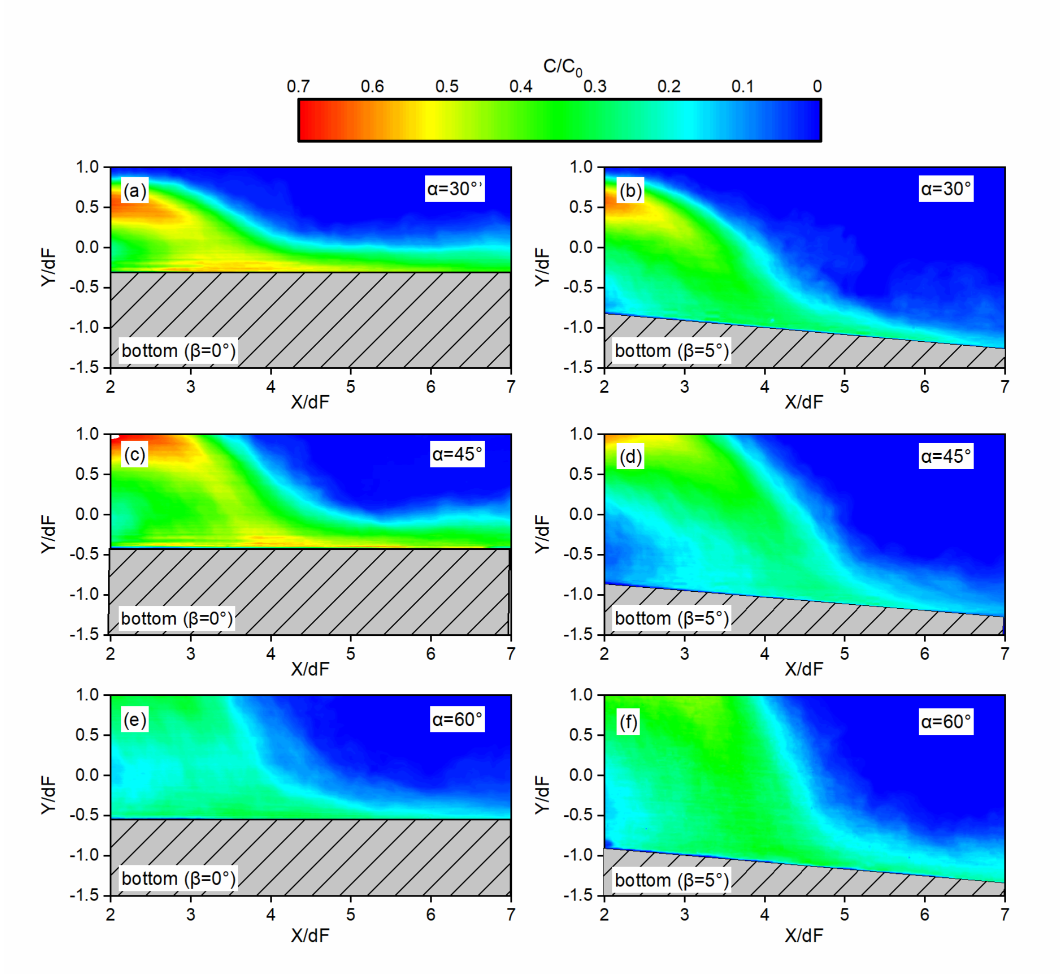

Figure 3.11. Brine concentration at impingement area: (a) $\alpha = 30° \,\&\, \beta = 0°$*; (b)* $\alpha = 30° \,\&\, \beta = 5°$*; (c)* $\alpha = 45° \,\&\, \beta = 0°$*; (d)* $\alpha = 45° \,\&\, \beta = 5°$*; (e)* $\alpha = 60° \,\&\, \beta = 0°$*; (f)* $\alpha = 60° \,\&\, \beta = 5$

The concentration buildup on the physical bottom is visible and consistent with studies by Shao and Law (2010) and Zhang et al (2017). As the discharge angle increases from 30° to 60°, the area of concentration buildup on the 5° sloped bottoms expands and dilution increases. The location of the impact point will change based on the different slopes. The horizontal distance from the nozzle to the impact point X_i on different slopes is normalized with the Froude number (Fr) and diameter (D) and plotted against various bottom slopes β in Figure 3.12. The impact point location moves downstream when β increases. The 30 and 45 ° discharge angles have a longer impact point distance than the 60° discharge angle on four sloped bottoms. These results align with Jirka's study(2008), which used an integral model to investigate the key properties of inclined dense jets across various sloped bottoms. He found that discharge angles between 30° and 45° on slopes less than 10° provided the largest impact point locations. Oliver et al (2013) conducted a similar study using LIF experiments. However, that study employed a nominal bottom (0°–30°) rather than a physical one, therefore, they did not account for bottom impact, leading to lower results compared to this study.

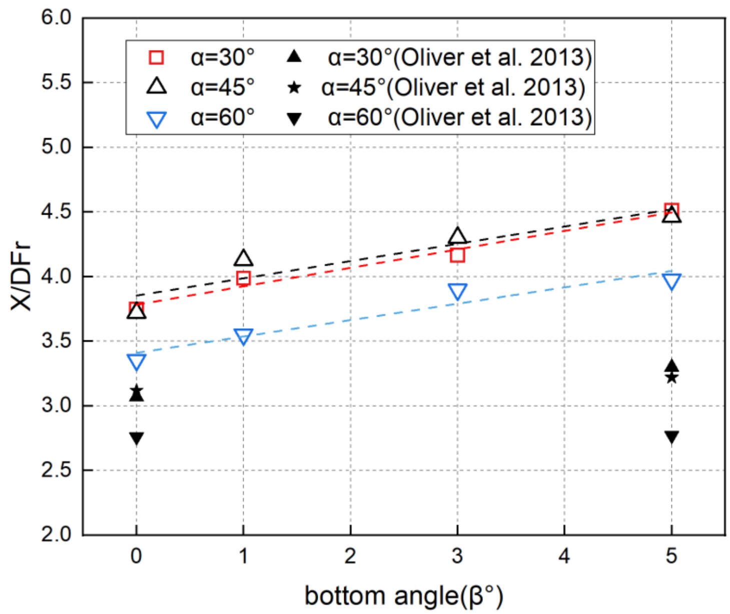

Figure 3.12 Nondimensional location of impact point on the different sloped bottom

The normalized distance can be expressed as a linear function of the bottom slope angle (β): $X_i/dF = A + B\beta$.

All parameters are listed in Table 3.5. The linear fit for three discharge angles shows excellent agreement, with R-squared values higher than 0.86.

Table 3.5 Coefficient of linear fitting function.

Discharge angle	Intercept(A)	Slope(B)	R-squared	Residual sum of squares
30	3.31	0.14	0.97	0.007
45	3.85	0.13	0.86	0.01
60	3.41	0.13	0.93	0.004

3.4.5 The dilution at impact point

Figure 3.13 illustrates the relationship between the impact point dilution (S_i/F) on various bottom slopes ($\beta = 0°, 1°, 3°, 5°$) and discharge angles ($\alpha = 30°, 45°, 60°$). It can be observed that the sloped bottom can increase the dilution at the impact point, and the larger discharge angle (60°)

has the highest value. The dilution increases as the slope angle increases. These findings are consistent with semi-analytical solutions (Oliver et al.2013) and the experimental findings from Oliver (2012), confirming that a sloped bottom improves the mixing for inclined dense jets at the impact point. On different sloped bottoms (β), the dilution at the impact point (S_i/F) follows a linear equation with the discharge angle (α). The equations are listed in Table 3.6.

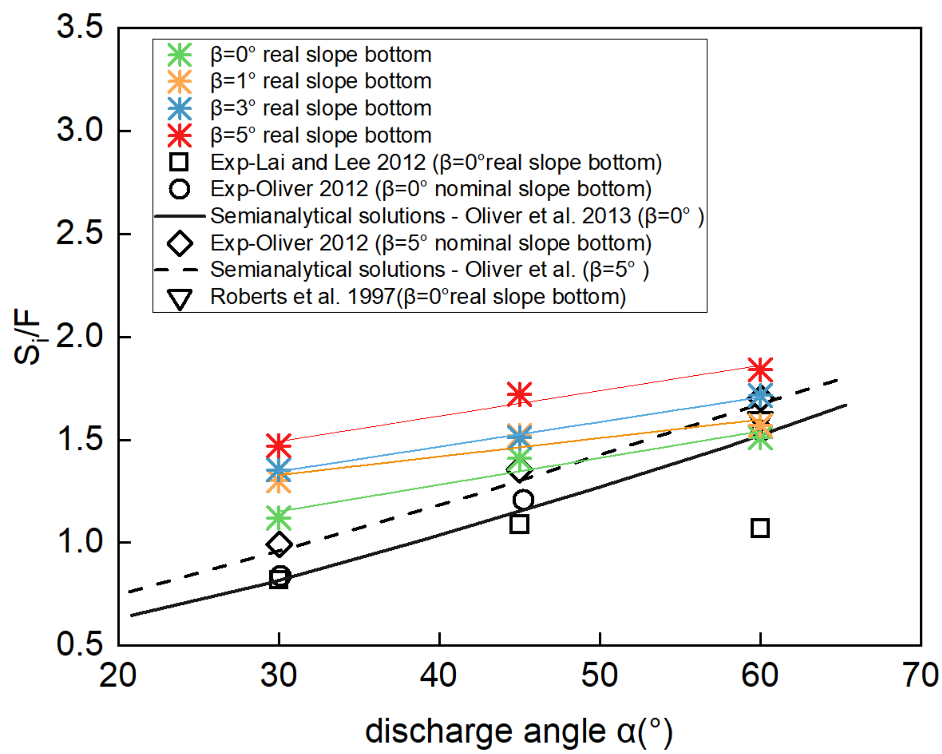

Figure 3.13 Normalized dilution near impact point on different sloped bottom

Table 3.6 Linear fitting function of the dilution at impact point with different sloped bottom.

β	Linear function	R-squared	Residual sum of squares
0	$\frac{S}{Fr} = (0.76 \pm 0.17) + (0.013 \pm 0.003) * \alpha(°)$	0.93	0.006
1	$\frac{S}{Fr} = (1.06 \pm 0.15) + (0.009 \pm 0.003) * \alpha(°)$	0.88	0.004
3	$\frac{S}{Fr} = (0.98 \pm 0.04) + (0.012 \pm 0.003) * \alpha(°)$	0.99	0.0004
5	$\frac{S}{Fr} = (1.12 \pm 0.12) + (0.012 \pm 0.003) * \alpha(°)$	0.96	0.003

Dilution information, including the minimum dilution at the centerline peak (S_m/F) and dilution at impact point (Si/Fr) for different slopes ($\beta = 0°, 1°, 3°, 5°$) is summarized in Table 3.7, Table 3.8 and Table 3.9.

Table 3.7 Dilution information for 30° discharge angle

Parameters		This study	Lai and Lee (2012)	Shao and Law (2010)
Centerline peak dilution	S_m/F	0.39	0.4	0.66
Impact point dilution ($\beta = 0°$)	S_i/F	1.12		1.45
Impact point dilution ($\beta = 1°$)	S_i/F	1.3		
Impact point dilution ($\beta = 3°$)	S_i/F	1.35		
Impact point dilution ($\beta = 5°$)	S_i/F	1.47		

Table 3.8 Dilution information for 45° discharge angle

Parameters		This study	Lai and Lee (2012)	Shao and Law (2010)	Papakonstantis (2011b)	Zeitouns (1971)
Centerline peak dilution	S_m/F	0.43	0.45	0.46	0.52	0.42
Impact point dilution ($\beta = 0°$)	S_i/F	1.41	1.09	1.26	1.55	
Impact point dilution ($\beta = 1°$)	S_i/F	1.52				
Impact point dilution ($\beta = 3°$)	S_i/F	1.51				
Impact point dilution ($\beta = 5°$)	S_i/F	1.72				

Table 3.9 Dilution information for 60° discharge angle

Parameters		This study	Lai and Lee (2012)	Papakonstantis (2011b)	Zeitouns (1971)	(Roberts and Toms 1987)	Roberts et al. (1997)
Centerline peak dilution	S_m/F	0.45	0.44	0.56	0.56		
Impact point dilution ($\beta = 0°$)	S_i/F	1.51	1.07	1.68	-	1.03	1.6
Impact point dilution ($\beta = 1°$)	S_i/F	1.57					
Impact point dilution ($\beta = 3°$)	S_i/F	1.72					
Impact point dilution ($\beta = 5°$)	S_i/F	1.84					

3.4.6 Lateral spreading at the impact point

By analyzing the transversal images of the impact region, we can obtain more information regarding the influence of the sloped bottom on the jet flow. After the brine falls to the bottom surface, it spreads outward in all directions (Papakonstantis and Christodoulou 2010). To quantify the lateral spreading near the impact point, the spreading width is defined by measuring the vertical distance (Z/dF) at the two lateral sides of the jet of the selected concentration threshold lines.

Figure 3.14 is a schematic diagram indicating the coordinate system of the transversal section of the jet.

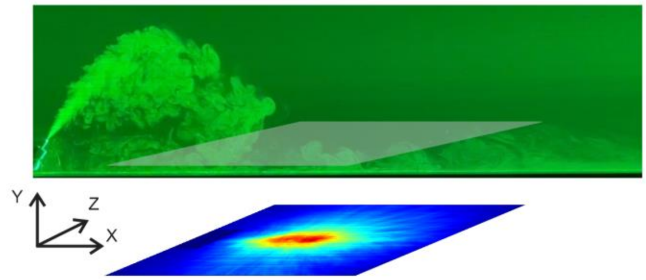

Figure 3.14 Illustration of the transverse cross-section of concentration variance plots

Due to the limited size of the images, the 75%, 50%, and 25% C_{max} threshold lines are selected to determine the Y/dF values for evaluating the lateral spreading width.

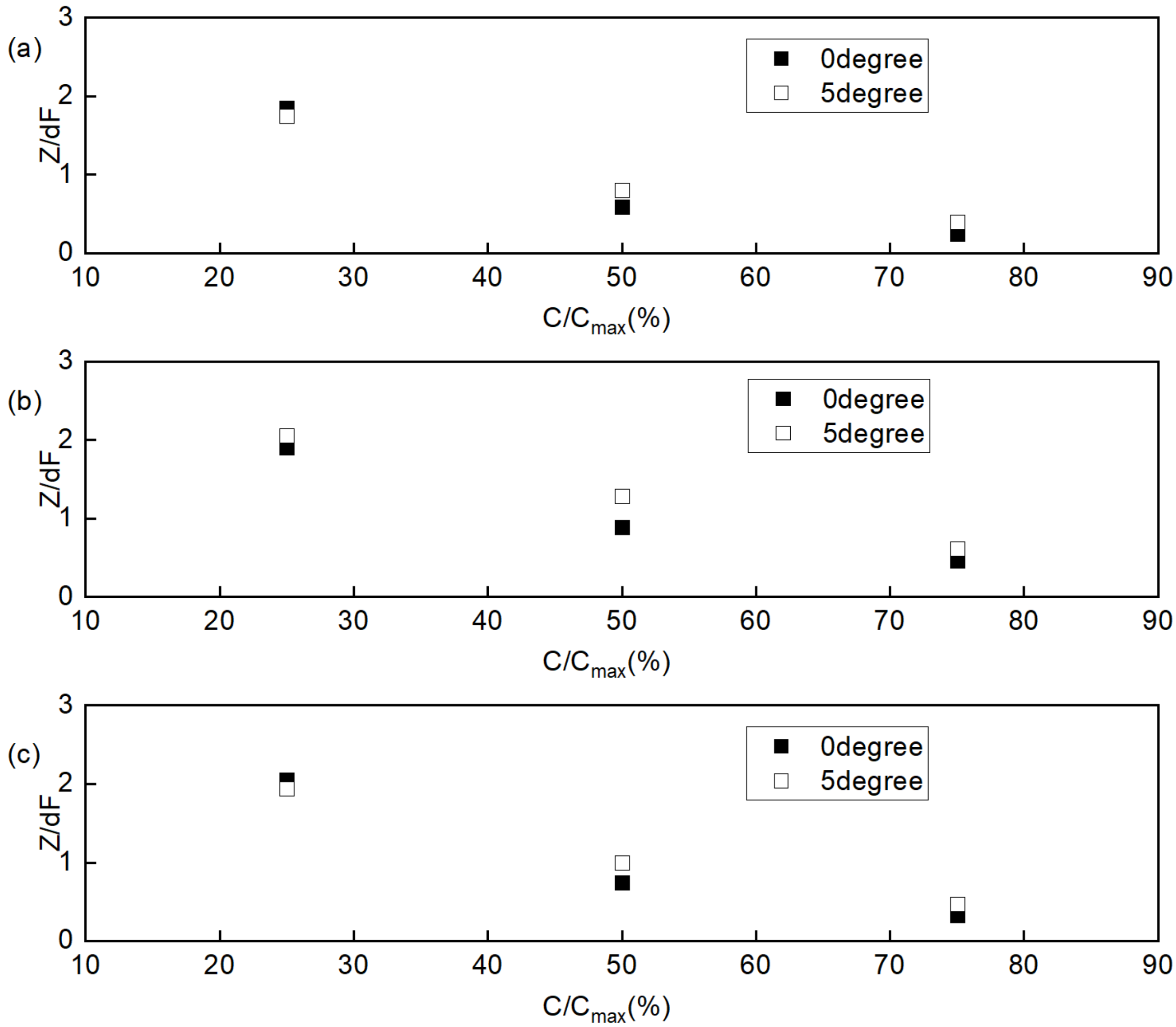

Figure 3.15. Comparison of lateral spreading width (Z/dF) at three threshold lines (25%, 50%, and 75% C_0 at the impact point on horizontal and 5° sloped bottoms (a)$\alpha = 30°$(b) $\alpha = 45°$; (c)$\alpha = 60°$

Figure 3.15 presents the comparison of lateral spreading width (Z/dF) at three threshold lines (25%, 50%, and 75% C_{max}) at the impact point on horizontal and 5° bottoms. The sloped bottom enables the fluid to slide along the surface, generating stronger lateral turbulence near the impact point, which accelerates lateral concentration distribution. The Z/dF values of high concentration region for both 75% C_{max} and 50% C_{max} on 5° bottom are higher than the horizontal bottom. However, for the 25% C_{max}, the differences become minimal.

3.4.7 Cross-sectional concentration along the bottom after the impact point

To examine the concentration profile variation along the bottom after impingement, the streamwise concentration profile at various locations is plotted in Figure 3.16. The concentration profile is nondimensionalized as C/C_{max} versus $Y/Y_{cmax/2}$, where C_{max} is the maximum mean concentration at the vertical section and $Y_{cmax/2}$ is the distance from the bottom to the point where $C=C_{max}/2$. Figure 3.16 shows that the maximum concentration on the bottom is close to the boundary itself, and all the profiles show self-similarity, compared with the previous studies (Shao and Law 2011; Palomar, Lara, and Losada 2016; Zhang, Law, and Jiang 2017; Pérez Díaz et al. 2018). It shows that after the impact point, the dense flow behaved similarly to a dense wall jet (Shao and Law,2011) and a nonconfined density current (Pérez Díaz et al., 2018).

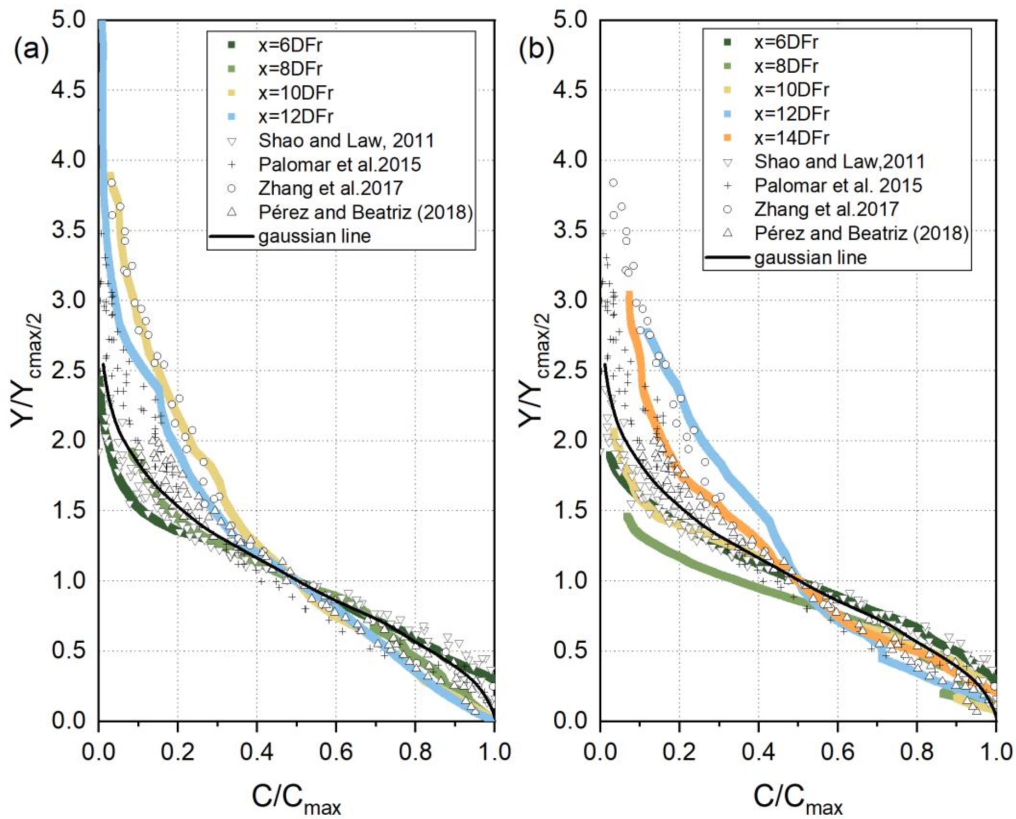

Figure 3.16 Normalized concentration profiles along the spreading layer (a) horizontal bottom; (b)5° sloped bottom.

On the sloped bottom (5°), the maximum concentration is still closer to the bottom, the self-similarity as a Gaussian profile can still be observed on the sloped bottom. The sloped bottom does not affect the flow characteristics and the flow behavior remains the same.

3.4.8 The concentration variation along the bottom after the impact point

Since the sloped bottom could provide a higher dilution at the impact point, this section focuses on the development of dilution along the bottom surface after the impact point. The relationship between dilution (S/F) and the normalized distance along the bottom (X/dF) is presented in Figure 3.17.It can be observed that dilution increases gradually along the bottom surface in both cases (horizontal and sloped bottoms).

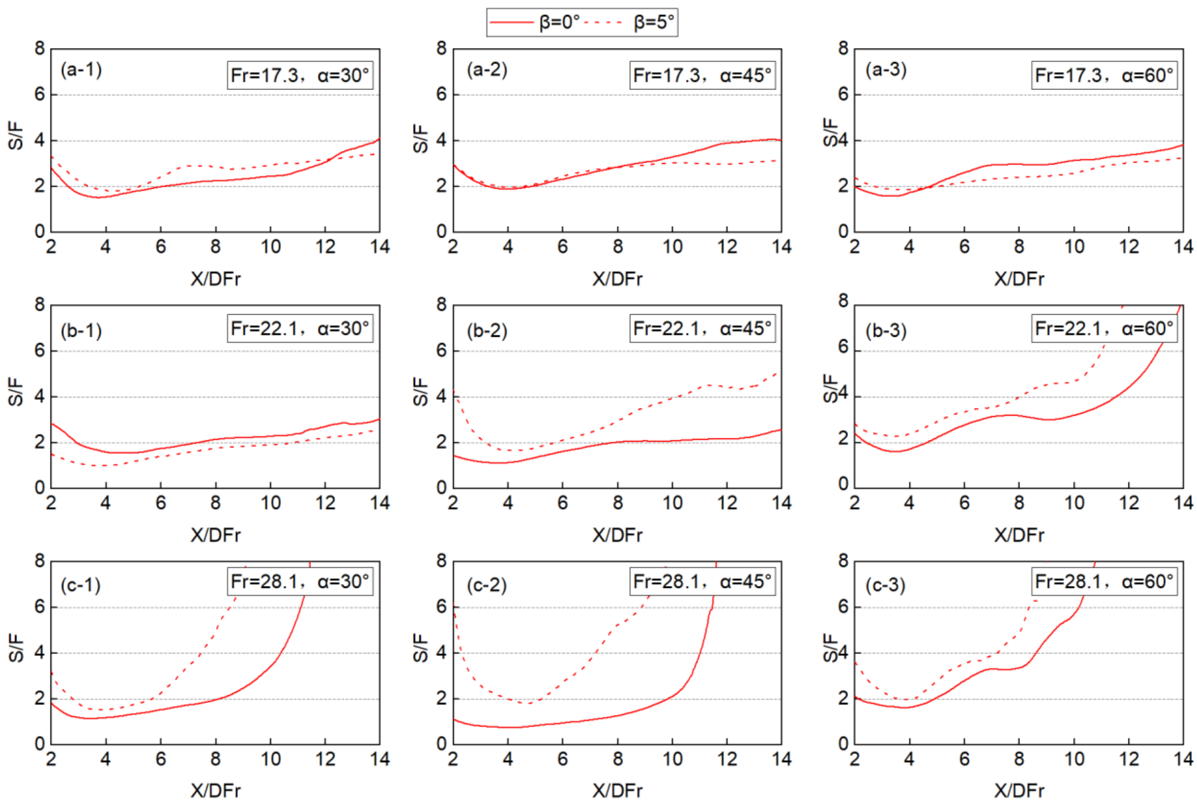

Figure 3.17. Dilution Profiles along the bottom surface for different Froude numbers (a: F= 17.3, b: F= 22.1, c: F= 28.1)

It can be observed that, when plotting the normalized dilution (S/F) under varying discharge angles and slopes, for lower Froude numbers, the difference in dilution behavior between the horizontal and sloped bottoms is relatively small. As the Froude number increases, the impact of the bottom slope becomes more significant, particularly at higher discharge angles (e.g. 45° and 60°).

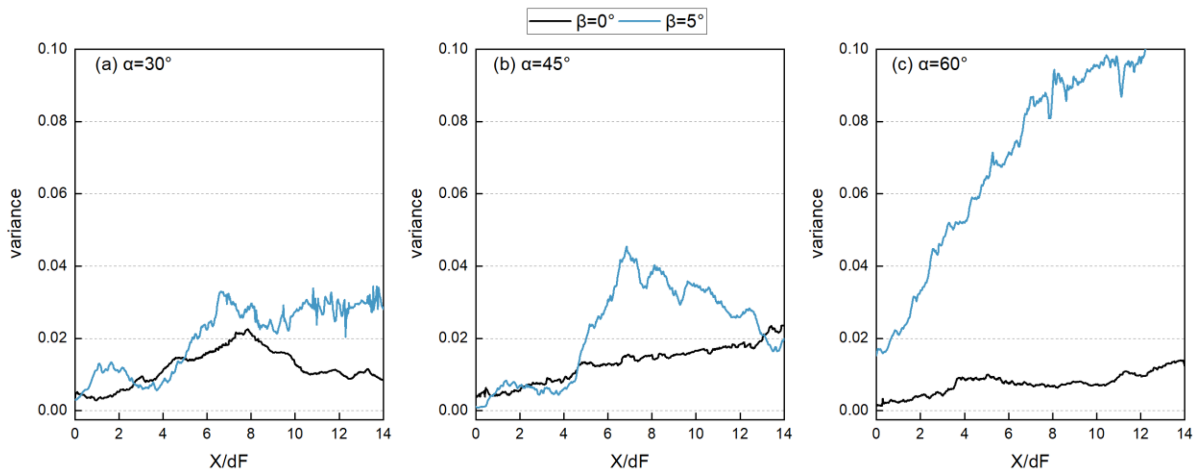

Figure 3.18 Variance of the concentration along the different sloped bottom for F=17.3

This suggests that the interaction between the jet and the bottom surface is highly sensitive to the jet's Froude number. Figure 3.18 presents dimensionless variance (σ^2/C_0^2) distribution along the bottom surface for F=17.3 with three different discharge angles. The variance on the sloped bottom is higher than that on the horizontal bottom for all three discharge angles. The Froude number affects the jet behavior. A higher Froude number indicates stronger initial jet momentum, enhancing interactions with the bottom surface and improving dilution efficiency. Conversely, a lower Froude number jet has less momentum, allowing density differences to dominate and causing the fluid to spread along the bottom with lower dilution. However, it can still be concluded that the variance of the jet on the sloped bottom is higher than that on the horizontal bottom, and this increased fluctuation promotes the mixing and dilution of brine. In the design of discharge outlets, the Froude number is typically higher than 25 to ensure sufficient jet momentum (Roberts et al. 1997), enhancing dilution and mixing efficiency, thus, the sloped bottom could further enhance the dilution efficiency of the brine.

3.4.9 Concentration fluctuation and Energy spectrum along the bottom

In the present study, turbulence structures have been observed along the bottom surface after the impact point (Figure 3.5). In order to investigate the variations along the bottom and the influence of the sloped bottom, five measurement points were selected evenly from the jet nozzle to the end of the bottom surface as shown in Figure 3.19.These points represent different locations within the flow field, including (P1: an upstream location before the impact point; P2: near the impact point; P3: immediately downstream of the impact point; P4: the middle of the bottom region;

and P5: the far end of the brine flow. The light intensity fluctuations at these points are used to represent concentration variation, and data were collected over approximately 3,000-4000 frames for each measurement point on the horizontal and sloped bottom.

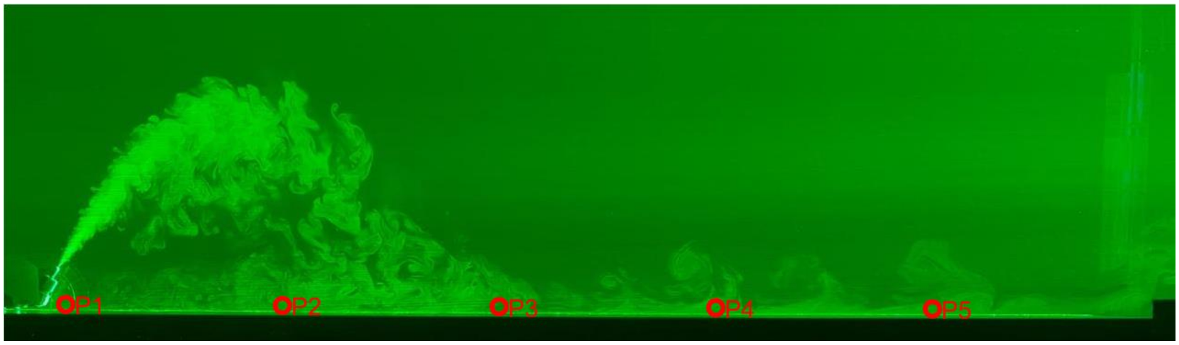

Figure 3.19 Illustration of the five points selected along the bottom ($\alpha = 60°, F = 28.1$)

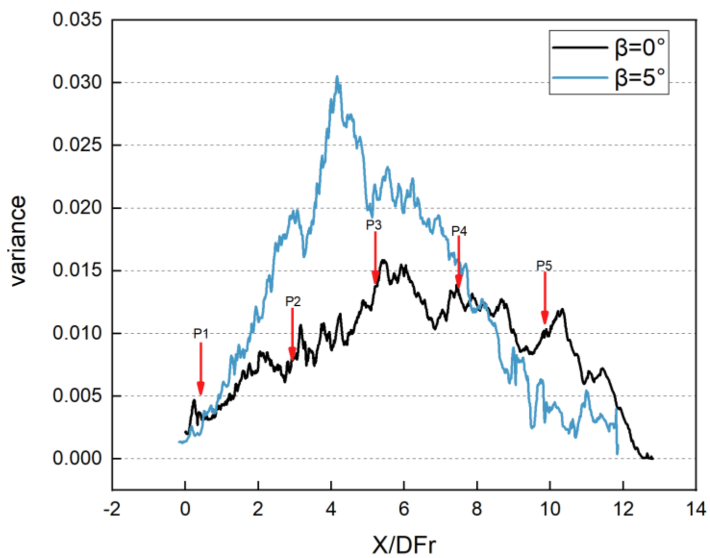

Figure 3.20 Variance along the two bottoms ($\alpha = 60°, F = 28.1$)

For a clearer comparison, the variance distribution along the bottom surface at the highest Froude number (F=28.1) is also presented in Figure 3.20, with the locations of five measurement points indicated by arrows. It shows that on the 5° bottom, the variance has a higher value and it drops quickly, which suggests a stronger local mixing and an efficient mixing on the sloped bottom.

In turbulent flow, energy can be analyzed using power spectra, which describe the kinetic energy distribution across different eddy sizes. According to Kolmogorov's theory, the power distribution of turbulent flow within the inertial region follows the well-established -5/3 -scaling law (Zakharov, L'vov, and Falkovich 2012). Papanicolau and List (1988) confirmed the applicability of the -5/3 scaling law to vertical dense jets. Similarly, Fellouah and Pollard (2009) conducted experiments on horizontal jets and provided additional validation of Kolmogorov's theory. To further investigate this phenomenon, the energy spectrum at five measurement points on two bottom conditions is presented in Figure 3.21, for F=28.1.

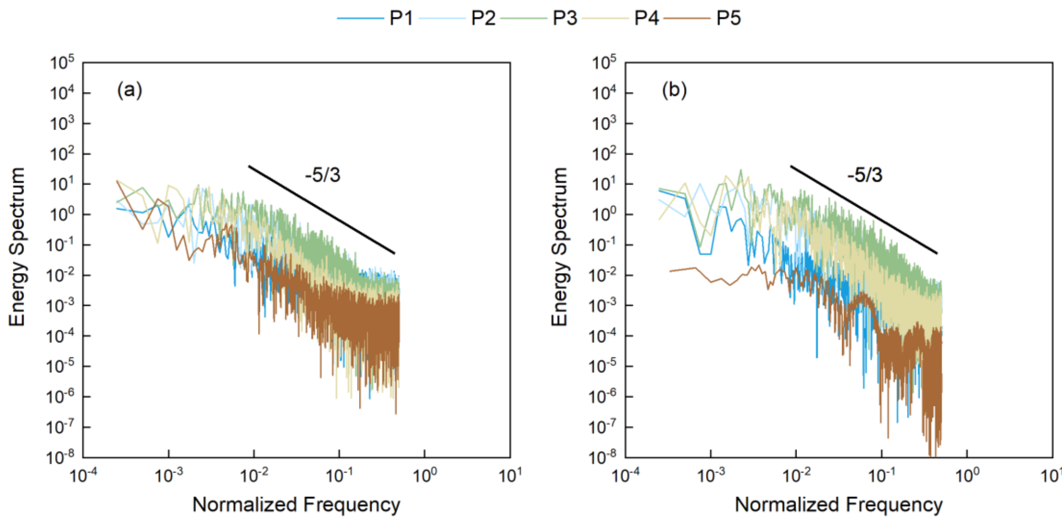

Figure 3.21 Energy spectrum at two bottoms: (a) $\beta = 0°$ (b) $\beta = 5°$ *for F=28.1.*

The results show that most measurement points align with the −5/3 scaling law, indicating that after the impact point, the flow on the sloped surface remains turbulent. For F = 28.1, at P5, the lower energy confirms that the turbulence intensity has decayed, suggesting reduced mixing activity near this region. Turbulence energy levels on the sloped bottom are generally higher, which means that the sloped bottom has more efficient turbulence energy transfer and enhances the breakdown of large-scale vortices into smaller structures, which accelerates the cascade process and improves the mixing efficiency. Additionally, the sloped bottom can induce stronger shear flow along the bottom surface after the impact point, which increases local turbulence intensity and enhances both lateral spreading and vertical mixing of the jet. It also helps achieve higher dilution efficiency.

3.4.10 End of mixing zone

Since the discharge of the inclined dense jet is a continuous process, the brine continuously mixes with the surrounding water while moving on the bottom surface. Therefore, studying the size of the mixing zone and assessing the extent of the effect on the bottom environment is important.

According to Roberts et al. (1997), the end of the mixing zone is defined as the point where the intensity of fluctuations decreases to 5% and turbulence collapses. In this study, we adopt a similar approach, calculating the coefficient of variation ($CoV = \frac{Standard\ deviation}{Mean}$) at ten measurement points along the bottom surface after the impact point to determine the mixing zone's extent. Figure 3.22 presents an example of measurement point selection and the coefficient of variation distribution for each point. Once the coefficient of variation drops significantly, the corresponding location represents the end of the mixing zone.

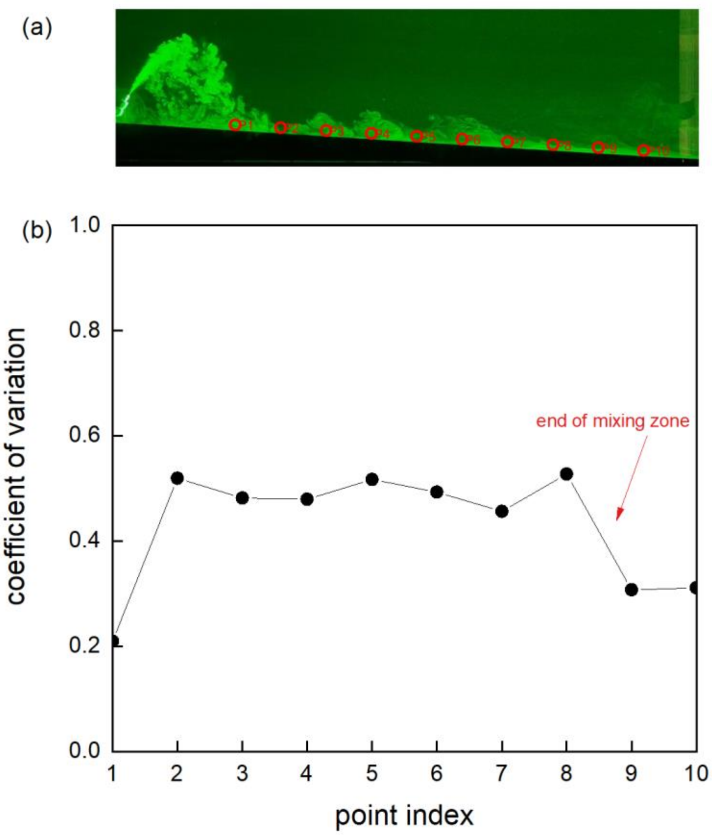

Figure 3.22 (a) Illustration of ten points selected along the sloped bottom ($\alpha = 60°, \beta = 3°, F = 17.3$) (b) Coefficient of variation of ten points

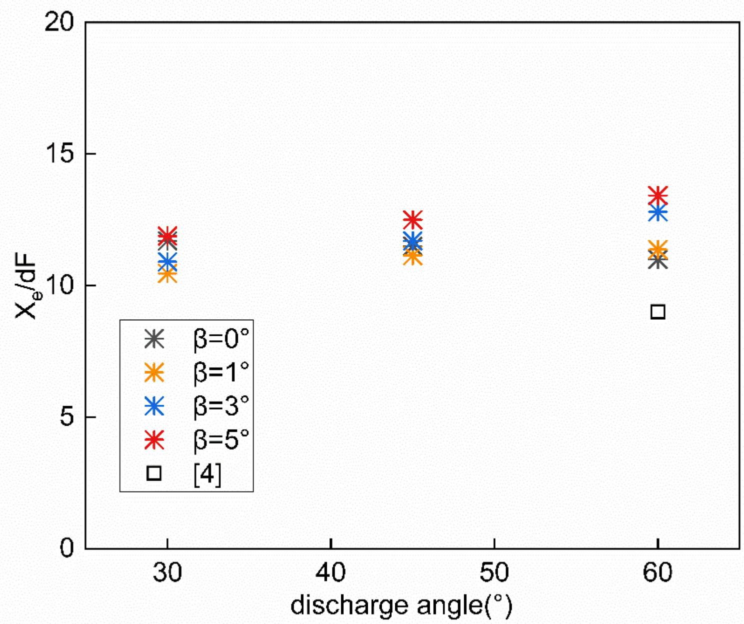

Figure 3.23. The end of the mixing zones X_e/dF for three discharge angles on different sloped bottom.

The end of mixing zone for three discharge angles and four sloped bottoms is shown in Figure 3.23. The end of mixing zone is increased on the sloped bottom as the sloped angle increases. On the horizontal bottom ($\beta = 0°$), the X_e/dFr values for three discharge angles are close to each other, and for the 60° discharge angle the X_e/dFr value is 11, which is 22% higher than the result reported by Roberts et al. (1997), which was 9. This difference might be attributed to the different measurement methods, as well as the difference in bottom surface roughness caused by the materials used— the previous study used a wooden bottom, while the present study employed an acrylic one, but the results can still be considered comparable when $\beta = 5°$ the end of mixing zone is extended by nearly 1.6%, 8% and 22% for discharge angles of $30°, 45°$ and $60°$, respectively. The sloped bottom makes the heavy brine prone to move downwards, and less brine will move towards the seashore, and the flow will have extra mixing along the sloped bottom because of the acceleration on the sloped bottom.

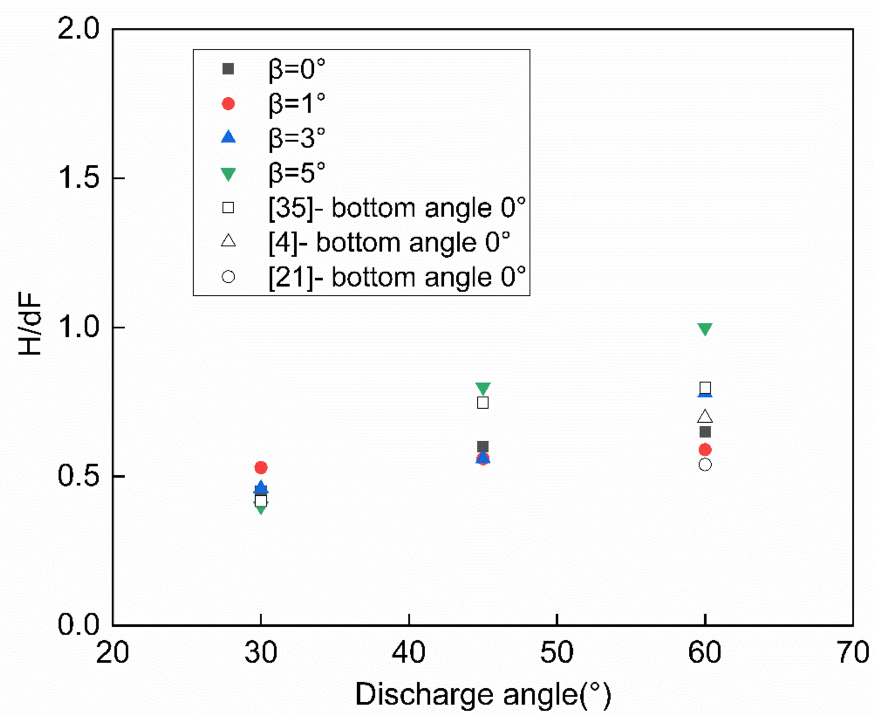

Figure 3.24 Spreading layer thickness at the end of mixing zone.

The thickness of the spreading layer at a 60° discharge angle at the end of the mixing zone is compared with previous studies from Palomar et al. (2015), Zhang et al. (2017), and Roberts et al. (1997) in Figure 24. The mixing layer thickness for the 60° discharge angle on a horizontal bottom is 0.65, which shows good agreement with the results from Roberts et al. (1997) of 0.7 and Palomar et al. (2015).

The thickness of the bottom layer depends on the discharge angle. As the discharge angle increases, the thickness of the layer increases. The 60° discharge angle results in the greatest thickness, especially on the sloped bottom. This is because the 60° discharge angle has a larger vertical component for velocity compared to 30° or 45°. This larger vertical component allows the jet to penetrate deeper in the vertical direction, increasing the fluid's vertical spread and thus the layer thickness. At the same time, the steeper slope would facilitate the brine velocity and lead to more eddies and eddy structures.

3.5 Conclusions and recommendations

This study applied the LIF experimental technique to investigate the effect of an inclined bottom on the mixing of inclined dense jets discharged into a stationary water environment. A total of 36 experiments were conducted, including three common discharge angles (30°, 45°, and 60°), four different bottom slopes (0°, 1°,3°, 5°), and three different Froude numbers (Fr=17.3, 22.1, 28.1). Vertical and transverse profiles were studied in detail to obtain a comprehensive understanding of the mixing properties. The findings and conclusions are summarized below.

Jet Behavior and Impact Location

The sloped bottom does not affect the behavior of the inclined dense jet before it reaches the bottom, as expected. The terminal rise height, the location of the centerline peak, and the return point remain consistent with those observed over a horizontal bottom. However, the normalized location of the impact point is influenced by the slope angle. A linear relationship was established, showing that smaller discharge angles (30° and 45°) result in longer impact distances on both horizontal and sloped bottoms.

Mixing Structure and KH Vortices

The flow structure near the impact point becomes highly complex. A large ring-shaped vortex forms immediately after impingement, likely associated with a hydraulic jump phenomenon. Following this, a series of Kelvin–Helmholtz (KH) vortices develop along the bottom. These vortices arise from the shear between the jet flow and the ambient fluid near the bed. The variance distribution confirms that KH vortices are more prominent on the sloped bottom than on the horizontal one, indicating stronger shear and enhanced mixing intensity under sloped conditions.

The analysis of variance shows that the highest fluctuation intensity before impact occurs near the outer edge of the jet during its downward motion, indicating that the outer region plays a key role in pre-impact mixing. After the jet reaches the bottom, the maximum variance shifts to the impact point, especially on the sloped bed. This further confirms the role of the bottom surface in intensifying mixing due to increased shear and turbulence.

Effect of Bottom Slope on Lateral Spreading and Dilution at the Impact Point

On the horizontal bottom, concentration tends to accumulate near the impact point. In contrast, the inclined surface introduces more complex hydrodynamic behaviors. The 5° sloped bottom increases both the variance of concentration fluctuations and the lateral dispersion at the impact point. As the slope increases from 0° to 5°, the concentration at the impact point decreases, and the dilution value increases approximately linearly, indicating that steeper slopes promote more effective lateral mixing. This trend suggests that the bottom slope has a non-negligible influence on the lateral extent of the near-field mixing zone.

On the inclined bottom, the concentration at the impact point decreases, and as the bottom slope increases (0°, 1°, 3°, 5°), the dilution value increases linearly.

Compared to the horizontal bottom, the 5° sloped bottom increases the dilution at the impact point by 31%,22% and 22%, corresponding to the three discharge angles (α=30°, α=45° and α=60°).

Bottom layer and Froude Number Influence on Mixing Behavior

After the impact point, the brine continues to move along the bottom surface. The flow behaves like a wall jet and shows characteristics of an unrestricted density current. The concentration variance along the sloped bottom is significantly higher than that on the horizontal bed. This result indicates stronger local fluctuations and more intense shear-induced turbulence beyond the impact region.

However, the distribution of concentration along the sloped bottom depends on the Froude number. At moderate Froude numbers, where the brine has relatively high density and strong buoyancy contrast with the ambient fluid, the jet remains more stable. In these cases, gravity dominates the motion, and the brine tends to flow steadily along the slope with limited mixing, resulting in lower dilution.

In contrast, at higher Froude numbers (Fr = 22 and 28), the jet becomes more momentum driven. The increased discharge velocity enhances the interaction between the brine and the surrounding water, promoting stronger entrainment and higher dilution rates along the sloped bottom. These results suggest that both bottom slope and Froude number jointly affect mixing intensity after impingement.

Turbulence Energy Distribution

Energy spectrum analysis at various locations on both horizontal and sloped bottoms confirms that the turbulence energy distribution follows Kolmogorov's –5/3 scaling law. The turbulence energy levels on the sloped bottom remain consistently higher than those on the horizontal bottom. The slope enhances turbulent mixing and increases dilution efficiency. These experimental results demonstrate that the bottom slope plays a significant role in flow dynamics and should be considered in the design of brine discharge systems. In addition, an inclined dense jet with a higher Froude number achieves greater mixing efficiency.

End of the Mixing Zone and Spreading Layer Thickness

Xe/dF (end of mixing zone) increased with the slope angle. If the slope angle exceeds 3°, the 60° discharge angle produces the largest X_e/dF value. Meanwhile, since the thickness of the spreading layer is influenced by both the discharge angle and the bottom slope angle, the 60° discharge angle on the sloped bottom results in the greatest thickness compared to the 30° and 45° discharge angles for all slope angles considered in this study.

Engineering Implications and Future Work

In practical applications, engineers should assess how different slope angles influence key parameters such as impact location, bottom layer thickness, and near-field dilution. The results indicate a clear interaction between gravity effects induced by the slope and the momentum of the jet. This interaction plays a key role in affecting the flow structure and concentration distribution along the receiving bottom.

Further research should explore brine transport and mixing under various slope conditions and wide range of Froude numbers, especially the differences between pre- and post-impact behavior. These findings can improve the accuracy of environmental impact assessments and support design strategies for outfall systems under different bottom conditions, which could help protect the marine environment more effectively.

CRediT authorship contribution statement

Xinyun Wang: Writing – original draft, Visualization, Validation, Software, Resources, Methodology, Investigation, Formal analysis, Data curation, Conceptualization. Abdolmajid

Mohammadian: Writing – review & editing, Supervision, Software, Project administration, Methodology, Funding acquisition, Data curation, Conceptualization. Simone Ferrari: Writing – review & editing, Supervision, Software, Resources, Methodology, Investigation, Data curation. Philip J.W. Roberts: Writing – review & editing, Formal analysis, Data curation.

Funding Statement

This research was funded by the Natural Sciences and Engineering Research Council of Canada (NSERC).

Declaration of competing interest

The authors declare that they have no known competing financial interests or personal relationships that could have appeared to influence the work reported in this paper.

Data availability

The data that support the findings of this study are available from the corresponding author upon reasonable request.

Chapter 4 Influence of a Sloped Bottom on a 60-Degree Inclined Dense Jet Discharged into a Stationary Environment: A Numerical Simulation Study

Xinyun Wang(corresponding author)[1], Abdolmajid Mohammadian[1]

1. Department of Civil Engineering, University of Ottawa, Ottawa, Canada

Abstract

In the present study, Large Eddy Simulation (LES) was applied to investigate the behavior of a 60° inclined dense jet discharged onto horizontal (0°) and sloped (5°) bottoms in a stagnant environment. The objective of this study is to evaluate the capability of LES to capture both the kinematic and mixing characteristics of inclined dense jets interacting with different bottom boundaries. A common Reynolds-Averaged Navier-Stokes (RANS) model was also included for comparison.

LES accurately captured the key kinematic and mixing characteristics, including the jet trajectory, centerline peak location, impact point, and terminal rise height, and showed strong agreement with the experimental observations. It also predicted the concentration distributions and variations along both the horizontal and sloped bottoms. In contrast, the RANS model underestimated both geometrical and dilution properties. A Gaussian fitting function was proposed to estimate the concentration distribution under both bottom conditions, providing a practical tool for predicting concentrations within and beyond the near field at the bottom. Analysis of the spreading layer indicated that the concentration profiles exhibited self-similarity under both bed conditions. Energy spectrum analysis showed that the sloped bottom enhanced shear and turbulence, thereby improving the mixing efficiency.

Overall, this study confirmed the reliability of LES in modeling the interaction between inclined dense jets and bottom boundaries and highlighted the critical influence of bed slope on jet dilution and mixing behavior.

Keywords: LES(Large Eddy Simulation), inclined dense jet, sloped bottom, OpenFOAM, jet-bottom interaction.

4.1 Introduction

As population growth and climate change increase the risk of drought, the number of desalination plants is steadily growing(Sedlak 2023). However, the concentrated brine byproduct generated during desalination has raised significant environmental concerns because its high salinity can be harmful to marine ecosystems if it is not properly discharged (Elsaid et al. 2020; Meerganz von Medeazza 2005). Therefore, it is essential to ensure that outfall designs can enhance brine mixing to achieve optimal dilution and minimize environmental impacts.

Inclined dense jets (or inclined negatively buoyant jets) are widely adopted in brine discharge systems (Zeitoun and McIlhenny 1971). In this method, brine is discharged as a turbulent jet through a submerged pipeline and nozzle system, with the nozzle set at an upward inclination angle, as illustrated in Figure 4.1.

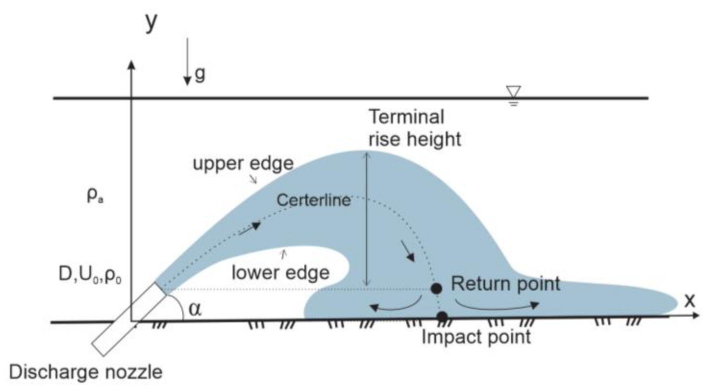

Figure 4.1 A schematic view of the single inclined dense jet discharged into the stationary ambient water.

The brine jet (ρ_{jet})is discharged from the round nozzle (D) at velocity U with an inclination angle α. Due to its initial momentum, the jet ascends along the discharge angle, reaching a maximum height before descending towards the seabed(Roberts, Ferrier, and Daviero 1997). The point at which the jet touches the seabed is known as the impact point. Throughout this process, entrainment and re-entrainment occur continuously(Ferrari and Querzoli 2010), and the brine jet is diluted to decrease its concentration.

Nondimensional analysis of an inclined dense jet is important for both practical applications and theoretical studies. All jet parameters can be expressed in a dimensionless form(Roberts et al. 1997). The geometric properties of the jet can be represented as:

$$\frac{X}{DFr} = C_1$$

Where X represents the horizontal location of a point in the Cartesian coordinate system, and Fr is the densimetric Froude number, given by

$$Fr = U_0/D\sqrt{g_0'},$$

where $g_0' = g\frac{(\rho_0-\rho_a)}{\rho_a}$.

Here, ρ_0 is the density of the brine, ρ_a is the density of the receiving water. Similarly, the concentration of the jet is often described in terms of dilution, which is noted by S, and also can be nondimensionalized as:

$$\frac{S}{Fr} = C_2$$

Where:

$$S = \frac{(\rho_0 - \rho_a)}{\rho - \rho_a}$$

Where ρ is the local density.

These parameters are typically correlated with the discharge angle of the jet (α). C_1 and C_2 are empirical coefficients obtained from numerical or experimental results.

Experimental efforts have been made to investigate the characteristics of single-port inclined dense jets in stationary receiving-water environments. Zeitoun et al. (Zeitoun and McIlhenny 1971) were the first to use photographic methods and point measurements to investigate the geometry and concentration distribution of inclined dense jets at various discharge angles (α=30, 45, and 60°). They observed that key properties, such as the maximum rise height (Y_t), centerline peak (X_c, Y_c), and return point (X_r) or impact point (X_i), were influenced by the discharge angle(α). In particular, the 60-degree discharge angle had the longest jet path and greatest dilution at the impact point. Later studies expanded the range of discharge angles, improved the empirical models, and provided additional experimental data(Bloomfield and Kerr 2002; Cipollina et al. 2005; Bashitialshaaer, Larson, and Persson 2012; Papakonstantis, Christodoulou, and Papanicolaou 2011, 2011b; Yang et al. 2024). Meanwhile, advanced techniques such as Light Attenuation (LA) and Laser-Induced Fluorescence (LIF) have further improved the measurement accuracy (Roberts et al. 1997; Kikkert, Davidson, and Nokes 2007; Shao and Law 2010; Lai and Lee 2012; Azizi, Goharikamel, and Vafaei 2020; Papakonstantis and Mylonakou 2021; Ferrari et al. 2013; Jiang, Law, and Lai 2019).

In addition to experimental research, Computational Fluid Dynamics (CFD) has been widely applied as a powerful alternative in the study of inclined dense jets, owing to its capability to resolve high-resolution flow fields and simulate long-term flow evolution under varying boundary conditions (Mohammadian, Gildeh, and Nistor 2020). CFD numerically solves the Navier-Stokes equations using three main approaches: Direct Numerical Simulation (DNS), Reynolds-Averaged Navier–Stokes (RANS), and Large Eddy Simulation (LES)(Anderson and Wendt 1995). Among these, RANS and LES are the most commonly used in engineering applications. Both approaches have been applied to the study of inclined dense jets (Mohammadian, Gildeh, and Yan 2023). Vafeiadou et al. (2005) conducted early numerical simulations using the k–ε model in ANSYS CFX, and showed good agreement with the experimental data. Oliver et al. (2008) found that the k–ε model could accurately predict the jet trajectory, but underestimated the concentration prediction. Gildeh et al. (2015) and Wang and Mohammadian (2025) highlighted the importance of turbulence model selection in simulating inclined dense jets. They compared different common two-equation turbulence models, and the results indicated that the realizable k–ε and q-zeta turbulence models performed better than the RNG k–ε model. The latter study also pointed out that RANS models are less effective in accurately predicting concentration results, especially when the discharge angle exceeds 45°, thereby reinforcing the growing use of LES, which offers improved and more detailed flow-field characteristics. Zhang et al. (2016; 2017) conducted LES simulations of inclined dense jets discharged at angles of 45° and 60° in a stationary environment. Their results showed that LES accurately captured turbulence structures and performed better in predicting geometric parameters and concentration distributions, which is consistent with the experimental observations(Roberts et al. 1997).

After the jet reaches the seabed, gravitational effects cause brine to spread and accumulate along the bottom, particularly beyond the impact point(Papakonstantis and Christodoulou 2010). Considering that desalination outfalls operate continuously over long periods, undiluted brine along the seabed may pose significant environmental risks. Moreover, natural seabeds are often sloped rather than flat, making it essential to investigate how seabed slopes influence jet behavior after impingement.

Several studies have extended the analysis beyond the return point and impact of different sloping bottoms. Oliver et al. (2013) examined the impact point properties of inclined dense jets for different discharge angles (30°, 45°, and 60°) and seabed slopes (0–20°) using CorJet and an extended semi-analytical model based on Kikkert et al. (2007). Their results showed that both the discharge angle and seabed slope influenced the impact location, with the extended model outperforming CorJet in predicting concentrations at the impact point. However, both models exhibited limitations in capturing the detailed mixing and dilution processes beyond the impact region.

Nikiforakis et al. (2014) conducted the first experimental study on inclined dense jets over a 5° sloped bottom, using conductivity probes for point measurements. Their findings indicated that the dilution increased with the discharge angle, with the 60° jet achieving a 20% higher overall dilution than the 45° jet. However, their study relied on discrete point measurements, which limited their ability to capture the full spatial and temporal concentration evolution in the entire flow field. Wang and Mohammdian (2022) used RANS turbulence models to simulate a 15° inclined dense jet discharged over three sloped bottoms (0°,3°and 6°). While the RANS model successfully captured the geometrical characteristics of the jet on different slopes and provided a linear equation for point dilution along the bottom after the impact point, it tended to underestimate dilution. Habibi et al. (2022, 2023) employed LES to investigate the effects of seabed slopes (0°–20°) on inclined dense jets and analyzed the key vortex structures. Their study demonstrated the advantages of LES in capturing the impact point locations of inclined dense jets and vortex structures. However, previous research has not sufficiently explored the effects of seabed slopes on the geometrical characteristics of the impact point and evolution of the concentration fields along the bottom after impingement.

To address this gap, Wang et al. (Wang et al. In prep.) conducted comprehensive laboratory experiments using a Laser-Induced Fluorescence (LIF) system to study inclined dense jets discharged over sloped bottoms (0°–5°) at discharge angles ranging from 30° to 60°. Their experiments provided detailed and comprehensive concentration measurements near the impact point and along the seabed and offered valuable new insights into the post-impingement spreading behavior.

Building on these experimental findings, the present study further investigated the influence of seabed slopes through numerical modeling. Large Eddy Simulation (LES) was employed to investigate the impact of seabed slopes on inclined dense jet behavior. Simulations were conducted for a 60° discharge angle and two seabed slopes (β =0° and β =5°) in a stationary receiving environment, focusing on both the impact point dynamics and the downstream spreading of brine along the seabed. A commonly used two-equation RANS turbulence model (the realizable k–ε model) was applied to assess the relative performance of different CFD approaches and support the development of predictive tools for outfall design under varying environmental conditions.

4.2 Methodology

4.2.1 Large eddy simulation

Large Eddy Simulation (LES) applies a filtering function with a cutoff width(Δ) to separate the flow field into two components: resolved and unresolved scales (Mason 1994). The larger eddies, which were greater than the filtering cutoff, were directly computed by solving the Navier-Stokes equations. These resolved eddies contain essential flow structures that accurately capture the turbulence in the flow. Eddies smaller than the cutoff width are modelled as subgrid-scale (SGS) stresses, which can be obtained using different SGS models (Smagorinsky 1963). In this study, the K-equation model was adopted. The reader is referred to (Greenshields 2015) for further details.

4.2.2 RANS model

In RANS, each flow property is separated as a mean value, and the fluctuation part is expressed as $u(x,t) = \bar{u}(x) + u'(x,t)$ in the Navier–Stokes equations. k-ε models are one of the common two-equation models and have been proven to have a good prediction of inclined dense jets in many previous studies (Alfaifi, Mohammadian, and Bonakdari 2022; Gildeh et al. 2015). The realizable k–ε model has been widely applied in numerical studies and has shown a better performance than other k–ε models. Its accuracy was also validated in studies by Wang and Mohammadian (Wang and Mohammadian 2025) and Gildeh et al. (Kheirkhah Gildeh et al. 2015). In this study, the realizable k–ε model was employed for comparison with LES results.

Both the RANS and LES models used the open-source software OpenFOAM to solve the NS equations. In this study, the solver TwoLiquidiMixingFoam was specifically applied and designed to simulate the mixing of two incompressible fluids. This solver has been extensively employed in various CFD studies and its reliability and accuracy have been demonstrated (Ghorbani et al. 2021; Gruber et al. 2011; Zhang et al. 2016). The reader can find detailed information on the LES and RANS model case setups in Appendix D.

4.3 Computational domain

The computational domain for both the realizable k–ε and LES in this study is a rectangular water tank with dimensions 1.6m(L)×0.8m(W)×0.35m(H), as shown in Figure 4.2. A cylinder shape with dimensions 0.1m×0.0035m is placed at the center plane of the tank to simulate the discharge nozzle, which is inclined at an angle of 60°.

A mesh generator called SnappyhexMesh in OpenFOAM is used. This mesh generator employs an adaptive meshing algorithm that allows for the generation of a mesh with an optimized cell size and minimized computational costs (Greenshields 2015). A multilevel structured meshing strategy was applied to balance the accuracy and efficiency (Figure 4.2 (b)). This approach used a finer mesh in the jet development region to ensure accurate jet simulation results. At the same time, it maintains a sufficient mesh resolution to capture the flow behavior after the impact point (where the jet reaches the bottom) without high computational costs.

.

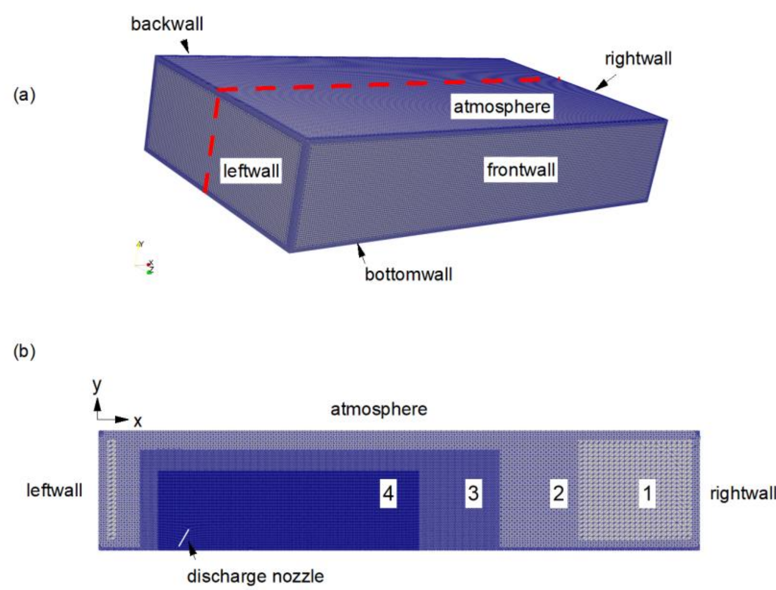

Figure 4.2 (a)the computational domain (b) detailed multiple-level mesh in the center-plane of the tank

4.4 Mesh sensitivity check and analysis

RANS mesh

Mesh sensitivity analysis was performed on three meshes with different mesh setups. Based on the number of mesh grids, they were categorized as coarse, medium, or fine grids. The grid details are presented in Table 4.1. For brevity, only the mesh details of the horizontal bottom are included.

Table 4.1 Comparison of Mesh Quality for RANS Models

Mesh density	Cells number	Max skewness	Max aspect ratio
Coarse	839,075	2.92	9.32
Medium	1,848,426	3.02	2.15
Fine	2,954,166	2.64	4.05

Further comparisons were made by plotting the concentrations at various vertical sections (X/DFr=0.41, X/DFr=1.24, and X/DFr=2.06) of the flow region using different mesh configurations.

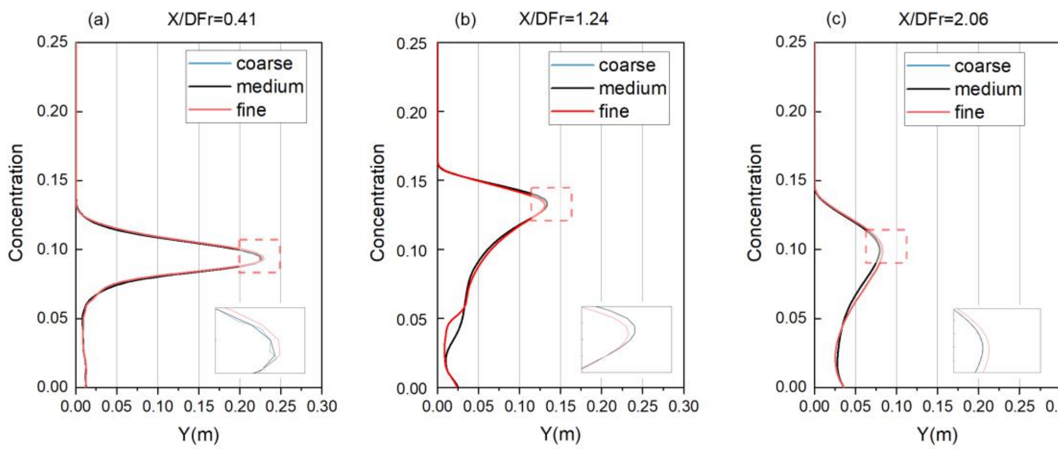

Figure 4.3 Comparison of concentration profiles at three different locations in the flow region extracted using different RANS meshes

As shown in Figure 4.3, the concentration prediction exhibited minimal differences among the three mesh configurations. The three meshes have almost similar simulation results; in particular, the coarse and medium meshes almost overlapped at X/DFr=1.24 and 2.06. The enlarged area in the image is highlighted with a red dashed box for further comparison, which provides smoother results than the coarse mesh, while maintaining good agreement with the fine mesh. In addition, it shows better computational efficiency by reducing the simulation time compared with the fine mesh. Therefore, in this study, a medium mesh was selected for all RANS simulations because of its reliable results and high computational efficiency.

LES mesh

For LES, the mesh size controls the ratio between the resolved large eddies and subgrid-scale (SGS) stresses. A finer mesh improves the accuracy but also increases the computational time and resource consumption. In this study, over eight million mesh cells (8,810,147) were generated using SnappyHexMesh for the LES simulation. A four-level meshing strategy is applied to the entire simulation domain, including the 5-degree sloped bottom.

According to Pope (2004), a well-resolved LES mesh should capture at least 80% of the total turbulent kinetic energy (TKE). This criterion was also adopted in other studies (Sullivan et al. 1994). Figure 4.4 shows the ratio of $\frac{\text{KRES (Resolved kinetic energy)}}{\text{TKE(Total kinetic energy)}}$ in the flow region.

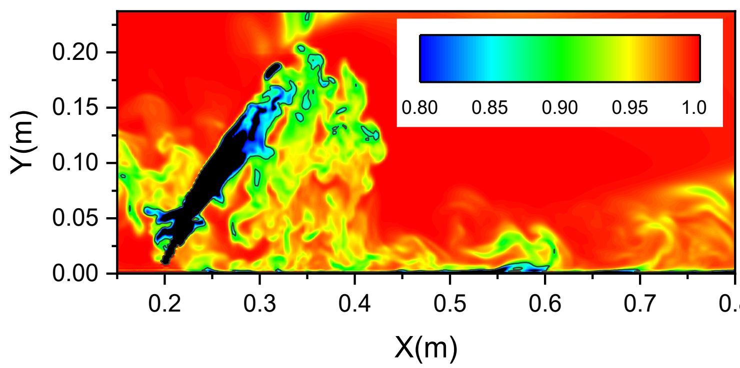

Figure 4.4 Turbulent Kinetic Energy (TKE) Resolution Ratio in LES Simulation

The employed four-level grid successfully resolved over 80% of the total turbulent kinetic energy (TKE) across most computational domains. However, in stagnant regions, where both KRES and TKE are zero, the ratio becomes misleadingly equal to 1 due to ParaView's default treatment of 0/0. In the region near the nozzle, where the turbulence is highly intense and small scale, the resolved TKE ratio falls below 80%. Accurately capturing the turbulence in this area requires an extremely fine mesh, leading to a significant increase in computational cost. Nevertheless, as this study focused on the overall jet behavior after the impact point rather than on the detailed structures near the nozzle, such refinement was not prioritized. Across the majority of the jet region and along the bottom surface, the resolved TKE ratio exceeded 0.8, confirming that the mesh quality was adequate for LES simulations in this study.

Simulation setup

The inlet boundary conditions are $u = U_0 \times cos\ (a\ )$, $v = U_0 \times sin\ (a)$, $w = 0, k = 0.006u^2, and\ \varepsilon = 0.06u^3/D$, where U_0 is the velocity of the jet discharge, and $u, v,$ and w are the velocities for the $x, y,$ and z-axes, respectively(Gildeh et al. 2015). The flow was assumed to be incompressible, and the densities for both the jet and ambient water were the same as those in the experimental setup of Wang et al.(in prep.) The densities of the brine and ambient water were $1052 kg/m^3$ and $1000 kg/m^3$, respectively. The Froude number in all the numerical simulations (RANS and LES) was 17.3, which was the same as that in the experiments. In the RANS and LES simulations, the simulation time was set to 120 s to focus on the flow characteristics after the impact point at the bottom, thereby ensuring that the jet flow was fully developed.

4.5 Results and discussion

4.5.1 The instantaneous and time-averaged results

Figure 4.5 presents the instantaneous and time-averaged concentration contours (C/C_0) of the LES and RANS models on the 5° sloped bottom as an illustration of the simulation results. In Figure 5 (a), the LES simulation represents complex turbulent structures formed during the development of the inclined dense jet discharged into stationary ambient water. As expected, after being discharged from the nozzle, the jet initially moved upward due to its initial discharge momentum and reached its maximum height before being driven downward by negative buoyancy. Eventually, the jet fell to the inclined bottom boundary, and the overall flow pattern in the LES simulation was consistent with the experimental observations of Lai and Lee(Lai and Lee, 2012) and (Wang et al. in prep.).

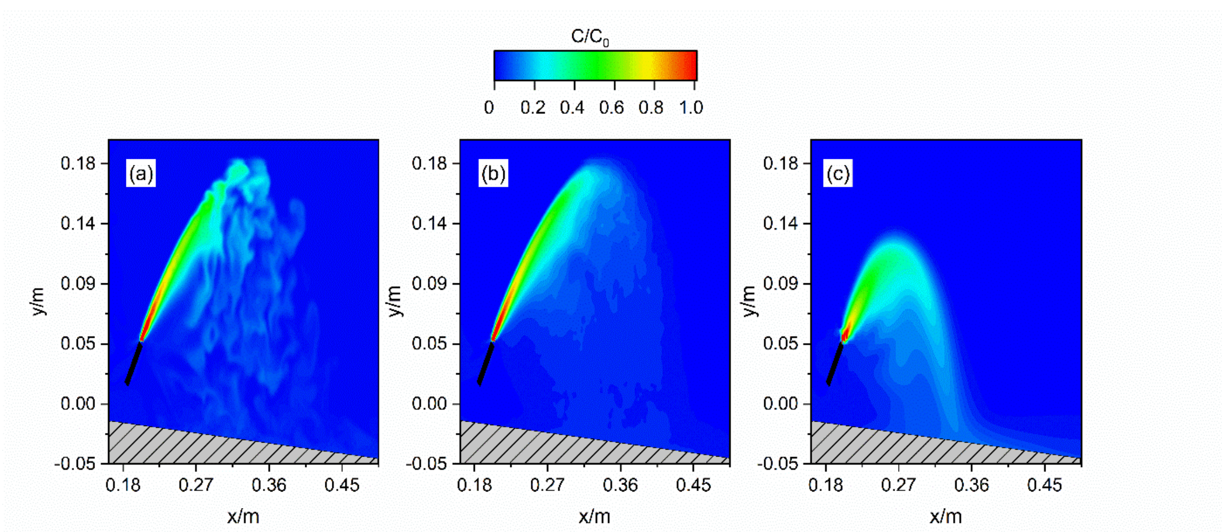

Figure 4.5 (a) LES instantaneous and (b) LES time-averaged (c) the realizable k–ε concentration contour

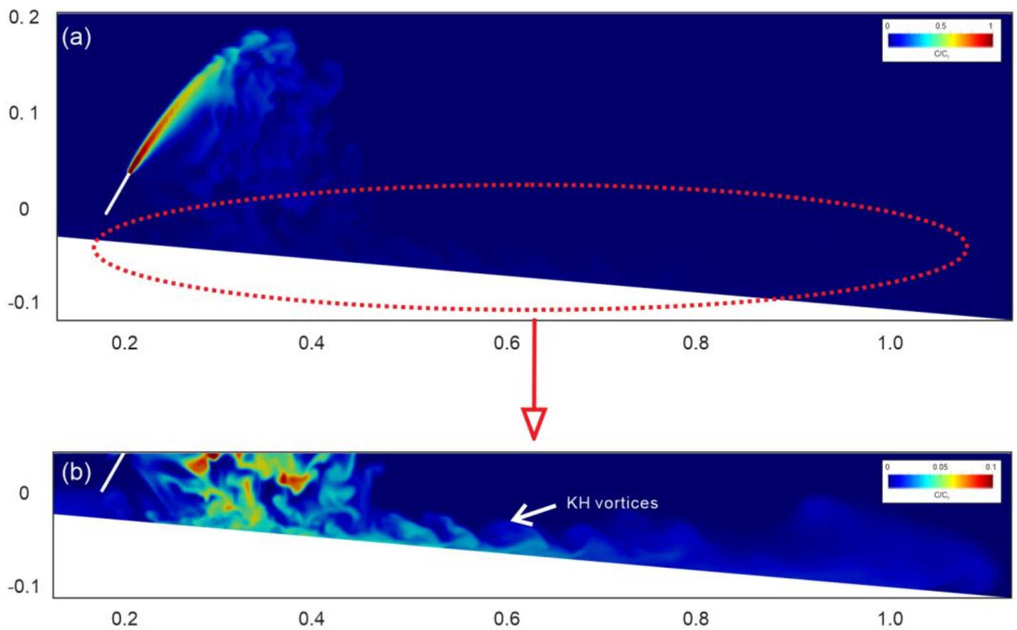

Figure 4.6 illustration of the Kelvin–Helmholtz vortices along the bottom from the LES simulation

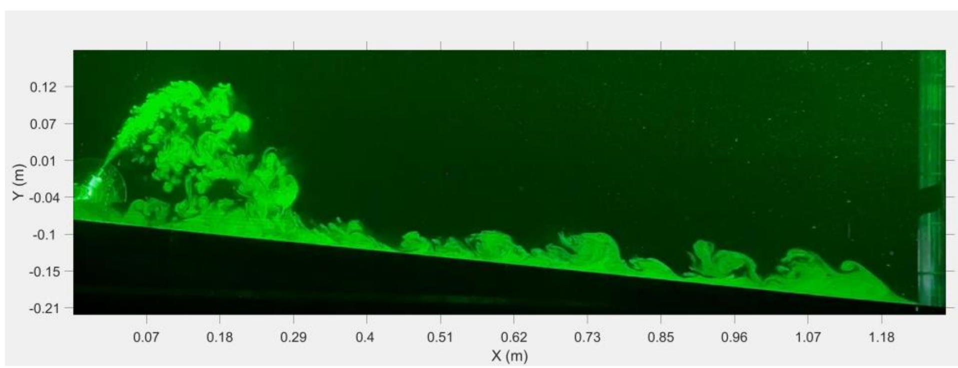

Figure 4.7 An image of the KH vortices along the bottom from LIF experiment (Wang et al. in prep.).

Throughout the jet development, LES captures detailed turbulent structures, particularly around the jet boundary. Shear instability generates a series of vortical structures that evolve, interact, and eventually break down, enhancing entrainment and accelerating the mixing of the momentum and mass. A series of Kelvin-Helmholtz (KH) vortices after the impact point along the bottom were also captured in the LES simulation (Figure 4.6) This phenomenon is also well observed in the experimental study from (Wang et al. in prep.)(Figure 4.7) and in other studies (Ferrari et al. 2013; Roberts et al. 1997).

Figure 4.5 (b) shows the time-averaged concentration field of an inclined dense jet. The turbulent structures (turbulent eddies and Kelvin–Helmholtz vortices) were smoothed. Near the nozzle, the jet concentration remained high, and the influence of ambient water was minimal, resulting in a strong concentration gradient and jet-like characteristics. As the jet reached its maximum height and descended, the brine jet mixed more with the surrounding ambient water, leading to a gradual decrease in concentration. Turbulent structures were not visible near the impact point. Figure 4.5(c) presents the concentration field simulated using the realizable k–ε model. Compared to the LES results, the jet appears smaller in size, more confined, with a lower maximum rise height, and a shorter distance to the impact point. This difference is likely due to the realizable k–ε model underestimating the initial momentum and turbulent kinetic energy, which also results in a higher concentration compared to the LES results. Similar observations were reported by Wang and Mohammadian (Wang and Mohammadian, 2025), who found that RANS models generally underperformed when simulating inclined jets with higher discharge angles (60°). Zhang et al. (Zhang et al. 2017) also emphasized that LES exhibits better performance in complex turbulent jet simulations.

4.5.2 Jet trajectory

The trajectory is important for tracking the jet movement and determining the jet-affected area, which is derived from the maximum concentration or velocity along the perpendicular sections of the jet. According to previous studies(Shao and Law 2010; Wang and Mohammadian 2022; Zhang et al. 2016), the difference between the velocity and concentration of the indicated trajectory was very small. To simplify the analysis, the maximum concentration is used to determine the trajectory.

The jet trajectories were normalized using the Froude number (Fr) and nozzle diameter (D), and the results are shown in Figure 4.8. To facilitate a comparison with previous studies, the numerical results under the horizontal bottom condition were first presented.

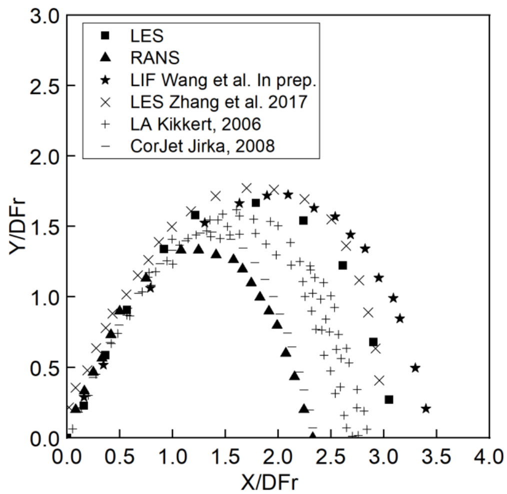

Figure 4.8 Trajectory of the inclined dense jet with a 60-degree discharge angle on a horizontal bottom

By comparing the results of LES, realizable k–ε models, and data from related studies (Jirka 2008; Kikkert 2006; Zhang et al. 2017), it was found that the LES results showed good agreement with the experiments (Wang et al. In prep.) and Zhang et al. 's LES simulations (Zhang et al. 2017). The realizable k–ε model results were consistent with Jirka's integral model predictions[43]; however, both methods underestimated the jet trajectory. The trajectory difference between RANS and LES was consistent with Zhang's numerical study(Zhang et al. 2017). Zhang et al. compared the jet trajectories predicted by LES and the k–ε model and concluded that the k–ε model underestimated the jet trajectory. The trajectory results from Kikkert (Kikkert 2006), which are based on the light attenuation method, lie between the realizable k–ε and LIF results. This indicates that different data-collection methods can lead to different outcomes.

4.5.3 Overview of geometrical information

Some important geometrical information, such as the terminal rise height (Y_t), centerline peak point(X_c, Y_c) and impact point(X_i), which are relevant to design considerations, are summarized in Table 4.2and Table 3. Since research on sloped bottoms is limited, the comparison results in Table 4.2 with previous studies are primarily based on simulations on a horizontal bottom. In Table 4.3, only the geometrical and concentration coefficients at the impact point are listed, because the slope mainly affects the jet at this location.

Table 4.2 Coefficients from the results for the horizontal bottom ($\beta = 0°$)

Quantity	Terminal rise height	Horizontal location of centerline peak	Vertical location of centerline peak	Horizontal location of impact point	dilution at centerline peak	dilution at impact point
	Yt/DFr	Xc/DFr	Yc/DFr	Xi/DFr	Sm/Fr	Si/Fr
LES	2.17	1.82	1.72	3.17	0.5	1.5
Realizable $k-\varepsilon$	1.65	1.24	1.33	2.46	0.22	0.60
Exp (Wang et al. In prep.)	1.82	1.8	1.8	3.33	0.45	1.44
LES (Zhang et al. 2017)	2.00	1.75	1.70	2.67	0.35	1.10
Exp(Lai and Lee 2012)	2.08	1.78	1.64	-	0.44	1.07
Exp(Papakonstantis 2011b; Papakonstantis et al. 2011)	2.14	1.83	1.68	2.75	0.56	1.68
Exp(Kikkert et al. 2007)	2.44	1.8	1.74	2.81	-	1.82

Table 4.3 Coefficients from the results for the sloped bottom ($\beta = 5°$)

Quantity	Horizontal location of impact point	dilution at impact point
	Xi/DFr	Si/Fr
LES	3.62	1.7
Realizable $k-\varepsilon$	2.51	0.72
Exp (Wang et al. In prep.)	3.76	1.51
CorJet (Jirka 2008)	~2.4	~1.25
Exp (Oliver et al. 2013)	2.79	1.71
Extended solution (Oliver et al. 2013)	2.71	1.68
LES (Habibi et al. 2022)	-	1.77

~ means estimation, because in Jirka's study (Jirka 2008), the sloped bottom angles were 0°, 10°, 20°, and 30°.

In the following section, relevant geometrical point information is compared with previous studies. It is important to note that the numerical simulation results presented here were obtained from simulations with a 5° slope bottom. This not only verifies that the sloped bottom has a minimal impact on the jet behavior before the jet reaches the bottom but also confirms that the grid modifications caused by the sloped bottom in the simulation domain did not significantly affect the overall numerical results, which ensured the reliability of the numerical simulations.

4.5.4 Terminal rise height and centerline peak

The location of the terminal rise height is useful for outfall system design because it can predict the level that the jet can reach to prevent it from reaching the water surface (Jiang, Law, and Lee 2014).

Figure 4.9 presents the normalized terminal rise height (Y_t/DFr) plotted against the discharge angle compared with previous experimental studies(Bashitialshaaer et al. 2012; Bloomfield and Kerr 2002; Kikkert et al. 2007; Lai and Lee 2012) and LES results from Zhang et al. (2017). As shown in Figure 4.9, both the previous experimental data and the numerical results exhibit a certain degree of scatter. This is possibly due to uncertainties in the experimental measurements and numerical modeling approaches. Compared to the LIF experimental results, LES slightly overestimates the terminal rise height, but shows good agreement with (Kikkert et al. 2007; Lai and Lee 2012). The realizable k–ε predictions are closer to the LIF measurements but still tend to be lower. However, the realizable k–ε values were in good agreement with the results of (Bashitialshaaer et al. 2012).

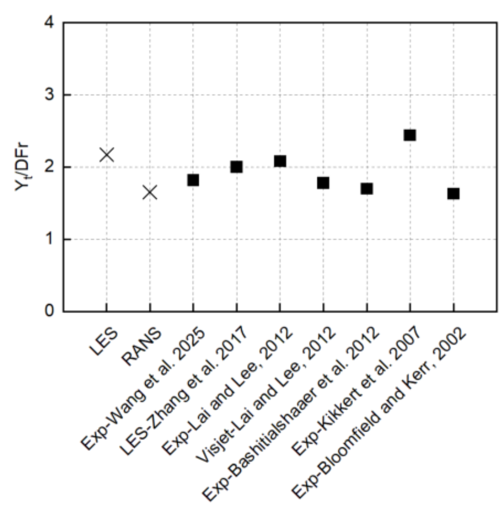

Figure 4.9 Normalized terminal rise height ($\frac{Y_t}{DFr}$) compared with previous studies.

The location of the centerline peak (X_c, Y_c) was also normalized with the Froude number (Fr) and diameter (D) compared to previous studies, as shown in Figure 4.10. The realizable k–ε results showed good agreement with those from the integral model Visjet (Lai and Lee 2012) and an experimental study(Cipollina et al. 2005), but all of them underestimated the value compared to other experimental studies. The slightly lower Xc value in Cipollina's experiment (2005) is likely due to the use of photographic methods to capture the jet centerline, which may introduce higher measurement errors compared to advanced technologies such as Laser-Induced Fluorescence (LIF). In contrast, Yc values showed better consistency across different studies. The LES results from this study for both Xc and Yc exhibit improved agreement with previous works, including experimental results (Kikkert 2006; Lai and Lee 2012) and LES results reported by Zhang et al. (Zhang et al. 2017).

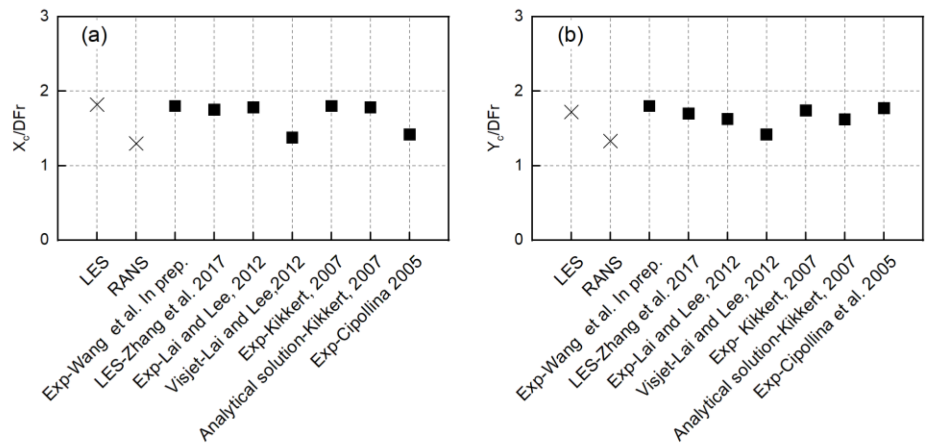

Figure 4.10 Normalized location of centerline peak compared with previous studies: (a) ($\frac{X_c}{DFr}$) (b) $\frac{Y_c}{DFr}$

4.5.5 The effect of the sloped bottom at impact point

As previously mentioned, the impact point was highly dependent on the bottom condition. When a sloped bottom is present, the impact point is distinctly different from that at the horizontal bottom. According to Roberts et al. (Roberts et al. 1997), the impact point can be identified based on concentration variations along the bottom, as the highest concentration value along the bottom corresponds to the impact point. A similar method was adopted in this study to determine the impact-point location. The normalized impact points for both the horizontal and sloped bottom conditions are shown in Figure 4.11 (a)and Figure 4.11 (b).

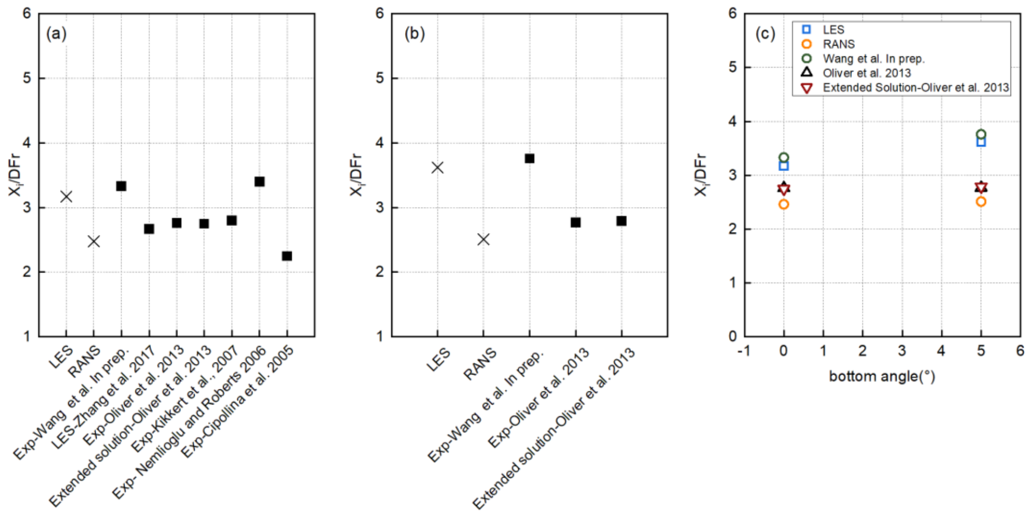

Figure 4.11 (a) Comparison of Present and Previous Studies of the impact point on the horizontal bottom (b) Comparison of Present and Previous Studies of the impact point on the 5° bottom(c) Influence of Bottom Slope on impact point location ($\frac{X_i}{DFr}$)

Figure 4.11 (a) shows that on a horizontal bottom, the realizable k–ε model slightly underestimates the impact point location but still agrees well with previous studies(Cipollina et al. 2005; Kikkert et al. 2007; Oliver et al. 2013; Zhang et al. 2017). The LES model exhibited a better agreement with the experimental results reported by Nemlioglu and Roberts (2006) and Wang et al. (Wang et al. In prep). Figure 4.11(b) presents the impact point location on a 5° sloped bottom, and the data are compared with Wang et al.(Wang et al. In preparation) and Oliver et al.(2013). The result is consistent with the experiment from Wang but slightly higher than Oliver et al.(2013). The main difference may be the experimental setup- Oliver et al.(Oliver et al. 2013) The main difference may be the experimental setup; Oliver et al.(Oliver et al. 2013) conducted experimental studies on a nominally sloped bottom without considering the physical impact and accumulation effects of the jet on the actual bottom surface. Similar to the horizontal bottom, the RANS model continued to slightly underestimate the impact point location, whereas the LES model performed better. Figure 4.11 (c) shows the impact point locations on both the horizontal and sloped bottoms to study the effects of different bottoms on the impact point locations. It can be observed that the jet reached a longer distance on the sloped bottom. This trend was also observed in (Oliver et al. 2013).

The location of the impact point is affected by the sloped bottom, which may also influence the concentration distribution. The dilution at the impact point from this study on both bottoms is shown in Figure 4.12.

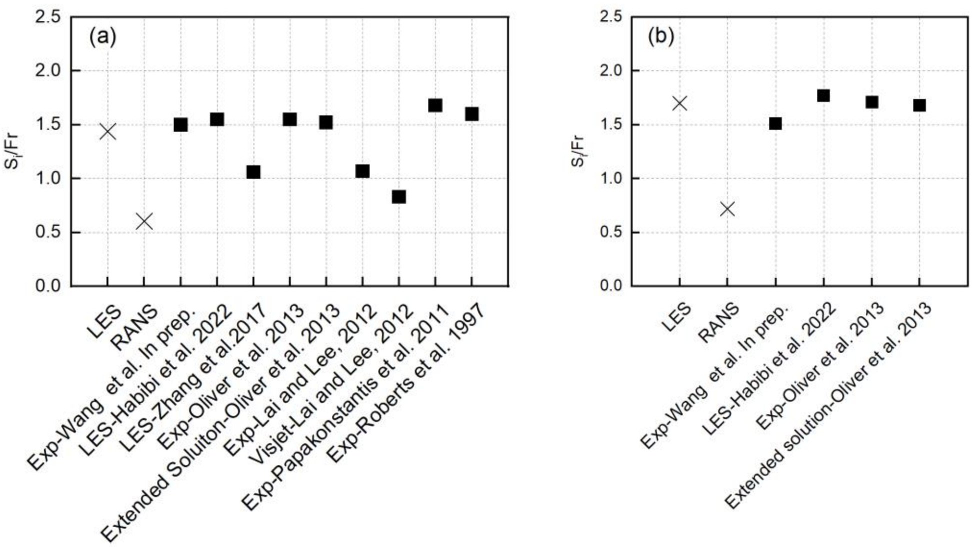

Figure 4.12 Dilution at impact point on (a) 0° slope (b) 5° slope

Dilution was normalized to the Froude number. The results showed that the LES model outperformed the RANS model in predicting the mixing behavior of the jet. The realizable k–ε model significantly underestimates the dilution but yields results closer to those of Visjet, a Lagrangian model (Lai and Lee 2012). The conservative performance of the realizable k–ε model in predicting mixing properties has been widely discussed in the previous literatures(Kheirkhah Gildeh et al. 2015; Oliver et al. 2008; Wang and Mohammadian 2025). The dilution at the impact point on the 5-degree sloped bottom was higher than that on the horizontal bottom, as expected, which is also consistent with the observations in the experiment(Oliver et al. 2013). The sloped bottom affects the jet and bottom interactions, thereby enhancing the mixing.

4.5.6 Concentration distribution near the impact point

To investigate the concentration distribution at the impact point on different bottom conditions, Figure 4.13 illustrates the concentration contour lines at the impact point region from the LES numerical simulation. RANS was not analyzed here because of its poor performance in dilution prediction. In Figure 4.13, the contour lines for 2.5% and 1% C_0 (where C_0 is the initial concentration set to 1 in this study) for both slopes are shown. The 1% C_0 contour line on the horizontal bottom was not included because the flow reached the boundary wall of the simulation tank. The coordinates (0,0) represent the impact point, and all lengths are normalized using the Froude number Fr and nozzle diameter D.

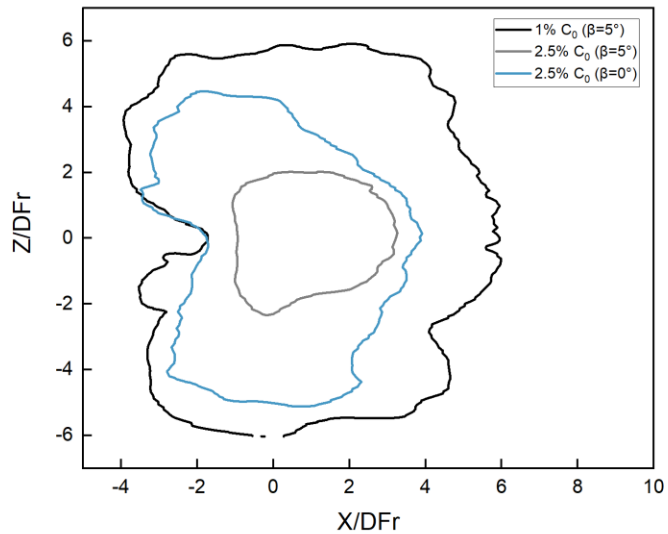

Figure 4.13 The concentration contour line at the impact point region on the horizontal and sloped bottom

For the 2.5% C_0 contour line (blue and gray), the area is larger on the horizontal bottom(blue) than on the sloped bottom(gray), suggesting that brine spreads more on the horizontal bottom, while mixing is enhanced by the sloped bottom. Stronger mixing on the sloped bottom leads to faster dilution of the brine, reducing the lateral spreading near the impact point area. At the same time, the sloped bottom appears to prevent the brine flow from moving towards the shoreline, which may help reduce pollution risks. These findings are consistent with the experimental observations in(Wang et al. In prep.). As the impact-point region continuously receives the brine jet, it is important to examine the concentration distribution around this area. To characterize this distribution, surface fitting was applied to describe the concentration (C/C_0) in relation to its location. The Gaussian fitting functions are listed in Table 4.4.

Table 4.4 Surface fitting function for the concentration distribution near the impact point area on both slopes

	Surface fitting function	R^2
on the horizontal bottom	$C(x,y) = 0.0137 + 0.0287 \cdot \exp\left(-\frac{(x-0.13)^2}{2(2.29)^2} - \frac{(y+0.33)^2}{2(3.37)^2}\right)$	0.90
on the sloped bottom	$C(x,y) = 0.0032 + 0.0282 \cdot \exp\left(-\frac{(x-0.91)^2}{2(2.75)^2} - \frac{(y-0.09)^2}{2(3.73)^2}\right)$	0.92

In these fitting functions, C(x,y) is the local concentration(C/C_0, where $C_0 = 1$), $x = \frac{X}{DFr}, y = \frac{z}{DFr}$. The origin point (0,0) represents the location of the impact point. The correlation R^2 of both fitting functions were approximately 0.9, indicating good fitting results. With a deeper analysis of these functions, it can be seen that on the sloped bottom, the peak concentration at the horizontal bottom occurs at (x, y) ≈ (0.13, -0.33) with a higher baseline concentration of 0.0137, whereas for the sloped bottom, the peak moves downstream to (x, y) ≈ (0.91, -0.09) with a lower baseline concentration of 0.0032. This suggests that on the sloped bottom, the impact point extends longer, and mixing is stronger, leading to greater dilution and lower concentration.

4.5.7 Spreading layer characteristics - dilution along the bottom

After the jet fell to the bottom, the brine spread in all directions and continued to move along the bottom(Papakonstantis and Christodoulou 2010). At the center plane of the simulation, the result of the normalized dilution (S/Fr) along the bottom is plotted against the location on the bottom (X/DFr), as shown in Figure 4.14, including the numerical results from LES and RANS compared with previous LES simulations (Zhang et al. 2017) and experimental studies (Nemlioglu and Roberts 2006).

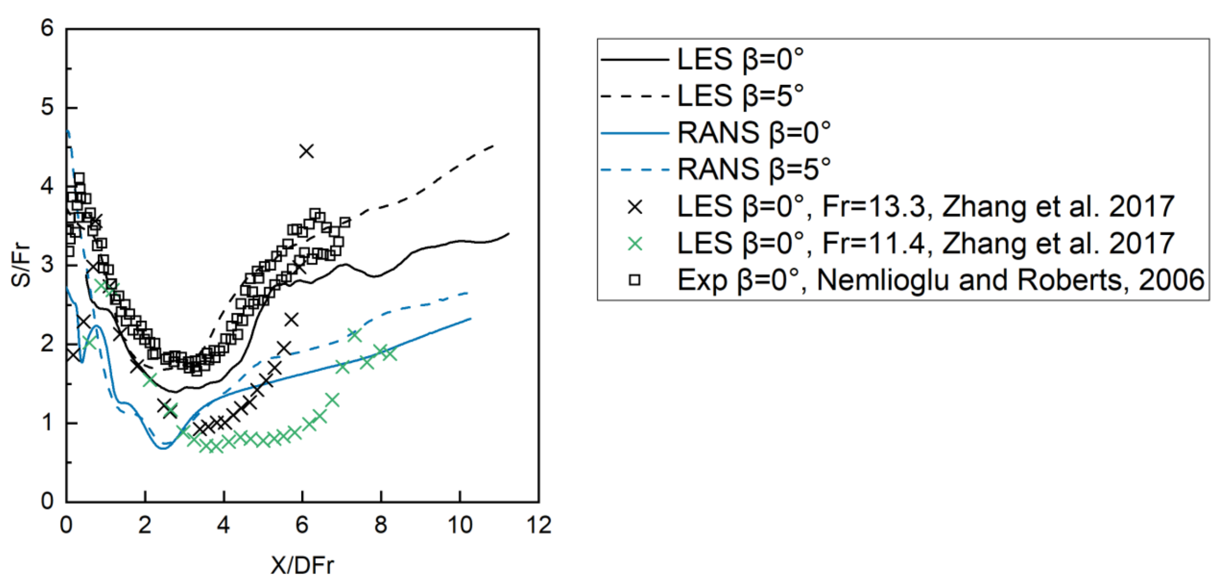

Figure 4.14 The dilution (S/Fr) along the bottom (X/DFr)

The LES results at the horizontal bottom showed good agreement with experimental data(Nemlioglu and Roberts 2006). The dilution was the lowest at the impact point and then increased along the bottom surface. Zhang's LES results(Zhang et al. 2017) became more scattered as the Froude number (Fr) varied. Their study tested several values of Fr. Lower Fr values (e.g., Fr = 11.4) indicate heavier brine and weaker jet momentum, which may have reduced dilution efficiency. Wang's experimental study (Wang et al. In prep.) also discussed the effects of different initial Froude numbers on jet mixing. Roberts et al. (1997) recommended that the Froude number of inclined dense jets should exceed 20 to achieve sufficient mixing and minimize environmental impact.

Based on the LES and RANS results, the dilution along the sloped bottom (dashed line) was higher than that on the horizontal bottom, which extended the jet trajectory and contributed to the downward movement of brine under gravity, which enhanced the mixing. However, the RANS model underestimated the dilution compared with this study and the experimental data (Wang et al. In prep.), and its prediction was closer to the LES results reported by Zhang et al. (2017).

Figure 4.15 presents the concentration profiles along the streamwise direction at different locations after the impact point on the two bottom slopes. Y represents the vertical distance from the bottom and C_{max} is the maximum concentration at each location. These results were compared with those of experimental studies (Palomar, Lara, and Losada 2016; Pérez Díaz et al. 2018) and LES studies (Zhang et al. 2017).

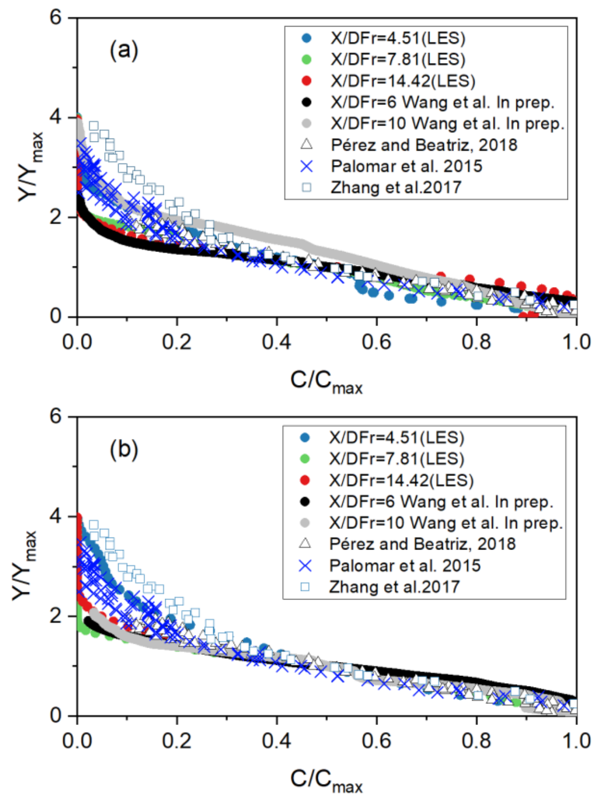

Figure 4.15 Normalized concentration profiles along the bottom on two bottom slopes: (a) horizontal bottom and (b)5-degree sloped bottom

These results were in good agreement with those reported in the literature. Regardless of whether the receiving bottom was horizontal or sloped, the maximum concentration consistently occurred near the bottom. The self-similarity of the concentration profiles suggests that the dilution process follows a consistent mixing mechanism.

4.5.8 Energy spectrum analysis

According to Kolmogorov (Frisch and Kolmogorov 1995), in the inertial subrange of turbulence, the energy spectrum function is expressed as $E(\kappa)\sim\kappa^{(-\frac{5}{3})}$, which indicates that large-scale vortices transfer energy to smaller scales through an energy cascade. To investigate the turbulent characteristics along the bottom, the energy spectra at different locations downstream of the impact point on various bottom slopes are plotted, as shown in Figure 4.16. Because only LES can resolve the turbulence structures, only the LES results are presented here.

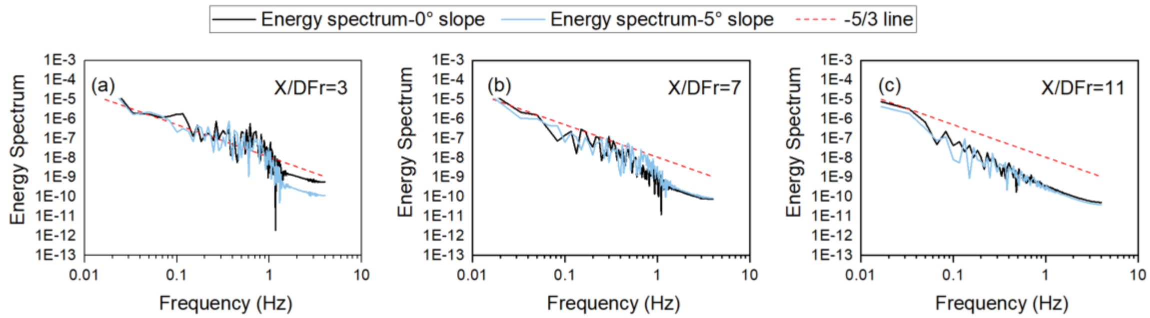

Figure 4.16 Energy spectrum at different locations along the bottom: (a) X/DFr =3;(b) X/DFr =7; (c) X/DFr=11

The black and blue solid lines represent the energy spectra on the horizontal and sloped bottoms, respectively, and the red dashed line indicates the Kolmogorov −5/3 slope. It can be observed that the energy spectra at different bottoms had different forms. Figure 4.16(a) corresponds to the region near the impact point (X/DFr=3). It can be seen that the energy spectrum on both slopes does not completely follow the Kolmogorov −5/3 slope, indicating that near the impact region, turbulence is still in the early development stage. The flow structure was influenced by wall interference, and an inertial subrange was not formed. As X/DFr increases (Figure 4.16(b) and(c)), the energy spectrum becomes closer to the −5/3 slope, indicating that turbulence is more developed and the inertial subrange gradually forms, with a more stable energy cascade. The energy level was significantly higher for the sloped bottom Figure 4.16(b), implying more mixing for the sloped bottom. At X/DFr = 11, the overall energy level is quite low for both cases, which indicates a low turbulent intensity, implying that the mixing is significantly reduced and the flow has dissipated.

4.6 Conclusion

This study confirmed the effectiveness of Large Eddy Simulation (LES) in capturing the behavior of a 60º inclined dense jet discharged onto horizontal and 5ºsloped physical bottom surfaces. The key conclusions are summarized as follows.

- LES accurately predicted the jet trajectory, centerline peak location, impact point position, and dilution properties on both horizontal and sloped bottoms, showing strong agreement with the experimental measurements.

- The realizable k–ε RANS model underestimated both the geometrical features and the dilution performance.
- The geometrical and dilution characteristics at the impact point were affected by the bottom slope; the 5° sloped bottom extended the impact point location and increased dilution.
- The present work also extended the analysis to systematically investigate jet characteristics and concentration evolution beyond the impact region over sloped bottoms. For the horizontal bottom condition, the LES results exhibited improved consistency with experimental measurements compared to previous LES simulation studies. In addition, this study further explored the concentration distribution along the sloped bottom after the impact point, and the simulation results showed good agreement with the experimental observations.
- Dilution along the bottom after the impact point was enhanced by the presence of a sloped bottom.
- The lateral concentration profiles confirmed that the sloped bottom enhanced mixing near the impact point. The concentration distributions exhibited symmetrical behavior, and a Gaussian fitting approach was proposed to characterize the concentration distribution near the impact point over the sloped bottoms.
- The concentration profiles along the bottom layer exhibited self-similar behavior over both the horizontal and sloped surfaces, which is consistent with classical jet theory.
- Energy spectrum analysis at different points along the bottom confirmed that the sloped bottoms enhanced shear-induced turbulence and improved the mixing efficiency.

These findings highlight the capability of LES to resolve complex jet–bed interactions and offer valuable insights for optimizing discharge system designs and brine management. Future studies are recommended to explore alternative LES modeling approaches, investigate a broader range of discharge angles and bottom slopes, and extend simulations to stratified ambient environments to better represent real-world ocean conditions. In addition, future research could examine the long-term accumulation of brine along the seabed and its potential impacts on marine plants and organisms, as well as possible ecological feedback effects.

Chapter 5 Application of gene expression programming for prediction of dilution of inclined dense jet after the impact point based on experimental data

Xinyun Wang[1], Abdolmajid Mohammadian[1]

Department of Civil Engineering, University of Ottawa, 161 Louis Pasteur Private, Ottawa, ON K1N 6N5, Canada

Abstract: Due to its high mixing efficiency, the inclined dense jet is commonly used as a discharge method in outfall systems. In this study, a new evolutionary-based model is developed to predict the concentration information of the receiving bottom for both horizontal and inclined bottoms after the impingement point. This prediction is crucial for understanding the far-field mixing and dilution of the jet. Experimental results are analyzed using gene expression programming (GEP). The concentration model and the location of the impact point model consider the discharge angle (α), bottom angle (θ), the location after the impact point (X/D), and jet density (Fr) as the input variables. Different GEP parameter settings and error indicator analyses are applied to evaluate the model's accuracy. The GEP model shows good accuracy in predicting concentration and impact point under various discharge angles and sloping conditions.

Key Words: Gene Expression Program, inclined dense jet, mixings, sloped bottom

5.1 Introduction

Over the past few decades, several regions around the world have experienced and will experience long-term water shortages due to high population growth and climate change. A successful solution to the problem is to treat and reuse resourceful ocean water, especially in semi-arid and coastal areas(Van Vliet, Jones et al. 2021). Desalination is an affordable and appropriate solution for many countries, and desalination plants can provide portable water for basic needs and relieve the pressure of growing water consumption. The design of the outfall system is also a key component of a successful desalination plant and industrial design (Roberts, Johnston et al. 2010). To minimize the harm to coastal environments and aquatic species caused by inappropriate discharge of desalinated water, it is important to understand the design of the effluent system and predict mixing after discharge. The most common method is an inclined dense jet, which involves discharging brine water through submerged pipes and a round nozzle as a turbulent jet with an inclined angle and initial velocity (Figure 5.1). The brine jet will rise due to its initial momentum to reach the highest point, then fall back to the receiving bottom under the effects of buoyancy momentum, and it continues moving along the bottom. As a result of this discharge process, the brine mixes with the surrounding water and gradually dilutes until it reaches an acceptable concentration.

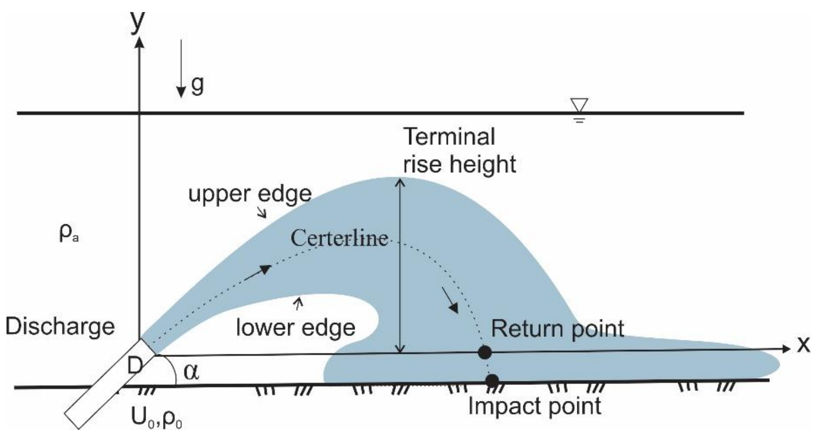

Figure 5.1 Schematic diagram of an inclined dense jet (discharge angle α) in stagnant water.

Some information at specific locations receives attention because it is critical for the design of the outfall system. For example, keeping the terminal rise height (Y_t) below the water surface can prevent extra surface pollution. Knowing the information about the concentration or the location at the impact point (X_i), where the jet falls back to the bottom, it is possible to estimate the discharge impact region and make practical recommendations for protecting marine fauna and flora. There have been several studies of inclined dense jet that either focused on the horizontal bottom with little consideration of the impact of the bottom conditions and also ignored the information provided by the brine after the impact point (Bashitialshaaer, Larson et al. 2012) (Cipollina, Brucato et al. 2005) (Abessi and Roberts 2015); however, near the seashore, not all of the sea bed is horizontal. When the receiving bottom has a sloped angle (θ), the schematic diagram of an inclined dense jet would be changed from Figure 5.1 to Figure 5.2. It is evident that the impact point and the brine after the impact point differ from those on a horizontal bottom. The angle of the seabed's slope affects the dense jet's trajectory and where it impacts the bottom. The brine flow will continue to move due to the angle of the slope. This requires further investigation of the different bottom conditions to understand the full implications.

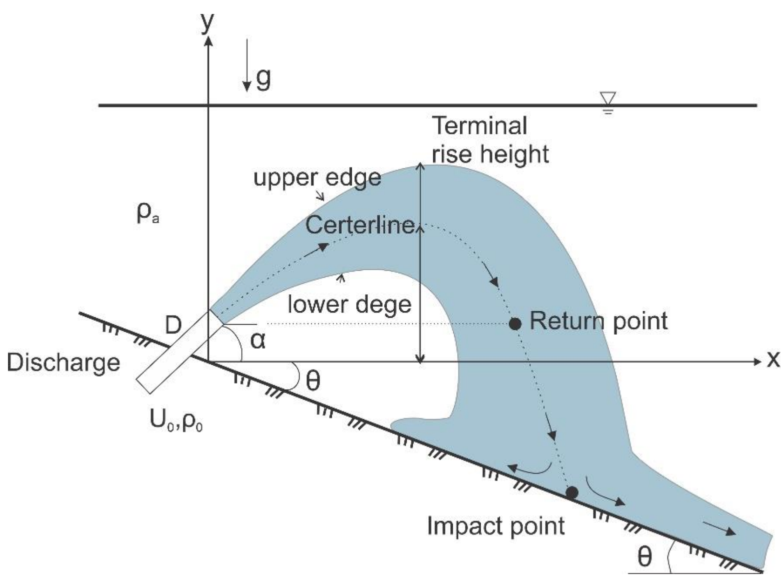

Figure 5.2 Schematic diagram of an inclined dense jet discharged over a sloped bottom (slope angle is θ)

Jirka (2008) is the first to apply the integral model-CorJet to study the effect of sloping bottoms on submerged negatively buoyant jet mixing. The complete range of discharge from 0 to 90 degree and for the various slope angles (0 to 30 degree) with zero discharge height were used in this model after it was validated, and the predictions of jet behavior and information at the impact site throughout the changing bottom angle were presented. Oliver and his colleagues reported a semi-analytical solution of jet characteristics with varying discharge angles (30 to 60º) and different nominal bottom angles (5 to 15º) (Oliver, Davidson et al. 2013) based on Kikkert's analytical solution (Kikkert, Davidson et al. 2007). As part of their studies, they eliminated the physical bottom to determine the jet characteristics at the nominal boundary. According to the results, the integral model cannot determine the location of the return point and impact point; the CorJet underpredicted dilution at these two locations, whereas the semi-analytical solution can match the actual data in these places. Nikiforakis et al. presented the first experimental study of inclined dense jets on a sloping bottom(Nikiforakis, Christodoulou et al. 2014). Point measurements were taken to determine the concentration of the inclined dense jet with 45- and 60-degree discharge angle after it touched the sloped bottom (5 degrees) with different Froude numbers (11~23). They discovered that after the impact point, the vertical concentration profiles are essentially linear and that the dilution value for discharge inclination 60° is greater than 45°. Upon contact with the bottom, the brine will accumulate and behaves as gravity flow. Few studies have been conducted on spreading layers at the horizontal bottom. These characteristics of spreading layers were first investigated by Roberts et al. (1997). They found important information about the end of the mixing zone. According to Abessi et al. (2015), dense jets with inclinations ranging from 15 ° to 85 ° occur at the horizontal bottom and the concentration of the brine flow rises toward the surface of the bed as fluid components build up. The accumulation of fluid components near the surface of the bed can lead to an increase in salinity levels, posing an additional threat to seagrasses or other species. The jets impacting the bottom surface result in more complex flow and mixing characteristics, which require additional studies.

The complexity of outfall systems is often influenced by multiple variables and environmental factors, such as global climate change or pollution control policies. Moreover, uncertainty makes it challenging to design systems based on expected behaviour. Machine learning techniques show promise in predicting the performance of complex systems by considering different factors. Despite physical experiments and numerical simulations being available, spatial limitations or computing costs limit solving such problems. Therefore, using machine learning modeling techniques is crucial in designing pollution control and sewage systems. Machine learning can help find an approximate optimal or satisfactory solution, and gene expression programming (GEP) is a promising model that uses genetic algorithms to generate equations or programs for approximate solutions to problems. GEP has been used in hydraulic research to determine key parameters, such as channel design and seepage under hydraulic structures(Mattar, Alamoud et al. 2020) (Khashan and Hassan 2021).

Bonakdari and Mohammadian(Bonakdari and Mohammadian 2019) were the first to apply GEP in inclined dense jet research, predicting geometrical and dilution information for inclined dense jets in shallow water using discharge angle, ambient water depth, and Froude number as input variables. Their sensitivity analysis demonstrated that the resulting equations could estimate the trajectory and provide valuable information on the jet under different receiving water conditions. Yan and Mohammadian (2020) also used the MGGP algorithm to generate explicit equations for inclined dense jets at multiple ports, predicting in-plane parameters and evaluating their best equation using confidence analysis. They concluded that MGGP is a valuable tool for constructing models to predict mixing features of inclined dense discharges from multiport diffusers.

This study focuses on the dilution on the bottom after jet impingement, including several discharge angles, sloping angles, and varying locations along the bottom. All data were collected from the author's experiment. Applying the GEP method in single-gene and multi-gene models, an equation can be derived to predict dilution along the bottom with different discharge and sloping bottom angles. The question of predicting the location of the impact point is also included and discussed. These equations will be compared using general error analysis and uncertainty analysis.

To the authors' knowledge, no study has focused on the dilution information of the bottom inclined dense jet after the impingement, especially on the sloping bottom. As there are gaps in the information after the impact point and the receiving bottom condition in the outfall system design, this study extends the inclined dense jet prediction to a larger area. Based on the results of this study, we can generate a formulation that can help estimate the dilution along the bottom of the inclined dense jet after the impact point. This can help engineers better understand the mixing of the inclined dense jet at the outfall system, benefiting the protection of the marine environment at the seashore and providing helpful information for evaluating marine environmental protection and wastewater management.

This paper is structured as follows. Sections 2 and 3 provide detailed information about GEP and dimension analysis of the inclined dense jet; Section 4 outlines the methodology and briefly introduces the GEP setup; Section 5 presents the results and discussion; and finally, the conclusion is provided, along with future recommendations.

5.2 Dimensionless analysis for inclined dense jet

For the inclined dense jet on the horizontal bottom, assuming the jet is fully turbulent flow (Reynold >2,000), the variables of the jet flow can be seen as a function of momentum (M), kinetic flux (Q) and buoyancy flux (B), the discharge angle α , discharge velocity U and nozzle diameter is D: $f(\phi) = (M, Q, B, \alpha)$

$$\mathrm{M} = \frac{\pi \mathrm{D}^2 \mathrm{U}^2}{4} \qquad (5.1)$$

$$Q = \frac{\pi d D^2 U}{4} \qquad (5.2)$$

$$B = g'Q \quad (5.3)$$

g' is specific gravitational acceleration, which is defined as $g' = g\,\Delta\rho/\rho_d$. $\Delta\rho = \rho_0 - \rho_a$. Two important length scales are commonly used in jet analysis from these fluxes.

$$L_m = \frac{M^{3/4}}{B^{1/2}} \quad (5.4)$$

$$L_q = \frac{Q}{M^{1/2}} \quad (5.5)$$

L_q is a measure of distance over which the volume flux of the entrained ambient fluid becomes approximately equal to the initial volume flux. L_m is a measure of the distance within which jet momentum is more important than buoyancy (Roberts, Ferrier et al. 1997). These two length scales L_m and L_q can be related to the jet diameter (D) and densimetric Froude number as $L_m = \left(\frac{\pi}{4}\right)^{\frac{1}{4}} FrD$ and $L_q = \left(\frac{\pi}{4}\right)^{\frac{1}{2}} D$. The jet's densimetric Froude number defined as $Fr = U/\sqrt{g_0 D}$.

The Q becomes dynamically unimportant when the distance from the nozzle is much greater than L_q. So, in most cases, the variables $(\phi)$of the jet in the stagnant water, such as terminal rise height(Y_t), the distance between the discharge source and terminal rise height (X_t), location of the return point(X_r) or impact point (X_i) even the dilution information (S) can be written as $f(\phi) = (M, Q, B, \alpha)$.

In GEP programming, the desired regression equation can be generated by entering the values of different and dependent variables. In this study, the angle θ of the bottom surface is added to account for the fact that the inclination of the bottom surface can impact the brine mixing. By adding this variable, the model can better capture the changes in flow that can occur due to changes in the angle of the bottom surface. Furthermore, the dimensionless position x/D is included in the equation variables to investigate the relationship between bottom surface concentration and position after the impact point. As a result, the dilution of the jet at the bottom (S) can be expressed as a function of $S = f(\alpha, \theta, x/D, Fr)$. The location of the impact point is also affected by the slope, so it can be written in dimensionless form as a function of $X_i/D = f(\alpha, \theta, Fr, D)$.

The data used in this study were collected through experimental studies, which included discharge angles of 30 to 45 and 60 degrees, as well as inclination angles of 0 and 5 degrees. Concentration information was obtained from (Wang, Mohammadian, 2023)

5.3 Methodology

5.3.1 Gene expression programming

Gene expression programming (GEP) was developed from genetic programming (GP), which belongs to the Genetic Algorithms (GA), and it was first invented by Ferreira (Ferreira 2001). It provides a new and efficient solution for evolutionary computations compared to genetic programming. Using a set of data points, the algorithm programs gene expressions to find the most suitable chromosomes for the population. It is achieved by simulating the mathematical expressions between the data points based on the law of genetic inheritance and the idea of survival of the fittest and elimination of the worst. The new language (Karva language or K-expression) created in GEP allows for the efficient reading and expression of GEP chromosomes. The Karva language creates a very concise manner to encode complex expressions. This leads to an effective way to obtain an optimal model through GEP operations.

In the ETs, the nodes conclude many variables and mathematical operators. Each operator node may have child nodes, which can link to other variables and operators. For example, the expression tree can be expressed in Figure 5.3 and represents the mathematic expression (a+b)*c-x/y.

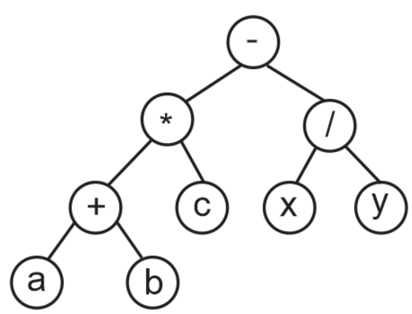

Figure 5.3 Expression tree

The corresponding Karva language for example ET is shown in FigureFigure 5.4.

012345678
—*/+cxyab

Figure 5.4 Example of Karva language

The first element in the gene (position number 0) is the root of the ET (In example ET is the ‘minus’), then it reads the expression trees from left to right, from top to bottom.

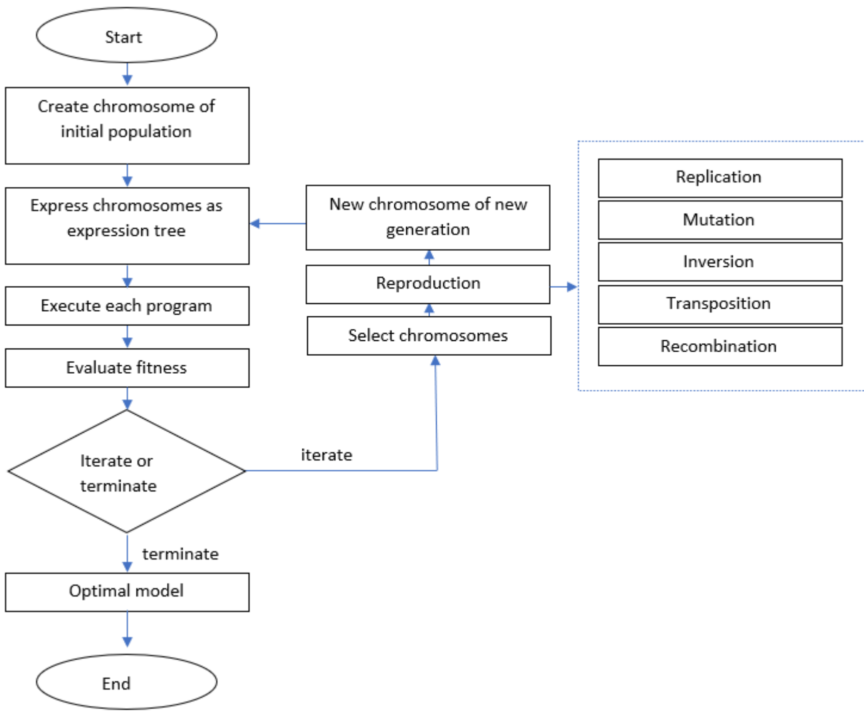

Figure 5.5 GEP Flowchart (modified from (Bethea, Bonakdari et al. 2015)

Figure 5.5 illustrates the standard procedure of GEP, which involves several steps. First, chromosomes are randomly generated from an initial sample of the population. A chromosome can either contain a single gene or multiple genes linked by a function operator. Each gene consists of a head and a tail, and the head contains a set of function operators and terminators, while the tail only consists of terminators. These chromosomes are expressed as an expression tree, which is then evaluated to determine their fitness. Then, based on the fitness, select where to terminate to reach a final optimal model or have more iteration in the chromosomes. In the iteration process, some individuals are selected to undergo modification processes, including replication mutations, inversion, transposition, and recombination. The new generation of chromosomes is then produced, repeated “iteration or termination ” until the optimal model is achieved(Ferreira 2001, 2006).

5.3.2 Gene expression programming setup

In this study, the GEP is applied using a software- GeneXpro tool[3] - to predict the jet's impact point's location and dilution information and the. Different settings of the GEP model were also included to understand the effect of different gene settings on the model results. The five GEP settings of the dilution model were named M1, M2, M3, M4, and M5 and are listed in Table 1. Initially, the "training" and "testing" datasets were defined. From 120 experimental data points, 66.66% (80) and 33.33% (40) of the data were randomly selected for the training and testing set, respectively. Two impact point GEP settings were MI1 and MI2 (Table 1). Fifty-two data points for the impact point were divided into 36 and 16 for the training and testing datasets. Another five main steps are outlined below 1: fitness function selection, the fitness (f_i) is a numerical value representing how well a particular solution (e.g. a particular set of gene expressions) fits the problem. Fitness is defined as

$$f_i = \frac{1000}{1 + fitness\ function} \tag{5.6}$$

After trial-and-error testing of 49 fitness functions, the enhanced mean absolute error (MAE) is chosen as it has the highest fitness value of the other 48 fitness functions; The second step in the process involves selecting the function set and testing to generate the chromosomes, some basic and essential functions were selected by trial and error to find the optimum function set. M5 has only the essential mathematical functions (+, -, ×, ÷). It aims to calculate the effect of the complexity of the function on the result. The detailed function set is listed in Table 5.1. As a next step, it is necessary to consider the chromosome structure, which consists of the number of chromosomes, the head size, and the number of genes. In this study, these values were 300, 9 and 3. However, these values can vary depending on the specific problem and are usually chosen by trial and error. The fourth step is to choose the linking function. The linking function combines the outputs of the individual genes and functions in a specific way to produce the result, such as addition or multiplication, or it can be more complex. In this study, the addition linking function is used, and the result is expressed as $Model = Gene\ 1 + Gene\ 2 + \cdots + Gene\ n$. The final step

[3] GeneXpro Tools 5.0; GEPSOFT Limited: Bristol, UK, 2013

is selecting the genetic operators, such as mutation rate, inversion rate, one-point recombination rate or two-point recombination rate. More details can be found in the GeneXpro tutorial (Gepsoft, Ltd., 2009).

The M1 and MI-1 were chosen to determine the effect of the number of genes; they both set only one gene. In contrast, there are other models have three genes. M2 was set to have five constants in each gene, while the other has ten constants. The value of these constants was generated automatically during the GEP process; details are in Appendix B.

The "head size" refers to the length or number of the main gene segments in each individual. It is responsible for the main functions, and the larger head size can present more complex expression and flexibility, however, it would increase the possibility of generating time and storage space. In order to test the effect of head size, the M3 is set to have a lower head size value, which is seven compared to the M4 with nine, while the model of the impact point (MI1 and MI2) is 8, which also indicates that the GEP set up requirements are highly dependent on the specific problems, the trail-and-error is necessary to obtain the best setup. The difference between M4 and M5 is the function combination. There are plenty of math function operators can be selected, but here in M5, we only test the four simple operators (+, -, ×, ÷) to figure out the influence of the complexity of math functions. The other models were selected from over 20 function operators; during the GEP process, the valid function would be selected automatically.

Seven models were run for over 24 hours, and the stop condition was set to 250 million generations. The model with the highest fitness value was selected and kept for the analysis.

Table 5.1 Parameter settings for GEP modeling

Parameter \ Model	M1	M2	M3	M4	M5	Model of Impact point (MI-1)	Model of Impact point (MI-2)
Chromosomes number	300	300	300	300	300	30	30
Number of gene	1	3	3	3	3	1	3
Head size	9	9	7	9	9	8	8
Linking function	addition	addition	addition	addition	addition	addition	addition
Constant per genes	10	5	10	10	10	10	10
Stop condition	2,500,000 generation	2,500,000 generation	2,500,000 generation	2,500,000 generation	2,500,000 generation	2,500,000 generation	2,500,000 generation
Variables	$X/D, Froude$ α, θ	$X/D, Froude$ α, θ	$X/D, Froude$ α, θ	$X/D, Froude$ α, θ	$X/D, Froude$ α, θ	$Froude$ α, θ Diameter	$Froude$ α, θ Diameter
Function set	Addition Subtraction Multiplication Division Square root Tangent	Addition Subtraction Multiplication Division x to the power of 3 x to the power of 4 Secant Power Tangent Cosecant Logarithm Cube root	Addition Subtraction Multiplication Division x to the power of 2 Natural logarithm Tangent x to the power of 4X Logarithm Arccosecant Arctangent Arccotangent	Addition Subtraction Multiplication Division Exponential x to the power of 2 Logarithm of base 10 Cosine Cotangent Cube root3 Quartic root Secant	Addition Multiplication Subtraction Division	Subtraction Addition Division Multiplication Cube root Cosecant	Subtraction Addition Division Multiplication Power Square root Cosecant

5.4 Results and discussion

5.4.1 Error estimation and model performance evaluation

The model choice depends on the problem and the data being analyzed. It is important to choose appropriate methods for the problem and provide meaningful information about the model's performance. However, there is no standard to pick the best model. As a result, a variety of methods can be used to estimate error and evaluate model performance.

Figure 5.6 presents the observed data (from experiments) plotted against predicted results (GEP models). Training and testing data were represented with squares and circles separately and labelled M1-a, M1-b, etc. The black line is y=x represented as the perfect line; the dashed line represents the $\pm 15\%$ error interval region. From the figure, the M1 case (single gene) has more data points that lie outside the $\pm 15\%$ region of a perfect line, especially for the test datasets, more data were laid out below the -15% line, indicating the model underestimated the dilution. For comparison, M4 (multiple genes) shows that more points lie in the $\pm 15\%$ region, and more data are close to the perfect line $y = x$.

The M2 model (five constants in the gene) also showed that some scatters fell outside the ±15% region for the training and testing datasets. The difference between the M3 (head size 7) and M4 (head size 9) is not significant, they both have a few scatters that fall outside the ±15% region in the training dataset. In the testing datasets, the data points were closer to the dashed line.

The impact point shows that all the training and test data lie between the ±15% region, whether in a single-gene or multiple-gene model.

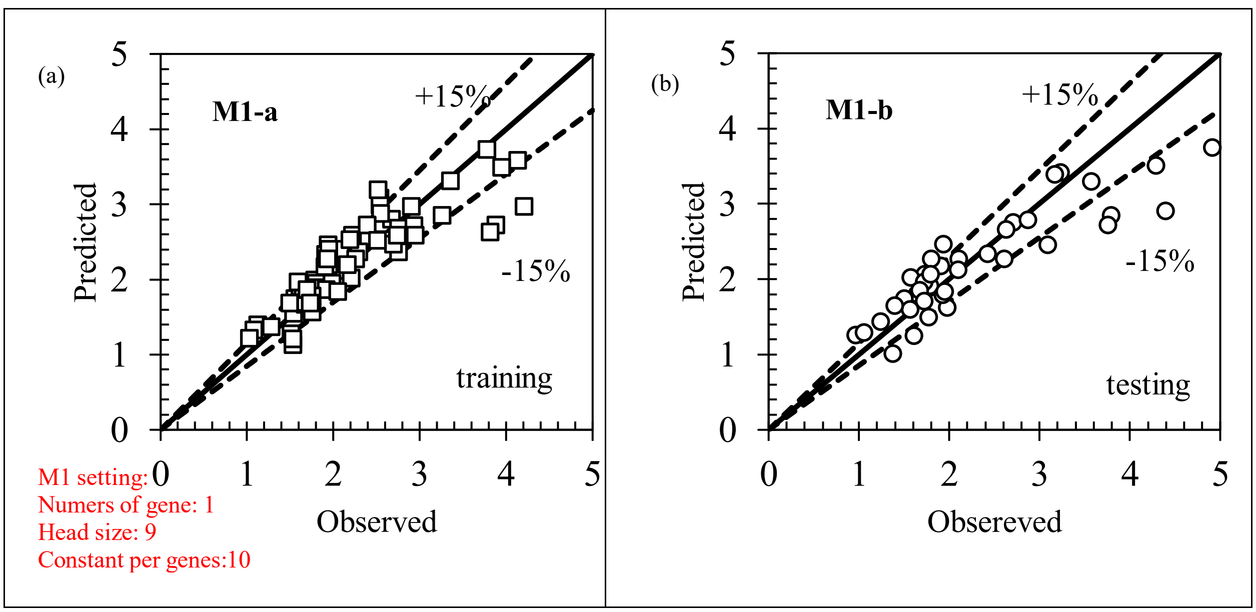

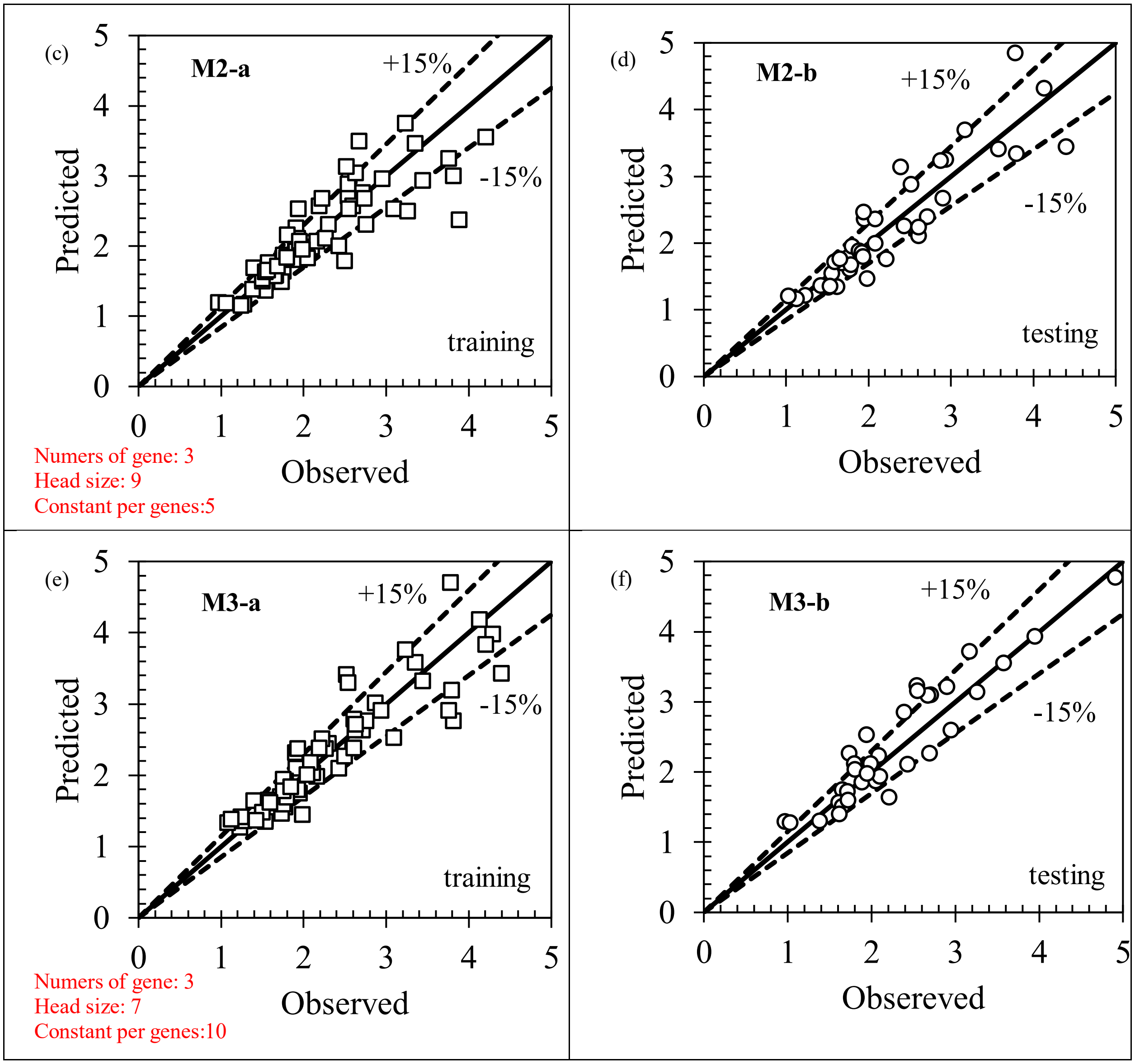
(c)
M2-a
+15%
-15%
training
Predicted
Observed
Numers of gene: 3
Head size: 9
Constant per genes:5
(d)
M2-b
+15%
-15%
testing
Predicted
Obsereved
(e)
M3-a
+15%
-15%
training
Predicted
Observed
Numers of gene: 3
Head size: 7
Constant per genes:10
(f)
M3-b
+15%
-15%
testing
Predicted
Obsereved

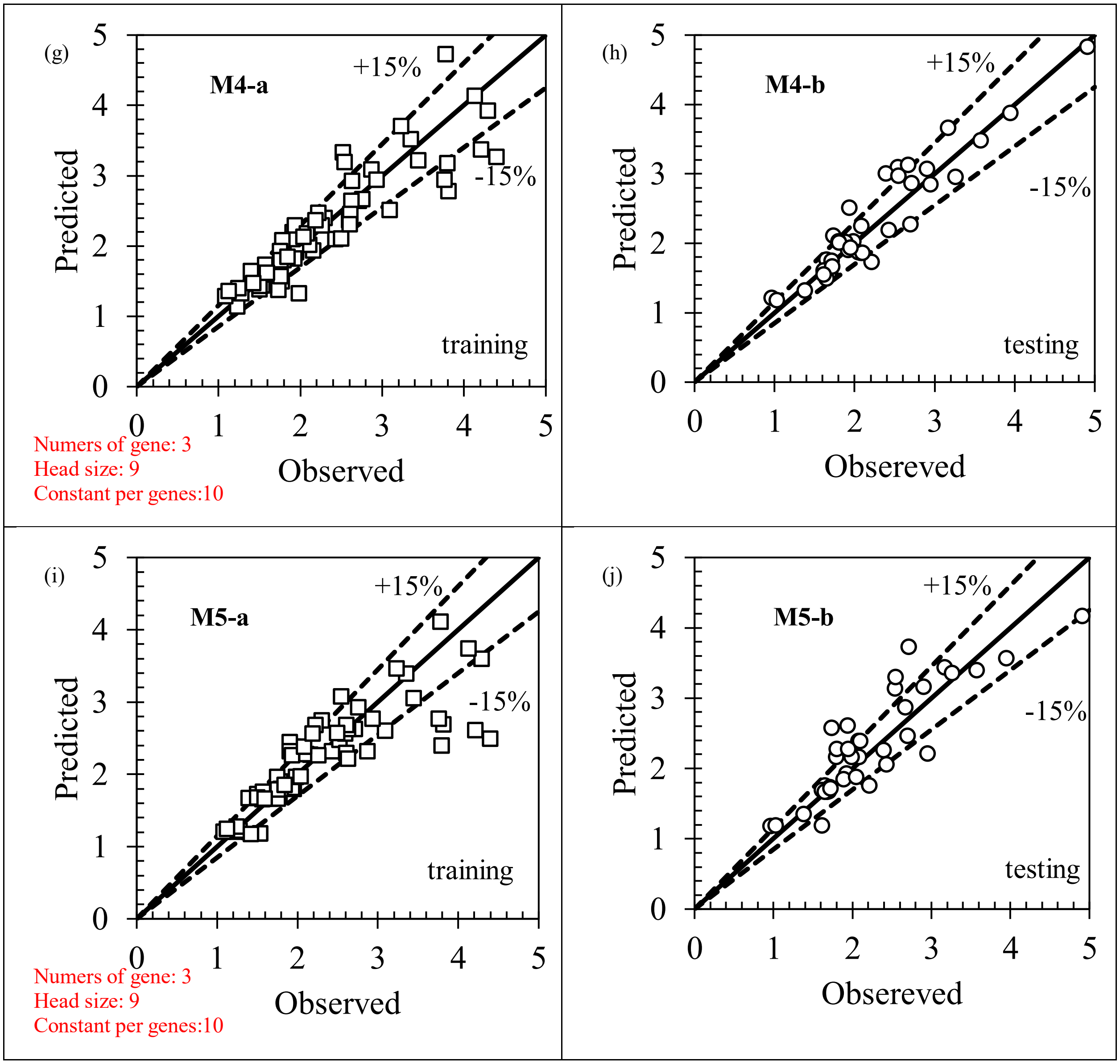
(g)
M4-a
+15%
-15%
training
Predicted
Observed
Numers of gene: 3
Head size: 9
Constant per genes:10
(h)
M4-b
+15%
-15%
testing
Predicted
Obsereved
(i)
M5-a
+15%
-15%
training
Predicted
Observed
Numers of gene: 3
Head size: 9
Constant per genes:10
(j)
M5-b
+15%
-15%
testing
Predicted
Obsereved

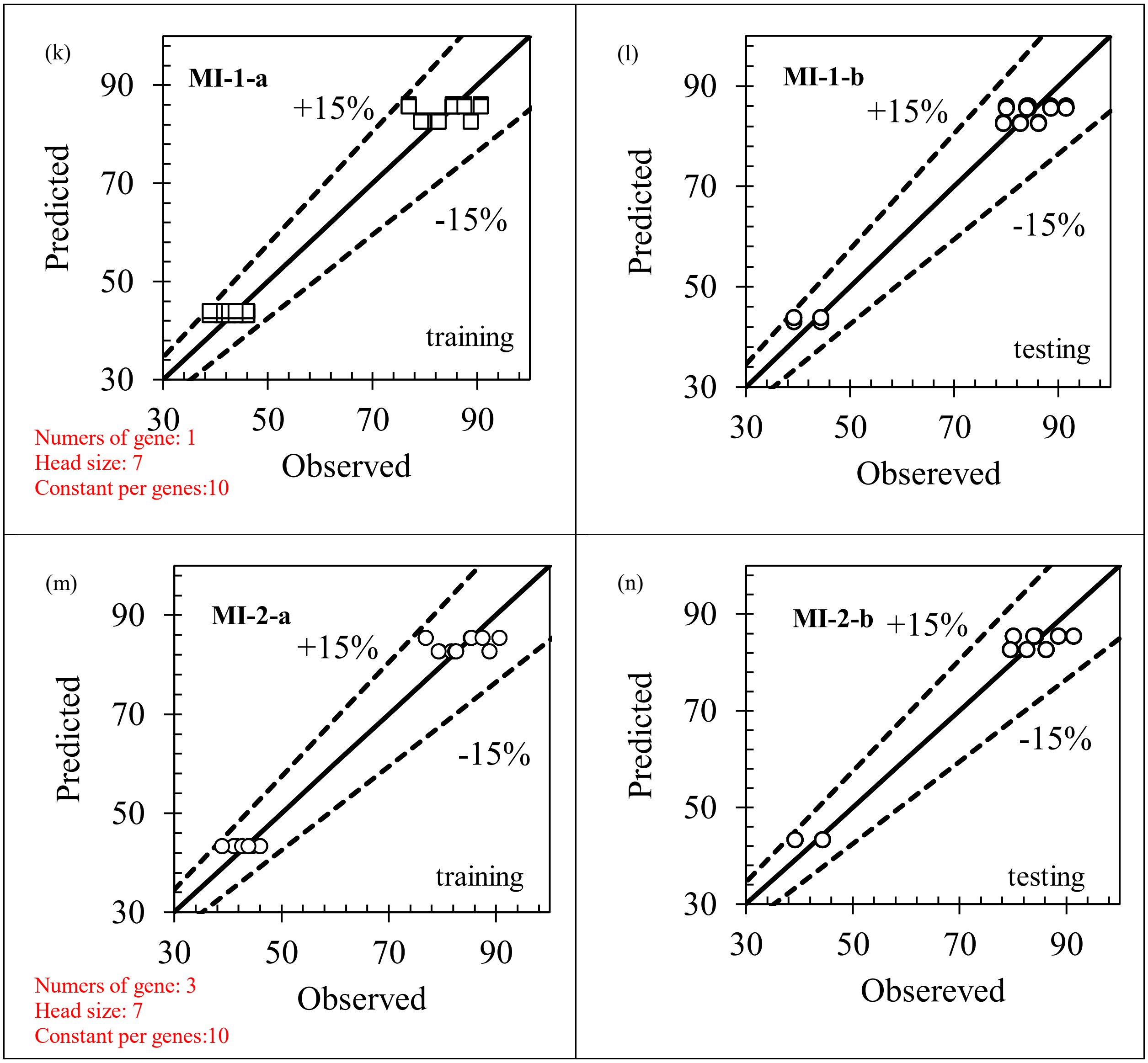

Figure 5.6 Comparison of the predicted (GEP model) and observed data.

The performance of these models is statistically evaluated through some common error indicators to analyze the accuracy of the GEP method. These error indicators typically measure the differences between the predicted and observed values from the testing data. This allows for objectively assessing the model's performance and accuracy in predicting outcomes. The error indicators include correlation coefficients, root mean squared error (RMSE), root relative squared error (RRSE), mean absolute deviation (MAD), mean squared error (MSE), mean absolute error (MAE), relative squared error (RSE), relative absolute error (RAE), mean absolute percentage error (MAPE), mean average relative error (MARE) and relative root mean square error (RRMSE).

5.4.2 Correlation Coefficient (R) and R-squared

A correlation coefficient (R) measures the strength and direction of the relationship between two variables. It indicates whether two variables are positively or negatively related, and the relationship's strength ranges from -1 to 1. The absolute value is closer to 1 which indicates that both variables have a stronger relationship.

The R is defined as:

$$R = \left(\frac{\sum_{i=1}^{N} (P_i - \bar{P})(O_i - \bar{O})}{\sqrt{\sum_{i=1}^{N} (P_i - \bar{P})^2 \ \sum_{i=1}^{N} (O_i - \bar{O})^2}} \right) \tag{5.7}$$

Where the O_i is the observed value (experimental results), P_i is the predicted value (GEP model results). $\bar{P}$ and $\bar{O}$ are the average value for the predicted value and the observed value, respectively.

The R-value and R^2 are calculated for the training and testing datasets listed in Table 4.1. For the dilution model (M1-M5), all the models have a strong positive correlation ($R > 0.8$). M1 has the lowest R-value for training and testing data, 0.878 and 0.879, respectively. M4 has the highest R for the testing data, which is 0.944, and the R for the training data is 0.886. Among the models for the impact point (MI), the multiple gene model (MI-2) has a higher value (0.974/0.979) than the single gene model (0.971/0.974) (MI-1).

5.4.3 Root Mean Squared Error (RMSE)

The RMSE is a common measure of how well the regression models fit the observed data when evaluating the accuracy of the regression models. It provides an overall summary of the model's accuracy, helping to compare, select, and make accurate predictions.

RMSE is calculated from

$$RMSE = \sqrt{\frac{\sum_{i=1}^{N} (O_i - P_i)^2}{N}} \tag{5.8}$$

Where N is the number of the data, which is 80 for the training data and 40 for the test datasets.

There is no specific standard for the RMSE value, as it depends on the specific application and the scale of the variables. Generally, the lower the RMSE value, the closer the predicted values are to the actual values, indicating a better fit of the model. In the training dataset, M1 had the lowest value of 0.386, and M5 had the highest value of 0.464; in the testing dataset, M4 performed the best with the lowest value (0.267), and M1 had the highest value (0.593). The RMSE for five models ranged from 0.267 to 0.593. Due to the consistently small RMSE values for all models, it becomes challenging to determine which model performs better in terms of RMSE, as they exhibit similar levels of accuracy. Therefore, they are considered appropriate.

Impact point (MI) models have a higher value range, from 3.475~4.503. The multiple-gene shows a lower value (3.475/3.522) than the single-gene (3.781/4.503) for both the training and testing datasets.

5.4.4 Root Relative Squared Error (RRSE)

Similar to R^2, RRSE provides a measure of the proportion of variance accounted for by the model in the actual values. The equation is:

$$\mathrm{RRSE} = \sqrt{\frac{\sum_{i=1}^{N}(P_i - O_i)^2}{\sum_{i=1}^{N}(O_i - \overline{O})^2}} \qquad (5.9)$$

The range of RRSE is 0 to infinity. A low RRSE value indicates a good fit of the model. The value of RRSE in the training dataset for M1~M5 varies from 0.449 (M3) to 0.492(M1), and 0.346 (M4) to 0.553(M1) for the testing dataset. The RRME in the testing and testing datasets RRME for the MI-1 and MI-2 are 0.247, 0.288 and 0.227, 0.225, respectively. These results demonstrated the overall effectiveness of all the models, and the multiple-gene model (M4 and MI-2) performed better than the single-gene.

5.4.5 Mean Absolute Deviation (MAD)

The MAD is the average distance between the value and the mean. It is an indicator of the variability of the dataset, a small value indicates that most of the data values are close to the mean. The MAD can be calculated as follows:

$$\mathrm{MAD} = \frac{\sum_{i=1}^{N}|P_i - \overline{P_i}|}{N} \qquad (5.10)$$

The MAD value of five dilution models in the training dataset and the testing dataset ranged from 0.502 (M1) to 0.654 (M3) and 0.567 (M1) to 0.697(M2). The MAD value in impact point models has higher values, in the range of 11.21 to 14.683. A larger MAD can be interpreted as a wider spread of data points around the mean, indicating a higher fluctuation in the dataset. It was reasonable because the dimensionless impact point locations were collected from three different discharge angles (30, 45 and 60 degree), the $\overline{P_i}$ is averaging value from a wide range (39.04~91.51). This large MAD can be overcome by creating three GEP models with specific discharge angles. However, in this study, we aimed to find one GEP model to predict the location of the impact point. As a result, this large MAD value is insufficient to indicate that the impact point model performs poorly.

5.4.6 Mean Squared Error (MSE)

Mean squared error (MSE) is another error indicator for predictive models that measures the average deviation of the predictions from the actual values. Obtaining the root value of MES leads to RMSE. The equation for MES is written as follows:

$$\mathrm{MSE} = \frac{1}{N}\sum_{i=1}^{N}(O_i - P_i)^2 \tag{5.11}$$

A good model will have an MSE value closer to zero. However, it calculated the square of the errors, if the dataset is too scattered, that can lead to a greater value of MSE, as it tends to be sensitive to outliers and extreme values.

In the training dataset and testing dataset, the MSE values ranged from 0.149 (M1) to 0.215 (M5) and from 0.071 (M4) to 0.352(M1). The MSE value for the two impact point models shows a higher range from 12.074 to 20.274. For the training and testing dataset for single-gene and multiple-gene is 14.301, 20.274 and 12.074, 12.408, it still showed that the multiple-gene model has a lower value than the single-gene model.

5.4.7 MEAN Absolute Error (MAE)

MAE is the average absolute value of the difference between the experimental and model results. Compared to MSE, it is less sensitive to extreme values. MAE can be calculated from

$$\mathrm{MAE}_{\mathrm{model}} = \frac{\sum_{i=1}^{N}|O_i - P_i|}{N} \tag{5.12}$$

The lower value indicates that the model prediction is reasonable. In this study, the MAE value of five dilution models in the training dataset and the testing dataset ranged from 0.254 (M2) to 0.292 (M4) and 0.206 (M4) to 0.39 (M1). Regarding the model for the impact point, the training and testing datasets of single-gene and multiple-gene were 2.88, 3.303 and 2.592, 2.721, respectively.

4.1.7 Relative Squared Error (RSE)

The output value of the RSE is expressed in terms of ratio. It is calculated by:

$$\mathrm{RSE} = \frac{\sum_{i=1}^{N} (O_i - P_i)^2}{\sum_{i=1}^{N} (O_i - \bar{O}_i)^2} \tag{5.13}$$

It can range from zero to one. The lower value indicates better model performance. RSE values of the training dataset and testing dataset were from 0.201(M3) to 0.242 (M5) and 0.12 (M4) to 0.306 (M1). The models for the impact point have this value 0.061, 0.083 and 0.051, 0.05 for the training and testing dataset.

5.4.8 Relative Absolute Error (RAE)

The RAE is calculated with the following:

$$\mathrm{RAE} = \frac{\sum_{i=1}^{N} |O_i - P_i|}{\sum_{i=1}^{N} |O_i - \bar{O}_i|} \tag{5.14}$$

Similar to RSE, the best value of RAE is zero. The GEP models all have small values. For the dilution model, the training dataset and the testing dataset ranged from 0.361(M2) to 0.429 (M1) and 0.35 (M4) to 0.476 (M5). The models for the impact point have this value 0.231, 0.237 and 0.208,0.195 for the training and testing dataset; the multiple-gene model is lower than the single-gene model.

5.4.9 Mean Absolute Percentage Error (MAPE)

MAPE is also known as mean absolute percentage deviation (MAPD). It shows the percentage of mean prediction error. Smaller MAPE values indicate that the model has a lower average prediction error. The equation is shown as follows:

$$\mathrm{MAPE} = \frac{1}{N} \sum \frac{O_i - P_i}{O_i} \times 100\% \tag{5.15}$$

The dilution model for the training and testing datasets ranged from 9.953% (M2) to 11.07%(M4) and from 11.545% (M4) to 17.416% (M1). The MAPE in the training and testing dataset of the impact point model was 4.74%, 4.201%, and 4.291%, 3.769%. All the models were considered reasonable.

5.4.10 Mean Absolute Relative Error (MARE)

Mean absolute relative error measures the relative error between predicted and observed values. The closer the value is to zero, the better the model is. MARE can be obtained from the following:

$$\mathrm{MARE} = \frac{1}{N}\left(\sum_{i=1}^{N}\left|\frac{O_i - P_i}{O_i}\right|\right) \quad (5.16)$$

In the dilution model, for training and testing datasets, the value ranged from 0.095 (M2) to 0.11 (M5) and 0.097 (M4) to 0.151(M1). The value ranges from 0.097 to 0.125. The model for the impact point was 0.047, 0.042 in the training dataset and 0.043, 0.038 in the testing dataset.

5.4.11 Relative Root Mean Square Error (RRMSE)

RRSME is a dimensionless form of RMSE. It is usually presented in a percentage form.

$$\mathrm{RRMSE} = \sqrt{\frac{\frac{1}{N}\sum_{i=1}^{N}(O_i - P_i)^2}{\sum_{i=1}^{N}(P_i)^2}} \quad (5.17)$$

A value of a good model should be less than 20%. When the value is greater than 30%, the model can be considered poor. The testing dataset for M1 has the highest value, 26.7%, which indicates that M1 has a poor performance among the other three. All M2, M3, M4 and M5 are smaller than 20%. The model for the impact point only ranges from 4.8%~6.1%, so they can be considered good models.

5.4.12 Performance Index (PI)

Besides the above error evaluation indicators, the performance index is also helpful for evaluating and comparing different models. The formula is as follows.

$$\mathrm{PI} = \frac{\mathrm{RRMSE}}{\mathrm{CC} + 1} \quad (5.18)$$

The value of the five models is shown in Table 3. Model 1 has the highest value for the training data, while the other 4 have similar performance. The values for the impact point model for multiple genes and single gene models are 0.024 and 0.031, respectively.

5.4.13 Bias

The bias can indicate the direction and the magnitude of the model's prediction error. A negative value indicates this model underestimates the actual value, and a positive value means overestimation (bias>0). It can be calculated by:

$$\mathrm{BIAS} = \frac{\sum_{i=1}^{N}(P_i - O_i)}{N} \tag{5.19}$$

All five dilution models and impact points have a little underestimation of the actual values, but the value is relatively small.

Previously, we evaluated the performance of models with different settings in both the training and testing datasets using various error indicators. For the impact point model, as the variation among models only involved a change in the number of genes, the multiple-gene models consistently outperformed the single-gene model regardless of the chosen indicator. However, for the dilution model, due to the increased complexity introduced by the five different model settings, there were some discrepancies between the training and testing datasets, making it challenging to find a single indicator to assess the model's performance.

Therefore, to facilitate comparison, we summarized the values of each indicator in the training and testing datasets, ranked them in descending order, and assigned scores to each model based on each error indicator. The best-performing model received 5 points, while the worst-performing model received 1 point for each indicator. By adding up these scores, the model with the highest total score was considered the best-performing model. The results are presented in Table 5.2.

Table 5.2 The scores for the dilution model based on statistical indicators.

Parameter scoring	M1	M2	M3	M4	M5
R	2	3	4	5	1
MSE	1	3	4	5	2
RMSE	1	3	4	5	2
RAE	1	3	4	5	2
MAE	1	3	4	5	2
RSE	1	3	4	5	2
RRSE	1	3	4	5	2
MAD	5	1	5	3	4
MARE	1	4	3	5	2

MAPE	1	4	3	5	2
RRMSE	1	3	4	5	2
PI	1	3	4	5	2
Sum of scores	**17**	**36**	**47**	**58**	**25**

The results clearly indicate that the performance of the GEP models varied based on different gene setups. The single gene model (M1) exhibited the worst performance (score 17), and the best model was M4. It can highlight the significant impact of gene number on the GEP model's outcomes.

Despite M5 having three genes, it only contained four basic functions (Table 1), resulting in performance degradation. It appears that the choice of functions can also affect the performance of the model. The best two models were M3 and M4, the difference between them is the head size, with M3 having a head size of 7 and M4 having a head size of 9. The head size refers to the number of functions and terminals within a single gene and can influence the model's complexity and performance. However, it should be noted that excessively large head sizes can also lead to a degradation in performance. For example, increasing the head size to 30 resulted in a reduced R^2 value of 0.5 (not presented). Therefore, a head size range of 7 to 10 is recommended for small data sizes, with adjustments based on specific requirements. These recommendations align with the research conducted by Azimi and Bonakdari (Azimi, Bonakdari et al. 2021). It is important to consider the number of genes, the choice of functions, and the size of the gene head when setting up the GEP models to achieve optimal performance.

5.4.14 Sensitivity analysis

It is important to conduct a sensitivity analysis to determine how input variables influence the output of the model. For each input value in this study, a 10% perturbation was applied (Bahreini Toussi, Mohammadian et al. 2021), and the results are shown in Table 5-3 and Table 5-4.

The following shows an example calculation: taking the Froude number (Fr) as an example:

$$Fr_{new} = 1.1 * Fr_{old}$$

$$\Delta S = \frac{|S_{new} - S_{old}|}{S_{old}} \quad (5.20)$$

$$Sensitivity = \frac{\Delta S}{0.1}$$

Where the Fr_{new} is the Froude number increased by 10%, Fr_{old} is the actual mean value of the Froud number. After employing the different models, the updated dimensionless dilution (S) would be calculated, and the sensitivity of each variable can be determined, listed in Table 5.3 and Table 5.4. The table shows that different parameters have different sensitivities in different models. In the impact point model, the single-gene model (MI-1) has a 0 % sensitivity to the discharge angle (α), which means that the model is less accurate because the location of the impact point is related to the discharge angle (in dimensionless analysis). The multiple-gene model is more reasonable because it also shows that the sloped bottom angle (θ) has around 10% sensitivity.

Table 5.3 Sensitivity to each variable in different "dilution" models

Variables in the model	M1	M2	M3	M4	M5
Alpha (α)	91.52(25%)	100.66(43%)	48.33(9%)	61.08(5%)	88.51(43%)
Theta (θ)	16.93(5%)	11.49(5%)	5.36(1%)	337.22(27%)	11.60(6%)
X/D	43.82(12%)	12.68(5%)	34.27(6%)	48.72(4%)	31.73(15%)
Fr	214.58(58%)	110.90(47%)	451.92(84%)	786.96(64%)	74.00(36%)

Table 5.4 Sensitivity for each variable in "impact point location" model

Variables in the model	MI-1	MI-2
alpha	0(0%)	0.69(34%)
theta	0.21(4%)	0.19(9%)
Fr	4.85(96%)	1.17(57%)
Diameter (D)	0(0%)	0(0%)

5.4.15 Uncertainty analysis

The uncertainty analysis aims to estimate the reliability of the model. It is an important technique for determining the impact of uncertainty or model changes on model predictions. It can be performed using either a limited set of parameters or through a comprehensive analysis involving all the model input parameters. In this study, a Monte Carlo Analysis (MCA) approach was adopted to fully assess the uncertainty level in the predictions. MAC utilizes the central limit theorem to generate a large number of random inputs, creating a representative sample for uncertainty analysis (Bahreini Toussi, Mohammadian et al. 2021). For the dilution model, 1,000,000 random inputs as a combination of the input parameters $\frac{x}{D}, Fr, \alpha\ and\ \theta$. Similarly, for the impact point model, the inputs included α, θ and Fr.

These datasets were generated randomly with Gaussian distribution, and the truncated Gaussian function was applied using MATLAB 2022. The range and histogram of four inputs generated from the truncated Gaussian function are shown in Figure 5.7.

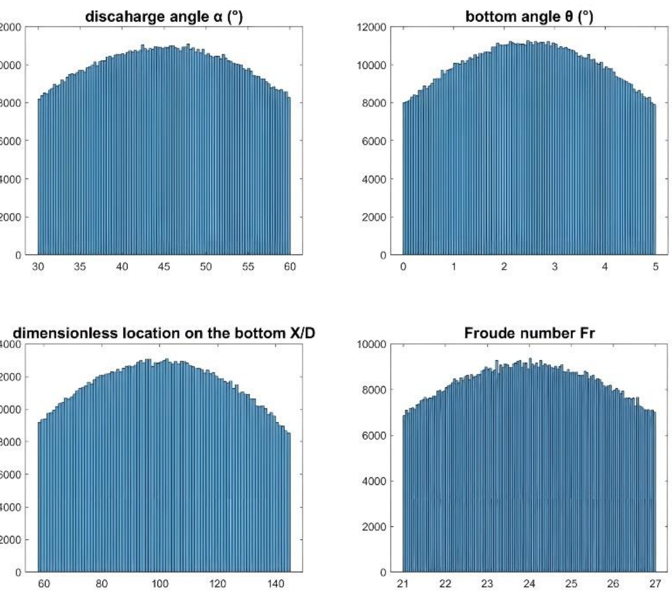

Figure 5.7 Histogram of random inputs in the form of truncated Gaussian distribution

Then, all the combinations of random variables were put into the GEP model. After the calculation, the mean absolute deviation (MAD) is calculated.

$$MAD = \frac{\sum_{i=1}^{N}|y - \bar{y}|}{N} \quad (5.21)$$

The uncertainty percentage of the function can be calculated as follows:

$$U = 100 \times \frac{MAD}{\bar{y}} \quad (5.22)$$

where N is the number of samples, 10,00,000, and $\bar{y}$ is the average result calculated by the models. Then the uncertainty can be calculated from five models of 30.04, 70.05, 61.87, 31.78 and 47.53. All five models have reasonable uncertainty. Similarly, the uncertainty analysis is also applied to the impact models, with the results of 33.55 (single gene) and 41.23 (multiple genes). This amount of uncertainty is also considered reasonable.

The uncertainty band can be obtained using the Wilson score technique (Wilson 1927) with mean prediction error $\bar{e}$ (Equation 22) and standard deviation S_e(Equation 23), the prediction error was calculated by $e_i = P_i, -O_i$, i.e. predicted value minus observed value. Overestimation and underestimation are indicated by positive and negative values, respectively. The 95% uncertainty band can be calculated from $\pm 1.98 S_e$. The results for the testing dataset are shown in Table 4.4.

$$\bar{e} = \frac{\sum_{i=1}^{n} e_i}{n} \tag{5.23}$$

$$S_e = \sqrt{\frac{\sum_{i=1}^{n} (e_i - \bar{e})^2}{n-1}} \tag{5.24}$$

Overestimation and underestimation are indicated by positive and negative values, respectively. The 95% uncertainty band can be calculated from $\pm 1.98 S_e$. The uncertainty analysis results are shown in Table 5.5.

Table 5.5 Uncertainty band width and 95% prediction error intervals

Model	Mean prediction error	Uncertainty interval half-width (1.98S_e)	95% prediction error intervals
M1	-0.156	1.147	(-0.336 0.024)
M2	-0.006	0.737	(-0.121 0.011)
M3	0.061	0.601	(-0.033 0.155)
M4	0.045	0.529	(-0.038 0.127)
M5	0.081	0.758	(-0.038 0.199)
MI1	-2.472	7.684	(-4.436 -0.051)
MI2	-1.433	6.580	(-3.115 0.249)

The results show that in the dilution model, the mean prediction error range from 0.156(M1) to 0.081(M5), and the uncertainty interval half width ranges from ± 0.529 (M4) to ± 1.147(M1). For the models for the impact point, the mean prediction errors are -2.472 and -1.433 for the single gene model and multiple gene models, and the interval half width ranges within ± 7.684 and ± 6.580, respectively.

Table 5.6 The error indicators for GEP models

No. Model	Group	R^2	CC	MSE	RMSE	RAE	MAE	RSE	RRSE	MAD	MARE	BIAS	RRMSE (%)	PI	MAPE (%)
M 1	Training	0.771	0.878	0.149	0.386	0.429	0.261	0.242	0.492	0.502	0.107	-0.044	17	0.091	10.947
	Testing	0.773	0.879	0.352	0.593	0.449	0.390	0.306	0.553	0.567	0.151	-0.156	26.7	0.142	17.416
M 2	Training	0.783	0.885	0.188	0.434	0.361	0.254	0.224	0.473	0.622	0.095	-0.063	18.5	0.098	9.593
	Testing	0.832	0.912	0.135	0.367	0.409	0.275	0.194	0.441	0.697	0.115	-0.006	16.5	0.086	13.782
M 3	Training	0.805	0.897	0.179	0.423	0.368	0.273	0.201	0.449	0.654	0.103	-0.062	18	0.095	10.602
	Testing	0.866	0.931	0.093	0.306	0.404	0.239	0.157	0.396	0.631	0.114	0.061	13.4	0.070	13.082
M4	Training	0.784	0.886	0.201	0.449	0.393	0.292	0.226	0.476	0.628	0.107	-0.081	19.1	0.101	11.070
	Testing	0.892	0.944	0.071	0.267	0.350	0.206	0.120	0.346	0.63	0.097	0.045	11.8	0.061	11.545
M 5	Training	0.768	0.877	0.215	0.464	0.382	0.284	0.242	0.492	0.584	0.110	-0.079	19.8	0.105	11.023
	Testing	0.770	0.877	0.149	0.386	0.476	0.281	0.250	0.500	0.604	0.125	0.081	16.8	0.090	14.476
MIP-1	Training	0.943	0.971	14.301	3.781	0.231	2.880	0.061	0.247	11.21	0.047	-0.050	6	0.031	4.740
	Testing	0.949	0.974	20.274	4.503	0.237	3.303	0.083	0.288	12.663	0.042	-2.472	6.1	0.031	4.201
MIP-2	Training	0.949	0.974	12.074	3.475	0.208	2.592	0.051	0.227	12.295	0.043	-0.346	5.5	0.028	4.291
	Testing	0.958	0.979	12.408	3.522	0.195	2.721	0.05	0.225	14.683	0.038	-1.433	4.8	0.024	3.769

5.4.16 Comparison with previous studies

From the previous analysis of error indicators and sensitivity analysis, it can be observed that the GEP model can predict the impact point location and dilution level along the bottom. In order to further validate the capability of the GEP model, we extracted partial experimental data from Roberts and Ferrier (1997), Shao and Law (2010), and Lai and Lee (2012) and applied them to the GEP model. For the sake of simplicity, only the best-performing GEP models (MI-2, M3, and M4) were selected, and their results are presented in Table 5.7.

It can be seen that the multiple-gene model (MI-2) exhibited good performance in simulating the impact point (Xi/D). The errors were less than 17%. However, there are significant differences in the performance of the dilution models (M3 and M4), which ranged from 3% to 198%. This could be attributed to several factors. First, the training data for the GEP model were obtained solely from our experiments, resulting in a relatively small dataset. Moreover, variations in experimental instruments and methods across different experiments can also contribute to the different results. Second, when extracting experimental data from other researchers, it should be noted that multiple experiments are often performed, and the concentration results are typically obtained from the average data from these experiments. Therefore, when different experimental conditions (α,θ, Fr) into the GEP model, variations in the results can appear due to the sensitivities of each variable in GEP models.

GEP still shows significant potential in predicting the physical and concentration characteristics of inclined jets from discharge outlets.

Table 5.7 Comparison between GEP model with previous experiments

Model parameter / Previous study	Discharge angle ($\alpha°$)	Slope angle ($\theta°$)	Fr	Xi/D (Exp)	Dilution	Xi/D (MI-1)	Xi/D MI-2	Dilution M1	Dilution M2	Dilution M3	Dilution M4	Dilution M5	Average
Roberts, Ferrier et al. (1997)	60	0	26.4	63.36	1.48~1.72	74.72	64.5	1.65	1.44	1.42	3.31	2.59	1.89
	60	0	25.4	60.96	1.48~1.72	64.85	58.4	1.79	1.46	2.01	1.67	2.80	1.82
	60	0	24	57.6	1.48~1.72	51.59	49.8	1.94	1.61	2.35	1.59	3.24	1.97
Shao and Law (2010)	30	0	25.3	75.9	1.45	63.88	72.5	1.00	1.32	1.41	1.94	1.34	1.36
	45	0	25.5	76.5	1.26	65.82	76.5	1.49	2.22	1.77	1.79	0.51	1.68
Lai and Lee (2012)	30	0	25.4	80.772	0.82	64.85	73.0	1.03	1.53	1.48	1.67	1.29	1.43
	30	0	26.8	85.224	0.82	78.77	79.5	1.40	1.21	1.19	2.10	1.23	1.28
	38	0	25.2	80.388	0.99	62.91	70.8	1.32	0.80	1.49	2.01	1.61	1.48
	38	0	26.7	85.173	0.99	77.75	78.5	-9.30	0.87	1.25	2.86	1.51	1.21
	45	0	26.7	89.178	1.09	77.75	83.1	-9.03	1.53	1.37	3.04	1.74	1.55
	45	0	23.8	79.492	1.09	49.76	67.2	1.82	2.10	2.35	2.21	2.13	2.15
	52	0	25.8	74.046	1.1	68.76	64.9	1.66	2.09	2.74	3.16	1.89	2.24
	52	0	26.7	76.629	1.1	77.75	70.07	-8.92	2.01	1.46	3.09	1.79	1.75
	60	0	25.8	73.272	1.07	68.76	60.8	1.92	1.63	2.92	3.19	2.32	2.39

5.5 Conclusion

This study aims to utilize the GEP technique to establish predictive models to capture both the geometric and dilution information of inclined dense jets under skewed bottom conditions. Mathematical equations were generated for predicting the impact point location (Xi/D) or the dilution information along the bottom (S/F) using the GEP method. Several input parameters, including emission angle (α), bottom slope angle (θ), nozzle diameter (D), and Froude number (Fr), were considered in the GEP models. For the dilution models, five different GEP configurations were explored, including various selections of mathematical functions and chromosome structures. In the model for predicting the impact point, the single- and multiple-gene models was generated. These models were compared and analyzed using error indicators, uncertainty analysis, and sensitivity analysis. The results demonstrated that GEP can construct models to predict the important jet properties.

The proper configuration of the GEP model plays a crucial role in achieving accurate predictions. Generally, multiple-gene models outperform single-gene models. The choice of mathematical functions and other gene structures, such as head size, also influences model outcomes. Testing and adjustments had to be performed during model establishment to obtain the best model performance. Additionally, it is important to apply different metrics to the model's results to assess its performance and stability.

Furthermore, GEP results are influenced by the quality of training and testing datasets. Considering the limited amount of experimental data available in this study, it is recommended that future research focus on extracting additional information regarding the concentration variations of inclined jets on sloped surfaces. It will be possible to develop a comprehensive GEP model to predict the physical and concentration properties of inclined jets in a wide range of receiving environments.

Chapter 6 Evolutionary prediction of geometrical and dilution characteristics of inclined dense jet over a sloped bottom using large eddy simulation

Xinyun Wang[1], Abdolmajid Mohammadian[1]

1. Department of Civil Engineering, University of Ottawa, 161 Louis Pasteur Private, Ottawa, ON K1N 6N5, Canada

Abstract: In desalination plants, inclined dense jets are a common discharge method. Several studies have investigated the characteristics of the inclined dense jet. Artificial intelligence has gained attention in recent years because of its high flexibility and accuracy. In this study, gene expression programming (GEP) models were developed using the results from Large Eddy Simulation to predict the characteristics of the inclined dense jet with different discharge angles (30º,45º,60º) and different sloping bottoms (0º and 5º). All jet characteristics related to the discharge angle and Froude number; the sloping bottom angle affected some characteristics, such as the location of the impact point. The results show that single- and multi-gene models can provide reasonable results. Analysis of error indicators, sensitivity and uncertainty indicated that the multi-gene model was more stable and accurate. Overall, the GEP model has the potential to predict the characteristics of inclined dense jets under various receiving water environments and conditions.

Key Words: inclined dense jet, gene expression program (GEP), sloped bottom, large eddy simulation (LES)

6.1 Introduction

The demand for freshwater is increasing with the growing global population and continuous urbanization. However, the supply of freshwater resources in response to this demand remains relatively limited. According to statistics, over 97.2% of the total water resources globally are saline water, with only a small fraction available as directly usable freshwater. Desalination technology appears to be a promising method of converting seawater into freshwater, especially in arid and semi-arid regions (Elsaie, Soussa et al. 2022). The primary role of desalination plants is to remove salt from seawater effectively; however, this process produces significant quantities of highly concentrated brines as a byproduct. Improper brine discharge can cause significant environmental risks and severe pollution (Elsaid, Kamil et al. 2020). Therefore, the treatment and appropriate discharge of brines are crucial considerations in designing desalination plants to minimize negative impacts and protect the local ecosystem.

Inclined dense jet is commonly used in desalination plant discharge systems. The brine is discharged through a combination of submerged pipelines and circular nozzles to form a jet (Roberts, Salas et al. 2010). It is believed that stagnant water bodies are the worst receiving conditions because they do not enhance the mixing between the jet and the surrounding water. Despite the idealized nature of the stagnant water condition, studying it can clarify how inclined dense jets mix during development and transportation. Figure 6.1 (a) presents a typical inclined dense jet discharged into the stagnant water. The jet is discharged through a round nozzle (D) with the velocity U and concentration (ρ_0), it can generate strong turbulence in the receiving water and be rapidly diluted to obtain an acceptable salinity. The discharge angle (α) is inclined upwards, allowing the brine to reach longer distances. With the initial momentum, the brine jet will move upward and reach the highest point (terminal rise height Y_t) where buoyancy momentum equals the initial momentum, then the brine flow will fall back to the bed and continue moving along the bottom due to the gravity until it dissipates; the point where the flow returns to the discharge height is the return point (X_r), the point where the flow touches the ground is called the impact point (X_i) or impingement point. These geometrical and dilution parameters were found to correlate with the Froude number. Therefore, when designing the discharge system of a desalination plant, it is critical to understand the physical and concentration variations at specific points of the inclined dense jet. For example, knowing the location of the highest point in an inclined dense jet can help prevent the jet from touching the water surface. Information about the concentration at the impact point can give an idea of the area of brine influence. This would be very helpful for protecting the local marine environment. In most of the research, the jet is considered discharged on the horizontal bottom, or the discharge port height is small, the return point and impact point can be considered as one point. However, these two points should be discussed separately when the bottom is sloped, or the height is unignorable. Furthermore, the brine flow will continue to move along the bottom after the impact point. It is necessary to analyze how mixing developed and how concentrations varied on the different receiving bottoms. This information can be used to determine the optimal discharge location and angle based on different receiving conditions to reduce the damage to the environment.

(a)

(b)

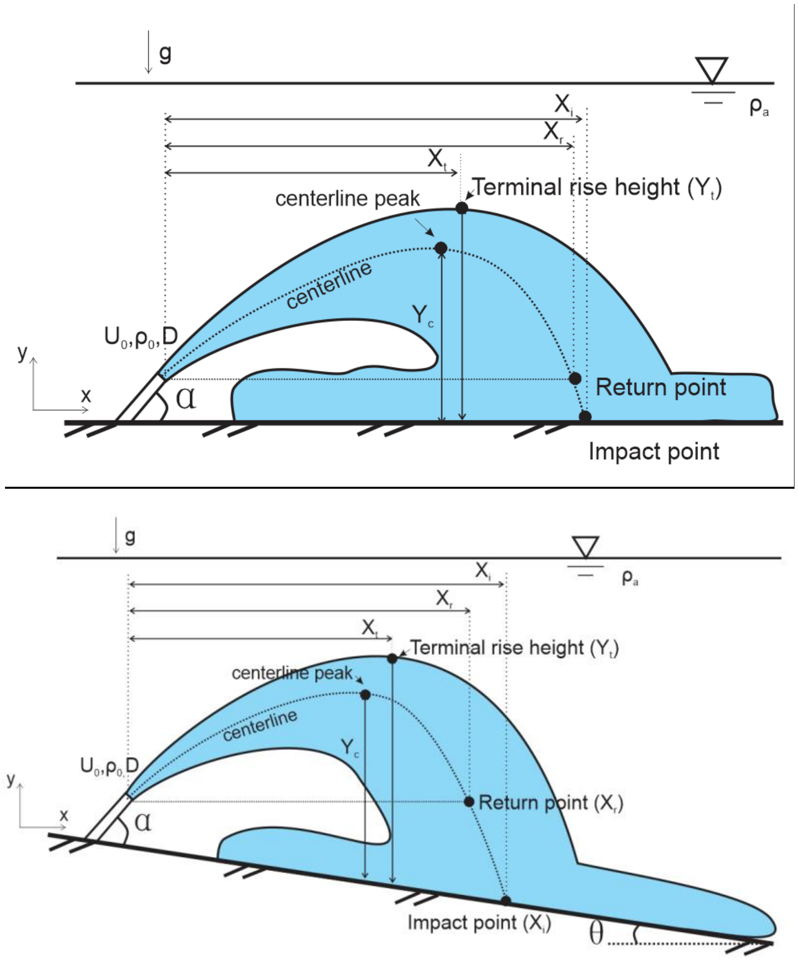

Figure 6.1 Diagram of an inclined dense jet (discharge angle α) on (a) horizontal bottom; (b) sloped bottom (slope angle θ) discharged in stagnant water

Similarly to the vertical negative buoyant jet, the properties of the inclined dense jet can be expressed using the dimensionless Froude number (Fr) as:

$\frac{X}{DFr} = f(\alpha, Fr)$ or $\frac{S}{Fr} = f(\alpha, Fr)$ where X represents the geometrical properties of the jet, S represents the dilution, which is calculated by the $s = \frac{C_0 - C_a}{C - C_a}$, here C is the local time-averaged concentration. The dimensionless Froude number is obtained from $Fr = U_0/\sqrt{Dg_0'}$, where $g_0' = g\frac{(\rho_0 - \rho_a)}{\rho_a}$. It means the essential normalized geometrical information is a function of the Froude number and discharge angle. Once the discharge angle is fixed, the function would be seen as a constant form as $\frac{X}{DFr} = C_1$ or $\frac{S}{Fr} = \ C_2$. These functions or constants C_1, C_2 are one of the most important objectives in the research of inclined dense jets. They can be derived from experiments or numerical simulations (Roberts et al. 1997).

There have been several studies on inclined dense jets. The effect of the nozzle inclination and jet trajectory has been widely studied. The optimal discharge angle is 60º because it provides the longest trajectory leading to more dilution of the jet (Roberts et al. 1997). However, in shallow water, the steeper discharge angle will have a higher terminal rise height, and the higher angle will increase the risk that the jet touches and pollutes the water's surface (Shao, 2010). So, the discharge angle of 30º and 45º are also widely investigated. The velocity and concentration information in the flow field has also been researched. (Cipollina, Brucato et al. 2005) (Kikkert, Davidson et al. 2007) (Lai and Lee 2012), (Kikkert, Davidson et al. 2007, Lai and Lee 2012), (Papakonstantis, Christodoulou et al. 2011, Papakonstantis, Christodoulou et al. 2011) (Zeitoun and McIlhenny 1971, Roberts, Ferrier et al. 1997, Shao and Law 2010, Papakonstantis and Tsatsara 2018, Papakonstantis and Tsatsara 2019, Azizi, Goharikamel et al. 2020).

Aside from experimental research, the advancement of supercomputers has significantly improved the research and application of computational fluid dynamics (CFD) in fluid engineering. It utilizes numerical methods and algorithms to solve complex fluid flow problems (Versteeg and Malalasekera, 2007). There are three categories in the CFD, which are Directed Navier-Stokes (DNS), Reynolds-average Navier-Stokes (RANS) and Large Eddy Simulation (LES). In RANS, the turbulence is modeled using an averaging method, which assumes that the flow properties can be divided into time-averaged quantities and turbulent fluctuations. Due to the effectiveness and reasonable accuracy of the RANS model, it has gained significant popularity in the fluid engineering industry. Vafeiadou and Papakonstantis conducted the first CFD simulation of inclined dense jet by ANSYS CFX software to analyze discharge angles ranging from 45 to 90 degrees(Vafeiadou, Papakonstantis et al. 2005). The simulation results revealed that the discharge angle significantly influences the jet's trajectory and characteristics. Oliver and his colleagues (Oliver, Davidson et al. 2008) compared the results of the standard k-ε model with experimental findings from prior studies conducted by Kikkert et al. (2007). They evaluated the effectiveness of the k-ε model in predicting the properties of the inclined dense jet. Seil and Zhang (2010) used SST and Renormalization Group (RNG) model and employed the ANSYS FLUENT software to simulate the single or multiple ports at discharge. Gildeh and Mohammadian (2015) also conducted a comprehensive CFD simulation to study the performance of five different RANS turbulence models on inclined dense jets with OpenFOAM software.

However, the RANS is limited in capturing small-scale turbulence structures, such as the flow near the wall and in complex geometry. The large eddy simulation (LES) model can overcome this shortage and enable more accurate prediction results. Zhang (2016) (2017) presented a detailed investigation of inclined dense jets with 45 and 60 degree inclination angles using a large eddy simulation (LES) approach with both the Smagorinsky and Dynamic Smagorinsky subgrid scale (SGS) models. The results showed that LES could predict satisfactory geometric information in most aspects while the dilution is underestimated by ∼20%.

Although large-eddy simulation (LES) provides more accurate predictions in computational fluid dynamics, its practical application in engineering is still limited by high computational and time costs. To solve these problems, researchers are exploring artificial intelligence (AI) to optimize the model more efficiently. An example of such a technique is gene expression programming (GEP). This novel machine learning algorithm automatically builds predictive models based on data without the need for any prior knowledge. The GEP uses the concept of gene expression, following the laws of inheritance and survival of the fittest, to identify the chromosome with the highest fitness. By simulating the mathematical expression relationship between data points, GEP is able to uncover complex patterns and determine the underlying relation(Ferreira 2001). This is an evolution of genetic algorithms and genetic programming that has shown promising results in a wide range of fields, including hydrological engineering, such as the prediction of hydraulic jump, seepage under hydraulic structures and open-channel hydraulic(Azimi, Bonakdari et al. 2021) (Khashan and Hassan 2021) (Zahiri, Dehghani et al. 2015) (Zahiri, Dehghani et al. 2015).

Bonakdari and Mohammadian (2019) are the first researchers to apply the GEP in the investigation of inclined dense jets. They employed the GEP to predict geometrical and dilution data for the inclined dense jet in shallow water. The results of their sensitivity study indicated that the derived equations could accurately predict the jet's trajectory and provide informative data for various receiving water conditions. Similarly, Yan and Mohammadian (2020) utilized the multi-gene genetic programming (MGGP) algorithm to generate explicit equations for the inclined dense jet at the multiple ports; the MGGP proved effective in predicting important parameters; it served as a valuable technique for developing models that predict the mixing characteristics of inclined dense jets discharged from multiport diffusers.

As mentioned earlier, the dilution and mixing characteristics of inclined dense jets, particularly after the impact point, have received limited attention in previous studies. In addition, the influence of the inclination of the bottom surface on brine mixing has also been rarely investigated. Therefore, this paper aims to fill these research gaps by studying the concentration variation after the impact point and examining the effects of a five-degree sloping bottom on the mixing characteristics of the brine flow.

This study considers various classical information related to the inclined dense jet, including geometrical parameters and dilution information, such as the terminal rise height and return/impact point. Three different discharge angles (30º,45º,60º) and two bottom angles (0º and 5º) in the stagnant water are considered. The training data for the GEP model is generated using the Large Eddy Simulation (LES) with the K-equation turbulence model in OpenFOAM. By using a large amount of data from LES simulations, GEP can construct a model to predict the physical and concentration variations of the jets. In addition, GEP can further improve the accuracy and precision of prediction by combining optimization algorithms and artificial intelligence techniques to optimize the parameters and structure of the model. To the best of the authors' knowledge, currently, no studies have used data from LES models to train GEP models, which means that exploring the performance of GEP models in simulating inclined dense jets can fill the gap in this research area and further improve the accuracy and reliability of simulation predictions. The application of GEP to the study of inclined dense jets can provide industry with a quicker and more accurate approach to jet prediction, which can effectively guide the design and optimization of discharge systems.

The paper is structured as follows. Section 2 briefly describes the LES, followed by an introduction to the computational domain. Section 3 introduces the GEP and describes the setup of the GEP model. Section 4 presents the results and discussions while conclusions are provided to complete the study.

6.2 Methodology

6.2.1 Large eddy simulation-governing equation

The governing equations for LES (large eddy simulation) are derived from the fundamental Navier-Stokes equations, which describe the conservation of mass, momentum, and energy in fluid dynamics. However, unlike the Reynolds-averaged Navier-Stokes (RANS) model, which applies a time-averaging process to all the movement properties in the flow, LES takes a different approach. In LES, a filtering function is employed to distinguish between the resolved large-scale and unresolved small-scale eddies. The filtering function acts as a cutoff width that separates the flow into two components: the resolved and unresolved scales(Mason 1994). The larger eddies, with sizes larger than the filtering cut-off, are directly computed by solving the Navier-Stokes equations. These resolved eddies contain important flow structures and dynamics crucial for accurately capturing the turbulence in the flow. The smaller eddies below the cutoff width are considered as sub-grid-scale (SGS) stresses with different SGS models (Smagorinsky (1963)). Various SGS models can be employed, and they can provide approximate descriptions of the smaller eddies and their influence on the main flow. LES achieves a more accurate representation of turbulence compared to the RANS model.

The filtered Navier-Stokes equations, including continuity and momentum equations for incompressible fluid, are:

$$\frac{\partial \bar{u}_i}{\partial x_i} = 0 \tag{6.1}$$

$$\frac{\partial \bar{\rho}\bar{u}_i}{\partial t} + \frac{\partial}{\partial x_j}\left(\bar{\rho}\bar{u}_i\bar{u}_j\right) = -\frac{\partial \bar{p}}{\partial x_i} + \frac{\partial}{\partial \mathrm{x_j}}\left(\mu \frac{\partial \bar{u}_i}{\partial x_j}\right) - \frac{\partial \tau_{ij}}{\partial x_j} \tag{6.2}$$

Where $\tau_{ij} = \rho\overline{u_i u_j} - \rho\bar{u}_i\bar{u}_j$ is the SGS Reynold stress, which can be modelled as

$$\tau_{ij} = 2\rho\nu_{sgs}S_{ij}^{*} - \frac{2}{3}\,\rho k_{sgs}\delta_{ij} \tag{6.3}$$

$$S_{ij}^{*} = \frac{1}{2}\left(\frac{\partial \bar{u}_i}{\partial x_j} + \frac{\partial \bar{u}_j}{\partial x_i} - \frac{1}{3}\frac{\partial \overline{u_k}}{\partial x_k}\delta_{ij}\right) \tag{6.4}$$

Where u_i, u_j are the velocity in i, j directions, p is the pressure, ρ is the fluid density, the bar symbol is the filtered function, ν_{sgs} is called SGS viscosity.

In this study, the K-equation model was employed to calculate the sub-grid-scale (SGS) viscosity. The ν_{SGS} can be calculated as:

$$\nu_{SGS} = C'_{sgs}\Delta\sqrt{k_{SGS}} \tag{6.5}$$

Where the C'_{sgs} is a constant equal to 0.094 and Δ is the LES filtering width determined by the grid size. k_{SGS} is the sub-grid-scale kinetic energy, it can be determined from one transport equation:

$$\frac{\partial(\rho k_{sgs})}{\partial t} + \frac{\partial(\rho \bar{u}_j k_{sgs})}{\partial x_j} = \frac{\partial}{\partial x_j}\left[\rho\left(\frac{\nu + \nu_{sgs}}{\sigma_k}\right)\frac{\partial k_{sgs}}{\partial x_j}\right] + P - \varepsilon_{sgs} \tag{6.6}$$

Where ε_{SGS} is the dissipation rate, $\varepsilon_{SGS} = C_\varepsilon \frac{k_{sgs}^{3/2}}{\Delta}$, $C_\varepsilon = 1.048, \sigma_k = 1.0$, Δ is the grid volume.

Using the open-source software OpenFOAM, Equation 6.6 was discretized using the finite volume method and solved directly. In this study, the solver TwoLiquidiMixingFoam was specifically applied, which is designed to simulate the mixing of two incompressible fluids. This solver has been extensively employed in various CFD studies and has demonstrated its reliability and accuracy in previous research(Ghorbani, Giljarhus et al. 2021) (Zhang, Jiang et al. 2016) (Gruber, Johnson et al. 2011).

6.2.2 Computational domain

The computational domain chosen for this study is a rectangular water tank with dimensions 2m(L)×0.8m(W)×0.8m(H), as shown in Figure 6.2a. The selection of this domain is based on its relevance to the specific problem being investigated experimentally. A mesh generator called SnappyhexMesh in OpenFOAM is utilized. This mesh generator employs an adaptive meshing algorithm, which allows for the generation of a mesh with optimized cell and minimized computational costs. In this study, a total of nine million cells are generated. The mesh is created with four different levels, as shown in Figure 6.2b. The grid in the level-1 region (1.7m×0.6m×0.2m) is finer, as well as the bottom of the domain, where the flow dynamics are expected to be more complex and require higher resolution. The sloped 5-degree bottom also adopted the same grid generation setup. Boundary conditions were assigned as follows: The inlet and outlet boundaries were specified as patches. The atmosphere boundary was set as a symmetry. The remaining boundaries were treated as solid walls. Before the simulations, a mesh independence analysis was conducted to ensure that the results obtained are not significantly affected by the mesh resolution.

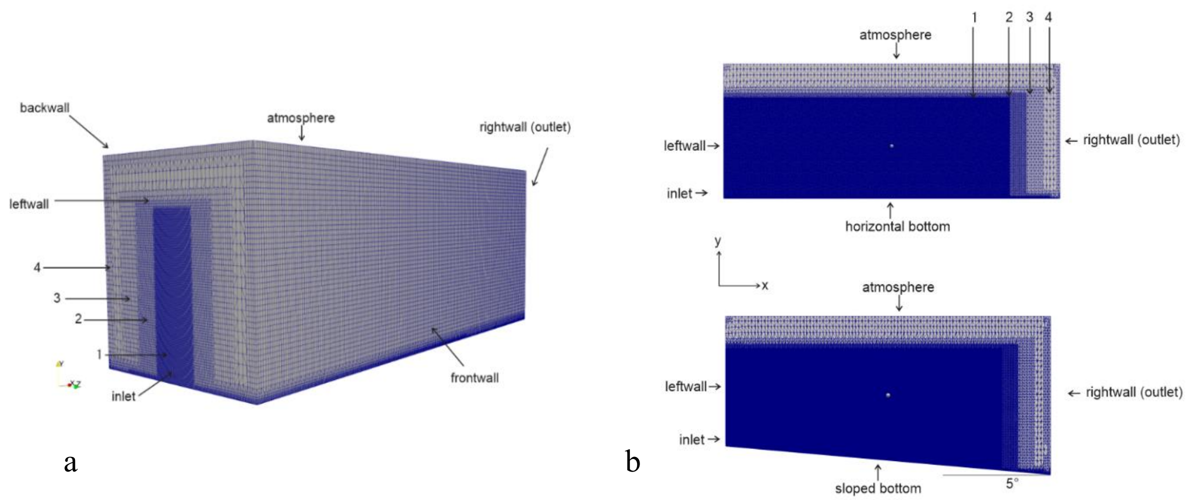

Figure 6.2 Computational domain (b) detailed multiple-level mesh in the center-plane of the tank

6.3 Gene expression programming setup

Gene Expression Programming (GEP) is a type of genetic algorithm being used to develop computer programs or mathematical expressions proposed by Ferreira in 2001 (Ferreira 2001) (Ferreira 2006). It is based on the idea of describing a program or expression as a series of genes, where each gene is associated with a particular function or terminal. In order to develop the string of genes and optimize the program or expression, the algorithm then utilizes genetic procedures, including mutation and crossover. GEP uses a library of expressions consisting of an expression tree (ET), and a set of "gene" sequences that encode these expression trees. It is usually expressed in the Karva language. Figure 6.3 shows an example of an expression tree.

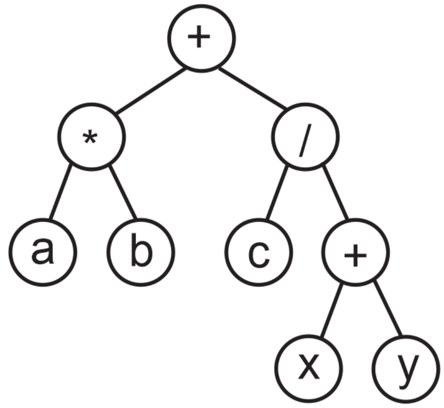

Figure 6.3 Expression tree (ET)

An expression tree is composed of nodes representing mathematical operations and variables. The expression trees in Figure 6.4 describe a mathematical expression that involves addition, multiplication, and division operations. The upper-level nodes labeled the mathematical operations, and then the two nodes attached below represent the variables or the next operation. Therefore, this expression tree represents the function as: $ab + c / (x + y)$.

The corresponding Karva language is illustrated in Figure 2.3. In the Karva language, the ET is expressed as a string of integers.

```
012345678
+*/abc+xy
```

Figure 6.4 Example of Karva language for Figure 6.3

To be more specific, there are nine integers (from 0 to 9) representing the nodes in the example ET. Then Karva language reads the ET starting from top to bottom and left to right as $+*/abc+xy$. Karva language effectively compresses the expression tree size, reducing the complexity and storage. Due to its simplicity, the Karva language allows efficient gene expression and evaluation during evolution.

A comprehensive flowchart for a GEP is presented in Figure 6.5. The first step is generating the initial population of chromosomes, which consists of randomly generated genes. Then the fitness value of each program is evaluated and compared with the observed results. Based on this evaluation, the program determines whether to continue iterating or terminate. In each iteration, the chromosomes undergo reproduction processes, including crossover, mutation, inversion, transposition, and recombination based on fitness values. These steps generate a new population. The iteration process will continue until a better solution is developed, which will ultimately lead to one optimal model.

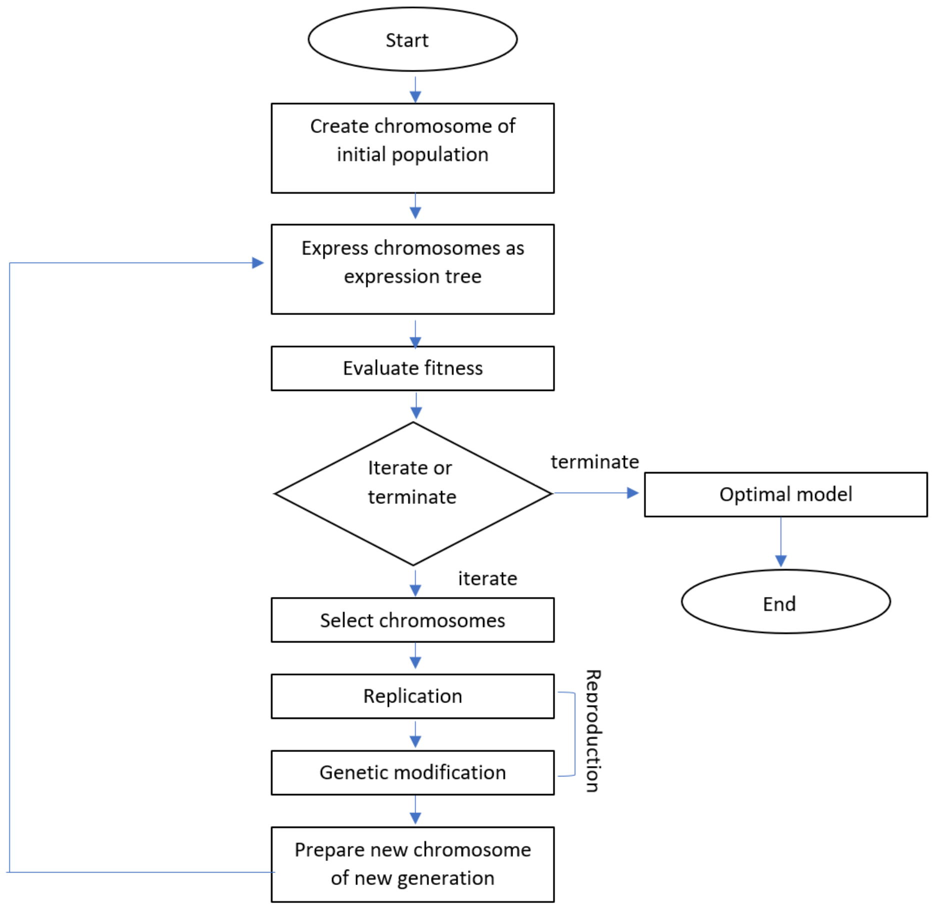

Figure 6.5 GEP flowchart

Completing a gene expression programming (GEP) setup typically involves five key steps, including determining the fitness function, chromosome number, head size, gene number, and linkage function. There are many options for selecting a fitness function. In this study, the root relative square error (RRSE) was chosen as the fitness function (Behnia et al. 2017).

The second step is the setup of the function. It usually contains mathematical or logical operators, and the choice of function combination depends on the specific problem. For this study, a set of common mathematical operators was selected, and additional details can be found in Table 6.1.

The third step is configuring the chromosome architecture setup, which includes the number of chromosomes, the head size, and the number of genes. These numbers are typically determined through a trial-and-error approach. In this study, the number of chromosomes and head size are 300 and 7, respectively. It is important to note that the specific setting of the number of genes needs to be adjusted according to the problem's complexity and the algorithm's performance requirements. Generally, a higher number of genes leads to more complex expression trees, but it also increases the computational cost and running time. To investigate the influence of gene numbers on the results, this study considered two scenarios: gene numbers set to 1 and 3, respectively. This analysis aims to explore the impact of gene numbers on the outcome of the GEP results.

The fourth step is the choice of a linking function that connects multiple genes. Common choices for the linking function included addition (+), subtraction (-), multiplication(×), division(/). In this study, we applied addition as the linking function. It means that in the multiple-gene model, it would be written as Model=Gene1+Gene2+Gene3.

A final setup includes a set of genetic operators which control gene reproduction, such as mutation rate and inversion rate. Table 6.2 lists the genetic operators that were applied in this study. All the GEP programs were applied using the software GeneXproTool[4].

The geometrical and dilution information included the location of the terminal rise height (X_t and Y_t), location of return point and impact point (X_r, X_i), dilution at the centerline peak (S_m), return point(S_r) and impact point (S_i) were collected from the LES results, the dilution variation along the different bottoms (S_b) after the impact point was also collected. All the models had one gene and three gene setups, respectively. The detailed setup is listed in Table 6.1, and the X_t, Y_t, X_r, X_i S_m, S_r, S_i had the input variables of discharge angle α, sloping bottom angle (θ) and Froude number (Fr), such as $X_t = f(\alpha, \theta, Fr)$. The dilution on the bottom (S_b) added another dimensionless location variableX/DF a$S_b = f(\alpha, \theta, Fr, X/DFr)$. In the X_t, Y_t, X_r, X_i S_m, S_r, S_i model, 61 data sets were randomly separated as 37 training data (60%) and 24 testing data (40%). The S_b model has 2577 data records, with 1546 (60%) as a training set and 1031 (40%) as a testing set.

[4] GeneXpro Tools 5.0; GEPSOFT Limited: Bristol, UK, 2013

The stop criterion for the evolutionary algorithm was set at 200,000 generations. The models with the highest R^2 value were selected and kept for analysis.

Table 6.1 GEP setting.

Name of model	Xt	Yt	Xr	Xi	Sm	Sr	Si	S_b
Chromosomes number	300	300	300	300	300	300	300	600
Number of genes	1and3	1and3	1and3	1and3	1and3	1and3	1and3	1and3
Head size	7	7	7	7	7	7	7	20
Fitness function	RRSE	RRSE	RRSE	RRSE	RRSE	RRSE	RRSE	RRSE
Linking function	addition	addition	addition	addition	addition	addition	addition	addition
Variables	α, θ, Fr	α, θ, Fr	α, θ, Fr	α, θ, Fr	α, θ, Fr	α, θ, Fr	α, θ, Fr	$\alpha, \theta, Fr, X/DFr$
Function setup	$+$ $-$ $\times$ $\div$ x^y $\sqrt[2]{x}$ $\sqrt[4]{x}$ Sin Exp 10^x x^4 E Cos Sec	$+$ $-$ $\times$ $\div$ $\log_{10} x$ x^3 $\sqrt[3]{x}$ Cos x^y 10^x Lnx x^3 $\sqrt[4]{x}$ pi Sin Tan Sec	$+$ $-$ $\times$ $\div$ $\sqrt[2]{x}$ Cos Sin Lnx $+$ $\sqrt[3]{x}$ Cot x^2 x^4 Log_{10} Tan $\sqrt[4]{x}$ x^y Sec Exp Csc	$+$ $-$ $\times$ $\div$ Csc Cos $\sqrt[3]{x}$ $\log_{10} x$ $\sqrt[4]{x}$ $\sqrt[2]{x}$	$+$ $-$ $\times$ $\div$ 10^x Csc Cos Cot Exp $Log_{10}x$ Ln_x $\sqrt[4]{x}$ Sec Sin $\sqrt[2]{x}$ Tan x^2 x^4 min	$+$ $-$ $\times$ $\div$ 10^x Sin Cos Cot Lnx x^2	$+$ $-$ $\times$ $\div$ Cos $\sqrt[3]{x}$ Exp $Log_{10}x$ $\sqrt[4]{x}$ Sec Tan x^4	$+$ $-$ $\times$ $\div$ Cos Csc Cot $\sqrt[3]{x}$ Exp $Log_{10}x$ Log_x^y Lnx x^y $\sqrt[4]{x}$ Sec Sin $\sqrt[2]{x}$ Tan x^2 x^3 x^4

Table 6.2 Value of parameters in the final setup of genetic operators

Genetic operators	value
Mutation rate	0.00138
Inversion rate	0.00546
One-point recombination	0.00277
Two-point recombination	0.00277
Gene Recombination	0.00277
Gene Transposition	0.00277
IS transposition	0.00546
RIS transposition	0.00546

6.4 Results and discussion

The application generated 16 GEP models, and the detailed equations for these models are shown in Appendix C. A comprehensive evaluation was conducted using various statistical indicators to assess their accuracy and reliability. Additionally, uncertainty and sensitivity analyses were performed to examine the robustness and stability of the models. Furthermore, a comparison was made between our results and previous studies to provide further insight into the potential of GEP models for predicting mixing and dilution in sloping bottoms.

6.4.1 Performance of model

Figure 6.6 shows the comparison between the observed (LES) and predicted (GEP) data for both the training and testing datasets, highlighting the performance of the models. A solid black line represents y=x, which corresponds to a perfect match between the observed and predicted values. Additionally, a dotted line indicated the $\pm 15\%$ error interval. Square-shaped markers represented the training dataset, and the testing dataset was denoted by dot-shaped markers. The single-gene and multiple-gene models were distinguished by the blank and filled grey colour, respectively.

It can be seen that single-gene and multiple-gene GEP models for $X_t, Y_t, X_r, X_i\ S_m, S_r, S_i$ both had equally good performance, and the training and testing datasets were close to the $\pm 15\%$ error interval. While for the GEP model for dilution along the bottom (Sb), particularly the multiple-gene model, it was observed that the data align more closely to the line y=x. Compared to the single-gene model, fewer data points fell outside the $\pm 15\%$ error interval for both the training and the testing dataset.

The performance of the GEP models was comprehensively assessed based on error indicators. These indicators quantify the differences between the predicted values generated by the models and the observed values obtained from LES. By analyzing these statistical indicators, we can evaluate the accuracy and reliability of the GEP models and determine the most suitable model for the given problem. In this analysis, the error indicators included correlation coefficient (R), mean squared error (MSE), root mean squared error (RMSE), mean absolute error (MAE), mean absolute deviation (MAD), mean absolute relative error (MARE), relative absolute error (RAE), relative squared error (RSE)root relative squared error (RRSE). Each of these indicators provided unique insights into the performance of the models, allowing for a comprehensive evaluation of their predictive capabilities.

The error measure equations are listed below, and all the results are presented in Table 6.3.

$$R = \left(\frac{\sum_{i=1}^{n} (P_i - \bar{P})(O_i - \bar{O})}{\sqrt{\sum_{i=1}^{n} (P_i - \bar{P})^2 \ \sum_{i=1}^{n} (O_i - \bar{O})^2}} \right) \tag{6.7}$$

$$MSE = \frac{1}{n} \sum_{i=1}^{n} (O_i - P_i)^2 \tag{6.8}$$

$$RMSE = \sqrt{\frac{\sum_{i=1}^{n} (O_i - P_i)^2}{n}} \tag{6.9}$$

$$MAE_{\text{model}} = \frac{\sum_{i=1}^{n} |O_i - P_i|}{n} \tag{6.10}$$

$$MAD = \frac{\sum_{i=1}^{n} |P_i - \bar{P}_i|}{n} \tag{6.11}$$

$$MARE = \frac{1}{n} \sum_{i=1}^{n} \left| \frac{O_i - P_i}{O_i} \right| \tag{6.12}$$

$$RAE = \frac{\sum_{i=1}^{n} |O_i - P_i|}{\sum_{i=1}^{n} |O_i - \bar{O}_i|} \tag{6.13}$$

$$RSE = \frac{\sum_{i=1}^{n} (O_i - P_i)^2}{\sum_{i=1}^{n} (O_i - \bar{O}_i)^2} \tag{6.14}$$

$$RRSE = \sqrt{\frac{\sum_{i=1}^{n} (P_i - O_i)^2}{\sum_{i=1}^{n} (O_i - \bar{O})^2}} \tag{6.15}$$

Where the P_i is predicted result from the GEP model, O_i represents the observed results from large eddy simulation, n is the number of data points.

The correlation coefficient (R) measures the strength and direction of the linear relationship between the predicted and observed values. When this value is closer to ± 1, it indicates a strong linear relationship between the two variables. In this study, the geometrical model had an R-value ranging from 0.932 to 0.999, and for the dilution model, it ranged from 0.870 to 0.990. Therefore, these high correlation coefficients indicate that the GEP model has high accuracy in the prediction of jet properties.

Mean squared error (MSE) and root mean squared error (RMSE) are used to quantify the average difference between predicted and observed values. All the geometry models exhibited a small MSE value ranging from 0 to 0.097. However, the model predicting the dilution along the bottom (S_b) showed larger MSE values ranging from 0.231 to 0.58; the multiple-gene model (0.935 to 0.999) showed a higher value than the single-gene model (0.932 to 0.993). A similar pattern can be observed in RMSE, where the values of the geometry model ranged from 0.014 to 0.311, the dilution model ranged from 0.019 to 0.761; the multiple-gene model (0.014 to 0.257) showed a lower value than the single-gene model (0.045 to 0.311).

Mean absolute error (MAE) and mean absolute deviation (MAD) are used to calculate the average absolute difference between predicted and actual values; the MAD can measure the dispersion of the data. The MAE and MAD for all the models ranged from 0.01 to 0.556 and 0.042 to 2.242, respectively; Mean absolute relative error (MARE) and relative absolute error (RAE) quantify the average relative difference between predicted and actual values, with values ranging from 0.004 to 0.24 and 0.034 to 0.732, respectively.

Models with lower relative squared error (RSE) and root relative squared error (RRSE) values indicate higher prediction accuracy, and the multiple-gene model had lower RSE and RRSE values compared to the single-gene model (except S_m and Y_t model, but the difference is small). This error analysis indicated that the multiple genes have better performance.

In addition to the statistical indicators, additional evaluation indicators can be used to assess the performance of the models. Two commonly used indicators are bias and mean absolute percentage error (MAPE).

Bias quantifies the degree of bias present in the models. A positive bias indicates that the predicted values tend to be higher than the actual values, while a negative bias suggests that the predicted values are lower than the actual values. Bias provides insights into the overall systematic deviation of the models from the observed data. MAPE measures the percentage of error between the predicted and actual values of the model. It is calculated by taking the absolute difference between the predicted and actual values. A lower MAPE value indicates a better fit between the predicted and actual values, demonstrating the model's high accuracy. The equations are listed below:

$$BIAS = \frac{\sum_{i=1}^{N}(P_i - O_i)}{N} \tag{6.16}$$

$$MAPE = \frac{1}{N}\sum \frac{O_i - P_i}{O_i} \times 100\% \tag{6.17}$$

Bias for all the models ranged from -0.008 to 0.075, the single gene ranged from -0.008 to 0.075, while the multiple genes ranged from 0 to 0.04. The small value showed that the predicted value is very close to the actual model, which implied that the performance of both the single-gene and multiple-gene model were equally good. MAPE results ranged from 0.381 to 24.0321, and the highest MAPE belonged to the single-gene model for dilution on the bottom (S_b). For the other GEP models, the multiple-gene model also had a lower value than the single-gene model, which indicated that the multiple-gene model has better performance.

Overall, the error analysis combined with the BIAS and MAPE results highlighted that the multiple-gene models perform better than the single-gene model across various error indicators. These findings demonstrate the effectiveness of incorporating multiple genes in GEP models for improved prediction accuracy.

prarameter	single-gene GEP model		multiple-gene GEP model	
Xt	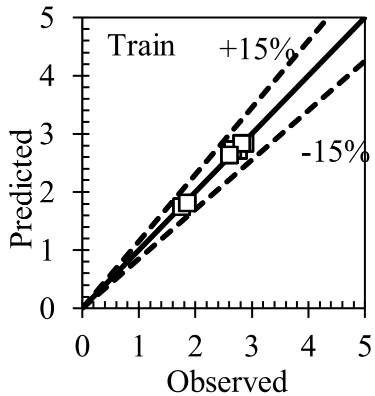	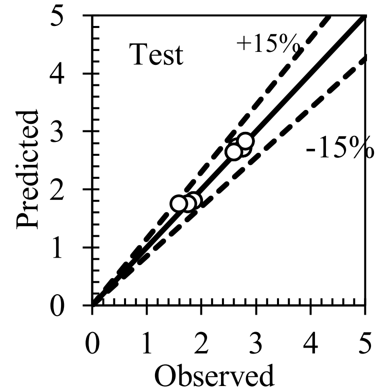	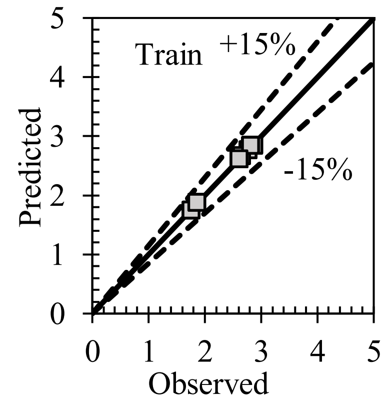	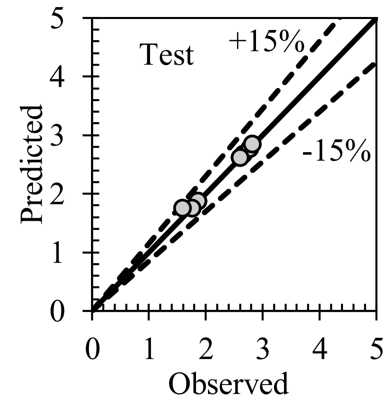
Yt	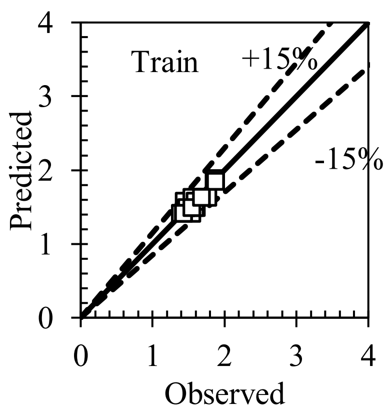	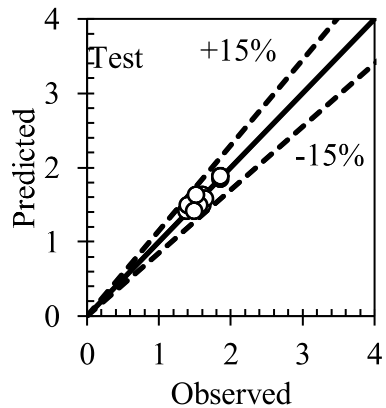	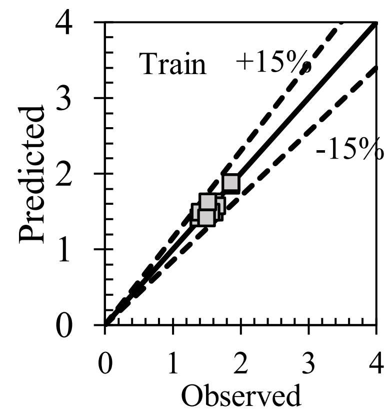	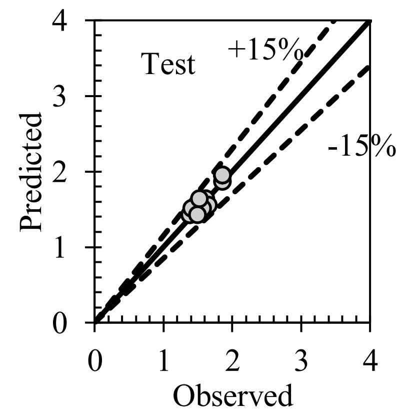

<table>
<tr>
<td>Xr</td>
<td>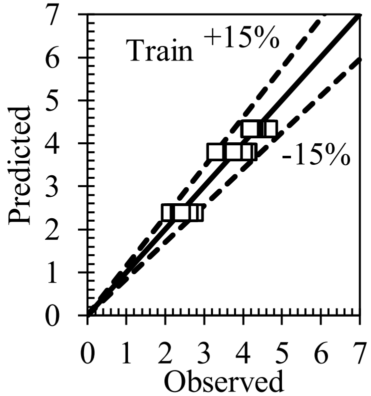
</td>
<td>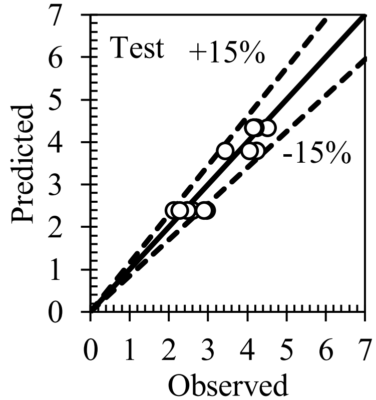
</td>
<td>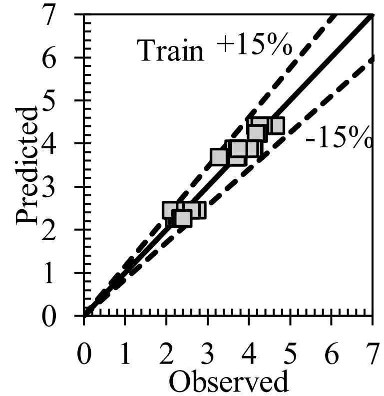
</td>
<td>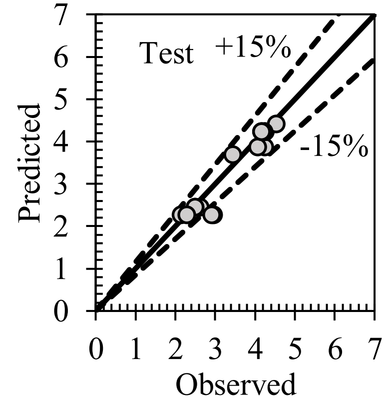
</td>
</tr>
<tr>
<td>Xi</td>
<td>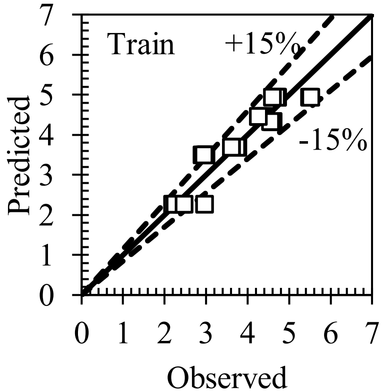
</td>
<td>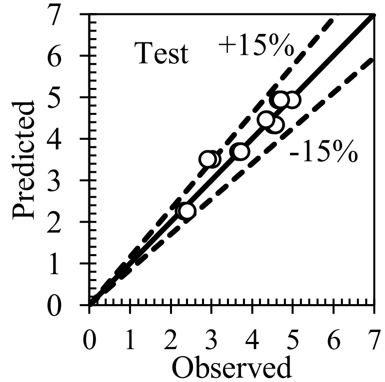
</td>
<td>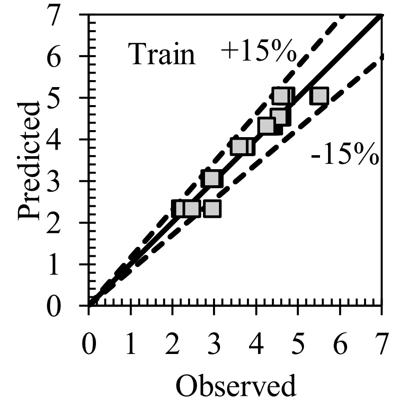
</td>
<td>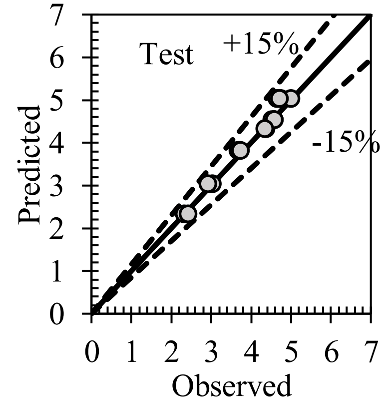
</td>
</tr>
</table>

Sm	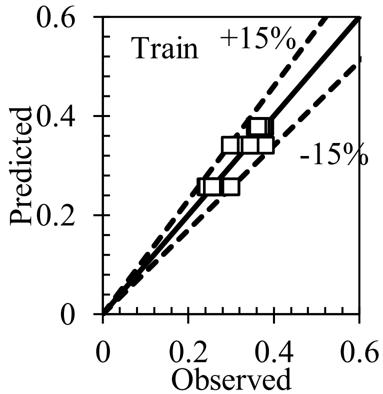	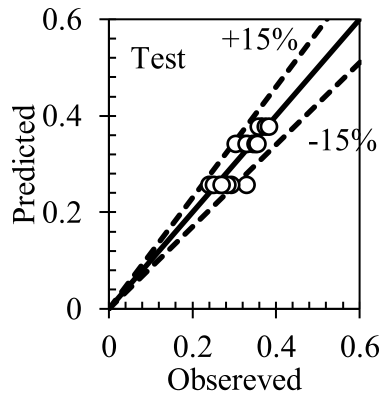	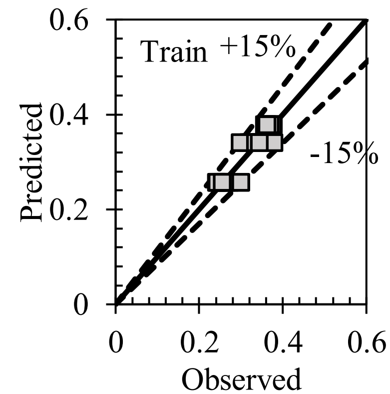	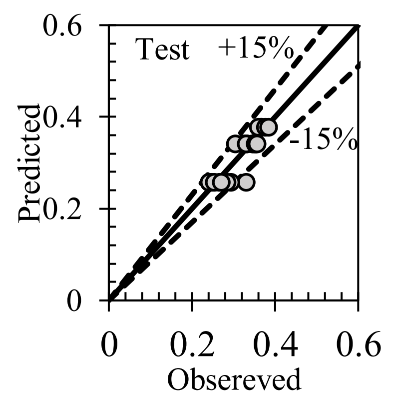
Sr	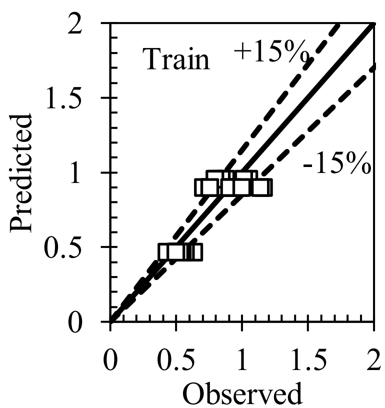	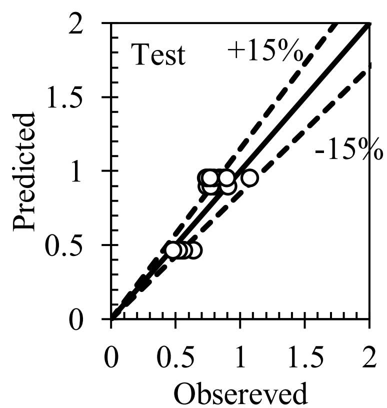	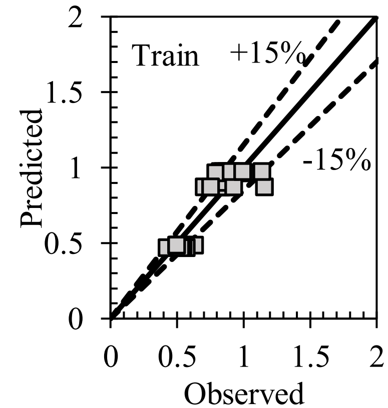	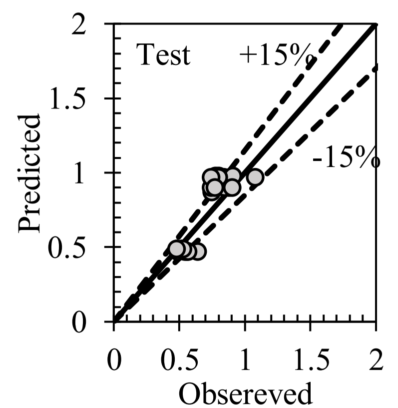

Train
+15%
-15%
Predicted
Observed
0
0.2
0.4
0.6

Test
+15%
-15%
Predicted
Obsereved
0
0.2
0.4
0.6

Train
+15%
-15%
Predicted
Observed
0
0.2
0.4
0.6

Test
+15%
-15%
Predicted
Obsereved
0
0.2
0.4
0.6

Train
+15%
-15%
Predicted
Observed
0
0.5
1
1.5
2

Test
+15%
-15%
Predicted
Obsereved
0
0.5
1
1.5
2

Train
+15%
-15%
Predicted
Observed
0
0.5
1
1.5
2

Test
+15%
-15%
Predicted
Obsereved
0
0.5
1
1.5
2

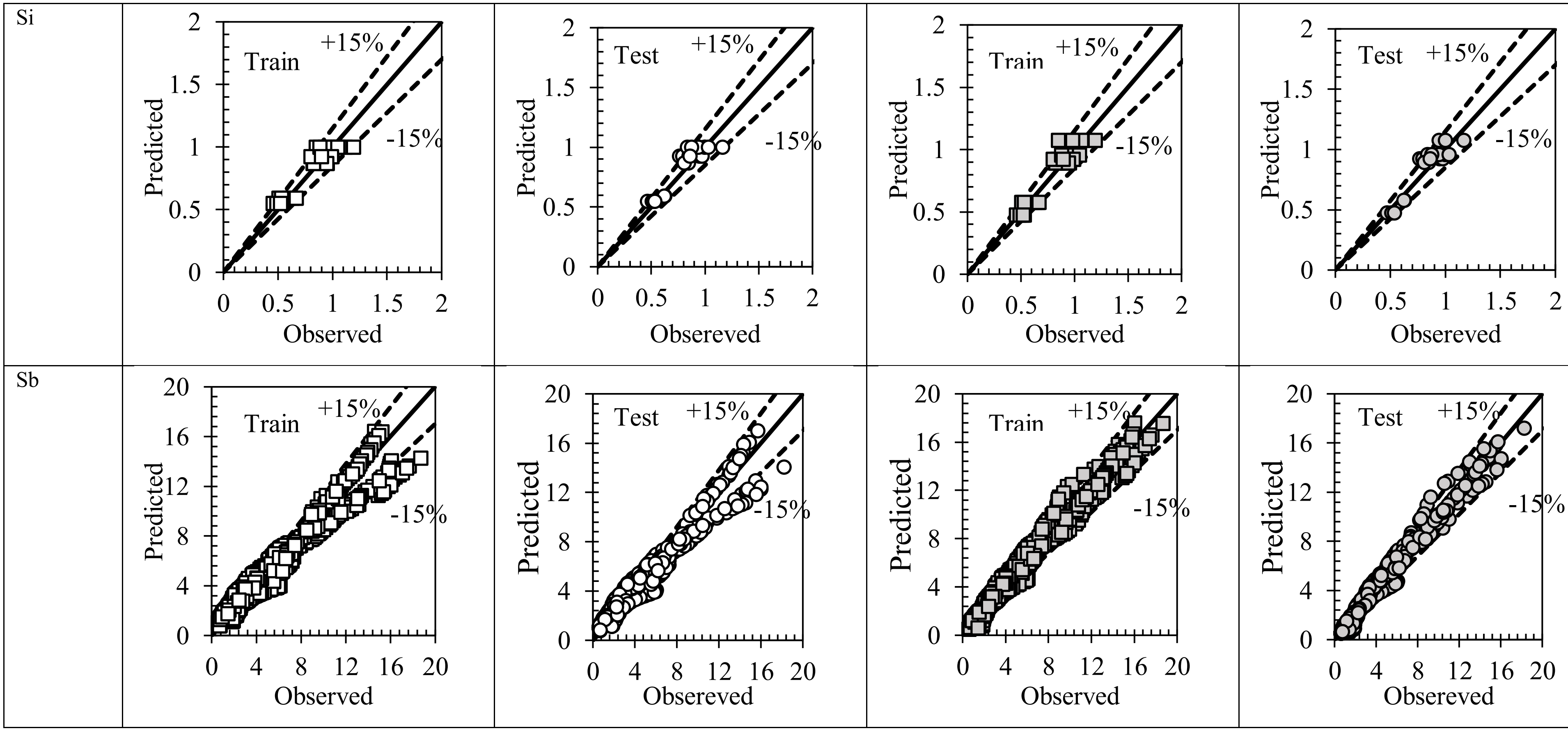

Figure 6.6 Comparison of the predicted (GEP model) and observed data (LES result) for both training and test dataset

Table 6.3 The error indicators for the GEP models

		Correlation Coefficient (R)	Mean Squared Error (MSE)	Mean Absolute Error (MAE)	Mean Absolute Deviation (MAD)	Mean Absolute Relative Erro (MARE)	Relative Absolute Error (RAE)	Relative Squared Error (RSE)	Root Relative Squared Error (RRSE)	Root Mean Squared Error (RMSE)	BIAS	Mean Absolute Percentage Error (MAPE)
$Sm-1gene$	Training	0.932	0.000	0.015	0.044	0.049	0.338	0.148	0.385	0.019	0.006	4.870
	Testing	0.895	0	0.015	0.042	0.051	0.400	0.210	0.486	0.021	0.003	5.118
$Sm-3gene$	Training	0.936	0	0.014	0.049	0.045	0.324	0.156	0.395	0.019	-0.003	4.53
	Testing	0.896	0.001	0.016	0.046	0.05	0.397	0.28	0.53	0.024	-0.007	5.001
$Sr-1gene$	Training	0.87	0.011	0.089	0.201	0.118	0.534	0.293	0.541	0.106	-0.007	11.788
	Testing	0.891	0.014	0.103	0.231	0.142	0.732	0.526	0.725	0.118	0.037	14.225
$Sr-3gene$	Training	0.888	0.01	0.077	0.201	0.102	0.464	0.251	0.501	0.098	0.002	10.154
	Testing	0.894	0.013	0.094	0.224	0.129	0.674	0.489	0.699	0.114	0.039	12.916
$Si-1gene$	Training	0.937	0.005	0.062	0.177	0.081	0.334	0.126	0.355	0.074	0.007	8.064
	Testing	0.927	0.006	0.061	0.176	0.076	0.384	0.166	0.408	0.078	0.03	7.618
$Si-3gene$	Training	0.946	0.005	0.059	0.205	0.077	0.317	0.116	0.34	0.071	-0.001	7.693
	Testing	0.94	0.006	0.065	0.293	0.016	0.412	0.154	0.392	0.075	-0.003	1.553
$Xt-1gene$	Training	0.993	0.002	0.391	0.455	0.021	0.138	0.014	0.12	0.045	-0.008	2.125
	Testing	0.993	0.003	0.046	0.397	0.022	0.103	0.014	0.12	0.055	-0.042	2.152
$Xt-3gene$	Training	0.999	0	0.01	0.283	0.004	0.034	0.001	0.037	0.014	0	0.381
	Testing	0.998	0.001	0.014	0.436	0.008	0.325	0.005	0.072	0.033	0.011	0.754
$Yt-1gene$	Training	0.932	0.004	0.045	0.127	0.028	0.333	0.142	0.377	0.06	-0.015	2.804
	Testing	0.948	0.004	0.047	0.164	0.03	0.306	0.119	0.345	0.061	-0.02	2.959
$Yt-3gene$	Training	0.935	0.004	0.048	0.14	0.03	0.357	0.144	0.379	0.06	-0.004	2.963
	Testing	0.939	0.005	0.06	0.176	0.037	0.394	0.158	0.398	0.07	0.002	3.711
$Xi-1gene$	Training	0.934	0.097	0.249	0.672	0.067	0.335	0.128	0.358	0.311	0.005	6.697
	Testing	0.941	0.085	0.226	0.713	0.065	0.312	0.126	0.356	0.292	-0.004	6.524
$Xi-3gene$	Training	0.972	0.043	0.141	0.728	0.036	0.19	0.057	0.239	0.207	0	3.626

	Testing	0.979	0.039	0.122	0.773	0.034	0.169	0.059	0.242	0.198	0.009	3.397
$Xr-1gene$	Training	0.973	0.033	0.137	0.657	0.041	0.204	0.052	0.229	0.182	0	4.057
	Testing	0.938	0.078	0.222	0.689	0.066	0.336	0.139	0.373	0.278	-0.025	6.632
$Xr-3gene$	Training	0.98	0.026	0.127	0.674	0.038	0.188	0.041	0.202	0.161	-0.001	3.834
	Testing	0.951	0.066	0.171	0.666	0.052	0.258	0.119	0.345	0.257	-0.075	5.152
$S_b-1gene$	Training	0.978	0.58	0.556	0.751	0.217	0.219	0.05	0.224	0.761	0.068	7.003
	Testing	0.975	0.554	0.552	2.14	0.24	0.234	0.055	0.234	0.744	0.075	24.032
$S_b-3\ gene$	Training	0.99	0.232	0.336	0.842	0.12	0.132	0.02	0.142	0.481	0.04	3.892
	Testing	0.989	0.231	0.335	2.242	0.126	0.142	0.023	0.151	0.48	0.013	12.616

6.4.2 Sensitivity and uncertainty analysis

In the GEP setup, many input variables were considered, including the jet discharge condition, such as the discharge angle α, sloping bottom angle θ, Froude number Fr, and the dimensionless location along the bottom X/DF. As a result, analyzing the models' sensitivity becomes important to measure how the model responds to changes in the inputs. In this study, a 10% perturbation was applied to the input variables, following the approach proposed by Bahreini and Mohammadian (Eq.(*6.18*) (Bahreini Toussi, Mohammadian et al. 2021).

As an example, let us consider the model calculation of terminal rise height (Y_t):

$$\alpha_{\mathrm{new}} = 1.1 * \alpha_{\mathrm{old}}$$

$$\Delta \mathrm{Y_t} = \frac{|\mathrm{Yt_{new}} - \mathrm{Yt_{old}}|}{\mathrm{Yt_{old}}} \qquad (6.18)$$

$$Sensitivity = \frac{\Delta S}{0.1}$$

By increasing the discharge angle by 10% (ranging from 30º to 60º) to obtain the new discharge angle α_{new} and then applied to the different models, the updated terminal rise height Yt_{new} can be calculated, the difference ΔY_t between the new and old values can be obtained, and the sensitivity of each variable can be determined using (Eq.(*6.18*). The results of the sensitivity analysis are summarized in Table 6.4.

Table 6.4 Sensitivity to each variable in different models

Variables in GEP	GEP model (Tail mark -1 means one gene, -3 means three genes)															
	Xt-1	Xt-3	Yt-1	Yt-3	Xr-1	Xr-3	Xi-1	Xi-3	Sm-1	Sm-3	Sr-1	Sr-3	Si-1	Si-3	Sb-1	Sb-3
α	99.3%	99.4%	97.2%	11%	100%	96.5%	74.2%	92.2%	100%	99.5%	100%	91.5%	39.2%	35.4%	61.1%	66.3%
θ	0.7%	0.6%	0.28%	89.0%	0%	3.5%	25.8%	7.8%		0.5%		8.5%	60.8%	64.6%	0	8%
X/DFr	-	-	-	-	-	-	-	-	-	-	-	--	-	-	38.8%	25.3%

It noted that the discharge angle (α) had the highest impact on all models in terms of predicting the geometrical and dilution information prediction, except the model Yt-3 (multiple-gene model for predicting the terminal rise height). The result from Yt-3 showed that the most significant impact is produced by a sloping bottom angle (θ) with 89% sensitivity, but this is not consistent with the physical understanding since the terminal rise height is independent of the slope of the bottom, despite this multiple-model (Yt-3) showed good performance in terms of error indicators. However, the single-gene model Yt-1 showed more reasonable results. For the geometrical information model at the horizontal location of terminal rise height (Xt-1 and Xt-3), the horizontal location of return point (Xr-1 and Xr-3), dilution models at centerline peak (Sm-1 and Sm-3) and return point dilution (Sr-1 and Sr-3) were all reasonable, they all had the higher sensitivity on the discharge angle(α). Only the information at the impact point, such as horizontal location (Xi) and dilution (Si), would be affected by the bottom angle (θ). The results were all reasonable. For the model predicting the dilution variation along the bottom(Sb-3 and Sb-1), the multiple-gene model had a better result than the single-gene model Sb-1, it is evident that the dilution on the bottom (S_b) is affected by the discharge angle (α), sloping bottom(θ), and dimensionless location along the bottom $X/DF,$ which also aligns with the expected behaviour. But the Sb-1 model with the 0% sensitivity of the sloped angle (θ) showed the unrealistic result. The reason for the poor results of the Yt-3 and Sb-1 might be related to the selection of the linking function; therefore, more research and adjustments are needed.

6.4.3 Uncertainty bands

The uncertainty interval can be calculated using the Wilson score technique (Wilson 1927) with the mean prediction error $\bar{e}$ (*(6.19)*) and standard deviation S_e (*(6.20)*) .The prediction error was calculated by $e_i = P_i, -O_i$.Overestimation and underestimation are indicated by positive and negative values, respectively. The 95% uncertainty band was calculated from $\pm 1.98S_e$. The results for the testing dataset were shown in Table 6.5.

$$\bar{e} = \frac{\sum_{i=1}^{n} e_i}{n} \tag{6.19}$$

$$S_e = \sqrt{\frac{\sum_{i=1}^{n} (e_i - \bar{e})^2}{n-1}} \tag{6.20}$$

Table 6.5 Uncertainty band width and 95% prediction error intervals

Model	Mean prediction error (Bias)	95% uncertainty band (1.98S_e)	95% prediction error intervals
Xt-1	-0.008	± 0.109	$(-0.117\ 0.102)$
Xt-3	0.011	± 0.062	$(-0.051\ 0.073)$
Yt-1	-0.020	± 0.116	$(-0.136\ 0.097)$
Yt-3	0.002	± 0.142	$(-0.139\ 0.144)$

Xr-1	−0.025	±0.561	(−0.586 0.536)
Xr-3	−0.075	±0.498	(−0.573 0.424)
Xi-1	−0.004	±0.590	(−0.594 0.586)
Xi-3	0.009	±0.401	(−0.392 0.410)
Sm-1	−0.004	±0.044	(−0.047 0.040)
Sm-3	−0.007	±0.046	(−0.053 0.039)
Sr-1	0.037	±0.227	(−0.190 0.264)
Sr-3	0.039	±0.216	(−0.177 0.256)
Si-1	0.03	±0.146	(−0.161 0.176)
Si-3	0.013	±0.149	(−0.136 0.162)
Sb-1	0.075	±1.466	(−1.390 1.541)
Sb-3	0.013	±0.950	(−0.938 0.963)

A smaller uncertainty band generally indicates that the model's prediction results have higher accuracy and reliability. Compared to the multiple-gene and single-gene results, the uncertainty band of the multiple-gene model for terminal rise height (Yt-3) was 22% higher than the single-gene model (Yt-1). Similarly, the multiple-gene model for Sm-3 and Si-3 were slightly higher than the single-gene model (Sm-1, Si-1). The percentages are 4.5% and 2%, respectively. However, the multiple genes showed a lower value for all the other models (Xt, Xr, Xi, Sr, Sb).

Figure 6.7 presents the 95% confidence region and 95% prediction band for each model. They are the indicators to describe the accuracy and stability of the model. The confidence region and prediction band of multiple-gene models were narrower than those of the single-gene model. It implied that the multiple-genes model was more accurate than the single-gene model on the corresponding data set and more reliable on new data.

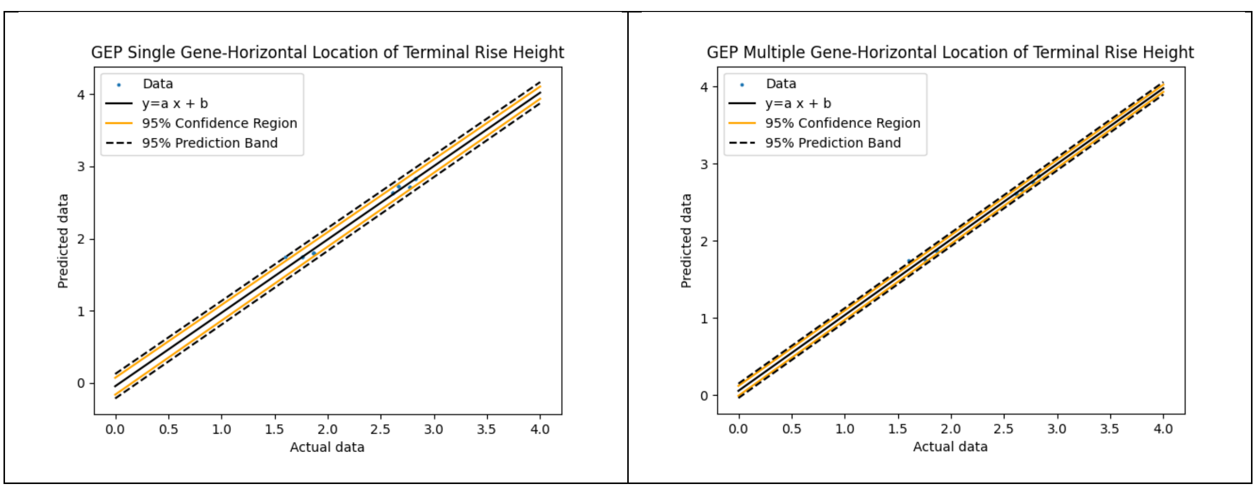

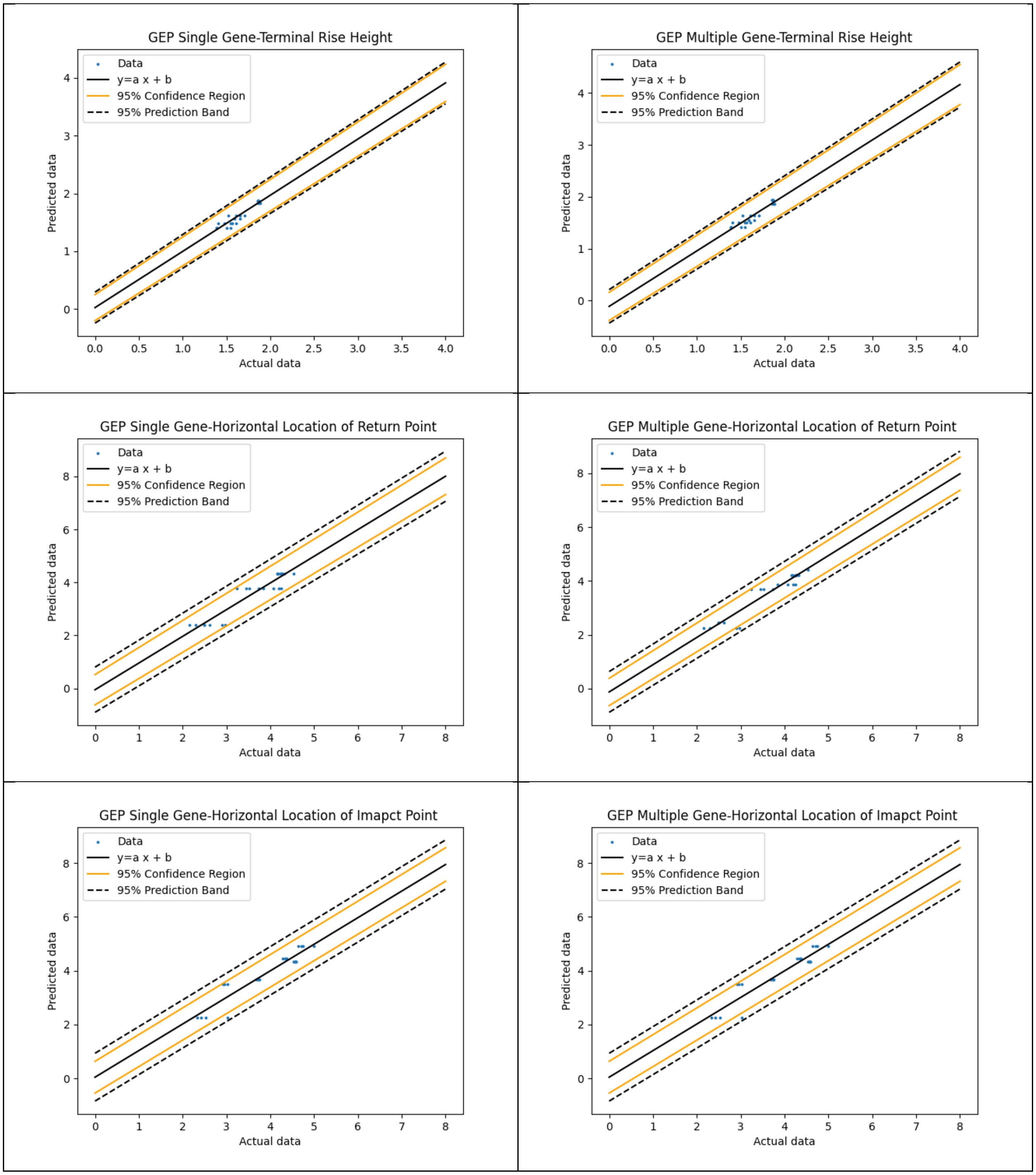
GEP Single Gene-Terminal Rise Height
Data
y=a x + b
95% Confidence Region
95% Prediction Band
Predicted data
Actual data
GEP Multiple Gene-Terminal Rise Height
Data
y=a x + b
95% Confidence Region
95% Prediction Band
Predicted data
Actual data
GEP Single Gene-Horizontal Location of Return Point
Data
y=a x + b
95% Confidence Region
95% Prediction Band
Predicted data
Actual data
GEP Multiple Gene-Horizontal Location of Return Point
Data
y=a x + b
95% Confidence Region
95% Prediction Band
Predicted data
Actual data
GEP Single Gene-Horizontal Location of Imapct Point
Data
y=a x + b
95% Confidence Region
95% Prediction Band
Predicted data
Actual data
GEP Multiple Gene-Horizontal Location of Imapct Point
Data
y=a x + b
95% Confidence Region
95% Prediction Band
Predicted data
Actual data

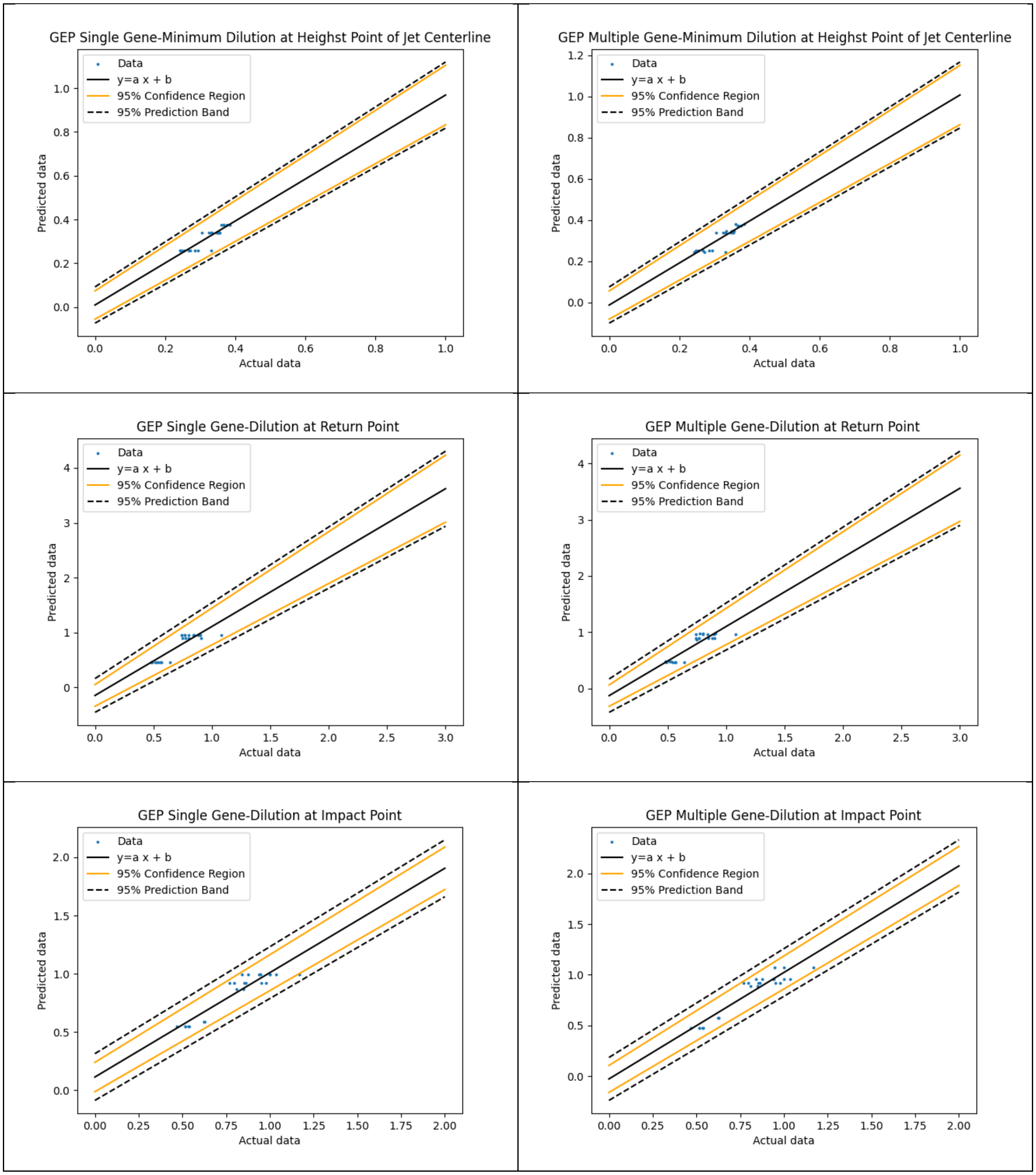
GEP Single Gene-Minimum Dilution at Heighst Point of Jet Centerline
GEP Multiple Gene-Minimum Dilution at Heighst Point of Jet Centerline
GEP Single Gene-Dilution at Return Point
GEP Multiple Gene-Dilution at Return Point
GEP Single Gene-Dilution at Impact Point
GEP Multiple Gene-Dilution at Impact Point
Data
y=a x + b
95% Confidence Region
95% Prediction Band
Predicted data
Actual data

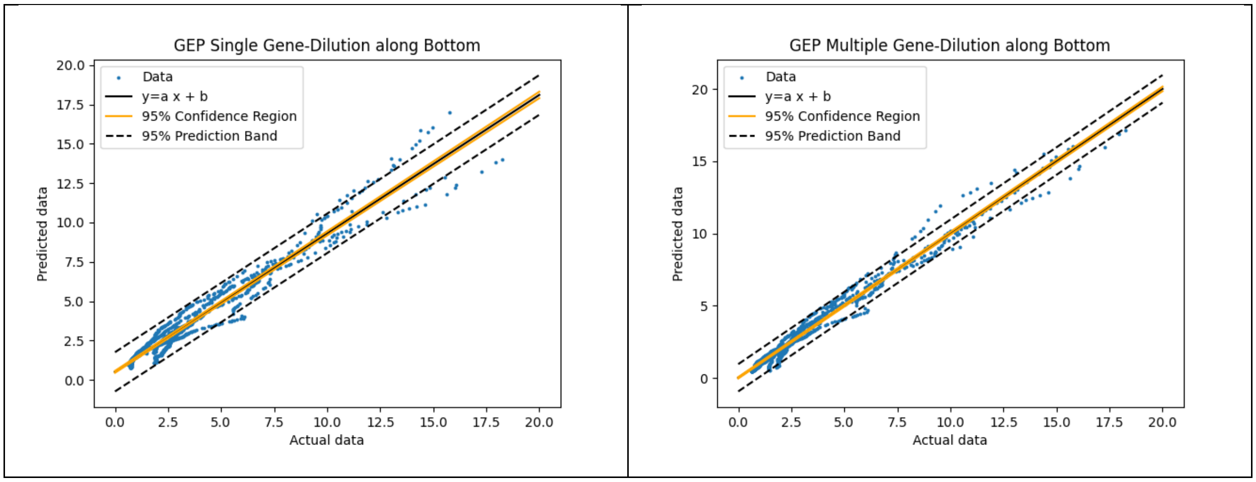

Figure 6.7 95% confidence region and 95% prediction band for each GEP model

6.4.4 Comparison with previous study

In this section, the performance of the GEP model was evaluated using the dataset from a previous study (Lai and Lee, 2012; Roberts et al., 1997; Zhang et al., 2016). The results were presented in Table 6.6. From the previous analysis, the multiple-gene model had the better performance, as a result, here only the multiple-gene models were applied. The results showed that the GEP model can predict the important information of the inclined dense jet for both geometrical and mixing properties.

Table 6.6 Comparison of experimental data and predictions by GEP

Previous research	discharge condition (input)			Actual results							Calculated by GEP model						
	$\alpha°$	$\theta°$	Fr	Xt	Yt	Xr	Xi	Sm	Sr	Si	Xt	Yt	Xr	Xi	Sm	Sr	Si
Roberts, Ferrier et al. (1997)	60	0	18.7		2.2	-	2.4	-	-	1.6	2.23	1.95	2.26	2.31	0.38	0.96	0.89
Lai and Lee (2012)	30	0	18.1	1.95	0.95	3.18	-	0.4	-	0.82	2.22	1.51	4.23	4.25	0.25	0.48	0.47
	38	0	18.1	1.95	1.2	3.19		0.45			0.96	1.53	2.38	4.28	0.27	0.76	1.23
	45	0	19.8	2.09	1.58	3.34	-	0.45	-	1.09	1.43	1.63	3.68	3.93	0.35	0.97	0.96
	52	0	18.5	1.87	1.69	2.87		0.47			2.5	1.92	4.02	3.08	0.33	1.02	0.78
	60	0	18.5	1.78	2.08	2.84	-	0.44	-	1.07	2.19	1.95	2.26	2.27	0.38	0.96	0.89

LES (Zhang, Jiang et al. (2016)	45	0	40	1.97	1.35	3.32	3.78	0.32	1	0.82	1.66	1.55	3.68	5.07	0.4	1.04	0.96
	60	0	40	1.75	2	2.86	2.67	0.35	1.29	1.1	2.21	1.86	2.26	4	0.46	1.08	0.89

6.5 Conclusion

To predict the properties of an inclined dense jet, we developed gene expression programming (GEP) models based on the results of the LES model to obtain the mathematical equations for calculating the important characteristics of the jet. These characteristics include the location of terminal rise height Xt and Yt, return point Xr, impact point Xi, minimum dilution at the centerline peak Sm, dilution at the return point (Sr) and impact point (Si). The input of the GEP has selected some important properties related to the initial discharge condition, including the discharge angle (α) and Froude number (Fr). Additionally, to investigate the influence of different bottom surfaces on jet mixing, we also considered the slope angle (θ) in the models and examined the concentration variations along the bottom (Sb). In order to assess the impact of gene number on the GEP result, GEP models were implemented using both single-gene and multiple-gene (3 genes). The GEP setup was adjusted and determined based on the trial-and-error method. In total, 16 models were generated to be used for the analysis of the results.

In analyzing the GEP model performance, in addition to the common error indicators, which included coefficient (R), mean squared error (MSE), root mean squared error (RMSE), mean absolute error (MAE), mean absolute deviation (MAD), mean absolute relative error (MARE), relative absolute error (RAE), relative squared error (RSE)root relative squared error (RRSE). The sensitivity and uncertainty analyses were also taken into consideration. The results show the sufficient capability of the GEP model in predicting the critical jet properties such as terminal rise height, return point, and impact point. All the geometrical and dilution information of the jet characteristic is very sensitive to the jet discharge angle (α). The properties of the jet at the impact point (Xi and Si) and the dilution information on the bottom (Sb) after the impact point were impacted by the sloped bottom (θ). While the multiple-gene models generally have better performance than the single-gene models, it is important to note that some multiple-gene models exhibited different results in the sensitivity analysis. Further adjustments on the gene setup are needed to improve the GEP models in terms of sensitivity performance. The results from the GEP model with previous studies as input data highlighted the GEP's potential as a reliable tool for analyzing and predicting jet parameters.

In future research, the application of GEP can be optimized through two aspects. Firstly, collecting more data and aspects from numerical simulation or experimental results, even the real case related to inclined dense jets or the desalination outfall system, such as the discharge angle, nozzle diameter, number of discharge ports, a more comprehensive range of Froude numbers, different angles of sloping bottoms, and hydraulic conditions of the receiving water body (e.g. stagnant water or crossing flow). Secondly, due to the high flexibility of GEP, adjustments and testing of gene process parameters should be carefully and comprehensively conducted to improve the accuracy and reliability of the GEP result. These adjustments could include the optimal number of genes, mathematical equations combination in each gene, the chromosome structures (number of chromosomes, head size, and gene number), and fitness functions. By considering these factors, the GEP model can be trained more effectively, leading to a more accurate and efficient model for predicting the characteristics of inclined dense jets under different environmental conditions.

Chapter 7 A Comparison of $k - \varepsilon$ - type Turbulence Models for Prediction of Inclined Dense Jets

Xinyun Wang[1]* and Abdolmajid Mohammadian[1]

[1] Department of Civil Engineering, University of Ottawa, 161 Louis Pasteur Private, Ottawa, ON K1N 6N5, Canada

Abstract

As a class of turbulence models in RANS schemes, k–ε turbulence models are widely used in simulations for engineering applications due to their computational efficiency and adequate accuracy. This study aims to investigate and evaluate the performance of four commonly used k–ε models - the standard k–ε model, the realizable k–ε model, the Renormalization Group (RNG) k–ε model, and the $q - \zeta$ (q-zeta) model–on the simulation of an inclined dense jet in a stagnant water environment. The important geometrical and dilution characteristics of inclined dense jets, such as terminal rise height, location of centerline peak, horizontal location of return point/impact point, and dilution at these points, were measured and analyzed. The mixing information was also investigated through the cross-section and axial direction of the jet. When comparing the results of these models with those of previous experimental studies, the four turbulence models were analyzed in terms of their ability to simulate the mixing characteristics of inclined dense jets. They showed good performance when the discharge angle was smaller than 60°. The $q - \zeta$ model and the realizable k–ε model show more accurate results than the other two models.

Keywords: k-ε; turbulence models; inclined dense jet; OpenFOAM

7.1 Introduction

In recent decades, due to the constantly increasing population and limited supply of freshwater resources, an increasing number of people and countries have been using desalination plants for daily consumption, significantly reducing water stress (Jones et al. 2019).

The desalination process produces extremely concentrated salty water, which can harm the marine environment if improperly discharged. An inclined dense jet at the outfalls is a common method for mixing brine (highly concentrated water after desalination) to reduce impact. Figure 1 shows a typical inclined dense jet diagram. Highly concentrated brine is discharged as a turbulent flow through a submerged pipeline attached to a circular nozzle system at a certain inclination angle. When the brine jet reached the highest point, it fell back to the bottom and continued to move. The design of these important properties relates to the discharge and mixing, discharge angle, discharge velocity, temperature, and salinity of the brine. This requires the design engineer to understand the important properties related to the discharge and mixing performance, for which the geometrical and dilution information at specific points is important. As a result, many studies have been conducted to obtain the characteristics of inclined dense jets under stagnant water condition (Cipollina et al. 2005; Kikkert 2006; Kikkert, Davidson, and Nokes 2007; Lai and Lee 2012; Papakonstantis, Christodoulou, and Papanicolaou 2011a, 2011b; Roberts, Ferrier, and Daviero 1997; Shao and Law 2010). However, the experimental studies have some limitations. For example, particle image velocimetry (PIV) and laser-induced fluorescence (LIF) experiments are advanced methods for tracking the movement and concentration of fluid particles or flow fields. However, they require a high-precision laser and a specific laboratory environment. In addition, errors in instruments and human error can affect the accuracy of the results. In addition, it is time-consuming to adjust to different discharge conditions (temperature, concentration level, discharge angle, etc.). With the exception of physical laboratory research, with the aid of supercomputers, Computational Fluid Dynamics (CFD) has been widely applied and has contributed to engineering applications, such as the prediction of jet mixing, in recent decades.

To capture fluid motion, CFD mathematically solves the Navier-Stokes equations (Anderson and Wendt 1995). Current technology and meshing methods can provide accurate flow-field information through Direct Numerical Simulation (DNS). It can solve the smallest turbulent eddies on a sufficiently fine grid for a sufficiently long time; however, DNS is too expensive to be used in practical engineering because of its computational costs. Therefore, more efficient numerical methods are typically applied in practical engineering. Reynolds-averaged Navier-Stokes (RANS) equations are fluid dynamics models that simulate the behavior of fluid motion by time-averaging flow components (Alfonsi 2009). Among the different RANS turbulence models, the k–ε model is one of the most common models for simulating complex turbulence properties, where the k and ε equations are solved numerically. Due to its reliable results, the k-ε model is widely used in several industrial fields, such as thermodynamics, maritime navigation, and pollution management (Czaplewski, Swierczynski, and Zwolan 2021; Issakhov and Omarova 2020; Zhao et al. 2021).

The simulation of inclined dense jets using RANS has been the subject of many studies in recent decades. Vafeiadou et al. (2005) numerically simulated a 60° angled dense jet using the K-Shear Stress transport (SST) turbulence model with the ANSYS software CFX-5. They discovered that the model underestimated the geometrical information compared to the experimental results from Roberts et al. (1997). Gildeh et al. (2015) investigated the performance of five RANS turbulence models in predicting the geometrical and mixing properties of an inclined dense jet with discharge angles of 30 and 45-degree discharge angle. The results showed that the LRR and realizable k–ε models had the most accurate results compared to the experimental results (Shao and Law 2010). These studies highlighted that RANS could predict the critical characteristics of inclined dense jets. Moreover, the choice of the turbulence model can affect the RANS results.

In this study, four Reynolds-averaged Navier–Stokes (RANS) turbulence models–the standard k–ε model, realizable k–ε model, RNG k–ε model and the $q-\zeta$ (k–ε type) will are studied extensively for a wide range of parameters to predict the properties of the inclined jet in stagnant water. A wide range of predictions is obtained using different discharge angles and Froude numbers, and numerical simulations are extensively compared with experimental results to assess the ability of these turbulence models to predict inclined dense jets. These comparisons provide insights into the performance of these commonly used turbulence models in predicting the turbulent mixing properties of inclined dense jets under various conditions.

7.2 Materials and Methods

7.2.1 Dimensional analysis

A typical inclined dense jet is shown in Figure 7.1. Highly dense brine (ρ_0) is discharged with an initial velocity U_0 through a round nozzle (D) into stagnant surrounding water (ρ_a). The inclined jet discharge angle was α.

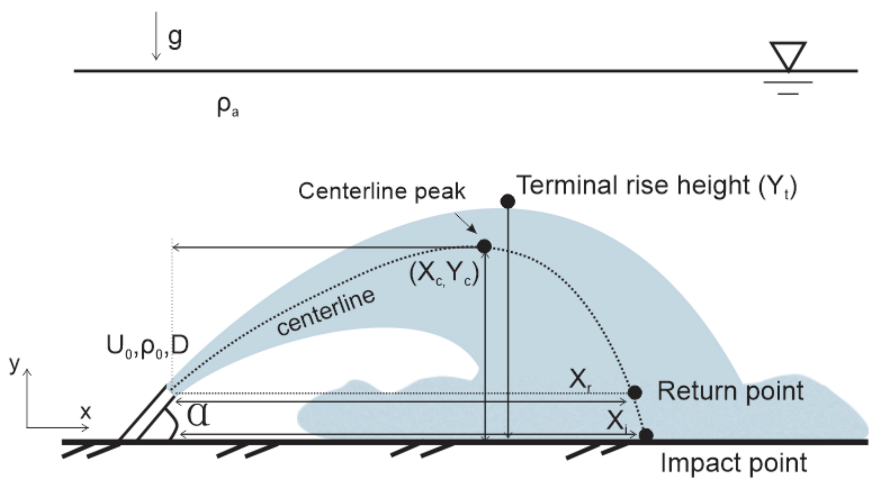

Figure 7.1 Schematic of an inclined dense jet discharged into stagnant water.

The inclined dense jet can be characterized by the fluxes of volume Q, momentum M and buoyancy B, and their equations are given by:

$$Q = \frac{\pi}{4} D^2 U_0 \tag{7.1}$$

$$M = UQ = \frac{\pi}{4} D^2 U^2 \tag{7.2}$$

$$B = \frac{\pi}{4} D^2 U_0 g_0' \tag{7.3}$$

Where $g_0' = g\frac{(\rho_0 - \rho_a)}{\rho_a}$

The two length scales can be derived from $Q, M\ and\ B$, which are L_Q and L_m. L_Q is the length at which the volume flux of the entrained ambient is equal to the initial volume flux,Q; L_m is the length at which the buoyant flux is equal to the initial momentum flux, M. These two lengths can also be expressed by the Froude number $Fr = U_0/\sqrt{g_0'}$, therefore, the two length scales can be described as

$$L_m = \frac{M^{3/4}}{B^{1/2}} = \left(\frac{\pi}{4}\right)^{\frac{1}{4}} FrD \qquad (7.4)$$

$$L_Q = \frac{Q}{M^{1/2}} = \left(\frac{\pi}{4}\right)^{\frac{1}{2}} D \qquad (7.5)$$

According to Pincince (1973) and Roberts (1997), the effect of the volume flux Q can be negligible, so only l_m length is adopted in the dimensional analysis. Hence, in an inclined dense jet, the characteristic length X can be expressed as:

$$\frac{X}{L_m} = C_1 \ or \ \frac{X}{DFr} = C_1 \qquad (7.6)$$

The scaled dilution is given by.

$$\frac{s}{Fr} = C_2 \qquad (7.7)$$

Where dilution is defined as $s = \frac{C_0 - C_a}{C - C_a}$, where C is the local time-averaged concentration.

7.2.2 Computational methodology

7.2.2.1 Governing equations

The governing equations for the Reynolds-averaged Navier-Stokes (RANS) modeling are listed below, including the continuity and momentum equations. Each flow property is separated as a mean value and the fluctuation as $u(x,t) = \bar{u}(x) + u'(x,t)$.

$$\frac{\partial \rho \bar{u}_i}{\partial i} = 0 \qquad (7.8)$$

$$\frac{\partial \bar{u}_i}{\partial t} + \frac{\partial}{\partial x_j}\left(\bar{u}_i \bar{u}_j\right) = -\frac{1}{\rho}\frac{\partial \bar{P}}{\partial x_i} + v\frac{\partial^2 \bar{u}_i}{\partial x_i x_j} - \frac{\partial \overline{u_i' u_j'}}{\partial x_j} \qquad (7.9)$$

Applied to the Boussinesq hypothesis (Schmitt 2007) on the unknown Reynolds stress tensor $\overline{u_i' u_j'}$, the RANS model can be

$$\frac{\partial u_i}{\partial t} + \frac{\partial}{\partial x_j}\left(u_i u_j\right) = -\frac{1}{\rho}\frac{\partial p}{\partial x_i} + \frac{\partial}{\partial x_j}\left[(v_t + v)\frac{\partial u_i}{\partial x_j} - \frac{2}{3}k\delta_{ij}\right] \qquad (7.10)$$

Two additional terms v_t (eddy viscosity) and k need to be determined. Several methods can be used to model the eddy viscosity (v_t). In the two-equation k–ε model, it is written as:

$$\nu_t = \frac{C_\mu k^2}{\varepsilon} \tag{7.11}$$

where k is the turbulent kinetic energy and ε is the dissipation rate. Both can be solved using the transport equations. The transport equation for the difference turbulence model is as follows. More information is available in (Anderson and Wendt 1995)

Standard $k - \varepsilon$ equation (Launder and Spalding 1983)

k equation:

$$\frac{\partial k}{\partial t} + \frac{\partial (k u_i)}{\partial x_i} = -\rho\, \overline{u_i' u_j'} \frac{\partial u_j}{\partial x_i} + \frac{\partial}{\partial x_j}\left(\left(v + \frac{v_t}{\sigma_k}\right)\frac{\partial k}{\partial x_j}\right) - \varepsilon \tag{7.12}$$

ε Equation:

$$\frac{\partial \varepsilon}{\partial t} + \frac{\partial (\varepsilon u_i)}{\partial x_i} = \frac{\partial}{\partial x_j}\left(\left(v + \frac{v_t}{\sigma_\varepsilon}\right)\frac{\partial \varepsilon}{\partial x_j}\right) + C_{\varepsilon 1}\frac{\varepsilon}{k}\left(-\rho\, \overline{u_i' u_j'} \frac{\partial u_j}{\partial x_i}\right) - C_{\varepsilon 2}\frac{\varepsilon^2}{k} \tag{7.13}$$

Where the constants are: $\sigma_\varepsilon = 1.3, \sigma_k = 1, C_{\varepsilon 1} = 1.44, C_{\varepsilon 2} = 1.92$

Realizable $k - \varepsilon$

The difference between the standard Realizable $k - \varepsilon$ equations is the Equation for ε and the constant for C_μ in Eq.11, so the ε Equation for the Realizable $k - \varepsilon$ model is given by

ε Equation：

$$\frac{\partial \varepsilon}{\partial t} + u_i\frac{\partial \varepsilon}{\partial x_i} = \frac{\partial}{\partial x_j}\left(\left(v + \frac{v_t}{\sigma_\varepsilon}\right)\frac{\partial \varepsilon}{\partial x_j}\right) + C_1 S\varepsilon - C_2\frac{\varepsilon^2}{k + \sqrt{v\varepsilon}} \tag{7.14}$$

Where the constant C_1 in Eq. 14 is

$$C_1 = \max\left\{0.43, \frac{\eta}{\eta + 5}\right\}, \eta = \frac{Sk}{\varepsilon}, S = \sqrt{2S_{ij}S_{ij}} \tag{7.15}$$

Where C_2=1.9, σ_ε=1.2.

The constant for C_μ Equation 11 is written as

$$C_\mu = \frac{1}{A_0 + A_s\frac{u^* k}{\varepsilon}} \tag{7.16}$$

Where $A_0 = 4.04, A_s = \sqrt{6}\cos\phi$

$$\phi = \frac{1}{3}\arccos\left(\sqrt{6}W\right), W = \frac{S_{ij}S_{jk}S_{ki}}{\tilde{S}^3}, \tilde{S} = \sqrt{S_{ij}S_{ij}}, S_{ij} = \frac{1}{2}\left(\frac{\partial u_i}{\partial x_j} + \frac{\partial u_j}{\partial x_i}\right), u^* = \sqrt{S_{ij}S_{ij} + \tilde{\Omega}_{ij}\tilde{\Omega}_{ij}} \tag{7.17}$$

RNG $k-\varepsilon$ (Renormalization Group)

Similar to the standard $k-\varepsilon$ model, there are two equations for the turbulence kinetic energy (k) and the rate of dissipation (ε). RNG was proposed by Yakhot and Smith (1992).

$k-$ equation:

$$\frac{\partial k}{\partial t}+\frac{\partial(ku_i)}{\partial x_i}=-\rho\,\overline{u_i'u_j'}\frac{\partial u_j}{\partial x_i}+\frac{\partial}{\partial x_j}\left(\alpha_k\mu_{eff}\frac{\partial k}{\partial x_j}\right)-\varepsilon \tag{7.18}$$

$\varepsilon-$ equation:

$$\frac{\partial\rho\varepsilon}{\partial t}+\frac{\partial(\rho\varepsilon u_i)}{\partial x_i}=\frac{\partial}{\partial x_j}\left(\alpha_\varepsilon\mu_{eff}\frac{\partial\varepsilon}{\partial x_j}\right)+C_{\varepsilon1}\frac{\varepsilon}{k}(\mu_t S^2)-C_{\varepsilon2}\rho\left(\frac{\varepsilon^2}{k}\right)-R \tag{7.19}$$

Where $\mu_{eff}=\mu+\mu_t.\ \mu_t=\rho C_\mu\frac{k^2}{\varepsilon}$, where $\rho C_\mu=0.0845, \alpha_k=\alpha_\varepsilon=1.39,\ C_{1\varepsilon}=1.42, C_{2\varepsilon}=1.6$.

$q-\zeta$ Turbulence Model

The $q-\zeta$ turbulence model, improves the model's performance near the walls, similar to the $k-\varepsilon$ model, and the two dependent variables in this two-equation turbulence model are expressed as $q=\sqrt{k}$ and $\zeta=\frac{\varepsilon}{2q}$. The eddy viscosity μ_t can be defined in terms of $\gamma_t=\frac{C_\mu f_\mu}{4}\frac{q^2}{\zeta}$, the reader can refer to (Gibson and Dafa'Alla 1995) for more model details.

q- Equation

$$u_i\frac{\partial q}{\partial x_i}=\frac{\partial}{\partial x_j}\left\{\left(v+\frac{v_t}{\sigma_q}\right)\frac{\partial q}{\partial x_j}\right\}+Q-\zeta \tag{7.20}$$

ζ- Equation

$$u_i\frac{\partial\zeta}{\partial x_i}=\frac{\partial}{\partial x_j}\left\{\left(v+\frac{v_t}{\sigma_\zeta}\right)\frac{\partial\zeta}{\partial x_j}\right\}+\frac{\zeta}{q}\left(C_{\zeta1}f_{\zeta1}Q-C_{\zeta2}f_{\zeta2}\zeta\right)+\psi'+\xi' \tag{7.21}$$

$$\psi'=\psi/2q$$

where ψ is an additional source term that represents an additional production by mean shear to achieve correct limiting behavior very close to a wall. Q is the rate of production of q

$$Q\equiv\frac{P}{2q}=\gamma_t\frac{\partial u_i}{\partial x_j}\left(\frac{\partial u_i}{\partial x_j}+\frac{\partial u_j}{\partial x_i}\right) \tag{7.22}$$

$$\gamma_t \equiv \frac{C_\mu f_\mu}{4} \frac{q^2}{\zeta} \quad (7.23)$$

The basic constants are the same as those of the standard $k - \varepsilon$ mode with additional parameters $\sigma_q = \sigma_k = 1.0$ and $\sigma_\zeta = \sigma_\varepsilon = 1.3$.

7.2.2.2 Flow Configuration and Computational Domain Setup

OpenFOAM, an open-source computational fluid dynamics (CFD) software, was used in this study. The Navier-Stokes equations were discretized using the finite volume method (FVM), and the governing equations were solved using an incompressible solver called "twoLiquidMixingFoam." This solver is specifically designed to predict the mixing of two incompressible flows and has been widely adopted in many studies due to its excellent performance and accuracy (Alvir et al. 2022; Jiang, Law, and Lai 2019; Saeidi Hosseini et al. 2022; Wang and Mohammadian 2022; Yan, Mohammadian, and Chen 2020; Zhang et al. 2016).

Figure 7.1 (a) shows the schematic of the simulated experimental tank. The dimensions of the tank were 2m×0.8m×0.8m. The mesh was generated by the *snappyHexMesh* mesh generator, which uses a mesh generation method to refine the areas as required. A smaller mesh with dimensions 1.8m×0.4m×0.6m is established as the refinement region (Figure 7.2 (b)). This refined mesh was used for simulations to better capture the velocity and concentration in the near-field zone, especially for the bottom area (Figure 7.2 (c)). A grid of 2,000,000 unstructured cells was found to be adequate for resolving the flow characteristics of the considered domain based on mesh sensitivity analysis.

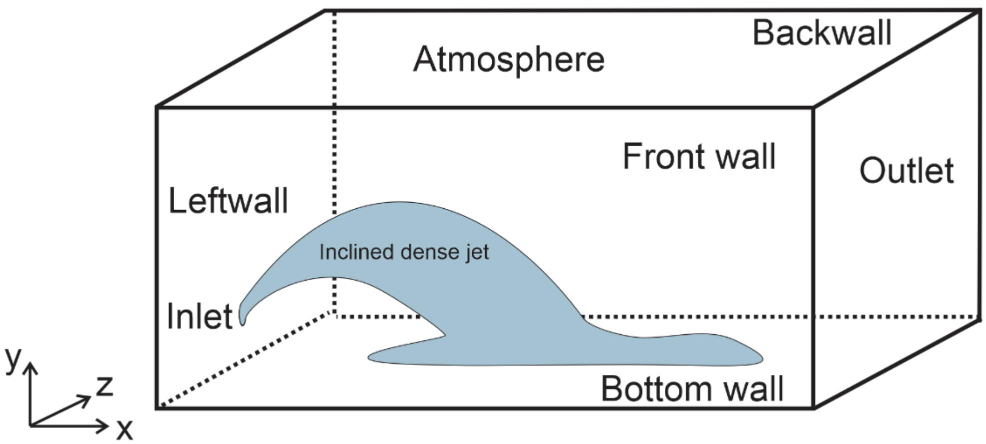

(a)

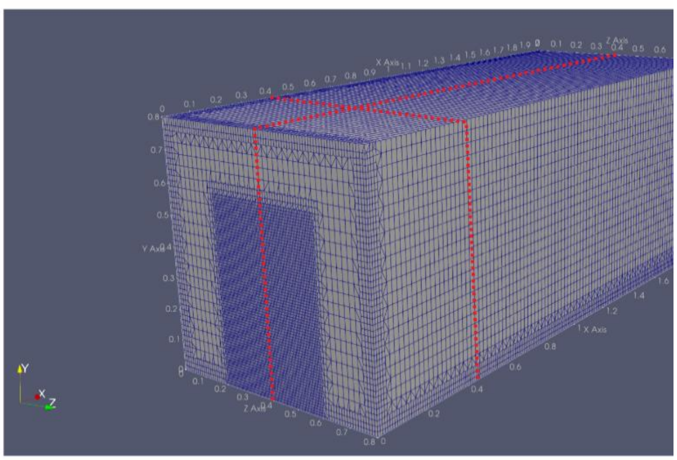

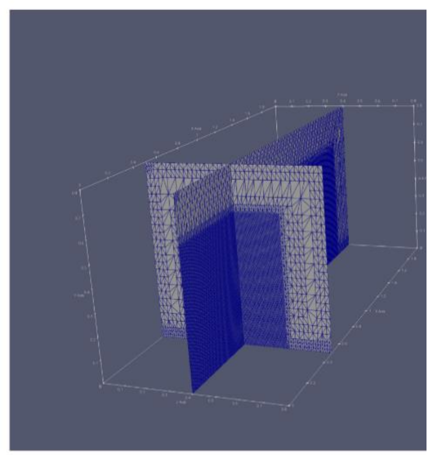

(b) (c)

Figure 7.2 Schematic figure of computational domain setup; (b) Computational domain with refined mesh; (c) example of mesh on z-y plane and x-y plane.

The diameter of the inlet nozzle (D) is $0.02m$, and the center of the nozzle tip is fixed at $0.05m$ (Y_0) with a positive inclination angle. The inlet and outlet boundary types were set as patches, the atmosphere was set as symmetrical, and the others were set as walls. A standard wall function was used. The inlet boundary conditions are $u = U_0 \times cos\ (\theta)$, $v = U_0 \times sin\ (\theta)$, $w = 0, k = 0.006u^2, and\ \varepsilon = 0.06u^3/D$, where U_0 is the velocity of the jet discharge, $u, v,$ and w are the velocities for the $x, y,$ and z-axes, respectively. The flow rate is fixed at $U = 0.7m/s$. Simulations are carried out for four different discharge angles = $15°, 30°, 45°, 60°$ and three different Froude numbers (10.6, 14.2, and 17.6). The flow is assumed to be incompressible, and the density for both the jet and ambient water is calculated using Equation (24) proposed by Millero and Poisson (Millero and Poisson 1981). The density of the surrounding water was set as $998.21 kg/m^3$ with at a temperature of $20°C$. The initial conditions are listed in Table 7.1.

Table 7.1 Initial conditions of the simulation

Velocity (m/s)	Froude Number	Density difference (kg/m^3)	Jet density (kg/m^3)
0.65	10.6	19.11	1017.32
0.65	14.2	10.71	1008.92
0.65	17.6	6.81	1005.02

$$\rho = \rho_t + AS + BS^{3/2} + CS \tag{7.24}$$

$$\rho_t = 999.842594 + 6.793952 \times 10^{-2}T - 9.095290 \times 10^{-3}T^2 + 1.001685 \times 10^{-4}T^3 - 1.120083 \times 10^{-6}T^4 + 6.536336 \times 10^{-9}T^5$$

$$A = 8.24493 \times 10^{-1} - 4.0899 \times 10^{-3}T + 7.6438 \times 10^{-5}T^2 - 8.2467 \times 10^{-7}T^3 + 5.3875 \times 10^{-9}T^4$$

$$B = -5.72466 \times 10^{-3} + 1.0227 \times 10^{-4}T - 1.6546 \times 10^{-6}T^2$$

$$C = 4.8314 \times 10^{-4}$$

ρ_t is the density of water, which varies with the temperature as follows:

$$\rho_t = 999.842594 + 6.793952 \times 10^{-2}T - 9.095290 \times 10^{-3}T^2 + 1.001685 \times 10^{-4}T^3 - 1.120083 \times 10^{-6}T^4 + 6.536336 \times 10^{-9}T^5$$

7.3 Results and discussion

Forty-eight simulations are carried out with three different Froude numbers and four discharge angles ($15°, 30°, 45°, 60°$) using Realizable and standard $k-\varepsilon$ turbulence, RNG $-\varepsilon$ and $q-\zeta$ models.

7.3.1 Mesh quality and independent analysis

The mesh was generated using snappyHexMesh with a refining box area to accurately capture the flow characteristics of the jet. It is important to note that mesh quality greatly affects the results and accuracy of the CFD simulation. Although a finer and smaller mesh can yield more precise simulation results, it comes at the cost of increased computational resources and significant time consumption. Therefore, it is crucial to achieve a balance and choose an appropriate mesh size within the computational domain to obtain efficiency and reasonable accuracy. In this study, mesh test runs were conducted using a moderate mesh (2 million cells) and a fine mesh (4 million cells) for a specific case involving a 45° discharge angle and a Froude number of 17.6. Standard k-epsilon models were employed in these simulations. Some of the important details of the two generated meshes are presented in Table 7.2. The concentration values at two locations ($x = 5D$ and $x = 10D$) were plotted against the vertical line for both meshes, as shown in Figure 7.3. The results indicate that the fine mesh did not significantly improve the results. Consequently, only a moderate mesh was adopted for all subsequent simulations in this study.

Table 7.2 Mesh quality information

Mesh	Num. of Cells	Max aspect ratio	Max skewness	Min volume	Max volume	Mesh non-orthogonality
Moderate mesh	2,131,224	5.39	0.68	1.25e-07	0.00012	Average: 3.9 Max: 56.2
Fine mesh	4,269,931	6.91	0.466	5.10e-09	0.00012	Average: 4.3 Max: 45.7

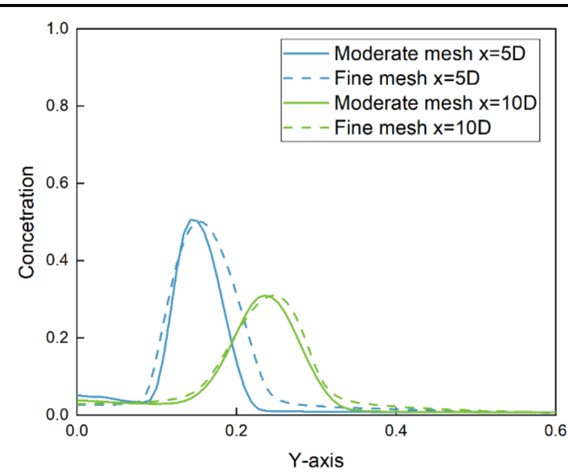

Figure 7.3 The concentration comparison between two meshes.

7.3.2 Geometrical and dilution information

Understanding the geometrical characteristics of inclined dense jets is critical for the design of effective outfalls. It aims to minimize the environmental impact and improve discharge efficiency. These geometrical characteristics include the terminal rise height and horizontal location of the return or impact point. Dimensionless analysis can provide a means of presenting the geometrical and dilution information in relation to the jet densimetric Froude number Fr and nozzle diameter D. The relevant coefficients from previous studies, including the results of this study, are summarized in Table 7.3, Table 7.4, Table 7.5 and Table 7.6. The results demonstrate that the four turbulence models effectively predict the geometrical information of inclined dense jets when the discharge angle is less than 60°. The observations indicate an under-prediction of geometrical information at a discharge angle of 60°. Nevertheless, it is worth noting that the dilution information remained within an acceptable range, thereby highlighting the ability of the turbulence model to capture relevant parameters.

Table 7.3 Comparison of geometrical and mixing coefficients (α=15°)

Quantity	Terminal rise height	Horizontal location of centerline peak	Vertical location of centerline peak	Horizontal location of return point	Horizontal location of impact point	Centerline peak dilution	Return point dilution	Impact point dilution
	Y_t/DFr	X_m/DFr	Y_m/DFr	X_r/DFr	X_i/DFr	Sm/Fr	Sr/Fr	Si/Fr
Standard $k-\varepsilon$	0.43	1.11	0.17	1.83	2.42	0.22	0.38	0.46
Realizable $k-\varepsilon$	0.43	1.20	0.18	1.92	2.51	0.21	0.38	0.31
RNG $k-\varepsilon$	0.45	1.05	0.18	1.78	2.33	0.22	0.45	0.52
q-zeta	0.5	1.50	0.17	1.93	2.41	0.21	0.38	0.46
Lai and Lee (2012)-Exp	0.44	1.22	0.21	2.41		0.27		0.43

Lai and Lee (2012)-VISJET	0.44	1.19	0.21	2.15		0.24	0.41
Kikkert (2006) (LIF/LA)	0.52/0.52	1.47/1.22	0.21/0.21	2.53/2.13			

Table 7.4 Comparison of geometrical and mixing coefficients (α=30°)

Quantity	Terminal rise height Y_t/DFr	Horizontal location of centerline peak X_m/DFr	Vertical location of centerline peak Y_m/DFr	Horizontal location of return point X_r/DFr	Horizontal location of impact point X_i/DFr	Centerline peak dilution Sm/Fr	Return point dilution Sr/Fr	Impact point dilution Si/Fr
Standard $k-\varepsilon$	0.76	1.39	0.47	2.36	2.80	0.29	0.57	0.62
Realizable $k-\varepsilon$	0.82	1.47	0.51	2.47	2.82	0.31	0.59	0.63
RNG $k-\varepsilon$	0.80	1.2	0.48	2.28	2.55	0.30	0.66	0.70
q-zeta	0.83	1.61	0.54	2.61	2.84	0.26	0.58	0.66
Lai and Lee (2012)-Exp	0.95					0.40		0.82
Lai and Lee (2012)-VISJET	0.86					0.31		0.64
Shao and Law (2010) (Shao and Law 2010)	1.05	1.70	0.66	2.88/3.0		0.62/0.66	1.18/1.45	
Kikkert (2007) (LIF/LA)	1.19/1.00	1.85/1.75	0.66/0.56	3.44/3.14				
Cipollina et al. (2005)	1.08	1.95	0.79	3.03				

Table 7.5 Comparison of geometrical and mixing coefficients (α=45°)

Quantity	Terminal rise height Y_t/DFr	Horizontal location of centerline peak X_m/DFr	Vertical location of centerline peak Y_m/DFr	Horizontal location of return point X_r/DFr	Horizontal location of impact point X_i/DFr	Centerline peak dilution Sm/Fr	Return point dilution Sr/Fr	Impact point dilution Si/Fr
Standard $k-\varepsilon$	1.30	1.32	1.1	2.4	2.65	0.35	0.70	0.75
Realizable $k-\varepsilon$	1.35	1.33	1.05	2.3	2.7	0.34	0.71	0.76
RNG $k-\varepsilon$	1.36	1.25	1.05	2.08	2.26	0.37	0.75	0.79
q-zeta	1.46	1.51	1.11	2.53	2.7	0.4	0.76	0.82
Lai and Lee (2012)-Exp	1.58	2.09	1.19	3.34		0.45		1.09
Lai and Lee (2012)-VISJET	1.33	1.58	1.00	2.78		0.32		0.77
Shao and Law (2010)	1.47	1.69	1.14	2.83		0.46	1.26	
Kikkert (2007)	1.60	1.84	1.06	3.26				
Papakonstantis (2011a, 2011b)	1.59		1.17	3.16		0.52		1.55
Cipollina et al. (2005)	1.61	1.80	1.17	2.82				

Table 7.6 Comparison of geometrical and mixing coefficients (α=60°)

Quantity	Terminal rise height	Horizontal location of centerline peak	Vertical location of centerline peak	Horizontal location of return point	Horizontal location of impact point	Centerline peak dilution	Return point dilution	Impact point dilution
	Y_t/DFr	X_m/DFr	Y_m/DFr	X_r/DFr	X_i/DFr	Sm/Fr	Sr/Fr	Si/Fr
Standard $k-\varepsilon$	1.53	0.9	1.3	1.62	1.80	0.36	0.76	0.88
Realizable $k-\varepsilon$	1.55	0.82	0.95	1.5	1.62	0.36	0.75	0.81
RNG $k-\varepsilon$	1.46	0.74	1.2	1.42	1.53	0.36	0.84	0.88
q-zeta	1.63	0.93	1.35	1.75	1.88	0.35	0.87	0.91
Lai and Lee (2012)-Exp	2.08	1.78	1.64	2.84		0.44		1.07
Lai and Lee (2012)-VISJET	1.78	1.34	1.42	2.40		0.29		0.83
Papakonstantis (2011a, 2011b)	2.15		1.68	2.75		0.56		1.68

7.3.2.1 Terminal rise height

Similar to vertical jets, inclined dense jets rise to a point where the vertical component of the initial momentum drops to zero, after which the jet falls back to the bottom due to gravity (Chen and Rodi 1980). The highest point is called the terminal rise height, which in our study is defined as Y_t based on the coordinate system setting. This geometric information is crucial for designing outfalls because it can help prevent the brine jet from touching the water surface. Two approaches can be employed to determine the terminal rise height. According to Jirka (2004), the visual boundary of turbulent buoyant jets can be defined as the $0.25C_{max}$ of the concentration centerline value based on the analysis of the experimental intermittency distribution (Chu 1996; Chu, Lee, and Chu 1999). Another method involves estimating the terminal rise height from the $3\%C_0$ cutoff of the center plate concentration data (Shao and Law 2010). Both methods were tested, and the differences between them were found to be negligible. Therefore, the results obtained using the $3\%\ C_0$ cutoff method will be presented in this study for brevity. Figure 7.4 illustrates the normalized terminal rise height (Y_t/DFr) plotted against the discharge angle, and a comparison was made with previous experimental studies (Bashitialshaaer, Larson, and Persson 2012; Bloomfield and Kerr 2002; Kikkert et al. 2007; Lai and Lee 2012; Shao and Law 2010; Zeitoun and McIlhenny 1971). The results show good agreement and demonstrate the reliability of the four turbulence models.

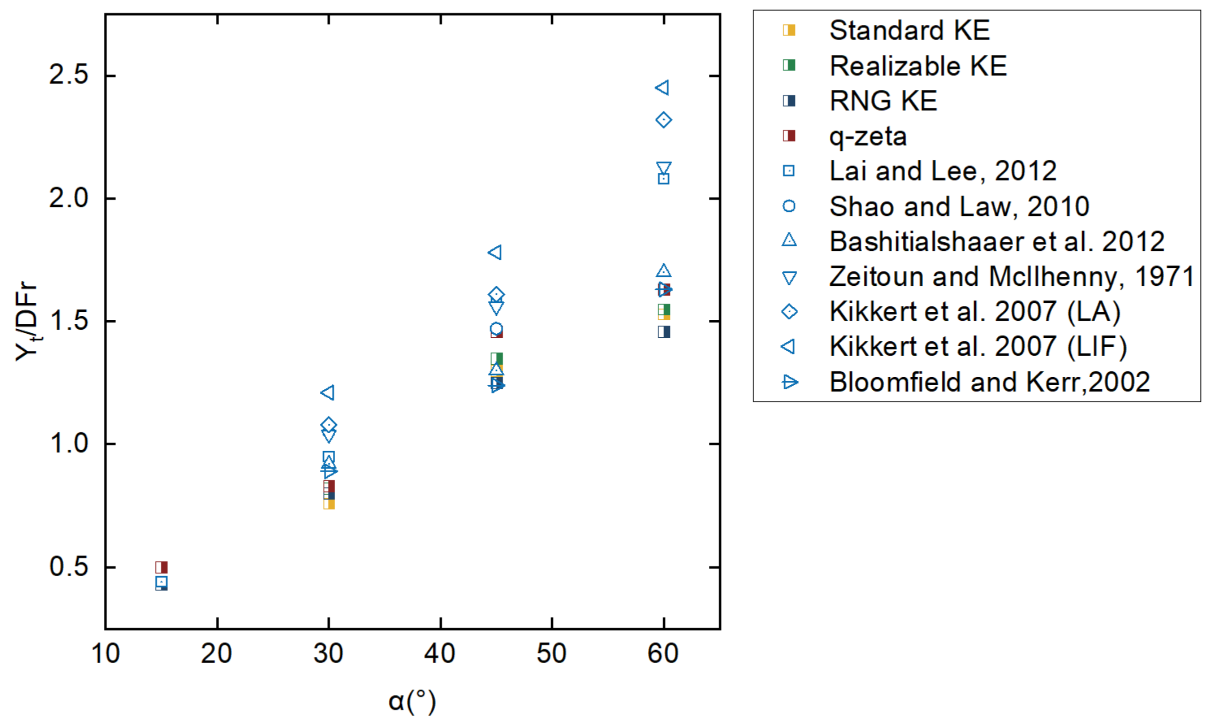

Figure 7.4 Normalized terminal rise height plotted against discharge angle.

7.3.2.2 The location of the jet centerline peak

The centerline peak can be determined from a previously established centerline trajectory. The horizontal and vertical locations of the centerline peak, denoted by X_c and Y_c, respectively, were normalized and plotted against the discharge angle (α), as shown in Figure 7.5. The results were compared with those of previous studies. The results are in good agreement with those of a previous study. However, at a discharge angle of 60°, the predicted horizontal location of the centerline peak (X_c) was slightly under-predicted in the experimental study, and a similar pattern can be observed in the vertical location of the centerline peak Y_c at a 60-degree angle. The $q - \zeta$ model showed the best agreement among the four models.

To investigate the influence of the Froude number, the horizontal location of the centerline peak was normalized with the nozzle diameter and plotted against the Froude number, as shown in Figure 7.6. The comparison was only carried out for the 30 ° and 45 ° discharge angles because of the comparable previous results (Cipollina et al. 2005; Kikkert 2006; Shao and Law 2010). The results show that the normalized X_c and Y_c exhibit an increasing linear relationship with the Froude number within a certain range. The results from $q - \zeta$ have the best agreement among the four turbulence models.

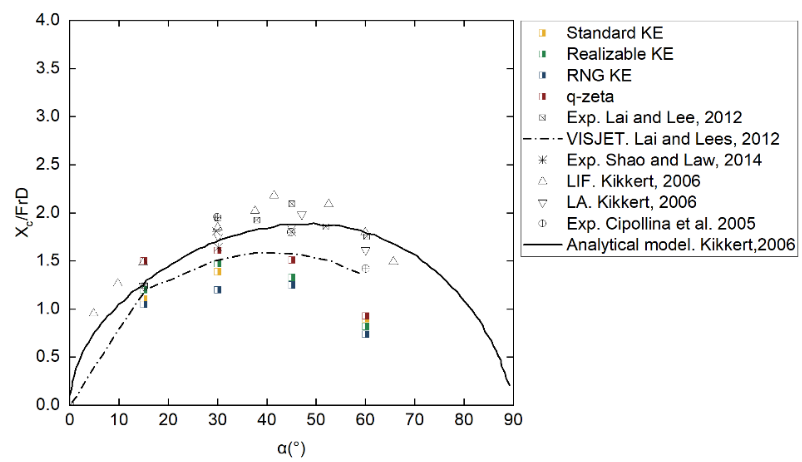

(a)

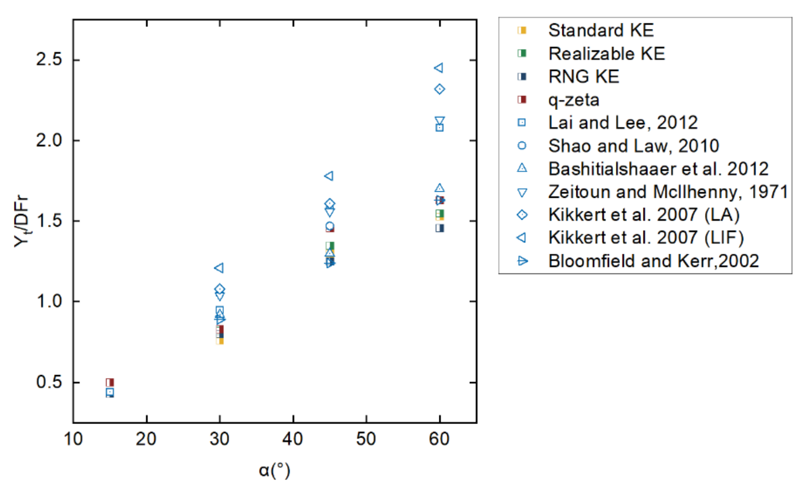

(b)

Figure 7.5 Normalized centerline peak: (a) horizontal location; (b) vertical location $\boldsymbol{Y_c}$ *as a function of discharge angle.*

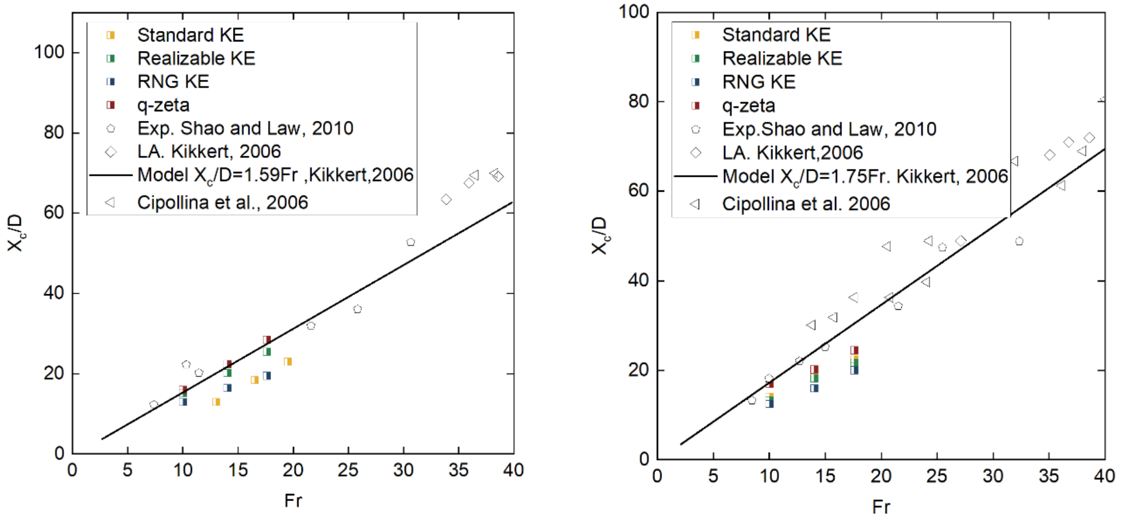

(a) (b)

Figure 7.6 Normalized horizontal location (Xc) of centerline peak versus Froude number: (a) discharge angle 30°; (b) discharge angle 45°

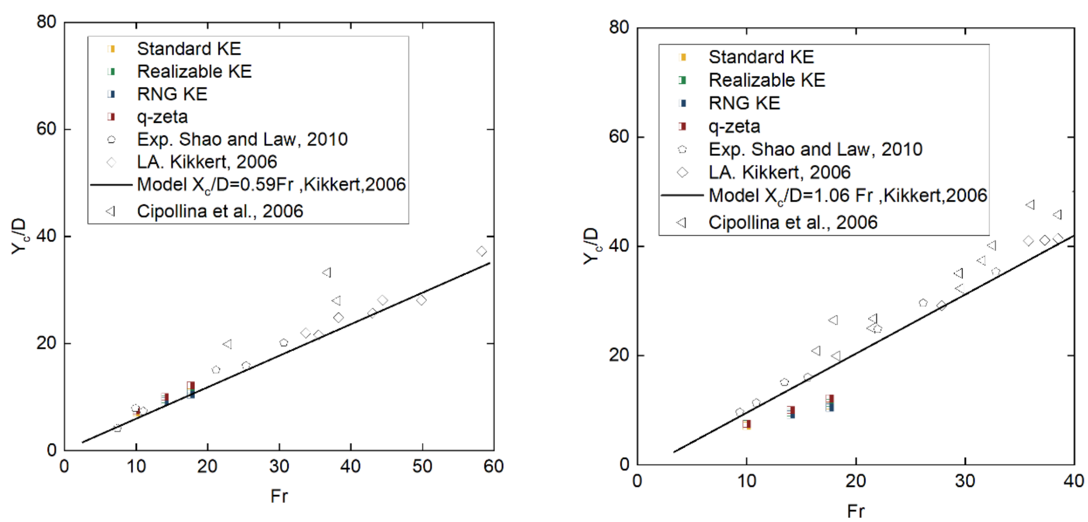

(a) (b)

Figure 7.7 Normalized vertical location (Yc) of centerline peak versus Froude number: (a) discharge angle 30°; (b) discharge angle 45°

7.3.2.3 The location of the return point

Under negative buoyancy and gravity, the inclined dense jet returns to the receiving bottom. During this process, two points gained the attention of researchers: the return point and the impact point. Typically, the return point (X_r) is where the flow returns to the discharge source height (Y_0) (Figure 7.1), whereas the location where the flow impinges on the boundary is called the impact point or impingement point (X_i). Although these two points are similar from a jet geometrical perspective, the impact point highly depends on other factors, such as the discharge height or the bottom condition. One common conclusion that can be agreed upon is that the mixing of the jet is reduced due to the presence of the bottom (Shao and Law 2010). More information can be found in (Oliver, Davidson, and Nokes 2013; Wang and Mohammadian 2022:15). In this study, the locations of both the points were analyzed.

The return point was derived from the highest concentration in the horizontal slices at the discharge elevation ($Y_0 = 0.05m$). The concentration results are plotted along the X-axis in Figure 7.8. The highest value in the concentration profile (Figure 8b) indicates the location of the return point.

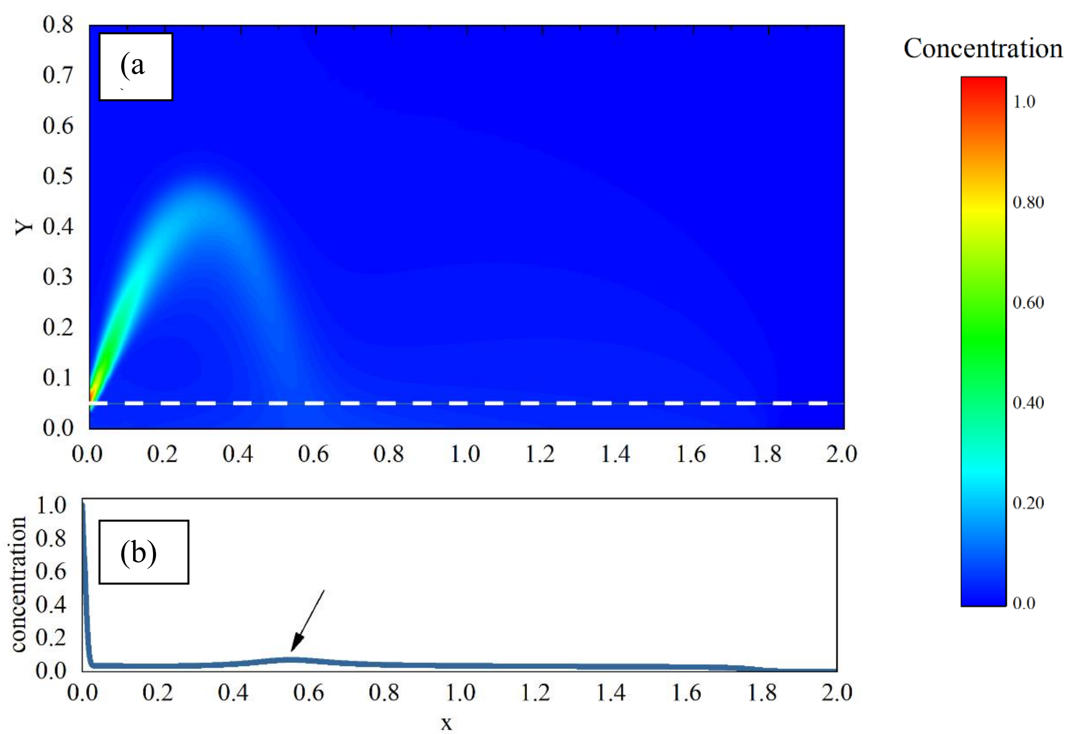

Figure 7.8 Schematic diagrams of the concentration: (a) Concentration contours; (b) variation on the horizontal slice shown by a white dashed line at the source elevation. The arrow points to the return point.

The return point was collected, normalized, and plotted against the discharge angle, as shown in Figure 7.9. It can be observed that the X_r/DFr can be represented as a function of the discharge angle, and the result is slightly underpredicted in previous experimental studies. This is because in the previous experimental study, the return point was always substituted with the impact point. The return point was derived from the trajectory of the experimental study. However, during actual experimental investigations, it is challenging to determine the exact location of the return point (Shao and Law 2010). The impact point can be determined by the variation in concentration along the lower boundary of the horizontal bottom (Roberts et al. 1997). Consequently, the locations of the impact points (X_i) were also collected along the bottom from the four turbulence models for comparison. They are normalized and plotted against the Froude number shown in Figure 7.10. It can be seen that all the results are in good agreement with the experimental study on the prediction at the impact point. The 45 °and 60 °angles show a slight underprediction. A similar pattern was observed by Zhang (2017). In their study, for the simulation of a 45 ° discharge angle, the RANS model had an under-predicted trend. This limitation can be overcome by employing large-eddy simulation (LES). However, given the higher computational demands and time constraints associated with LES, RANS models remain indispensable for engineering applications. To enhance the numerical modeling capabilities of RANS models, further detailed studies are still needed, particularly for inclined dense jets at large discharge angles ($\geq 45°$). Among these four turbulence models, the RNG model exhibited the least accurate results compared to the other three models, and the $q - \zeta$ model had the best performance. The difference between the standard $k - \varepsilon$ and realizable $k - \varepsilon$ results was insignificant.

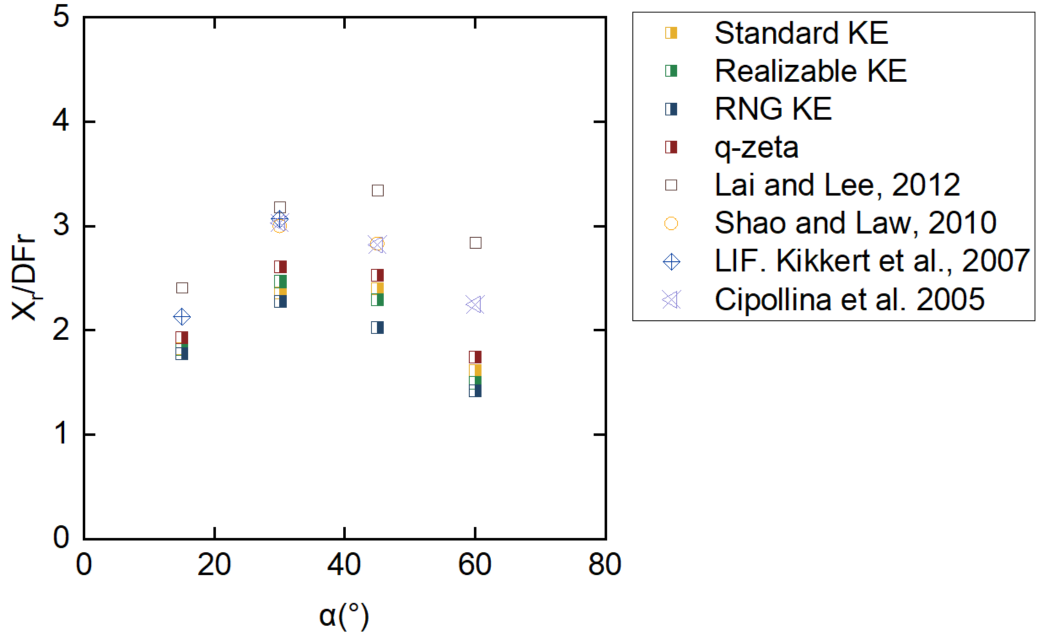

Figure 7.9 Normalized location of the return point (Xr/DFr) plotted against the discharge angle.

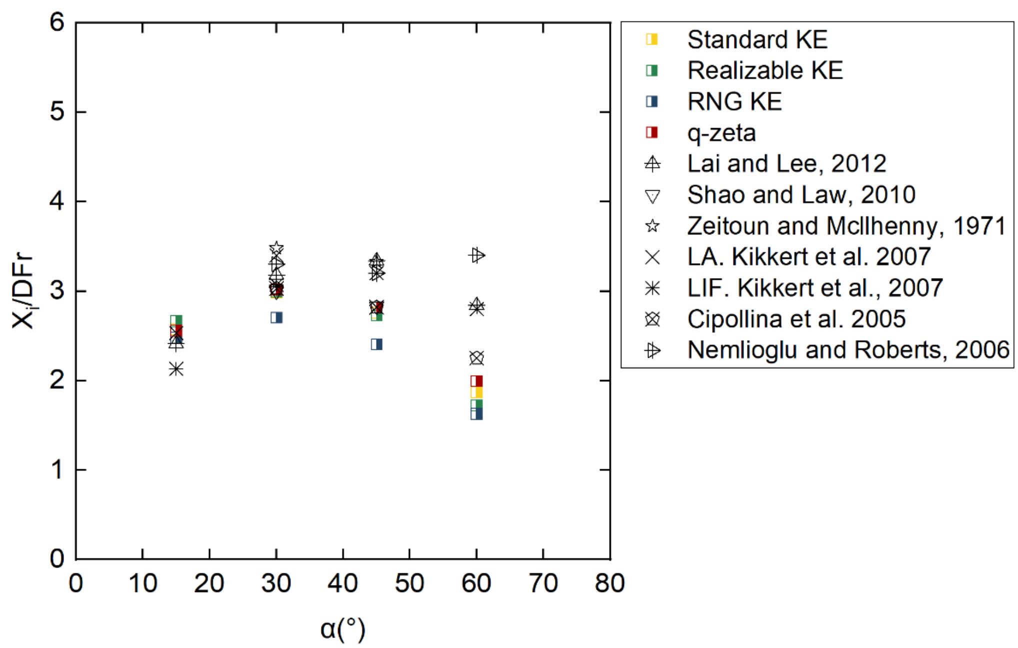

Figure 7.10 Normalized horizontal location of impact point (Xi/DFr) plotted against discharge angle.

The dilution information at the centerline peak and return/impact point

The normalized dilution at the centerline peak is plotted against the discharge angle in Figure 7.11, where the dilution at the centerline peak was obtained from the turbulent models. The dilution at the centerline peak exhibits an increasing trend, with the discharge angle changing from 15° to 60°.

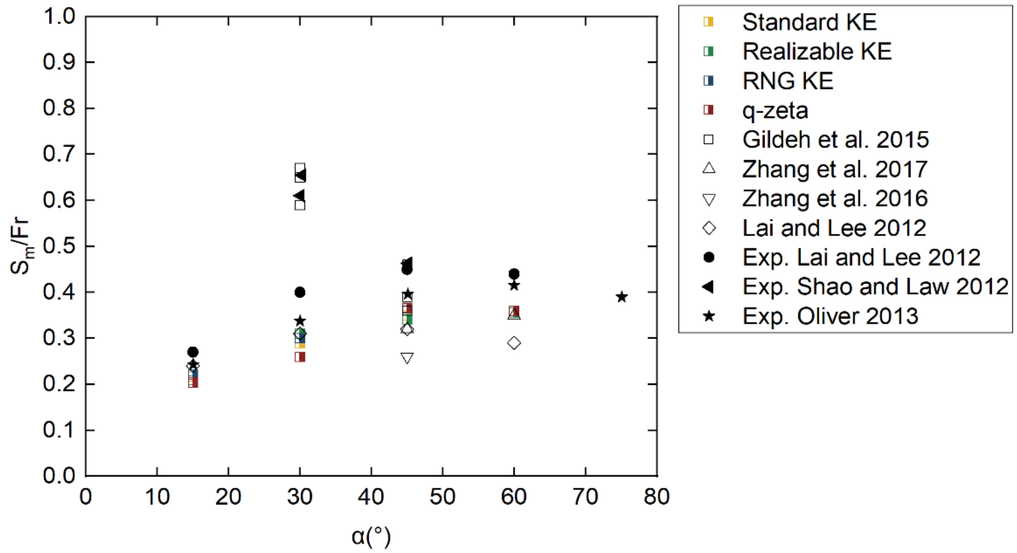

Figure 7.11 Centerline peak dilution compared to previous studies.

As previously mentioned, it is common in many studies to refer to the impact and return points as the same. In this study, the dilution at the impact point was selected for analysis to ensure consistency with previous studies. Figure 7.12 shows the normalized dilution at the impact point (S_i) as a function of discharge angle (α). With an increase in the discharge angle, the dilution at impact points increases, and 60° has the highest dilution at the return point and impact points, which is in agreement with Roberts's research (1997) that a 60° discharge angle is recommended in the outfall design. The four turbulence models were in good agreement with the predictions of commercial tools. The results in Tables 3–6 indicate that the dilution at the impact point is higher than the return point. Therefore, in future studies, it is recommended to separate these two points and consider the effect of the bottom condition.

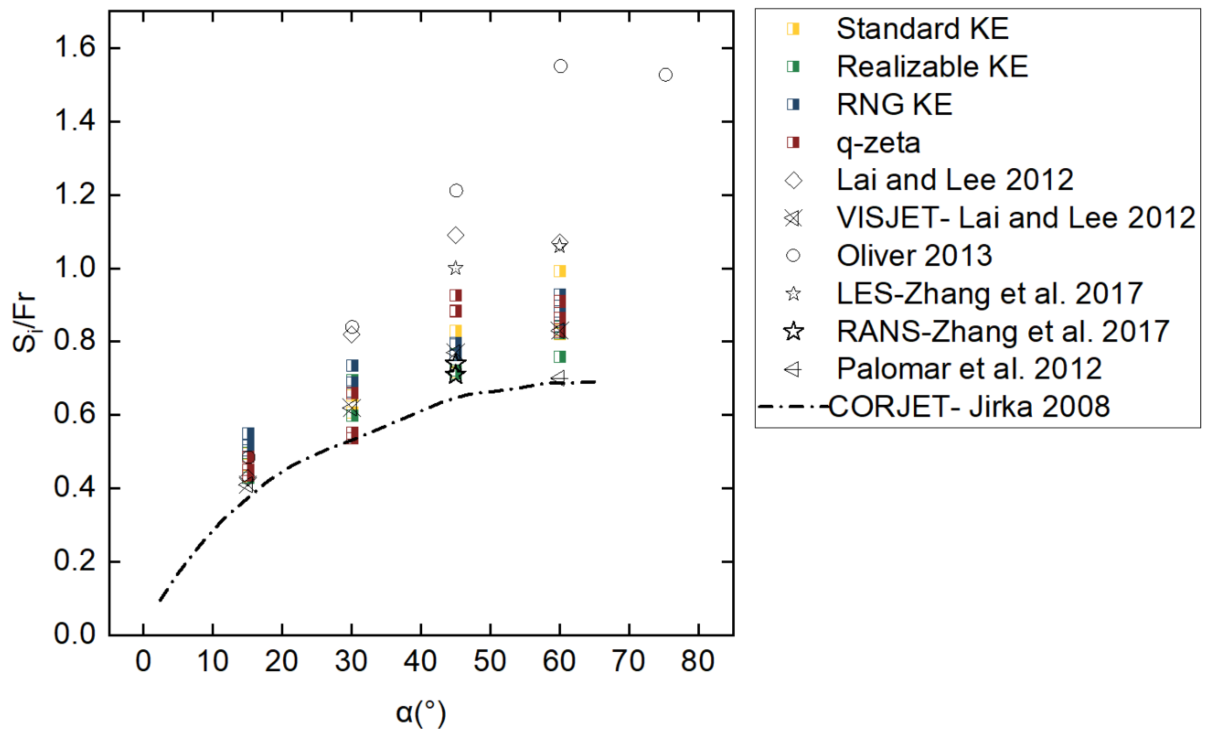

Figure 7.12 Impact point dilution plotted against discharge angle.

7.3.3 Cross-sectional concentration profile

The mixing characteristics of an inclined dense jet can be analyzed at different locations using its concentration profiles. Figure 7.13a shows one of the simulations of an inclined dense jet from the centerline of the computational domain. The jet rises, touches the highest point, and then falls back to the bottom. During this process, more mixing and detraining occurred. Three concentration profiles were chosen at three different locations (white dashed line in Figure 13a) of the jet. On each crossing section, the nondimensional concentration C/C_m is plotted against the dimensionless normalized coordinate r/b_c, where C is the location concentration at the cross-section. C_m is the maximum concentration of the cross-section, r is the radial distance, b_c is the radius defined by $\frac{C}{C_{max}} = 1/e$.

(a)

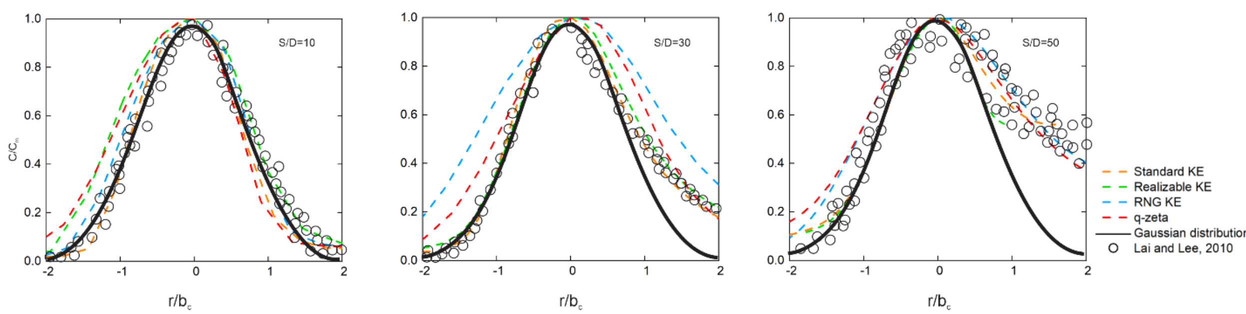

(b)

Figure 7.13 Simulation result of concentration profile (α=30°, Fr=14.2): (a) simulation results of realizable k-ε; (b) cross-sectional profiles for s/D=10,30,50, respectively.

Figure 7.13b presents three representative cross-sectional profiles of concentration fields from two different turbulence models that are compared with the results of Lai and Lee (2012). The concentration profiles had a Gaussian distribution near the nozzle area. This is also defined as the "initial stage" of the jet ($s/D < 20$, where s is the streamwise distance). In this stage, the jet is dominated by the initial momentum, after which it is close to the terminal rise height ($s/D \ = 30$). The inner (lower) half of the had a trend that started to depart from the Gaussian distribution, whereas the outer (upper) half remained Gaussian. This stage is also called the "developed stage," in which the profile is nearly stabilized. After the terminal rise height, at the $s/D \ = 50$, the upper half of the jet can maintain a Gaussian distribution, indicating that detrainment occurred in the lower half. This implies that more brine flow is peeled from the core flow. Comparing the four turbulence models, the RNG model performed poorly at s/D=30 with a spreading phenomenon. This was also found in a study by Gildeh (2015).

7.3.4 Centerline Maximum Velocity Decay

In the case of vertical buoyant jets, Chen and Rodi (1980) indicated that the maximum concentration along the jet centerline can be represented by a power-law relationship with the dimensionless centerline dilution (C_m/C_0), Froude number (Fr), and nondimensional vertical elevation:

$$F \cdot C_m/C_0 = a(y/D/Fr)^b \qquad (7.25)$$

Where C_m is the maximum profile concentration, C_0 is the initial concentration, y is the elevation distance from the nozzle. a and b are constants related to the flow type. A similar relationship can be observed for the normalized maximum centerline velocity in the cases of U_m/U_0 (Shao and Law, 2010) and Gildeh et al. (2015). The variations in the maximum centerline velocity (U_m/U_0)with different discharge angles using two turbulence models with the non-dimensional downstream distance ($s/D/Fr$) are presented in Figure 7.14 and Figure 7.15 with four turbulence models. All figures are on a logarithmic scale. It can be observed that there is a linear relationship exists between U_m/U_0 and $s/D/Fr$, which corresponds to Shao and Law's research (2010). The equations for 30° and 45° discharge angles were $F \cdot U_m/U_0 = 5.237(s/D\,/F)^{-1.093}$ and $F \cdot U_m/U_0 = 4.831(s/D\,/F)^{-1.141}$, respectively. Compared to other turbulence models, the RNG $k-\varepsilon$ model has a relatively poorer performance.

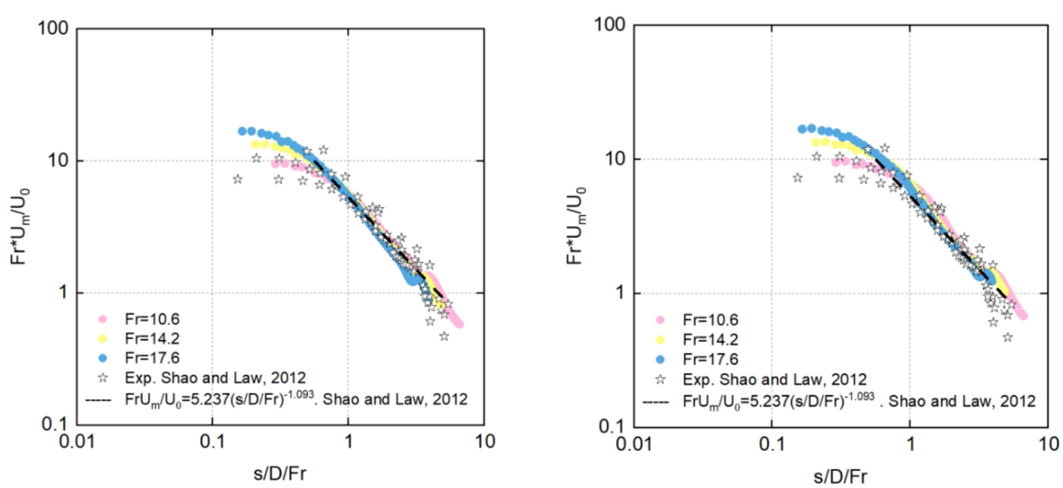

(a)

(b)

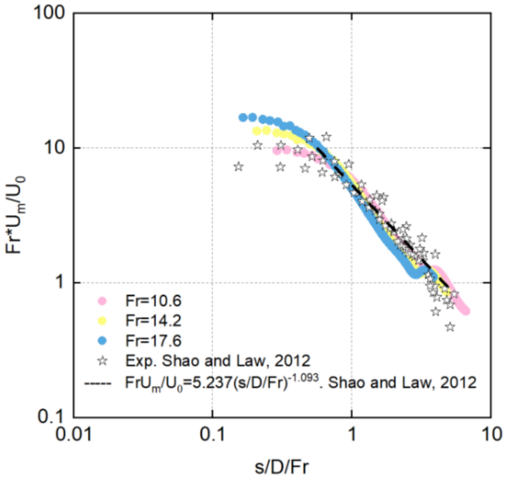

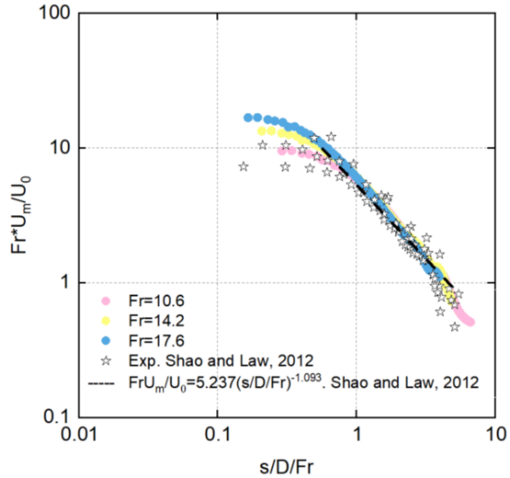

(c)

(d)

Figure 7.14 Comparison of nondimensionalized centerline maximum velocity magnitude decay with 30-degree discharge angle by four turbulence models: (a) Standard k-ε; (b) Realizable k-ε; (c) RNG k-ε; (d) q-zeta

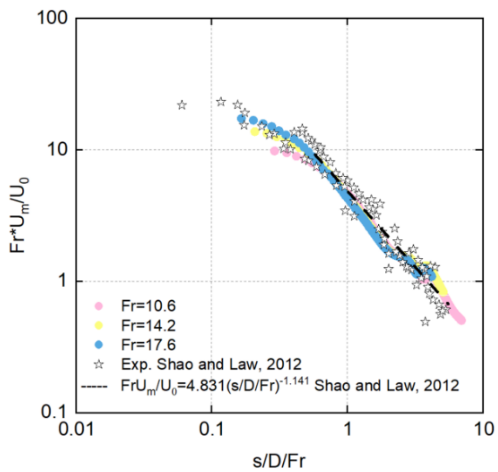

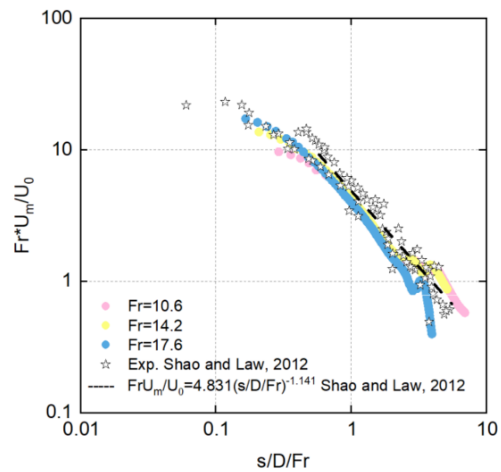

(a)

(b)

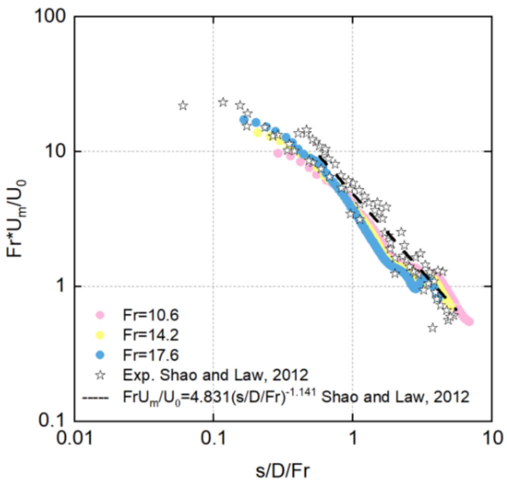

(c)

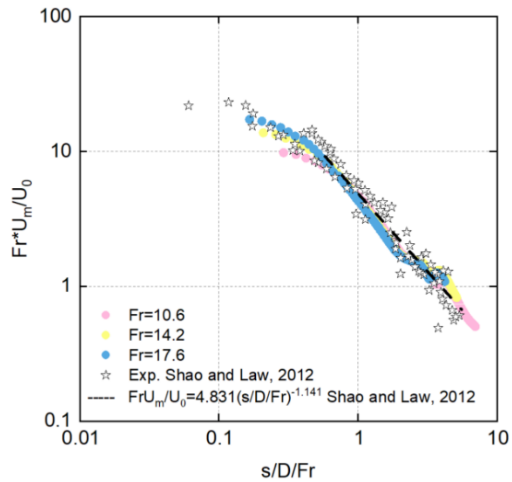

(d)

Figure 7.15 Comparison of nondimensionalized centerline maximum velocity magnitude decay with 45-degree discharge angle by four turbulence models: (a) Standard k-ε; (b) Realizable k-ε; (c) RNG k-ε; (d) q-zeta

7.3.5 Jet spreading width

During the movement of an inclined dense jet, the jet moves and diffuses into the surrounding environment. Understanding the jet spreading width is critical for engineering design and for assessing the impact area of the jet. Based on the concentration profile analysis, each section of the inclined dense jet had a Gaussian profile for concentration or velocity, especially in the upper half of the jet profile. To comprehensively evaluate the four turbulence models, we analyzed the jet spreading width at 30° and 45° angles. The width of the jet was obtained from the width of the e^{-1} ratio of the maximum concentration or the velocity value of the centerline. All jet width values derived from the concentration (bc) and velocity (bu) profiles are plotted in Figure 7.16. All results are consistent with those of previous experimental studies in the range of $s/D/Fr < 4$ (Shao and Law 2010). The upper width of the spreading concentration is consistent with the analytical solution from Kikkert (Kikkert, 2006). The upper and lower half data increased along the trajectory, and the upper half was less scattered, which was consistent with the experimental results. This indicates that more mixing occurred in the lower part of the jet. The results of the RNG $k-\varepsilon$ turbulence models were more scattered than those of the other models.

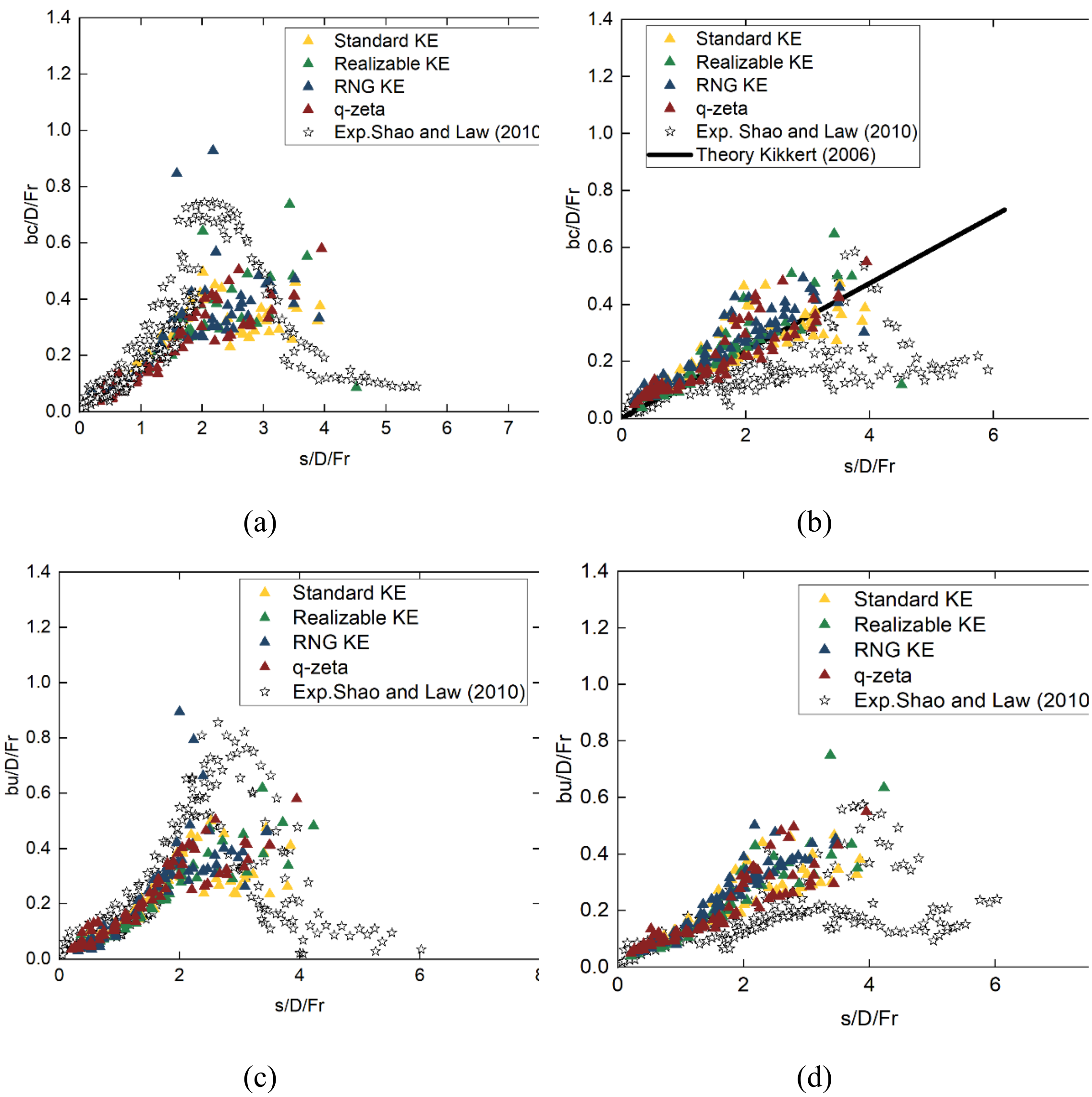

Figure 7.16 Variation of the spread width of the concentration (bc) and velocity (bu) along the trajectory for α=30° and 45°. (a) lower bc; (b) upper bc; (c) lower bu; (d) upper bu

7.4 Conclusions and recommendations

This study compares and evaluates four RANS turbulence models, namely standard k–ε, realizable k–ε, RNG k–ε, and $q - \zeta$ models, in predicting the mixing characteristics of inclined dense jets. Four different discharge angles (15, 30, 45, and 60°) with three different Froude numbers were investigated using OpenFOAM. A comprehensive analysis of the geometric and mixing properties of the jet was conducted and compared with previous experimental and numerical studies.

Compared with previous experimental studies, the RNG model demonstrated relatively poor performance in simulating the geometric characteristics of inclined dense jets. Conversely, the Realizable k–ε, standard k–ε turbulence, and $q - \zeta$ models provided reliable predictions of the geometric properties, including the terminal rise height, centerline peak location, and return and impact points, which are consistent with previous experimental findings. While the dilution values were slightly underestimated compared to the experimental data, they remained consistent with other numerical simulations and integral models. Notably, the RNG k–ε and $q - \zeta$ turbulence models performed better than the others in predicting dilution at the impact point. Employing advanced simulation methods, such as large-eddy simulations or more complex turbulence models, may be beneficial for improving the mixing predictions of inclined dense jets.

With regard to the concentration field, all four turbulence models exhibited a good performance. They accurately predicted the cross-sectional concentration profiles of inclined dense jets with a Gaussian pattern. The standard k-ε model and $q - \zeta$ models showed particular proficiency in modeling concentration profiles in the descending part of the jet. In addition, a non-dimensional decay equation ($Fr \cdot U_m/U_0 = a(s/D\,/Fr)^b$) for the maximum centerline velocity decay in inclined dense jets with 30° and 45° discharge angles was developed. The standard k-ε, realizable k-ε, and $q - \zeta$ turbulence models showed excellent agreement with previous experimental studies, indicating that the decay of the centerline maximum velocity follows a typical jet behavior.

An analysis of the jet spread width revealed that the concentration and velocity had similar developed patterns. All four turbulence models obtained satisfactory predictions of the velocity and concentration fields, which is consistent with previous experimental studies. Additionally, the velocity and concentration exhibited slower increases near the upper boundary than near the lower boundary. The scattered lower boundary width suggests a greater influence of buoyancy forces at the lower part of the inclined dense jet.

In conclusion, the realizable k–ε, standard k–ε, and $q - \zeta$ turbulence models could perform well in simulating the geometric properties and concentration field of inclined dense jets. The Geometric information prediction is limited when the inclined dense jet has a steep discharge angle (60°). Therefore, it would be beneficial to use other advanced numerical simulation methods. However, for a mild to moderate discharge angle ($\leq 45°$), the realizable k–ε and $q - \zeta$ models are more recommended.

Chapter 8 Conclusion and future recommendations

8.5 Conclusion

This thesis investigated the behavior of inclined dense jets over a sloped bottom in stagnant ambient conditions using experimental, numerical and AI-based methods. The laboratory experimental study was conducted using Laser-Induced Fluorescence (LIF) to examine the characteristics of IDJs with three common discharge angles (30°, 45°, 60°) over four sloped bottoms (0°, 1°, 3°, 5°). The numerical simulations were performed using Large Eddy Simulation (LES) and RANS models for a 60° discharge angle on 0° and 5° sloped bottoms. Two studies using Gene Expression Programs were built based on the numerical and experimental results. The study aimed to improve the understanding of the influence of the sloped bottom on the characteristics of the IDJ in stagnant water mixing performance and post-impingement development under realistic receiving environments. The key conclusions are summarized below:

- The results showed that the jet shape during the ascending and descending phases was governed by the discharge angle and remained unaffected by the bottom slope before the return point. Instantaneous images confirmed that after impingement, a series of shear-induced Kelvin–Helmholtz vortices developed along both horizontal and sloped bottoms. These vortices enhanced mixing by increasing local turbulence and accelerating the breakdown of flow structures near the bottom.
- The results from variance analysis at different heights of the jet showed that mixing was concentrated along the outer edges, with peak values near the terminal rise height where the jet changed from ascending to descending. The jet core had low variance, which indicated limited mixing in the central region of the jet.
- The results showed that the sloped bottom had a negligible effect on the geometrical and dilution behavior before the return point but significantly influenced the location of the impact point. The impact point moves downstream with an increasing bottom slope. The 30º and 45º discharge angles have a longer impact point on both bottoms compared to 60º. Linear relationships were established to describe the impact point location on different slopes.

- The results showed that concentration buildup occurred near the impact point, and the dilution at the impact point was also increased with the bottom angle. The 5° sloped bottom enhanced the dilution at the impact point by 31%, 22%, and 21.8% for discharge angle of 30º,45º and 60º, respectively. A linear fitting function of the dilution at the impact point with different sloped bottoms was also proposed.
- The results showed that after the impact point, the jet continued to move along the bottom surface for both horizontal and sloped beds. The normalized mean concentration profiles exhibited wall-jet-like and gravity current characteristics and demonstrated self-similarity, which showed good agreement with previous studies.
- The results showed that the Froude number significantly influenced the concentration distribution along the bottom. For Fr < 20 (buoyancy-dominated), the brine mixed less with the ambient water and remained more stable along the slope. In contrast, for higher Fr values (Fr = 22.1 and 28.1, momentum-dominated), the jet exhibited greater mixing and dilution due to increased momentum.
- The sloped bottom enhanced turbulence and concentration fluctuations, which could contribute to a longer mixing zone. For the buoyancy-dominated jet (Fr<20), the 60° discharge angle results in a longer mixing zone on a 5° sloped bottom. Meanwhile, the thickness of the bottom layer is influenced by both the discharge angle and bottom slope, with the 60° discharge angle on the sloped bottom producing the greatest layer thickness. These conditions provided a conservative upper bound for mixing zone length and layer thickness, offering a practical reference for discharge system design in similar environmental settings.
- The results showed that the 5° sloped bottom enhanced lateral mixing at the impact point and reduced in the shoreward movement of the jet, as the brine tended to flow downslope along the bottom due to gravity.
- Based on energy spectrum analysis along the bottom, the results showed that most measurement points followed the −5/3 Kolmogorov scaling law, confirming that the flow remained turbulent after the impact point. The sloped bottom showed higher energy levels at most locations, which reflected stronger turbulence, more efficient energy transfer, and improved mixing.

- The results of numerical simulations were compared with those of the LIF experiment and previous experimental studies. LES captured the main jet dynamics and mixing properties and showed good agreement with the experimental results. It also successfully reproduced the series of Kelvin–Helmholtz (KH) vortices along the sloped bottom, which was consistent with experimental observations.
- The results showed that important geometrical and dilution parameters of the IDJ from LES simulations matched well with experimental results. These included the jet terminal rise height (Yt), the location of the centerline peak (Xc and Yc), and the location of the impact point (Xi). The dilution at the impact point also agreed with the results of the LIF experiment.
- The dilution near the impact point on the horizontal bottom and sloped bottom can be described with a Gaussian fitting function. This makes it suitable for use in semi-analytical model development.
- The RANS model underpredicted both the geometrical and dilution parameters of the jet. This conclusion was also supported by a comparative study using four different RANS models for IDJs with discharge angles of 15°, 30°, 45°, and 60° on a horizontal bottom. The results confirmed that the choice of RANS model affected the simulation results. The standard k–ε, realizable k–ε, and q–ζ models performed better than the RNG model when $\alpha \leq 45°$, but all RANS models showed rather poor performance when the discharge angle exceeded 45°.
- The results showed that the multiple-level mesh method served as an effective approach in the numerical simulation. It allowed local refinement where needed, avoided unnecessary mesh density, and ensured sufficient accuracy without excessive computational cost.
- The results of the GEP confirm its strong potential for constructing predictive regression models for inclined dense jet behavior under various discharge angles and bottom slopes. The performance of the GEP was evaluated using multiple error indicators, including correlation coefficient (R), mean squared error (MSE), root mean squared error (RMSE), mean absolute error (MAE), mean absolute deviation (MAD), mean absolute relative error (MARE), relative absolute error (RAE), relative squared

error (RSE), and root relative squared error (RRSE). Sensitivity analysis and uncertainty analysis were also conducted to assess the model's robustness.

- The setup of the GEP model involved five key components: fitness function, function set, chromosome architecture, gene number, and linking function. The results showed that the number of genes had a notable impact on model complexity and performance. A multiple-gene model had better results but required more computational cost, while the single-gene model was simpler and faster. In the GEP, testing and adjustments were necessary during model development to achieve the best performance.
- One GEP model was developed based on experimental results to predict the impact point location (Xi/D) and bottom dilution (S/F) of inclined dense jets under sloped bottom conditions. The model used key input parameters such as discharge angle (α), bottom slope (θ), nozzle diameter (D), and Froude number (Fr), and the output mathematical equation showed good accuracy.
- Another GEP model was developed based on LES simulation results to predict key jet properties, including terminal rise height (Xt, Yt), return point (Xr), impact point (Xi), and dilution parameters (Sm, Sr, Si, Sb). The input parameters included discharge angle (α), Froude number (Fr), and bottom slope (θ). Sensitivity analysis showed that jet discharge angle (α) strongly influenced all geometrical and dilution properties. The impact point (Xi, Si) and bottom dilution (Sb) were also significantly affected by the slope angle (θ), confirming the important role of the bottom slope in mixing performance.

8.6 Future recommendations

The findings of this study deepen the understanding of inclined dense jet behavior over sloped bottoms. The experimental, numerical, and AI-based methods developed here also offer practical tools for performance prediction and support more effective, environmental friendly discharge system design. Future work could build on this research by exploring inclined dense jets under unsteady flow conditions, wave interactions, and other dynamic ambient environments. Additional potential research directions are listed below:

1. Vegetation and Roughness Effects on Sloped Bottoms-flow-bottom plant interaction

The presence of submerged vegetation or bottom roughness elements could significantly affect flow behavior and mixing performance along the bottom. Modeling flow–plant interactions and analyzing their influence on jet spreading and dilution may be especially valuable for nearshore discharge applications and for supporting ecological protection.

2. Multiple Diffuser Configurations and dynamic receiving environment

   Many real-world outfalls adopted multiple diffusers. Future research could explore the multiple inclined dense jets on sloped bottoms and also consider the dynamic receiving environment.

3. Extended the Froude Number Range

   The Froude number was shown to influence dilution along the bottom. Further studies should systematically vary Froude number across a wider range to uncover far-field mixing behavior and mixing efficiency.

4. Advanced Turbulence Modeling for discharge angles > 60°

   For steep discharge angles (e.g., 60°), LES remains more accurate than RANS. When LES is not feasible due to computational limitations, alternative RANS models such as the Reynolds Stress Model (RSM) may provide improved accuracy over standard two-equation models. Future work could also perform model sensitivity studies to determine the most appropriate turbulence model for IDJs with larger discharge angles.

5. Mesh Optimization and Numerical Strategy Improvements

   Dynamic meshing or particle-based methods like Smoothed Particle Hydrodynamics (SPH) may offer good potential for capturing complex interface behavior of the jet with receiving environment.

6. Expansion of Data-Driven Prediction Models

   While the Gene Expression Programming (GEP) models developed in this study show promising results, their performance could be improved by incorporating more diverse datasets. This includes data spanning a broader range of geometric and discharge conditions. The integration of experimental, numerical, and field datasets could enhance its generalizability. Further exploration of symbolic regression and other machine learning methods may also offer more flexible tools for predicting IDJ behavior.

8.7 Limitations of the Current Work

Although this study has adopted a comprehensive experimental setup, multiple numerical modeling approaches, and an advanced data-driven method (Gene Expression Programming), which together provide valuable insights into how a sloped bottom affects inclined dense jets, there are still some limitations that should be acknowledged. They are listed below:

In the experiment, this study only covered a limited number of discharge angles, bottom slopes, and jet densities. Additionally, velocity measurements were not included. Combining velocity data with concentration measurements could provide a more complete understanding of flow behavior over sloped bottoms.

For the CFD simulation, the limitation is the choice of the solver. The selected solver, *twoLiquidMixingFoam*, is mainly focused on scalar mixing and may underpredict jet–wall interactions near the sloped bottom. While the use of multiple mesh layers could provide a balance between accuracy and computational cost, further refinement near the bottom boundary is necessary to accurately capture the flow structures and jet impingement behavior.

For the GEP model, the main limitation is the small and selective input dataset. To develop a more powerful and generalizable predictive tool, it is important to expand the dataset to include a wider range of discharge conditions from different studies.

References

Abessi, O., & Roberts, P. J. W. (2015). Effect of nozzle orientation on dense jets in stagnant environments. *Journal of Hydraulic Engineering, 141*(8), 06015009. https://doi.org/10.1061/(ASCE)HY.1943-7900.0001032

Abraham, G. (1967). Jets with negative buoyancy in homogeneous fluid. *Journal of Hydraulic Research, 5*(4), 235–248. https://doi.org/10.1080/00221686709500209

Ahmed, M., Shayya, W. H., Hoey, D., Mahendran, A., Morris, R., & Al-Handaly, J. (2000). Use of evaporation ponds for brine disposal in desalination plants. *Desalination, 130*(2), 155–168. https://doi.org/10.1016/S0011-9164(00)00083-7

Akar, P. J., & Jirka, G. H. (1991). CORMIX2: An Expert System for Hydrodynamic Mixing Zone Analysis of Conventional and Toxic Multiport Diffuser Discharges. DeFrees Hydraulics Laboratory, Cornell University. PB-93-166924/XAB.

Albertson, M. L., Dai, Y. B., Jensen, R. A., & Rouse, H. (1950). Diffusion of submerged jets. *Transactions of the American Society of Civil Engineers, 115*(1), 639–664. https://doi.org/10.1061/TACEAT.0006302

Alfaifi, H. Mohammadian, A. & Bonakdari, H. (2020). Experimental investigation and model development of geometric characteristics of negatively buoyant jets inclined at 15° and 52° using GMDH method. Journal of Coastal Research, 36(3), 636–653.

Alfaifi, H. Mohammadian, A. & Bonakdari, H. (2022). Predicting the Geometrical Characteristics of an Inclined Negatively-Buoyant Jet for Angles from 30° to 60° Using GMDH Neural Network. Proceedings of the Canadian Society of Civil Engineering Annual Conference 2021: CSCE21 Hydrotechnical and Transportation Track, 369–377.

Alfonsi, G. (2009). Reynolds-averaged Navier–Stokes equations for turbulence modeling. Applied Mechanics Reviews, 62(4).

Al-Mutaz, I. S. (2015). Features of multi-effect evaporation desalination plants. Desalination and Water Treatment, 54(12), 3227–3235. https://doi.org/10.1080/19443994.2014.910842

Al-Mutaz, I. S. (1991). Environmental impact of seawater desalination plants. *Environmental Monitoring and Assessment, 16*(1), 75–84. https://doi.org/10.1007/bf00399594

Alvir, M. Grbčić, L. Sikirica, A. & Kranjčević, L. (2022). OpenFOAM-ROMS nested model for coastal flow and outfall assessment. Ocean Engineering, 264, 112535.

Amokrane, M. & Salmi, A. (2021). Surface spreading of the brine discharge from the seawater reverse osmosis plants: Hamma Water Desalination plant in Algeria. Desalination and Water Treatment, 222, 81–91. https://doi.org/10.5004/dwt.2021.27103

Anderson, J. D., & Wendt, J. (1995). *Computational fluid dynamics* (Vol. 206). Springer.

Azadi, A. & Firoozabadi, B. (2022). New criterion for characterization of thermal-saline jets discharged from thermal desalination plants. International Journal of Heat and Mass Transfer, 195, 123142. https://doi.org/10.1016/j.ijheatmasstransfer.2022.123142

Azimi, H., Bonakdari, H., & Ebtehaj, I. (2021). Gene expression programming-based approach for predicting the roller length of a hydraulic jump on a rough bed. *ISH Journal of Hydraulic Engineering, 27*(sup1), 77–87.

Azizi, M., Goharikamel, D., & Vafaei, F. (2020). Experimental investigation of nozzle angle effects on the brine discharge by inclined dense jets in stagnant water ambient. *SN Applied Sciences, 2*, 1–9.

Bahreini Toussi, I., Mohammadian, A., & Kianoush, R. (2021). Prediction of maximum pressure at the roofs of rectangular water tanks subjected to harmonic base excitation using the multi-gene genetic programming method. *Mathematical and Computational Applications, 26*(1), 6.

Bashitialshaaer, R., Larson, M., & Persson, K. M. (2012). An experimental investigation on inclined negatively buoyant jets. *Water, 4*(3), 720–738.

Baumann, T., Haaszio, S., & Niessner, R. (2000). Applications of a laser-induced fluorescence spectroscopy sensor in aquatic systems. *Water Research, 34*(4), 1318–1326.

Behnia, D. M., Behnia, M., Shahriar, K., & Goshtasbi, K. (2017). A new predictive model for rock strength parameters utilizing GEP method. *Procedia Engineering, 191*, 591–599.

Besalduch, L. A. Badas, M. G. Ferrari, S. & Querzoli, G. (2013). Experimental Studies for the characterization of the mixing processes in negative buoyant jets. EPJ Web of Conferences, 45, 01012.

Besalduch, L. A. Badas, M. G. Ferrari, S. & Querzoli, G. (2014). On the near field behavior of inclined negatively buoyant jets. EPJ Web of Conferences, 67, 02007.

Bhattacharyya, S., Abraham, J. P., Cheng, L., & Gorman, J. (2021). Introductory chapter: A brief history of and introduction to computational fluid dynamics. In Applications of Computational Fluid Dynamics Simulation and Modeling. IntechOpen. https://doi.org/10.5772/intechopen.97235

Bilsky, A. V. Gobyzov, O. A. & Markovich, D. M. (2020). Evolution and recent trends of particle image velocimetry for an aerodynamic experiment (review). Thermophysics and Aeromechanics, 27(1), 1–22. https://doi.org/10.1134/S0869864320010011

Bloomfield, L. J. & Kerr, R. C. (2002). Inclined turbulent fountains. Journal of Fluid Mechanics, 451, 283–294. https://doi.org/10.1017/S0022112001006528

Bonakdari, H. & Mohammadian, A. (2019). Evolutionary prediction of an inclined dense jet in shallow water. Desalination and Water Treatment, 155, 32–47.

Bosanquet, C. H., Horn, G., & Thring, M. W. (1961). The effect of density differences on the path of jets. Proceedings of the Royal Society of London. Series A. Mathematical and Physical Sciences, 263(1314), 340–352. https://doi.org/10.1098/rspa.1961.0164.

Brebbia, C. A. Marinov, A. M. Mammoli, A. A. & Safta, C. A. (2013). Energy and Sustainability IV. WIT Press.

CEAM. (2001). Visual Plumes. USEPA, Center for Exposure Assessment Modeling (CEAM). https://www.epa.gov/ceam/visual-plumes.

Chen, C. J., & Rodi, W. (1980). *Vertical turbulent buoyant jets: A review of experimental data*. NASA STI/Recon Technical Report A, 80–23073.

Christodoulou, G. C. & Papakonstantis, I. G. (2010). Simplified estimates of trajectory of inclined negatively buoyant jets. Environmental Hydraulics, 1, 165–170.

Christodoulou, G. C., Papakonstantis, I. G., & Nikiforakis, I. K. (2015). Desalination brine disposal by means of negatively buoyant jets. *Desalination and Water Treatment, 53*(12), 3208–3213.

Chu, C. (1996). Mixing of turbulent advected line puffs. HKU Theses Online (HKUTO).

Chu, P. C. K. Lee, J. H. & Chu, V. H. (1999). Spreading of Turbulent Round Jet in Coflow. Journal of Hydraulic Engineering, 125(2), 193–204. https://doi.org/10.1061/(ASCE)0733-9429(1999)125:2(193)

Cipollina, A., Brucato, A., Grisafi, F., & Nicosia, S. (2005). Bench-scale investigation of inclined dense jets. *Journal of Hydraulic Engineering, 131*(11), 1017–1022.

Crowe, A. T. Davidson, M. J. & Nokes, R. I. (2016). Velocity measurements in inclined negatively buoyant jets. Environmental Fluid Mechanics, 16(3), 503–520. https://doi.org/10.1007/s10652-015-9435-y

Czaplewski, K. Swierczynski, S. & Zwolan, P. (2021). Increasing the Reliability of Simulation Tests in Navigation and Maneuvering Simulators Using the k-Epsilon Model Based on the RANS Method. Sensors, 21(15), Article 15. https://doi.org/10.3390/s21154995

Doneker, R. L., & Jirka, G. H. (1990). Expert System for Hydrodynamic Mixing Zone Analysis of Conventional and Toxic Submerged Single Port Discharges (CORMIX1). Technical Report EPA/600/3-90/012, U.S. Environmental Protection Agency.

Doneker, R. L., & Jirka, G. H. (2001). CORMIX-GI Systems for Mixing Zone Analysis of Brine Wastewater Disposal. Desalination, 139(1), 263–274. https://doi.org/10.1016/S0011-9164(01)00318-6

Doneker, R. L., & Jirka, G. H. (2007). CORMIX User Manual: A Hydrodynamic Mixing Zone Model and Decision Support System for Pollutant Discharges into Surface Waters. U.S. Environmental Protection Agency, Washington, D.C.

Ebtehaj, I., Bonakdari, H., Zaji, A. H., Azimi, H., & Sharifi, A. (2015). Gene expression programming to predict the discharge coefficient in rectangular side weirs. *Applied Soft Computing, 35*, 618–628.

Elsaid, K. Kamil, M. Sayed, E. T. Abdelkareem, M. A. Wilberforce, T. & Olabi, A. (2020). Environmental impact of desalination technologies: A review. Science of The Total Environment, 748, 141528. https://doi.org/10.1016/j.scitotenv.2020.141528

Elsaie, Y. H., Soussa, M., Gado, A., & Balah, A. (2022). Water desalination in Egypt: Literature review and assessment. *Ain Shams Engineering Journal*, 101998. https://doi.org/10.1016/j.asej.2022.101998.

Ferrari, S., & Querzoli, G. (2010). Mixing and re-entrainment in a negatively buoyant jet. *Journal of Hydraulic Research, 48*(5), 632–640.

Ferrari, S., Badas, M. G., & Querzoli, G. (2018). An investigation on the effects of different stratifications on negatively buoyant jets. In *EPJ Web of Conferences* (Vol. 180, 02025). EDP Sciences. https://doi.org/10.1051/epjconf/201818002025.

Ferrari, S., Badas, M. G., Besalduch, L. A., & Querzoli, G. (2013). Experimental investigation of inclined negatively buoyant jet. In *Eighth International Symposium on Turbulence and Shear Flow Phenomena*. Begel House Inc.

Ferrari, S., Badas, M. G., Besalduch, L. A., & Querzoli, G. (2014). A feature tracking velocimetry technique applied to inclined negatively buoyant jets. In *Proceedings of the 17th International Symposium on Applications of Laser Techniques to Fluid Mechanics* (pp. 1–12).

Ferreira, C. (2001). Gene expression programming: A new adaptive algorithm for solving problems. *arXiv preprint*, arXiv:cs/0102027.

Ferreira, C. (2006). *Gene expression programming: Mathematical modeling by an artificial intelligence*. Springer.

Forbes, P. B. (2010). *Development of a laser induced fluorescence technique for the analysis of organic air pollutants* (PhD thesis, University of Pretoria). https://repository.up.ac.za/handle/2263/25255

Forstall, W. & Gaylord, E. W. (1955). Momentum and Mass Transfer in a Submerged Water Jet. Journal of Applied Mechanics, 22(2), 161–164. https://doi.org/10.1115/1.4011034

Fox, D. G. (1970). Forced plume in a stratified fluid. Journal of Geophysical Research (1896-1977), 75(33), 6818–6835. https://doi.org/10.1029/JC075i033p06818

Frankel, R. J. & Cumming, J. D. (1965). Turbulent Mixing Phenomena of Ocean Outfalls. Journal of the Sanitary Engineering Division, 91(2), 33–62. https://doi.org/10.1061/JSEDAI.0000544

Frick, W. E. (2004). Visual Plumes mixing zone modeling software. Environmental Modeling & Software, 19(7), 645–654. https://doi.org/10.1016/j.envsoft.2003.08.018

Frisch, U. & Kolmogorov, A. N. (1995). Turbulence: The Legacy of A. N. Kolmogorov. Cambridge University Press.

Galeshi, A. Abessi, O. Yousefifard, M. & Rahmani Firoozjaee, A. (2023). Inclined dense discharge in stagnant and wave environments: An experimental and numerical study. Ocean Engineering, 278, 114045. https://doi.org/10.1016/j.oceaneng.2023.114045

Ghorbani, M., Giljarhus, K. E. T., Skadsem, H. J., & Time, R. W. (2021). Computational fluid dynamics simulation of buoyant mixing of miscible fluids in a tilted tube. *Journal of Physics: Conference Series, 1201*, 012021.

Gibson, M. M. & Dafa'Alla, A. A. (1995). Two-equation model for turbulent wall flow. AIAA Journal, 33(8), 1514–1518. https://doi.org/10.2514/3.12691

Gildeh, H. K. Mohammadian, A. Nistor, I. & Qiblawey, H. (2015). Numerical modeling of 30 °and 45° inclined dense turbulent jets in stationary ambient. Environmental Fluid Mechanics, 15(3), 537–562.

Graham, J. B. (2005). MARINE BIOLOGICAL CONSIDERATIONS RELATED TO THE REVERSE OSMOSIS DESALINATION PROJECT AT THE ENCINA POWER PLANT, CARLSBAD, CA.

Greenshields, C. J. (2015). OpenFOAM user guide. OpenFOAM Foundation Ltd, Version, 3(1), 47.

Gruber, M. F., Johnson, C. J., Tang, C. Y., Jensen, M. H., Yde, L., & Hélix-Nielsen, C. (2011). Computational fluid dynamics simulations of flow and concentration polarization in forward osmosis membrane systems. *Journal of Membrane Science, 379*(1–2), 488–495.

Habibi, S., Azadi, A., & Firoozabadi, B. (2022). Large Eddy Simulation of inclined negatively buoyant jets with sloped beds. *Journal of Hydraulic Engineering, 148*(11), 04022023.

Habibi, S. Azadi, A. & Firoozabadi, B. (2023). Identification of turbulent structures of inclined negatively buoyant jets with bed effects. International Journal of Heat and Mass Transfer, 208, 124040. https://doi.org/10.1016/j.ijheatmasstransfer.2023.124040

Hoepner, T. & Lattemann, S. (2003). Chemical impacts from seawater desalination plants—A case study of the northern Red Sea. Desalination, 152(1–3), 133–140.

Issakhov, A. & Omarova, P. (2020). Numerical simulation of pollutant dispersion in the residential areas with continuous grass barriers. International Journal of Environmental Science and Technology, 17, 525–540.

James, W. P. Vergara, I. & Kim, K. (1983). Dilution of a Dense Vertical Jet. Journal of Environmental Engineering, 109(6), 1273–1283. https://doi.org/10.1061/(ASCE)0733-9372(1983)109:6(1273)

Jiang, B. Law, A. W.-K. & Lee, J. H.-W. (2014). Mixing of 30° and 45° Inclined Dense Jets in Shallow Coastal Waters. Journal of Hydraulic Engineering, 140(3), 241–253. https://doi.org/10.1061/(asce)hy.1943-7900.0000819

Jiang, M. Law, A. W.-K. & Lai, A. C. H. (2019a). Turbulence characteristics of 45° inclined dense jets. Environmental Fluid Mechanics, 19(1), 27–54. https://doi.org/10.1007/s10652-018-9614-8

Jirka, G. H., & Akar, P. J. (1991). Hydrodynamic Classification of Submerged Multiport Diffuser Discharges. Journal of Hydraulic Engineering, 117(9), 1113–1128.

Jirka, G. H. (2007). Buoyant Surface Discharges into Water Bodies. II: Jet Integral Model. Journal of Hydraulic Engineering, 133(9), 1021–1036.

Jirka, G. H., Adams, E. E., & Stolzenbach, K. D. (1981). Buoyant Surface Jets. Journal of Hydraulic Division, ASCE, 107(HY11), 1467–1487.

Jirka, G. H., & Doneker, R. L. (1991). Hydrodynamic Classification of Submerged Single-Port Discharges. Journal of Hydraulic Engineering, 117(9), 1095–1112. https://doi.org/10.1061/(ASCE)0733-9429(1991)117:9(1095)

Jirka, G. H. (2004). Integral model for turbulent buoyant jets in unbounded stratified flows. Part I: Single round jet. Environmental Fluid Mechanics, 4(1), 1–56.

Jirka, G. H. (2008). "Improved discharge configurations for brine effluents from desalination plants." Journal of Hydraulic Engineering 134(1): 116-120.

Jones, G. R., & Jirka, G. H. (1991). CORMIX3: An Expert System for the Analysis and Prediction of Buoyant Surface Discharges. Technical Report, DeFrees Hydraulics Laboratory, Cornell University. (Also to be published by U.S. EPA, Environmental Research Lab, Athens, Georgia, 1993).

Jones, R., Nash, D., & Doneker, R. L. (2007). Buoyant Surface Discharges into Water Bodies. I: Flow Classification and Prediction Methodology. Journal of Hydraulic Engineering, 133(9), 1010–1020. https://doi.org/10.1061/(ASCE)0733-9429(2007)133:9(1010)

Jones, E., Qadir, M., van Vliet, M. T. H., Smakhtin, V., & Kang, S. (2019). The state of desalination and brine production: A global outlook. *Science of The Total Environment, 657*, 1343–1356. https://doi.org/10.1016/j.scitotenv.2018.12.076

Joshi, J. & Nayak, A. K. (2019). Advances of Computational Fluid Dynamics in Nuclear Reactor Design and Safety Assessment. Woodhead Publishing.

Khashan, D. H., & Hassan, W. H. (2021, February). evaluation of seepage under hydraulic structures using gene expression programming. In IOP Conference Series: Materials Science and Engineering (Vol. 1067, No. 1, p. 012085). IOP Publishing.

Kheirkhah Gildeh, H. Mohammadian, A. Nistor, I. & Qiblawey, H. (2015). Numerical modeling of 30∘ and 45∘ inclined dense turbulent jets in stationary ambient. Environmental Fluid Mechanics, 15, 537–562.

Kikkert, G. A. (2006). Buoyant jets with two and three-dimensional trajectories. https://doi.org/10.26021/1639

Kikkert, G. A. Davidson, M. J. & Nokes, R. I. (2007). Inclined negatively buoyant discharges. Journal of Hydraulic Engineering, 133(5), 545–554.

Kim, J. Park, K. Yang, D. R. & Hong, S. (2019). A comprehensive review of energy consumption of seawater reverse osmosis desalination plants. Applied Energy, 254, 113652. https://doi.org/10.1016/j.apenergy.2019.113652

Lai, C. C., & Lee, J. H. (2012). Mixing of inclined dense jets in stationary ambient. *Journal of Hydro-Environment Research, 6*(1), 9–28.

Lai, C. C. K. & Lee, J. H. W. (2014). Initial mixing of inclined dense jet in perpendicular crossflow. Environmental Fluid Mechanics, 14(1), 25–49. https://doi.org/10.1007/s10652-013-9290-7

Lai, W. T. (1996). Particle Image Velocimetry: A New Approach in Experimental Fluid Research. In Th. Dracos (Ed.), Three-Dimensional Velocity and Vorticity Measuring and Image Analysis Techniques (Vol. 4, pp. 61–92). Springer Netherlands. https://doi.org/10.1007/978-94-015-8727-3_3

Lai, W. T. (1996). Particle image velocimetry: A new approach in experimental fluid research. In Th. Dracos (Ed.), Three-dimensional velocity and vorticity measuring and image analysis techniques (Vol. 4, pp. 61–92). Springer Netherlands.

Lane-Serff, G. F. Linden, P. F. & Hillel, M. (1993). Forced, angled plumes. Journal of Hazardous Materials, 33(1), 75–99.

Laputz, A., Pelletier, G., & Roberts, P. (2010). On visual plumes and associated applications. In 6th International Conference on Marine Waste Water Discharges and Coastal Environment. Langkawi, Malaysia.

Lattemann, S. & Höpner, T. (2008). Environmental impact and impact assessment of seawater desalination. Desalination, 220(1), 1–15. https://doi.org/10.1016/j.desal.2007.03.009

Lattemann, S., & Amy, G. (2013). Marine monitoring surveys for desalination plants—A critical review. Desalination and Water Treatment, 51(1–3), 233–245.

Launder, B. E. & Spalding, D. B. (1983). The numerical computation of turbulent flows. In Numerical prediction of flow, heat transfer, turbulence and combustion (pp. 96–116). Elsevier.

Lee, J. H. Cheung, V. Wang, W. P. & Cheung, S. K. (2000). Lagrangian modeling and visualization of rosette outfall plumes. In Proc. 4th Conf. on Hydroinformatics. Iowa City, Iowa: Iowa Institute of Hydraulic Research.

Lee, J. H. W., Cheung, V., Kuang, C. P., Choi, D. K. W., Wang, W. P., Tu, C. H., Chan, B., & Choi, Y. K. (2003). VISJET & VISFLOOD: Software for environment hydraulic modeling & visualization. In *The Asian Symposium on Visualization*.

Lee, J. H. & Cheung, V. (1990). Generalized Lagrangian model for buoyant jets in current. Journal of Environmental Engineering, 116(6), 1085–1106.

List, E. J. (1982). Turbulent Jets and Plumes. Annual Review of Fluid Mechanics, 14(Volume 14, 1982), 189–212. https://doi.org/10.1146/annurev.fl.14.010182.001201

Mason, P. J. (1994). "Large-eddy simulation: A critical review of the technique." Quarterly Journal of the Royal Meteorological Society 120(515): 1-26.

Mattar, M. A. A. I. Alamoud, A. A. Al-Othman, H. O. Elansary and A.-H. H. Farah (2020). "Hydraulic performance of labyrinth-channel emitters: experimental study, ANN, and GEP modeling." Irrigation Science 38(1): 1-16.

Meerganz von Medeazza, G. L. (2005). "Direct" and socially-induced environmental impacts of desalination. Desalination, 185(1), 57–70. https://doi.org/10.1016/j.desal.2005.03.071

Mendez-Diaz, M. M., & Jirka, G. H. (1996). Buoyant Plumes from Multiport Diffusers in Deep Water. Journal of Hydraulic Engineering, 122(8), 443–450.

Michelsen, H. A., Schulz, C., Smallwood, G. J., & Will, S. (2015). Laser-induced incandescence: Particulate diagnostics for combustion, atmospheric, and industrial applications. *Progress in Energy and Combustion Science, 51*, 2–48.

Millero, F. J. & Poisson, A. (1981). International one-atmosphere equation of state of seawater. Deep Sea Research Part A. Oceanographic Research Papers, 28(6), 625–629.

Missimer, T. M. & Maliva, R. G. (2018). Environmental issues in seawater reverse osmosis desalination: Intakes and outfalls. Desalination, 434, 198–215.

Mohammadian, A., Kheirkhah Gildeh, H., & Nistor, I. (2020). CFD modeling of effluent discharges: A review of past numerical studies. Water, 12(3), 856. https://doi.org/10.3390/w12030856

Mohammadian, A., Gildeh, H. K., & Yan, X. (2023). Numerical simulation of effluent discharges: Applications with OpenFOAM. CRC Press. https://doi.org/10.1201/9781003181811

Morton, B. R. (1959). Forced plumes. Journal of Fluid Mechanics, 5(1), 151–163. https://doi.org/10.1017/S002211205900012X

Morton, B. R., Taylor, G., & Turner, J. S. (1956). Turbulent gravitational convection from maintained and instantaneous sources. *Proceedings of the Royal Society of London. Series A, Mathematical and Physical Sciences, 234*(1196), 1–23.

Navarro, R. & Lizaso, J. L. S. (2021). Mitigation cost of desalination intake impact on coastal wetlands. Desalination and Water Treatment, 224, 136–143.

Nemlioglu, S. & Roberts, P. (2006). Experiments on dense jets using three-dimensional laser-induced fluorescence (3DLIF). The 4th international conference on marine waste water disposal and marine environment, Antalya, Turkey.

Nien Fan, L. (1967). TURBULENT BOUYANT JETS INTO STRATIFIED OR FLOWING AMBIENT FLUIDS. USPHS WP-00428 AND WP-00680. FWPCA GRANT WP-01256-01. W M KECK LABORATORY OF HYDRAULICS AND WATER RESOURCES, REPORT NO KH-R-15, JUN 1967. 196 P, 25 REF.

Nikiforakis, I. K. Stamou, A. I. & Christodoulou, G. C. (2015). A modified integral model for negatively buoyant jets in a stationary ambient. Environmental Fluid Mechanics, 15(5), 939–957. https://doi.org/10.1007/s10652-014-9388-6

Nikiforakis, I. K., Christodoulou, G. C., & Stamou, A. I. (2014). Bottom concentration field due to impingement of inclined dense jets on a slope. In *Proceedings of the 7th International Symposium on Environmental Hydraulics*, Singapore.

Oliver, C. J. (2012). *Near field mixing of negatively buoyant jets* (Ph.D. thesis). University of Canterbury, New Zealand.

Oliver, C. J. Davidson, M. J. & Nokes, R. I. (2008). K-ε Predictions of the initial mixing of desalination discharges. Environmental Fluid Mechanics, 8, 617–625.

Oliver, C. J. Davidson, M. J. & Nokes, R. I. (2013a). Removing the boundary influence on negatively buoyant jets. Environmental Fluid Mechanics, 13, 625-648.

Oliver, C. J. Davidson, M. J. & Nokes, R. I. (2013b). Behavior of dense discharges beyond the return point. Journal of Hydraulic Engineering, 139(12), 1304–1308.

Palomar, P. J. L., Lara, J. L., & Losada, I. J. (2016). PIV-PLIF experimental study of the spreading layer arisen from brine jet discharges. En preparación.

Palomar, P. J. L. Lara, I. J. Losada, M. Rodrigo, and A. Alvárez. 2012a. "Near Field Brine Discharge Modeling Part 1: Analysis of Commercial Tools." Desalination 290:14–27. doi: 10.1016/j.desal.2011.11.037.

Palomar, P. J. L. Lara, and I. J. Losada. 2012b. "Near Field Brine Discharge Modeling Part 2: Validation of Commercial Tools." Desalination 290:28–42. doi: 10.1016/j.desal.2011.10.021.

Papakonstantis, I. G. and E. I. Tsatsara (2018). "Trajectory characteristics of inclined turbulent dense jets." Environmental Processes 5: 539-554.

Papakonstantis, I. G. & Christodoulou, G. C. (2010). Spreading of round dense jets impinging on a horizontal bottom. Journal of Hydro-Environment Research, 4(4), 289–300.

Papakonstantis, I. G. & Mylonakou, E. L. (2021). Flow visualization experiments of inclined slot jets with negative buoyancy. Environmental Processes, 8, 1549–1565.

Papakonstantis, I. G. Christodoulou, G. C. & Papanicolaou, P. N. (2011a). Inclined negatively buoyant jets 1: Geometrical characteristics. Journal of Hydraulic Research, 49(1), 3–12. https://doi.org/10.1080/00221686.2010.537153

Papakonstantis, I. G. Christodoulou, G. C. & Papanicolaou, P. N. (2011b). Inclined negatively buoyant jets 2: Concentration measurements. Journal of Hydraulic Research, 49(1), 13–22.

Pérez Díaz, B. Palomar, P. Castanedo, S. & Álvarez, A. (2018). PIV-PLIF Characterization of Nonconfined Saline Density Currents under Different Flow Conditions. Journal of Hydraulic Engineering, 144. https://doi.org/10.1061/(ASCE)HY.1943-7900.0001511

Pincince, A. B. & List, E. J. (1973). Disposal of Brine into an Estuary. Journal (Water Pollution Control Federation), 45(11), 2335–2344.

Prandtl, L. (1925). *Report on investigation of developed turbulence*. *Mechanik, 5*(2).

Ramakanth, A. (2016). *Quantifying boundary interaction of negatively buoyant jets* [Master's thesis]. University of Canterbury. http://hdl.handle.net/10092/12936

Ramezani, M. Abessi, O. & Firoozjaee, A. R. (2021). Effect of proximity to bed on 30° and 45° inclined dense jets: A numerical study. Environmental Processes, 8, 1141–1164.

Reichardt, H. (1942). Gesetzmassigkeiten der freien Turbulenz. VDI-Forschungsh. 414. https://cir.nii.ac.jp/crid/1573105974953843456

Ren, X. Harder, H. Martinez, M. Faloona, I. C. Tan, D. Lesher, R. L. Di Carlo, P. Simpas, J. B. & Brune, W. H. (2004). Interference Testing for Atmospheric HO x Measurements by Laser-induced Fluorescence. Journal of Atmospheric Chemistry, 47(2), 169–190. https://doi.org/10.1023/B:JOCH.0000021037.46866.81

Roberts, D. A., Johnston, E. L., & Knott, N. A. (2010). Impacts of desalination plant discharges on the marine environment: A critical review of published studies. *Water Research, 44*(18), 5117–5128.

Roberts, P. J. W., Ferrier, A., & Daviero, G. (1997). Mixing in inclined dense jets. *Journal of Hydraulic Engineering, 123*(8), 693–699.

Roberts, P. J. H. J. Salas, F. M. Reiff, M. Libhaber, A. Labbe and J. C. Thomson (2010). Marine wastewater outfalls and treatment systems, IWA publishing.

Roberts, Philip J. W. and G. Toms. 1987. "Inclined Dense Jets in Flowing Current." Journal of Hydraulic Engineering 113(3):323–40. doi: 10.1061/(ASCE)0733-9429(1987)113:3(323).

Rogers, S. R. Webster, T. Livingstone, W. & O'Driscoll, N. J. (2012). Airborne Laser-Induced Fluorescence (LIF) Light Detection and Ranging (LiDAR) for the Quantification of Dissolved Organic Matter Concentration in Natural Waters. Estuaries and Coasts, 35(4), 959–975. https://doi.org/10.1007/s12237-012-9509-8

Rouse, H. Yih, C. S. & Humphreys, H. W. (1952). Gravitational Convection from a Boundary Source. Tellus, 4(3), 201–210. https://doi.org/10.3402/tellusa.v4i3.8688

Saeidi Hosseini, S. A. R. Mohammadian, A. Roberts, P. J. & Abessi, O. (2022). Numerical Study on the Effect of Port Orientation on Multiple Inclined Dense Jets. Journal of Marine Science and Engineering, 10(5), 590.

Saeidi Hosseini, SAR, Mostafa Taherian, Abdolmajid Mohammadian, Simone Ferrari, and Philip J. W. Roberts. 2023. "Mixing Behavior of Multiport Diffusers with Non-Uniform Port Orientation." Desalination 567 (December):116962. https://doi.org/10.1016/j.desal.2023.116962.

Saito, K. (2012). Plant and vegetation monitoring using laser-induced fluorescence spectroscopy. In *Industrial Applications of Laser Remote Sensing* (pp. 99–114).

Sanza, M. A. Bonnélyea, V. & Cremerb, G. (2007). Fujairah reverse osmosis plant: 2 years of operation. Desalination, 203(1), 91–99. https://doi.org/10.1016/j.desal.2006.03.526

Sauvet-Goichon, B. (2007). Ashkelon desalination plant—A successful challenge. Desalination, 203(1), 75–81. https://doi.org/10.1016/j.desal.2006.03.525

Schmidt, F. H. (1957). On the Diffusion of Heated Jets. Tellus, 9(3), 378–383. https://doi.org/10.1111/j.2153-3490.1957.tb01893.x

Schmidt, W. (1941). Turbulente Ausbreitung eines Stromes erhitzter Luft. *ZAMM-Journal of Applied Mathematics and Mechanics/Zeitschrift für Angewandte Mathematik und Mechanik, 21*(5), 265–278.

Schmitt, F. G. (2007). About Boussinesq's turbulent viscosity hypothesis: Historical remarks and a direct evaluation of its validity. Comptes Rendus Mécanique, 335(9), 617–627. https://doi.org/10.1016/j.crme.2007.08.004

Schomacker, K. T. Frisoli, J. K. Compton, C. C. Flotte, T. J. Richter, J. M. Nishioka, N. S. & Deutsch, T. F. (1992). Ultraviolet laser-induced fluorescence of colonic tissue: Basic biology and diagnostic potential. Lasers in Surgery and Medicine, 12(1), 63–78. https://doi.org/10.1002/lsm.1900120111

Sedlak, D. (2023). Water for All: Global Solutions for a Changing Climate. Yale University Press.

Seil, G., & Zhang, Q. J. J. A. W. A. (2010). CFD modeling of desalination plant brine discharge systems. *Water and Wastewater Asia, 37*(6), 79–83.

Shao, D. (2010). *Desalination discharge in shallow coastal waters* (Doctoral dissertation).

Shao, D. and A. W.-K. Law (2010). "Mixing and boundary interactions of 30 and 45 inclined dense jets." Environmental fluid mechanics 10(5): 521-553.

Smagorinsky, J. (1963). General circulation experiments with the primitive equations: I. The basic experiment. Monthly weather review, 91(3), 99-164.

Sorour, M. H. Hani, H. A. Shaalan, H. F. & Al-Bazedi, G. A. (2015). Preliminary techno-economics assessment of developed desalination/salt recovery facility based on membrane and thermal techniques. Desalination and Water Treatment, 55(9), 2416–2422. https://doi.org/10.1080/19443994.2014.947775

Sullivan, P. P. McWilliams, J. C. & Moeng, C.-H. (1994). A subgrid-scale model for large-eddy simulation of planetary boundary-layer flows. Boundary-Layer Meteorology, 71(3), 247–276. https://doi.org/10.1007/BF00713741

Taherian, Mostafa, Seyed Ahmad Reza Saeidi Hosseini, Abdolmajid Mohammadian, Simone Ferrari, and Philip J. W. Roberts. 2024. "Laboratory Study on Inclined Desalination Discharges in Perpendicular Cross-Flow." Desalination 583 (August):117719. https://doi.org/10.1016/j.desal.2024.117719.

Tahmooresi, S. & Ahmadyar, D. (2021). Effects of turbulent Schmidt number on CFD simulation of 45∘ inclined negatively buoyant jets. Environmental Fluid Mechanics, 21(1), 39–62.

Tahmooresi, S. & Ahmadyar, D. (2022). Application of Reynolds flux modeling in CFD simulation of 45∘ inclined negatively buoyant jets. Environmental Fluid Mechanics, 22(1), 55–86.

Tahmooresi, S. Mohammadian, A. Nistor, I. & Kheirkhah Gildeh, H. (2023). Reynolds flux modeling; new numerical insights into inclined dense jets. Environmental Fluid Mechanics, 23(3), 551–577. https://doi.org/10.1007/s10652-023-09919-z

Taylor, A. T. & Lai, E. P. (2021). Current state of laser-induced fluorescence spectroscopy for designing biochemical sensors. Chemosensors, 9(10), 275.

Tofighian, H. Aghajanpour, A. Abessi, O. & Ramezani, M. (2022). Simulation of inclined dense jets in stagnant environments: An LES and experimental study. Environmental Fluid Mechanics, 22(5), 1161–1185. https://doi.org/10.1007/s10652-022-09884-z

Tong, S. S. & Stolzenbach, K. D. (1979). Submerged Discharges of Dense Effluent. MIT Report, No. 243. https://repository.tudelft.nl/islandora/object/uuid%3A397fe811-d155-430c-83ad-735073f07dc6

Turek, M. (2003). Dual-purpose desalination-salt production electrodialysis. Desalination, 153(1), 377–381. https://doi.org/10.1016/S0011-9164(02)01131-1

Turek, M. & Dydo, P. (2003). Hybrid membrane-thermal versus simple membrane systems. Desalination, 157(1), 51–56. https://doi.org/10.1016/S0011-9164(03)00382-5

Turner, J. S. (1966). Jets and plumes with negative or reversing buoyancy. Journal of Fluid Mechanics, 26(4), 779–792. https://doi.org/10.1017/S0022112066001526

UNESCO World Water Assessment Programme. (2024). *The United Nations World Water Development Report 2024: Water for prosperity and peace*. UNESCO. https://unesdoc.unesco.org/ark:/48223/pf0000386856.

Vafa, N. Azadi, A. & Firoozabadi, B. (2021). Effect of numerical schemes on advection terms for large eddy simulation of inclined dense jets. Environmental Fluid Mechanics, 21(6), 1227–1252. https://doi.org/10.1007/s10652-021-09818-1

Vafeiadou, P. I., Papakonstantis, I. G., & Christodoulou, G. C. (2005). Numerical simulation of inclined negatively buoyant jets. In *The 9th International Conference on Environmental Science and Technology*, September.

Van Vliet, M. T. E., Jones, R., Flörke, M., Franssen, W. H., Hanasaki, N., Wada, Y., & Yearsley, J. R. (2021). Global water scarcity including surface water quality and expansions of clean water technologies. *Environmental Research Letters, 16*(2), 024020.

Versteeg, H. K. & Malalasekera, W. (2007). An introduction to computational fluid dynamics: The finite volume method. Pearson education.

Voutchkov, Nikolay, and Gisela Noelle Kaiser. 2020. "Chapter 1 - Introduction to Concentrate Management." In Management of Concentrate from Desalination Plants, edited by Nikolay Voutchkov and Gisela Noelle Kaiser, 1–12. Elsevier. https://doi.org/10.1016/B978-0-12-818045-7.00001-4.

Wang, H. & Law, A. W.-K. (2002). Second-order integral model for a round turbulent buoyant jet. Journal of Fluid Mechanics, 459, 397–428. https://doi.org/10.1017/S0022112002008157

Wang, X. & Mohammadian, A. (2025). A Comparison of k − ε—Type Turbulence Models for Prediction of Inclined Dense Jets. In D. Zeidan, A. Hidalgo, L. T. Zhang, & E. Goncalves Da Silva (Eds.), Computational Fluid Dynamics: Novel Numerical and Computational Approaches: Methodology and Numerics (pp. 185–217). Springer Nature. https://doi.org/10.1007/978-981-97-8152-2_7

Wang, X., & Mohammadian, A. (2021, May). Numerical Simulations of 15-Degree Inclined Dense Jets in Stagnate Water Over a Sloped Bottom. In Canadian Society of Civil Engineering Annual Conference (pp. 63-74). Singapore: Springer Nature Singapore.

Water, P. (2019). *Carlsbad desalination plant*. https://www.sdcwa.org/wp-content/uploads/2025/01/State-of-the-Ocean-Report.pdf

Webster, D. R. Roberts, P. J. & Ra'Ad, L. (2001). Simultaneous DPTV/PLIF measurements of a turbulent jet. Experiments in Fluids, 30(1), 65–72.

Wenten, I. G. Ariono, D. Purwasasmita, M. & Khoirudin. (2017). Integrated processes for desalination and salt production: A mini-review. AIP Conference Proceedings, 1818(1), 020065. https://doi.org/10.1063/1.4976929

Westerweel, J. Elsinga, G. E. & Adrian, R. J. (2013). Particle Image Velocimetry for Complex and Turbulent Flows. Annual Review of Fluid Mechanics, 45(1), 409–436. https://doi.org/10.1146/annurev-fluid-120710-101204

Wilson, E. B. (1927). "Probable inference, the law of succession, and statistical inference." Journal of the American Statistical Association 22(158): 209-212.

Wolthek, N. Raat, K. de Ruijter, J. A. Kemperman, A. & Oosterhof, A. (2013). Desalination of brackish groundwater and concentrate disposal by deep well injection. Desalination and Water Treatment, 51(4–6), 1131–1136. https://doi.org/10.1080/19443994.2012.694205

Wright, S. J. (1984). Buoyant jets in density-stratified crossflow. *Journal of Hydraulic Engineering, 110*(5), 643–656. https://doi.org/10.1061/(ASCE)0733-9429(1984)110:5(643)

Yakhot, V. & Smith, L. M. (1992). The renormalization group, the ?-expansion and derivation of turbulence models. 7(1), 35–61. https://doi.org/10.1007/bf01060210

Yan, X. and A. Mohammadian (2020). "Evolutionary modeling of inclined dense jets discharged from multiport diffusers." Journal of Coastal Research 36(2): 362-371.

Yan, X. Mohammadian, A. & Chen, X. (2020). Numerical modeling of inclined plane jets in a linearly stratified environment. Alexandria Engineering Journal, 59(3), 1857–1867. https://doi.org/10.1016/j.aej.2020.05.023

Yan, Xiaohui, and Abdolmajid Mohammadian. 2019. "Numerical Modeling of Multiple Inclined Dense Jets Discharged from Moderately Spaced Ports." Water 11 (10): 2077.

Yang, L. Wei, Y. Law, A. W.-K. & Huai, W. (2024). Mixing and spreading of inclined dense jets with submerged aquatic canopies. Environmental Fluid Mechanics, 24(3), 439–463. https://doi.org/10.1007/s10652-024-09995-9

Zahiri, A. A., Dehghani, A., & Azamathulla, H. M. (2015). Application of gene-expression programming in hydraulic engineering. In *Handbook of Genetic Programming Applications* (pp. 71–97).

Zajaczkowski, F. J. Haupt, S. E. & Schmehl, K. J. (2011). A preliminary study of assimilating numerical weather prediction data into computational fluid dynamics models for wind prediction. Journal of Wind Engineering and Industrial Aerodynamics, 99(4), 320–329. https://doi.org/10.1016/j.jweia.2011.01.023

Zakharov, V. E. L'vov, V. S. & Falkovich, G. (2012). Kolmogorov Spectra of Turbulence I: Wave Turbulence. Springer Science & Business Media.

Zeitoun, M. A., & McIlhenny, W. F. (1971). *Conceptual designs of outfall systems for desalination plants*. Offshore Technology Conference.

Zeitoun, M. A., Reid, R. O., McHilhenny, W. F., & Mitchell, T. M. (1970). *Model studies of outfall systems for desalination plants*. Research and Development Progress Report, 804.

Zhang, S. Jiang, B. Law, A. W.-K. & Zhao, B. (2016). Large eddy simulations of 45 inclined dense jets. Environmental Fluid Mechanics, 16, 101–121.

Zhang, S. Law, A. W.-K. & Jiang, M. (2017). Large eddy simulations of 45° and 60° inclined dense jets with bottom impact. Journal of Hydro-Environment Research, 15, 54–66. https://doi.org/10.1016/j.jher.2017.02.001

Zhao, W. Li, R. Li, H. Zhang, Y. & Qiu, S. (2021). Numerical analysis of fluid dynamics and thermodynamics in a Stirling engine. Applied Thermal Engineering, 189, 116727.

Appendix A- Data summary

To date, researchers have continued to investigate various parameters of inclined dense jets in the stagnant stationary water.

Table A..2 summarizes all reported geometric and dilution coefficients from the studies discussed in **Chapter 2**, covering experimental work, numerical modeling approaches (including integral models, analytical solutions, and CFD), as well as artificial intelligence-based methods.

It is necessary to note that some studies present geometrical parameters normalized using the Froude number (Fr) and nozzle diameter (D), while others use the characteristic length scale L_m, For the sake of consistency in comparisons, they are all converted to the DFr, using the relation $L_m = 0.9414FrD$. The table is organized by **experimental and numerical studies separately**, and entries are listed **in chronological order by publication year**.

Table A.1 Geometrical and dilution coefficients of single inclined dense jets in stagnant water from previous experimental studies

Study	α°	X_m/DF	Y_m/DF	Yt/DF	Xr/DF	Xi/DF	S_m/DF	S_r/DF	S_i/DF
Morton (1959)	90			1.45					
(Turner 1966)	90			1.74					
(Abraham 1967)	90			1.93					
(Zeitoun et al. 1970)	30			1.15		3.48(Xedge)	0.36		
	45			1.43		3.33	0.42		
	60			1.15		3.28	0.56		
(Philip J. W. Roberts, G. Toms 1987)	60			2.08			0.38		
(Lane-Serff, Linden, and Hillel 1993)	90			1.8					
(Roberts, Ferrier, and Daviero 1997)	60			2.20		2.4			1.6
(Bloomfield and Kerr 2002)	30			0.9					

	45			1.3					
	60			1.76					
(Cipollina et al. 2005)	30	1.95	0.79	1.08		3.03			
	45	1.80	1.17	1.61		2.82			
	60	1.42	1.77	2.32		2.25			
Nemlioglu(Nemlioglu and Roberts 2006)	45								1.7
	60								1.7
	75								1.8
(Kikkert, Davidson, and Nokes 2007)	15	1.46/1.48	0.25/0.26	0.51/0.55	2.2/2.5			1.25	
	30	1.76/1.844	0.56/0.68	1.02/1.21	3.15/3.42			1.45	
	45	1.85	1.06/-	1.58/-	3.27/-		0.56	1.65	
	60	1.62/1.80	1.47/1.74	2.04/2.44	2.81/-		0.53	1.80	
(Ferrari and Querzoli 2010)	45			1.32		3.75			
	60			1.86		3.20			
	75			2.23		1.88			
	90			1.56		-			
(Shao and Law 2010)	30	1.70/1.54	0.66	1.05	2.88/3.00		0.62/0.66	1.18/1.45	
	45	1.69	1.14	1.47	2.83		0.46	1.26	
(Papakonstantis 2011a; Papakonstantis, Christodoulou, and Papanicolaou 2011b)	45	2.1		1.58		3.89(Xedge)	0.52	1.54	1.55
	60	1.84		2.14		3.59	0.56	1.70	1.68
	75	1.15		2.48		2.51	0.51	1.67	1.67
	80	0.88		2.60		2.16			
	85	0.6		2.53		1.60			
	90	-		1.91		-			

(Bashitialshaaer, Larson, and Persson 2012)	30		0.69/0.17(Fr<100 and Fr>100)	0.92/0.21		Xedge 3.12/0.65			
	45		1.0/0.26	1.3/0.31		2.90/0.53			
	60		1.4/0.24	1.7/0.29		2.66/0.36			
(Lai and Lee 2012)	15	1.22	0.21	0.44	2.41		0.27	0.43	
	30	1.95	0.65	0.95	3.18		0.40	0.82	
	38	1.95	0.87	1.20	3.19		0.45	0.99	
	45	2.09	1.19	1.58	3.34		0.45	1.09	
	52	1.87	1.37	1.69	2.87		0.47	1.10	
	60	1.78	1.64	2.08	2.84		0.44	1.07	
(Oliver, Davidson, and Nokes 2013a)	30					3.08			0.84
	45					3.13			1.22
	60					2.76			1.55
(Oliver, Davidson, and Nokes 2013b)	15	1.37	0.24	0.63	2.39		0.25	0.48	
	30	1.75	0.66	1.15	3.08		0.34	0.84	
	45	1.75	1.09	1.65	3.13		0.39	1.22	
	60	1.53	1.61	2.21	2.76		0.42	1.55	
	70	1.13	1.84	2.44	2.00		-	-	
	75	0.97	1.89	2.53	1.67		0.39	1.53	
(Abessi and Roberts 2015)	15			0.76		3.42			0.77
	20			0.92		3.71			0.91
	25			1.15		3.93			1.12
	30			1.35		4.08			1.21
	40			1.70		4.13			1.49
	45			2.09		4.09			1.67

	50			2.30		3.84			1.77
	55			2.50		3.75			1.82
	60			2.63		3.44			1.83
	65			2.81		3.10			1.74
	70			2.94		2.65			1.69
	75			3.04		2.10			1.52
	80			3.09		1.74			1.35
	85			2.99		1.00			1.13
	30	1.70	0.62	1.14	2.96		0.34	0.80	
(Ramakanth 2016)	45	1.83	1.11	1.69	3.09		0.39	1.24	
	60	1.51	1.54	2.22	2.52		0.42	1.49	
	15	1.61		0.59		Xedge 3.43			
	30	1.83		1.12		4.01			
(Papakonstantis and Tsatsara 2018)	35	1.90		1.22		3.98			
	50	1.94		1.83		4.04			
	70	1.22		2.35		3.05			
	15			0.54	1.84			0.84	
	30			0.93	2.86			0.97	
(Azizi, Goharikamel, and Vafaei 2020)	45			1.46	2.97			1.39	
	60			2.15	2.53			1.42	
	75			2.37	1.61			1.26	
	90			2.09					
	15		0.44	0.80		3.55			1.15/0.88
(Tofighian et al. 2022)	30		0.90	1.34		4.14			1.37/0.83
	45		1.63	2.16		4.29			1.89/1.42

	60		2.28	2.86		3.70			1.70/1.04
	75		2.33	3.00		1.92			1.56/1.34
(Galeshi et al. 2023) LIF	60	1.75	1.59	1.98	3.25		0.72	2.075	

Table A..2 Geometrical and dilution coefficients of single inclined dense jets in stagnant water from previous numerical studies (including integral models, analytical solutions, commercial tools, and CFD)

Study	α°	X_m/DF	Y_m/DF	Yt/DF	Xr/DF	Xi/DF	S_m/DF	S_r/DF	S_i/DF
(Jirka 2004)	90			2.337			0.24		
(Kikkert et al. 2007)(Analytical solutions)	15	1.27	0.25/0.26	0.5				1.0	
	30	1.70	0.64	1.03	2.93		-	1.15	
	45	1.87	1.15	1.59	3.03		0.88	1.30	
	60	1.78	1.70	2.217	2.69		0.44	1.45	
(Jirka 2008) - corjet	15	1.32	0.23	0.43		2.00	0.21		0.39-0.63
	30	1.58	0.61	0.87		2.73	0.27		0.56-0.90
	45	1.62	1.05	1.37		2.79	0.29		0.65-1.08
	60	1.32	1.47	1.85		2.35	0.28		0.70-1.18
	90	-	1.88	2.27		-	0.24		0.66-1.16
(Oliver, Davidson, and Nokes 2008)-KE model	15	1.16	0.20	0.6			0.85		
	30	1.55	0.58	1.05			0.89		
	45	1.65	1.00	1.54			0.83		
	60	1.41	1.39	1.95			0.81		
(Lai and Lee 2012)-VISJET	15	1.19	0.21	0.44	2.15		0.24	0.41	
	30	1.52	0.56	0.86	2.65		0.31	0.64	
	38	1.58	0.77	1.10	2.77		0.32	0.73	

	45	1.58	1.00	1.33	2.78		0.32	0.77	
	52	1.52	1.20	1.55	2.64		0.31	0.81	
	60	1.34	1.42	1.78	2.40		0.29	0.83	
(Palomar, Lara, and Losada 2012)	30	1.51 Corjet 1.30 UM3 1.46 JetLag	0.58 0.47 0.53	0.94 0.79 1.04		2.56 2.27 2.56			0.56 0.55 0.63
	45	1.52 Corjet 1.32 1.52	0.99 0.85 0.95	1.41 1.24 1.27		2.65 2.32 2.68			0.65 0.63 0.76
	60	1.20 1.09 1.32	1.39 1.16 1.36	1.85 1.60 1.69		2.22 1.97 2.33			0.70 0.62 0.79
(Kheirkhah Gildeh et al. 2015)	30	2.07	0.73	1.21	3.68		0.61	1.212	
	45	2.06	1.36	1.79	3.57		0.414	1.026	
(Nikiforakis, Stamou, and Christodoulou 2015)	30	2.13	0.7	0.99	3.23		0.44	1.0	
	45	1.98	1.15	1.53	3.20		0.49	1.2	
	60	1.83	1.66	2.02	3.09		0.46	1.3	
(Zhang et al. 2016)	45	2.06	1.26	1.46	3.71		0.26	1.06	
(Zhang, Law, and Jiang 2017)	45	1.97(LES) 1.38(RANS	1.13 0.72	1.35 1.04	3.32 2.45	3.78 2.97	0.32 0.45	1.00 0.74	0.82 0.87
	60	1.75	1.70	2.00	2.86	2.67	0.35	1.29	1.10
(Alfaifi, Mohammadian, and Bonakdari 2020)	15	1.21	0.32	0.56	2.26				
	52	1.60	1.12	1.44	2.68				

(Ramezani, Abessi, and Firoozjaee 2021)	30	1.50 1.61	0.55 0.59	0.91 0.95	3.01 2.97			0.65 0.71	
	45	1.65 1.69	1.03 1.14	1.47 1.47	3.02 2.83			0.82 1.26	
(Tahmooresi and Ahmadyar 2021) Sc=0.4~1.0 ave	45	1.65	0.89	1.31	2.81		0.39	0.88	
(Vafa, Azadi, and Firoozabadi 2021) AVE	45	2.15	1.28	1.41	4.04			1.47	
(Tahmooresi and Ahmadyar 2022)-AVE	45	1.68SGDH[5] 1.85SFM[6]	0.91 1.11	1.33 1.55	2.82 3.16		0.35 0.51	0.80 1.36	
(Wang and Mohammadian 2022)-ke	15	1.30		0.5	1.64		0.29	0.36	0.364
(Azadi and Firoozabadi 2022)	45	1.83	1.17		3.12			0.74	
(Tofighian et al. 2022)	15		0.28	0.58		3.28			0.71/0.69
	30		0.64	1.03		3.55			1.02/0.97
	45		1.09	1.53		3.30			1.30/1.13
	60		1.58	2.09		2.89			1.51/1.28
	75		2.00	2.43		1.90			1.59/1.15
(Tahmooresi et al. 2023)	45	1.82	1.10	1.46	3.07		0.46	1.14	
(Galeshi et al. 2023)	60	1.20	1.32	1.89	1.99		0.23	0.50	

[5] SGDH: standard gradient diffusion hypothesis

[6] SFM： scalar flux modeling

Appendix B. GEP equations for dilution (Chap. 5)

Table B..1 GEP equations for dilution (S is normalized with the Fr number)

No. model	Constant in genes	Model formula
M1	G1C3 = 10.2295851617963 G1C4 = 2.3459578234199	$S = \frac{\sqrt{\frac{\frac{x/D}{G1C3}}{alpha}} + (G1C4 \times theta - \tan(Fr))}{Fr}$
M2	G1C2 = -4.5354819513535 G1C4 = -11.6349029445103 G1C3 = -0.566435714140535 G2C0 = 11.2081143944505 G2C1 = 1.30180020581286 G2C2 = -1.98100803439773 G3C3 = 9.13607316903845	$S = S1 + S2 + S3$ $S1 = \frac{alpha}{\frac{(G1C4 + x/D) \times (theta - G1C3)}{(G1C2)^3} + Fr}$ $S2 = \frac{\frac{\sec(Fr^{G2C1})}{Fr + G2C2 - \alpha}}{\sec(\alpha) - \left(\frac{Fr}{G2C0}\right)}$ $S3 = \frac{\left[\ln\left(\frac{x}{DFr}\right) / \ln(\theta + G3C3)\right] / tan\alpha}{\sec\left(\sqrt[3]{\frac{x}{D}}\right)}$
M3	G1C0 = -6.19912320322276 G2C8 = -4.15067881133057 G3C9 = -4.2985320596942;	$S = S1 + S2 + S3$ $S1 = \left(Ln(G1C0 + \alpha) \cdot \left(\mathrm{arccot}(Fr) \cdot \frac{x}{DFr}\right)\right)^4$ $S2 = \left(\frac{Ln(\mathrm{arccot}(Fr + \theta))}{Ln\left(\frac{\alpha}{G2C8} + Fr\right)}\right)^2$

		$S3 = \operatorname{arccsc}\left[G3C9 \cdot \tan\left((Fr - G3C9) \cdot \arctan\left(\frac{x}{D}\right)\right)\right]$
M4	G1C4 = -3.40189825128941 G1C9 = -5.61192449720756 G1C5 = -4.04423200170904 G2C6 = 2.90240180669576	$S = S1 + S2 + S3$ $S1 = \cos\left(\left(\frac{G1C4 \cdot G1C5}{G1C9} \cdot Fr - \exp(Fr)\right) - \cos(\sqrt[3]{\alpha})\right)$ $S2 = \left(\left(\cot\left(\frac{Ln\left(\frac{Fr/(x/D)}{(\theta+\alpha)\cdot G2C6}\right)}{\mathrm{Ln}(10)}\right)\right)^{0.25}\right)^{2}$ $S3 = \left(\cos\left(\frac{\sec(\sec(Fr+\theta))}{\alpha/\exp(\theta)}\right)\right)^{2}$
M5	G1C2 = 7.03988769472335 G1C1 = -9.23420270758926 G1C5 = -6.45608799401837 G1C6 = -3.16385071352275 G2C8 = -7.30829372627644 G3C9 = 5.62836738865731 G3C1 = 1.32650242700332	$S = S1 + S2 + S3$ $S1 = \frac{\frac{Fr}{\frac{G3C1}{G3C5} \cdot \frac{G3C6}{\alpha}}}{(G3C2 + Fr) - \left(\frac{x}{D} - \alpha\right)}$ $S2 = \frac{\theta}{\alpha} + \frac{Fr}{(G2C8 + Fr) + \frac{x}{D} - \alpha}$ $S3 = \frac{\alpha}{Fr - \left(\frac{\frac{x}{D}}{G3C9} + \frac{\theta}{G3C2} - Fr\right)}$

Table B.2 GEP equations for dilution (S is normalized with the Fr number)

No. of Model	Constant in genes	Model formula
MI-1	G1C6 = 4.27020807480449 G1C5 = 5.83555616786764 G1C0 = 5.83827303019891 G1C3 = 9.48484756004517	$\frac{X_i}{D} = (Csc(G1C3) - \theta) \cdot G1C6 + \frac{Fr}{G1C5} \cdot (Fr + G1C0)$
MI-2	G1C6 = 5.99285670033876 G1C8 = -4.33948942533647 G3C7 = -4.58113345744194 G3C2 = 0.339294629652002 G3C1 = 0.554266603416074	$\frac{X_i}{D} = f_1 + f_2 + f_3$ $f_1 = \tan(D * G1C6 * \sin(G1C8) + Csc(\alpha) + \alpha)$ $f_2 = \left(\sqrt{(2\alpha)^4 + e^{Fr}}\right)^{1/3}$ $f_3 = G3C7 - D - \frac{G3C2}{Fr} - \frac{G3C1}{\alpha} - \tan(\alpha)$

Appendix C. GEP equations for Chap.6

No. of Model	Constant	Model
S_i-single gene	G1C4 = -0.102159004750162;	$S_i = Cos(Cos(Sec(G1C4+\alpha)*(\theta+Fr)*\theta))$
S_i-three gene	G2C3 = -2.31226408435389; G3C6 = 0.291264182415375; G3C1 = 6.45259654560991; G3C3 = -7.58415478988006;	$S_i = S_{i1}+S_{i2}+S_{i3}$ $S_{i1} = Log(abs(Sec(\sqrt[4]{Tan(Abs(\alpha^4)})))$ $S_{i2} = Tan(\sqrt[3]{\alpha*\theta*\alpha})*Exp(G2C3)$ $S_{i3} = Log(Exp(Sec(Cos((G3C6-G3C1)-\alpha*G3C3))$
Sr-single gene	G1C8 = 3.06283084133303;	$S_r = Cos(Cot(10^{Cot(\alpha+Fr)})+G1C8)$
Sr-three gene	G1C4 = 6.88920702513827; G2C3 = -4.65208151493881; G2C1 = -18.0677298191119; G3C0 = -2.62175030462074;	$S_r = S_{r1}+S_{r2}+S_{r3}$ $S_{r1} = Sin(\sqrt[3]{G1C4^2+Fr-(\theta-\alpha)})$ $S_{r2} = Sin(Ln(\alpha^2-G2C1*\theta)-G2C3^2)$ $S_{r3} = \sin\sqrt[3]{Sin(\alpha*\alpha)-(G3C0-\theta)}$
Sm-single gene	G1C8 = -5.58488723410749e-02;	$S_m = Ln(\sqrt[3]{\sqrt[3]{\min(\alpha-Fr),\frac{\alpha+G1C8}{2}}})$
Sm-three gene	G2C6 = 5.53814355906857;	$S_m = S_{m1}+S_{m2}+S_{r3}$ $S_{m1} = \sqrt{\sqrt{Log(Sec(\alpha)+Fr)-\cot(\alpha)}}$ $S_{m2} = Csc(Log(10^{G2C6}+\theta^4)*G2C6)$ $S_{m3} = Ln(\sqrt[4]{Log(Exp(\alpha))+Tan(Cot(\alpha)})$
Xi -single gene	G1C2 = -6.20602832117679;	$X_i = \sqrt[3]{Csc\ (G1C7)*(\alpha-Fr)-(\theta+Fr)*G1C2}$

	G1C7 = -0.402941679128391;	
Xi- three gene	G1C9 = 1.96334917737292; G1C3 = -9.66368602557451; G1C8 = 3.68383498489334; G2C3 = -3.0100405896176; G3C2 = 8.70091434878663; G3C5 = 2.19087337683844	$X_i = X_{i1} + X_{i2} + X_{i3}$ $X_{i1} = Cot\left(\sqrt{G1C8 * G1C3}\right) + \frac{Cos(\alpha)}{G1C9}$ $X_{i2} = pi - \sqrt{Fr} - G2C3 + \frac{Cos(G2C3)}{Fr/\alpha}$ $X_{i3} = \sqrt{\sqrt[4]{\theta} * \log G3C5} - \sqrt{G3C2/\alpha}$
Xt-single gene	G1C9 = -6.53370116000854; G1C2 = -1.05380202459897;	$X_t = Sin\left((G1C9 - \alpha) - G1C2^{\alpha}\right) + \sqrt[4]{\alpha - \theta}$
Xt-three gene	G1C8 = -4.11209994466332; G1C1 = 7.6385615277439; G2C9 = -5.06539498972863; G3C9 = 3.27435002330348; G3C1 = -0.337752249933914;	$X_t = X_{t1} + X_{t2} + X_{t3}$ $X_{t1} = Sec(\sqrt[3]{Cos\theta + \left(\frac{\alpha}{G1C1}\right) + G1C8 + \alpha})$ $X_{t2} = Cos\left(Fr^4 * (Fr - \alpha)\right) + \sqrt[4]{10^{G2C9}}$ $X_{t3} = (\alpha + Fr) * G3C9^{(G3C1-\theta)} + e + G3C9 + \alpha$
Yt-single gene	-	$Y_t = \sqrt[3]{Log^3(\alpha - \theta) + Cos(\alpha * \alpha)}$
Yt-three gene	G1C5 = 1.10263264473403; G1C8 = 3.27155894041936; G2C6 = -5.98336513293766; G2C4 = -0.649404855607569; G2C2 = -15.4178716146658; G2C7 = 9.05758842738121; G2C1 = 0.493484298226875; G3C4 = 6.84499649037141; G3C1 = 1.77566522521933;	$Y_t = Y_{t1} + Y_{t2} + Y_{t3}$ $Y_{t1} = Sec(Sin^3(G3C8) + 10^{\theta} + G1C5)$ $Y_{t2} = \frac{\sqrt[4]{Fr - G2C1}}{G2C6 - G2C4} + 3.1415;$ $Y_{t3} = Ln\left(\left(Sin(G3C4^{G3C4})\right)^{Tan\alpha - G3C1 + \alpha}\right)$
Xr-single gene	G1C9 = 0.343561341853936; G1C4 = 1.29245887630848;	$X_r = Cot^2\left(Sec(G1C4)\right) - Cos(\alpha^4 - G1C9)$

Xr-three gene	G1C9 = 9.86576912473341; G2C1 = 3.97593890194403; G3C3 = -0.283378531687055;	$X_r = X_{r1} + X_{r2} + X_{r3}$ $X_{r1} = Exp(Tan(\sqrt{\sqrt{G1C9}} - \sqrt{\log \alpha})$ $X_{r2} = Sin\left(Sec\left(Csc(\alpha)\right) * \left(Cos(\alpha) - \sqrt{G2C1}\right)\right)$ $X_{r3} = Tan(\sqrt{\sqrt{\sqrt[3]{Sec(Sin(G3C1 + \theta))}}})$
Sb-single gene	G1C9 = 1575.58788254641; G1C5 = 2.82514334609701; G1C2 = 0.167310086779926;	$S_b = \tan\left\{Log_{10}\sqrt{\left(\alpha * G1C5 * \frac{X}{DF} + Cot(Fr * \alpha)\right)^3 + \left(Csc\left(Sin\left(G1C2 * \frac{\frac{X}{DF}}{\exp\left(\frac{X}{DF}\right)}\right)\right) - G1C9\right)} - Fr\right\}$
Sb-three gene	G1C5 = 1.27984768790066; G1C1 = 8.48969334128186; G2C1 = 20.5579922758387; G2C8 = -0.259434522990706; G2C6 = 10.5142028004211; G2C7 = 6.34662657554122; G3C4 = 0.436657995756566; G3C8 = -4.29181798760948; G3C5 = -1.13257579384747;	$S_b = S_{b1} + S_{b2} + S_{b3}$ $S_{b1} = Tan\left(Tan\left(Sin\left(Cos^4\left(\left(\frac{\log\left(G1C1 * \sqrt{Sec\sqrt[3]{\theta} + Sin\left(\frac{X}{DF} + Fr^2\right)}\right)}{\frac{X}{DF} + \alpha}\right) * G1C5\right)\right)\right)\right)$ $S_{b2} = Ln\left(\frac{Cos\left(Cost\left(Cos\left(Sin\left(Exp\left(\sqrt[4]{\alpha - \left(\left(\left(\frac{\log(G2C7)}{\log\left(\frac{X}{DF}\right)}\right)^3 + G2C8 * G2C6\right) + Cos\left(Cos(\theta)\right)\right)}\right)\right)\right)\right)\right)}{\sqrt[4]{G2C1^4}}\right)$ $S_{b3} = \frac{\frac{X}{DF}}{Cos\left(Tan\left(CosG3C4 * \left(\left(\log\left(Cot\left(Tan\left(Tan(\alpha)\right) - (G3C8 - G3C5) - \left(Tan(\alpha)\right)^3\right) + \frac{X}{DF}\right)\right)^3\right)^2\right)\right)}$

Appendix D: Key OpenFOAM case files for numerical simulations

This appendix contains selected OpenFOAM input files used in the numerical simulations described in **Chapter 4** and **Chapter 7.** The files include mesh generation dictionaries, solver settings, and relevant boundary and initial condition configurations.

Large eddy simulation

0 folder- alpha.concentration

```
/*--------------------------------*- C++ -*----------------------------------*\
| =========                 |                                                 |
| \\      /  F ield         | OpenFOAM: The Open Source CFD Toolbox           |
|  \\    /   O peration     | Version:  2.1.0                                 |
|   \\  /    A nd           | Web:      www.OpenFOAM.org                      |
|    \\/     M anipulation  |                                                 |
\*---------------------------------------------------------------------------*/
FoamFile
{
    version     2.0;
    format      ascii;
    class       volScalarField;
    location    "0";
    object      alpha.sludge;
}
// * * * * * * * * * * * * * * * * * * * * * * * * * * * * * * * * * * * * * //
dimensions      [0 0 0 0 0 0 0];
internalField   uniform 0;
boundaryField
{
    inlet
    {
        type            fixedValue;
        value           uniform 1;
    }
    tubewall
    {
        type            zeroGradient;
    }
    tubebottom
```

```
    {
      type          zeroGradient;
    }
    leftwall
    {
      type          zeroGradient;
    }
rightwall
    {
      type          zeroGradient;
    }
  bottomwall
    {
      type          zeroGradient;
    }
    atmosphere
    {
     type          symmetry;
    }
    backwall
    {
      type          zeroGradient;
    }
frontwall
    {
      type          zeroGradient;
    }
}
// ************************************************************************* //
```

0 folder- U

```
/*--------------------------------*- C++ -*----------------------------------*\
| =========                 |                                                 |
| \\      / F ield          | OpenFOAM: The Open Source CFD Toolbox           |
|  \\    /  O peration      | Version:  2.1.0                                 |
|   \\  /   A nd            | Web:      www.OpenFOAM.org                      |
|    \\/    M anipulation   |                                                 |
\*---------------------------------------------------------------------------*/
FoamFile
{
    version     2.0;
    format      ascii;
    class       volVectorField;
    location    "0";
    object      U;
}
// * * * * * * * * * * * * * * * * * * * * * * * * * * * * * * * * * * * * * //
dimensions      [0 1 -1 0 0 0 0];
internalField   uniform (1e-10 0 0);
boundaryField
{
    inlet
    {
        type            fixedValue;
        value           uniform (0.365   0.633  0);
    }
tubewall
    {
        type            fixedValue;
        value           uniform (0 0 0);
    }
    tubebottom
    {
        type            fixedValue;
        value           uniform (0 0 0);
    }
    leftwall
    {
        type            fixedValue;
        value           uniform (0 0 0);
    }
```

```
rightwall
    {
    type        zeroGradient;
}
  bottomwall
{
    type        fixedValue;
    value       uniform (0 0 0);
}
atmosphere
{
    type        symmetry;
}
backwall
{
    type        fixedValue;
    value       uniform (0 0 0);
}
frontwall
{
    type        fixedValue;
    value       uniform (0 0 0);
}
}
// ************************************* //
```

Constant-transportProperties

```
/*--------------------------------*- C++ -*----------------------------------*\
| =========                 |                                                 |
| \\      /  F ield         | OpenFOAM: The Open Source CFD Toolbox           |
|  \\    /   O peration     | Version:  2.1.0                                 |
|   \\  /    A nd           | Web:      www.OpenFOAM.org                      |
|    \\/     M anipulation  |                                                 |
\*---------------------------------------------------------------------------*/
FoamFile
{
    version     2.0;
    format      ascii;
    class       dictionary;
    location    "constant";
    object      transportProperties;
}
// * * * * * * * * * * * * * * * * * * * * * * * * * * * * * * * * * * * * //
transportModel  Newtonian;
Dab          Dab [0 2 -1 0 0 0 0]     1e-06;
alphatab      alphatab [0 0 0 0 0 0 0] 1;

phases (sludge water);
sludge
{
    transportModel  Newtonian;
    nu              nu [0 2 -1 0 0 0 0] 1e-06;
    rho             rho [1 -3 0 0 0 0 0] 1052;
}
water
{
    transportModel  Newtonian;
    nu              nu [0 2 -1 0 0 0 0] 1e-06;
    rho             rho [1 -3 0 0 0 0 0] 1000;
}
// ************************************************************************* //
```

Constant-turbulenceProperties

```
/*--------------------------------*- C++ -*----------------------------------*\
| =========                 |                                                 |
| \\      /  F ield         | OpenFOAM: The Open Source CFD Toolbox           |
|  \\    /   O peration     | Version:  2.1.0                                 |
|   \\  /    A nd           | Web:      www.OpenFOAM.org                      |
|    \\/     M anipulation  |                                                 |
\*---------------------------------------------------------------------------*/
FoamFile
{
    version     2.0;
    format      ascii;
    class       dictionary;
    location    "constant";
    object      turbulenceProperties;
}
// * * * * * * * * * * * * * * * * * * * * * * * * * * * * * * * * * * * * * //
simulationType  LES;
LES
{
   LESModel      kEqn;
    turbulence      on;
    printCoeffs     on;
    delta           cubeRootVol;
  cubeRootVolCoeffs
    {
        deltaCoeff      1;
    }
   dynamicKEqnCoeffs
{
filter simple;
}
     vanDriestCoeffs
    {
        delta           cubeRootVol;
        cubeRootVolCoeffs
        {
            deltaCoeff      1;
        }

        smoothCoeffs
        {
```

```
            delta           cubeRootVol;
            cubeRootVolCoeffs
            {
                deltaCoeff      1;
            }

            maxDeltaRatio   1.1;
        }
        Aplus           26;
        Cdelta          0.158;
    }
}
// ************************************************************************* //
```

System- snappyHexMeshDict

```
/*--------------------------------*- C++ -*----------------------------------*\
| =========                 |                                                 |
| \\      /  F ield         | OpenFOAM: The Open Source CFD Toolbox           |
|  \\    /   O peration     | Version:  4.0                                   |
|   \\  /    A nd           | Web:      www.OpenFOAM.org                      |
|    \\/     M anipulation  |                                                 |
\*---------------------------------------------------------------------------*/
FoamFile
{
    version     2.0;
    format      ascii;
    class       dictionary;
    object      snappyHexMeshDict;
}

// * * * * * * * * * * * * * * * * * * * * * * * * * * * * * * * * * * * * //
castellatedMesh true;
snap            true;
addLayers       false;


geometry
{
    atmosphere.stl
    {
      type triSurfaceMesh;
      name atmosphere;
    }

    inlet.stl
    {
      type triSurfaceMesh;
      name inlet;
    }
    tubewall.stl
    {
      type triSurfaceMesh;
      name tubewall;
    }
```

```
  tubebottom.stl
  {
    type triSurfaceMesh;
    name tubebottom;
  }

  leftwall.stl
  {
    type triSurfaceMesh;
    name leftwall;
  }

  rightwall.stl
  {
    type triSurfaceMesh;
    name rightwall;
  }

  backwall.stl
  {
    type triSurfaceMesh;
    name backwall;
  }

  frontwall.stl
  {
    type triSurfaceMesh;
    name frontwall;
  }

  bottomwall.stl
  {
    type triSurfaceMesh;
    name bottomwall;
  }

box2
  {
   type searchableBox;
    min  (0.15 0 0.3);
   max  (0.8 0.2 0.5);
  }
```

```
    box3
    {
      type searchableBox;
       min  (0.1 0 0.25);
       max  (1.2 0.3 0.55);
    }
    box4
    {
      type searchableBox;
     min  (0.05 0 0.25);
     max  (1.5 0.4 0.65);
    }

};
castellatedMeshControls
{
    maxLocalCells 1000000;
    maxGlobalCells 5000000;
    minRefinementCells 0;
    nCellsBetweenLevels 3;

    features
    (
        {
            file "atmosphere.eMesh";
            level 2;
        }

         {
            file "inlet.eMesh";
            level 3;
        }

        {
            file "tubebottom.eMesh";
            level 3;
        }

         {
            file "tubewall.eMesh";
            level 3;
        }
```

```
    {
        file "leftwall.eMesh";
        level 2;
    }

    {
        file "rightwall.eMesh";
        level 2;
    }

    {
        file "bottomwall.eMesh";
        level 2;
    }

    {
        file "rightwall.eMesh";
        level 2;
    }

    {
        file "frontwall.eMesh";
        level 2;
    }


);
refinementSurfaces
{
    atmosphere
    {
        level (1 1);
    }
    inlet
    {
        level (4 4 ); //(2 3)
    }
     tubebottom
    {
```

```
        level (4 4 );
    }
    tubewall
    {
        level (4 4 );
    }
    leftwall
    {
        level (1 1);
    }
    rightwall
    {
        level (1 1);
    }
   frontwall
    {
        level (1  1);
    }

    backwall
    {
        level (1 2);
    }

    bottomwall
    {
        level (2 2);
    }
}
resolveFeatureAngle 80;

refinementRegions
 {
box2
    {
       mode  inside;
        levels ((2 3));
    }
   box3
    {
        mode  inside;
        levels ((2 2));
```

```
    }
    box4
    {
        mode  inside;
        levels ((1 1));
   }
  }

  locationInMesh (0.2122546 0.2254 0.395);
  allowFreeStandingZoneFaces true;
}
snapControls
{
  nSmoothPatch 3;
  tolerance 1.0;
  nSolveIter 400;
  nRelaxIter 5;
   nFeatureSnapIter 10;
   implicitFeatureSnap false;
   explicitFeatureSnap true;
   multiRegionFeatureSnap true;
}
addLayersControls
{
  relativeSizes true;

  layers
  {
    bottomwall
     {
        nSurfaceLayers 10;
          }
  }
  expansionRatio 1.0;
  finalLayerThickness 0.3;
  minThickness 0.00001;
  nGrow 0;
  featureAngle 130;
  nRelaxIter 5;
  nSmoothSurfaceNormals 3;
  nSmoothNormals 3;
  nSmoothThickness 10;
```

```
        maxFaceThicknessRatio 0.3;
        maxThicknessToMedialRatio 0.3;
        minMedianAxisAngle 90;
        nBufferCellsNoExtrude 0;
        nLayerIter 50;
        nRelaxedIter 20;
    }

meshQualityControls

    {
        //- Maximum non-orthogonality allowed. Set to 180 to disable.
        maxNonOrtho 65;
        //- Max skewness allowed. Set to <0 to disable.
        maxBoundarySkewness 20;
         maxInternalSkewness 4;
        //- Max concaveness allowed. Is angle (in degrees) below which concavity
        //  is allowed. 0 is straight face, <0 would be convex face.
        //  Set to 180 to disable.
       maxConcave 80;
        //- Minimum pyramid volume. Is absolute volume of cell pyramid.
        //  Set to a sensible fraction of the smallest cell volume expected.
        //  Set to very negative number (e.g. -1E30) to disable.
        minVol 1e-13;
        //- Minimum quality of the tet formed by the face-centre
        //  and variable base point minimum decomposition triangles and
        //  the cell centre.  Set to very negative number (e.g. -1E30) to
        //  disable.
        //     <0 = inside out tet,
        //      0 = flat tet
        //      1 = regular tet
        minTetQuality 1e-30;
        //- Minimum face area. Set to <0 to disable.
        minArea -1;
        //- Minimum face twist. Set to <-1 to disable. dot product of face normal
        //  and face centre triangles normal
        minTwist 0.05;

        //- Minimum normalised cell determinant
        //  1 = hex, <= 0 = folded or flattened illegal cell
       minDeterminant 0.001;
        //- minFaceWeight (0 -> 0.5)
```

```
            minFaceWeight 0.05;

            //- minVolRatio (0 -> 1)
            minVolRatio 0.01;
            //must be >0 for Fluent compatibility
            minTriangleTwist -1;
            //- If >0 : preserve single cells with all points on the surface if the
            //  resulting volume after snapping (by approximation) is larger than
            //  minVolCollapseRatio times old volume (i.e. not collapsed to flat cell).
            //  If <0 : delete always.
            minVolCollapseRatio 0.5;
            // Advanced
            //- Number of error distribution iterations
            nSmoothScale 4;
            //- Amount to scale back displacement at error points
            errorReduction 0.75;
            // Optional : some meshing phases allow usage of relaxed rules.
            // See e.g. addLayersControls::nRelaxedIter.
            relaxed
            {
                //- Maximum non-orthogonality allowed. Set to 180 to disable.
                maxNonOrtho 75;
            }
        }
        mergeTolerance 1E-6;
        writeFlags
        (
            scalarLevels
            layerSets
            layerFields
        );
        mergeTolerance 1E-6;

// ************************************************************************* //
```

System-fvSolution

```
/*--------------------------------*- C++ -*----------------------------------*\
        | =========                 |                                          |
        | \\      /  F ield         | OpenFOAM: The Open Source CFD Toolbox    |
        |  \\    /   O peration     | Version:  4.1                            |
        |   \\  /    A nd           | Web:      www.OpenFOAM.org               |
```

```
|   \\/     M anipulation  |                                          |
\*---------------------------------------------------------------------------*/
FoamFile
{
    version     2.0;
    format      ascii;
    class       dictionary;
    location    "system";
    object      fvSolution;
}
// * * * * * * * * * * * * * * * * * * * * * * * * * * * * * * * * * * * * * //
solvers
{
    "alpha.sludge.*"
    {
        nAlphaSubCycles     2;
        nAlphaCorr          1;

        solver          smoothSolver;
        smoother        GaussSeidel;
        tolerance       1e-9;
        relTol          0;
        nSweeps         1;
}
    pcorr
    {
        solver          PCG;
        preconditioner  DIC;
        tolerance       1e-5;
        relTol          0;
    }
    pcorrFinal
    {
        solver          PCG;
        preconditioner  DIC;
        tolerance       1e-5;
        relTol          0;
    }
 omegaFinal
    {
        solver          PBiCG;
        preconditioner  DILU;
```

```
        tolerance       1e-5;
        relTol          0;
    }
    p_rgh
    {
        solver          PCG;
        preconditioner  DIC;
        tolerance       1e-07;
        relTol          0.05;
    }
    p
    {
        solver          PCG;
        preconditioner  DIC;
        tolerance       1e-06;
        relTol          0.1;
    }
  pFinal
        {
        solver          PCG;
        preconditioner  DIC;
        tolerance       1e-06;
        relTol          0.1;
    }
    p_rghFinal
    {
        $p_rgh;
        relTol          0;
    }
   SFinal
    {
        solver          PBiCG;
        preconditioner  DILU;
        tolerance       1e-05;
        relTol          0;
    }
    S
    {
        solver          PBiCG;
        preconditioner  DILU;
        tolerance       1e-05;
        relTol          0;
```

```
    }
        "(U|k|epsilon|omega).*"
    {
        solver          smoothSolver;
        smoother        symGaussSeidel;
        tolerance       1e-06;
        relTol          0;
        minIter         1;
    }
}
PIMPLE
{
    momentumPredictor   no;
    nOuterCorrectors    1;
    nCorrectors         2;
    nNonOrthogonalCorrectors 0;
    pRefCell        1001;
    pRefValue       0;
}

// ************************************************************************* //
```

System-fvSchemes

```
/*--------------------------------*- C++ -*----------------------------------*\
  =========                 |
  \\      /  F ield         | OpenFOAM: The Open Source CFD Toolbox
   \\    /   O peration     | Website:  https://openfoam.org
    \\  /    A nd           | Version:  6
     \\/     M anipulation  |
\*---------------------------------------------------------------------------*/
FoamFile
{
```

```
    version     2.0;
    format      ascii;
    class       dictionary;
    location    "system";
    object      fvSchemes;
}
// * * * * * * * * * * * * * * * * * * * * * * * * * * * * * * * * * * * * * //

ddtSchemes
{
    default         Euler;
}
gradSchemes
{

    default         Gauss linear;
    grad(p)         Gauss linear;
    grad(U)         Gauss linear;
}

divSchemes
{
    default         none;

    div(phi,U)      Gauss cubic;
    div(phi,S)      Gauss limitedLinear 1;
    div(rhophi,S)      Gauss limitedLinear 1;
    div(phi,k)      Gauss limitedLinear 1;
    div(phi,epsilon) Gauss limitedLinear 1;
    div(phi,R)      Gauss limitedLinear 1;
    div(rho,R)      Gauss limitedLinear 1;
    div(R)          Gauss linear;
div(phi,alpha)  Gauss vanLeer;
    div(phi,nuTilda) Gauss limitedLinear 1;
    div(rhoPhi,U)  Gauss cubic;
    div((nuEff*dev(T(grad(U))))) Gauss linear;
    div(nonlinearStress) Gauss linear;
    div((nuEff*dev2(T(grad(U))))) Gauss linear;
    div(((rho*nuEff)*dev2(T(grad(U))))) Gauss linear;
  }

laplacianSchemes
```

```
{
    default         Gauss linear corrected;
}

interpolationSchemes
{
    default        linear;
    interpolate(U)  linear;
}

snGradSchemes
{
    default        corrected;
}

fluxRequired
{
    default        no;
    p              ;
}

 wallDist
      {
          method meshWave;
         // Optional entry enabling the calculation
         // of the normal-to-wall field
         nRequired false;
     }

// ************************************************************************* //
```

System-surfaceFeatureExtractDict

```
/*--------------------------------*- C++ -*----------------------------------*\
| =========                 |                                                 |
| \\      /  F ield         | OpenFOAM: The Open Source CFD Toolbox           |
|  \\    /   O peration     | Version:  2.3.0                                 |
|   \\  /    A nd           | Web:      www.OpenFOAM.org                      |
|    \\/     M anipulation  |                                                 |
\*---------------------------------------------------------------------------*/
FoamFile
{
    version     2.0;
```

```
        format      ascii;
        class       dictionary;
        object      surfaceFeatureExtractDict;
    }
// * * * * * * * * * * * * * * * * * * * * * * * * * * * * * * * * * * * * * //
    inlet.stl
    {
        extractionMethod    extractFromSurface; // extractFromFile or extractFromSurface
        extractFromSurfaceCoeffs
        {includedAngle   150;}
        writeObj              yes;    // Write options
    }
    rightwall.stl
    {
        extractionMethod    extractFromSurface; // extractFromFile or extractFromSurface
        extractFromSurfaceCoeffs
        {includedAngle   150;}
        writeObj              yes;    // Write options
    }
    atmosphere.stl
    {
        extractionMethod    extractFromSurface; // extractFromFile or extractFromSurface
        extractFromSurfaceCoeffs
        {includedAngle   150;}
        writeObj              yes;    // Write options
    }
    tubewall.stl
    {
        extractionMethod    extractFromSurface; // extractFromFile or extractFromSurface
        extractFromSurfaceCoeffs
        {includedAngle   150;}
        writeObj              yes;    // Write options
    }
    tubebottom.stl
    {
        extractionMethod    extractFromSurface; // extractFromFile or extractFromSurface
        extractFromSurfaceCoeffs
        {includedAngle   150;}
        writeObj              yes;    // Write options
    }
    frontwall.stl
    {
```

```
    extractionMethod    extractFromSurface; // extractFromFile or extractFromSurface
    extractFromSurfaceCoeffs
    {includedAngle   150;}
    writeObj              yes;    // Write options
}
bottomwall.stl
{
    extractionMethod    extractFromSurface; // extractFromFile or extractFromSurface
    extractFromSurfaceCoeffs
    {includedAngle   150;}
    writeObj              yes;    // Write options
}
leftwall.stl
{
    extractionMethod    extractFromSurface; // extractFromFile or extractFromSurface
    extractFromSurfaceCoeffs
    {includedAngle   150;}
    writeObj              yes;    // Write options
}
backwall.stl
{
    extractionMethod    extractFromSurface; // extractFromFile or extractFromSurface
    extractFromSurfaceCoeffs
    {includedAngle   150;}
    writeObj              yes;    // Write options
}
// ************************************************************************* //
```

Reynolds-Averaged Navier–Stokes

For the RANS simulations, the 0 folder files remain unchanged. Differences are mainly in the turbulenceProperties, fvSchemes, and fvSolution files.

Constant-turbulenceProperties

```
/*--------------------------------*- C++ -*----------------------------------*\
| =========                 |                                                 |
| \\      /  F ield         | OpenFOAM: The Open Source CFD Toolbox           |
|  \\    /   O peration     | Version:  4.1                                   |
|   \\  /    A nd           | Web:      www.OpenFOAM.org                      |
|    \\/     M anipulation  |                                                 |
\*---------------------------------------------------------------------------*/
```

```
FoamFile
{
    version     2.0;
    format      ascii;
    class       dictionary;
    location    "constant";
    object      turbulenceProperties;
}

// * * * * * * * * * * * * * * * * * * * * * * * * * * * * * * * * * * * * * //
simulationType RAS;
RAS
{
    RASModel       realizableKE; // RANS turbulence model used. Replace with kEpsilon, qZeta , etc. as needed.

    turbulence      on;
    printCoeffs     on;
}
// ************************************************************************* //
```

System-fvSchemes

```
/*--------------------------------*- C++ -*----------------------------------*\
  =========                 |
  \\      /  F ield         | OpenFOAM: The Open Source CFD Toolbox
   \\    /   O peration     | Website:  https://openfoam.org
    \\  /    A nd           | Version:  6
     \\/     M anipulation  |
\*---------------------------------------------------------------------------*/
FoamFile
{
    version     2.0;
    format      ascii;
    class       dictionary;
    location    "system";
```

```
    object      fvSchemes;
}
// * * * * * * * * * * * * * * * * * * * * * * * * * * * * * * * * * * * * * //

ddtSchemes
{
    default         Euler;
}

gradSchemes
{

    default         Gauss linear;
    grad(p)         Gauss linear;
    grad(U)         Gauss linear;
}
divSchemes
{
    default         none;


  default         none;
    div(((rho*nuEff)*dev2(T(grad(U))))) Gauss linear;
    div(phi,k)      Gauss limitedLinear 1;
    div(phi,epsilon) Gauss limitedLinear 1;
    div(phi,alpha)  Gauss limitedLinear 1;
    div(rhoPhi,U)  Gauss linear;
     div((nuEff*dev(T(grad(U))))) Gauss linear;
}
laplacianSchemes
{
    default          Gauss linear corrected;
}
interpolationSchemes
{
    default         linear;
    interpolate(U)  linear;
}
snGradSchemes
{
    default         corrected;
}
```

```
fluxRequired
{
    default         no;
    p               ;
}
 wallDist
       {
            method meshWave;
           // Optional entry enabling the calculation
           // of the normal-to-wall field
           nRequired false;
      }
// ************************************************************************* //
```

System-fvSoluiton

```
/*--------------------------------*- C++ -*----------------------------------*\
  =========                 |
  \\      / F ield         | OpenFOAM: The Open Source CFD Toolbox
   \\    /  O peration     | Website:  https://openfoam.org
    \\  /   A nd           | Version:  6
     \\/    M anipulation  |
\*---------------------------------------------------------------------------*/
FoamFile
{
    version     2.0;
    format      ascii;
    class       dictionary;
    location    "system";
    object      fvSolution;
}
// * * * * * * * * * * * * * * * * * * * * * * * * * * * * * * * * * * * * * //

solvers
{
 "alpha.sludge.*"
    {
        nAlphaSubCycles     2;
        nAlphaCorr          1;
        solver          smoothSolver;
        smoother        GaussSeidel;
        tolerance       1e-9;
        relTol          0;
        nSweeps         1;
}
      p_rgh
    {
        solver          GAMG;
        tolerance       1e-7;
        relTol          0.01;
        smoother        GaussSeidel;
    }
  p_rghFinal
    {
        $p_rgh;
        relTol          0;
```

```
    }
p
    {
        solver          GAMG;
        tolerance        1e-7;
        relTol          0.01;

        smoother        DICGaussSeidel;

    }

    pFinal
    {
        $p;
        relTol          0;
    }

            "(U|k|epsilon|nuTilda)"

    {
        solver          smoothSolver;
        smoother        symGaussSeidel;
        tolerance       1e-05;
        relTol          0.1;
    }

    "(U|k|epsilon|nuTilda)Final"
    {
        $U;
        tolerance       1e-05;
        relTol          0;
    }
    U
    {
        solver          PBiCG;
        preconditioner  DILU;
        tolerance       1e-05;
        relTol          0;
    }

    SFinal
    {
```

```
        solver          PBiCG;
        preconditioner  DILU;
        tolerance       1e-05;
        relTol          0;
    }
    S
    {
        solver          PBiCG;
        preconditioner  DILU;
        tolerance       1e-05;
        relTol          0;
    }
    T
    {
        solver          PBiCG;
        preconditioner  DILU;
        tolerance       1e-05;
        relTol          0;
    }

    rhoS
    {
        solver          PBiCG;
        preconditioner  DILU;
        tolerance       1e-05;
        relTol          0;
    }
    rhoT
    {
        solver          PBiCG;
        preconditioner  DILU;
        tolerance       1e-05;
        relTol          0;
    }
//

    k
    {
        solver          PBiCG;
        preconditioner  DILU;
        tolerance       1e-05;
        relTol          0;
```

```
    }

    epsilon
    {
        solver          PBiCG;
        preconditioner  DILU;
        tolerance       1e-05;
        relTol          0;
    }
omegaFinal
    {
        solver          PBiCG;
        preconditioner  DILU;
        tolerance       1e-05;
        relTol          0;
    }
    R
    {
        solver          PBiCG;
        preconditioner  DILU;
        tolerance       1e-05;
        relTol          0;
    }

    nuTilda
    {
        solver          PBiCG;
        preconditioner  DILU;
        tolerance       1e-05;
        relTol          0;
    }
}

PISO
{
    nCorrectors     2;
    nNonOrthogonalCorrectors 0;
    pRefCell        0;
    pRefValue       0;
}
PIMPLE
{
```

```
        momentumPredictor   yes;
        nOuterCorrectors 1;
        nCorrectors     2;
        nNonOrthogonalCorrectors 0;
        pRefCell        1001;
        pRefValue       0;
    }
    relaxationFactors
    {
        fields
        {
        }
        equations
        {
            "p.*"           0.3;
            "U.*"           0.7;
            "k.*"           0.7;
            "epsilon.*"     0.7;
        }
    }
// ************************************************************************* //
```